Paulo Ribeiro Maria Raposo *Editors* 

# Photoptics 2015

Revised Selected Papers



# **Springer Proceedings in Physics**

Volume 181

More information about this series at http://www.springer.com/series/361

Paulo Ribeiro · Maria Raposo Editors

# Photoptics 2015

Revised Selected Papers



Editors
Paulo Ribeiro
Faculdade de Ciências e Tecnologia
Universidade Nova de Lisboa
Caparica
Portugal

Maria Raposo Faculdade de Ciências e Tecnologia Universidade Nova de Lisboa Caparica Portugal

ISSN 0930-8989 ISSN 1867-4941 (electronic) Springer Proceedings in Physics ISBN 978-3-319-30135-8 ISBN 978-3-319-30137-2 (eBook) DOI 10.1007/978-3-319-30137-2

Library of Congress Control Number: 2015958853

#### © Springer International Publishing Switzerland 2016

This work is subject to copyright. All rights are reserved by the Publisher, whether the whole or part of the material is concerned, specifically the rights of translation, reprinting, reuse of illustrations, recitation, broadcasting, reproduction on microfilms or in any other physical way, and transmission or information storage and retrieval, electronic adaptation, computer software, or by similar or dissimilar methodology now known or hereafter developed.

The use of general descriptive names, registered names, trademarks, service marks, etc. in this publication does not imply, even in the absence of a specific statement, that such names are exempt from the relevant protective laws and regulations and therefore free for general use.

The publisher, the authors and the editors are safe to assume that the advice and information in this book are believed to be true and accurate at the date of publication. Neither the publisher nor the authors or the editors give a warranty, express or implied, with respect to the material contained herein or for any errors or omissions that may have been made.

Printed on acid-free paper

This Springer imprint is published by Springer Nature
The registered company is Springer International Publishing AG Switzerland

#### **Preface**

This book includes extended versions of a set of selected papers from PHOTOPTICS 2015 (the 4th International Conference on Photonics, Optics and Laser Technology), held in Berlin, Germany, in 2015, organized and sponsored by the Institute for Systems and Technologies of Information, Control and Communication (INSTICC).

PHOTOPTICS 2015 was held in cooperation with the European Optical Society (EOS) and The Japan Society of Applied Physics (JSAP). It was held in collaboration with the International Year of Light 2015 and technically sponsored by the IEEE Photonics Society and Photonics21. The Centre of Physics and Technological Research (CEFITEC) and Faculty of Sciences and Technology—New University of Lisbon (FCT) were Academic Partners and the Science and Technology Events (SCITEVENTS) was the Logistics Partner. The papers were peer-reviewed to the professional and scientific standards expected of a proceedings journal published by Springer. Papers were assessed according to the journal's Peer Review Policy which judges papers on aspects including scientific merit (notably scientific rigour, accuracy and correctness), clarity of expression and originality.

The technical program of PHOTOPTICS 2015 covered areas like "Optics", "Photonics" and "Lasers technology". We expect that these proceedings will appeal to a broad audience of researchers, engineers, scientists and business people interested in those areas. We further believe that the papers in these proceedings demonstrate new and innovative solutions, and highlight technical problems in the mentioned areas that are challenging and worthwhile.

The conference was also complemented with the first edition of the Special Session on Optical Sensors—OSENS 2015 (chaired by Orlando Frazão).

PHOTOPTICS 2015 received 113 paper submissions from 40 countries. From these, 12 papers were published and presented as full papers, 16 were accepted as short papers. These numbers, leading to a full-paper acceptance ratio of 11 % and the total oral acceptance ratio (including full papers and short papers) 25 % which show the intention of preserving a high quality forum for the next editions of this conference.

vi Preface

The high quality of the PHOTOPTICS 2015 programme was enhanced by five keynote lectures, delivered by experts in their fields, including: Ludger Wöste (Freie Universität Berlin) that delivered a keynote entitled "Fundamentals and Applications of Plasma Filaments", Orlando Frazão (INESC Porto) delivered a keynote on "New Advances in Fabry-perot Cavity for Sensing Applications", Klaus Petermann (Technische Universität Berlin) had a keynote entitled "Nonlinear Optics in Silicon Photonics", João Magueijo (Imperial College London) with a keynote entitled "Varying Speed of Light, Cosmic Structure and the Quest for Quantum Gravity" and Wolfgang Schade (Clausthal University of Technology) with the keynote "FiberLab—A Multi-sensing Approach in a Single Optical Fiber".

This book contains 10 papers from PHOTOPTICS 2015, which have been selected, extended and thoroughly revised.

We wish to thank all those who supported and helped to organize the conference. On behalf of the conference Organizing Committee, we would like to thank the authors, whose work mostly contributed to a very successful conference, the Keynote Lectures and to the members of the Program Committee, whose expertise and diligence were instrumental to ensure the quality of final contributions. We also wish to thank all the members of the Organizing Committee whose work and commitment was invaluable. Last but not least, we would like to thank Springer for their collaboration in getting this book to print.

Caparica, Portugal

Paulo Ribeiro Maria Raposo

#### **Organization**

#### **Conference Chair**

Paulo Ribeiro, CEFITEC/FCT/UNL, Portugal

#### **Program Chair**

Maria Raposo, CEFITEC/FCT/UNL, Portugal

#### **Local Chair**

Wolfgang Schade, Clausthal University of Technology, Germany

#### **Program Committee**

Manuel Abreu, Laboratory of Optics, Lasers and Systems (LOLS), Faculdade de Ciências da Universidade de Lisboa, Portugal

Gandhi Alagappan, Institute of High Performance Computing, Agency for Science, Technology and Research (A-STAR), Singapore

Augusto A. Iribarren Alfonso, Instituto de Ciencia y Tecnología de Materiales, Universidad de La Habana, Cuba

Tatiana Alieva, Universidad Complutense de Madrid, Spain

António Amorim, Departamento de Física da Faculdade de Ciências da Universidade de Lisboa, Portugal

Fortunato Tito Arecchi, Università degli Studi di Firenze, Italy

Alexander Argyros, Institute of Photonics and Optical Science, University of Sidney, Australia

viii Organization

Maria Flores Arias, Universidade de Santiago de Compostela, Spain

Andrea Armani, University of Southern California, United States

Jhon Fredy Martinez Avila, Universidade Federal de Sergipe, Brazil

Roel Baets, Ghent University—IMEC, Belgium

Naci Balkan, University of Essex, UK

Pedro Barquinha, Departamento de Ciência dos Materiais, Faculdade de Ciências e Tecnologia. Universidade Nova de Lisboa, Portugal

Almut Beige, University of Leeds, UK

Henri Benisty, Institut d'Optique, France

Oliver Benson, Humboldt University of Berlin, Germany

Gennady P. Berman, Los Alamos National Laboratory and New Mexico Consortium, United States

Antonella Bogoni, Scuola Superiore Sant'Anna-TeCIP, Italy

Ekaterina Borisova, Institute of Electronics—Bulgarian Academy of Sciences, Bulgaria

Remy Braive, Laboratory for Photonics and Nanostructures/CNRS, France

Gilberto Brambilla, Optoelectronics Research Centre, University of Southampton, UK

Tom Brown, University of St Andrews, UK

Enrique Castro Camus, Centro de Investigaciones en Optica A.C., Mexico

John Canning, University of Sydney, Australia

Gabriela Carja, Technical University Gh. Asachi of Iasi, Romania

Adolfo Cartaxo, Instituto de Telecomunicações, Instituto Superior Técnico, Portugal

Calvin C.K. Chan, The Chinese University of Hong Kong, Hong Kong

Zhao Changming, Beijing Institute of Technology, China

Jiajia Chen, Royal Institute of Technology (KTH), Sweden

Xianfeng Chen, Shanghai Jiao Tong University, China

Dominique Chiaroni, Alcatel-Lucent Bell Labs France, France

Vladimir G. Chigrinov, Hong Kong University of Science and Technology, Hong Kong

Gabriella Cipparrone, Università degli Studi della Calabria, Italy

João Coelho, Faculdade de Ciências da Universidade de Lisboa, Portugal

Michael J. Connelly, University of Limerick, Ireland

François Courvoisier, FEMTO-ST CNRS, Université de Franche-Comté, France

Yiping Cui, Southeast University, China

Mireille Cuniot-Ponsard, Laboratoire Charles Fabry, Institut d'Optique, C.N.R.S., France

Daoxin Dai, Zhejiang University, China

Antonio Delgado, Friedrich-Alexander University Erlangen-Nuremberg, Germany

Hilmi Volkan Demir, Bilkent University, Turkey

Yujie J. Ding, Lehigh University, United States

Ivan Divliansky, Laboratory at the College of Optics and Photonics—CREOL at UCF, United States

Alexandre Dmitriev, Chalmers University of Technology, Sweden

Organization ix

Chen-Yuan Dong, National Taiwan University, Taiwan

Arnaud Dubois, Laboratoire Charles Fabry, Institut d'Optique, France

Sadik Esener, UCSD—University of California at San Diego, United States

Robert Ferguson, National Physical Laboratory, UK

Mário F.S. Ferreira, University of Aveiro, Portugal

Paulo Torrão Fiadeiro, Centro de Óptica, Universidade da Beira Interior, Portugal

Hugo Hernandez Figueroa, UNICAMP, Brazil

Orlando Frazão, INESC Porto, Portugal

Norbert Frühauf, Institute for Large Area Microelectronics, University of Stuttgart, Germany

Alberto Garcia, Instituto de Física dos Materiais da Universidade do Porto, Spain Sanka Gateva, Institute of Electronics, Bulgaria

Malte Gather, University of St Andrews, UK

Marco Gianinetto, Politecnico di Milano, Italy

John Girkin, Department of Physics, Biophysical Sciences Institute, Durham University, UK

Guillaume Gomard, Light Technology Institute, Germany

Yandong Gong, Institute for Infocomm Research, Singapore

Norbert Grote, Fraunhofer Heinrich Hertz Institute, Germany

Bob Guenther, Duke University, United States

Vasco Guerra, Departamento de Física Instituto Superior Técnico, Portugal

Young-Geun Han, Hanyang University, Korea, Republic of

Gregory Herman, Oregon State University, United States

Daniel Hill, Universitat de Valencia, Spain

Werner Hofmann, Center of Nanophotonics at Technische Universität Berlin, Germany

Seppo Honkanen, Institute of Photonics, Finland

Mark Hopkinson, University of Sheffield, UK

Peter Horak, University of Southampton, UK

Wen-Feng Hsieh, National Chiao Tung University, Taiwan

Nicolae Hurduc, Gheorghe Asachi Technical University of Iasi, Romania

Chennupati Jagadish, Australian National University, Australia

Leszek R. Jaroszewicz, Military University of Technology, Poland

Jichai Jeong, Korea University, Korea, Republic of

Igor Jovanovic, Pennsylvania State University, United States

José Joatan Rodrigues Jr., Universidade Federal de Sergipe, Brazil

Yoshiaki Kanamori, Tohoku University, Japan

Fumihiko Kannari, Keio University, Japan

Pentti Karioja, VTT Technical Research Centre of Finland, Finland

Christian Karnutsch, Karlsruhe University of Applied Sciences, Faculty of

Electrical Engineering and Information Technology, Germany

Henryk Kasprzak, Wrocław University of Technology, Poland

Young-Jin Kim, Nanyang Technological University, Singapore

Stefan Kirstein, Humboldt-Universitaet zu Berlin, Germany

x Organization

Stanislaw Klosowicz, Military University of Technology, Faculty of Advanced Technologies and Chemistry Warsaw, Poland

Lyubomir Kovachev, Institute of Electronics, Bulgarian Academy of Sciences, Bulgaria

Leonid Krivitsky, Data Storage Institute, Singapore

Shoichi Kubodera, University of Miyazaki, Japan

Markku Kuittinen, Institute of Photonics, Finland

Vladimir Dmitrievitsh Kulakovsky, Institute of Solid State Physics Russian Academy of Sciences, Russian Federation

Jesper Lægsgaard, Technical University of Denmark, Denmark

Martin J. Leahy, National University of Ireland Galway, Ireland

Wei Lee, National Chiao Tung University, Taiwan

Antonio Gizzi Leonida, INO-Istituto Nazionale di Ottica, CNR, Italy

Dawei Liang, FCT/UNL, Portugal

Milton S.F. Lima, Instituto de Estudos Avancados, Brazil

Yi-Hsin Lin, National Chiao Tung University, Taiwan

Ai-Qun Liu, Nanyang Technological University, Singapore

Yu-Lung Lo, National Cheng Kung University, Taiwan

Carmen Mas Machuca, Technische Universität München, Germany

Mohd Adzir Mahdi, Universiti Putra Malaysia, Malaysia

Hervé Maillotte, Institut FEMTO-ST, France

Vladimir Makin, Institute for Nuclear Energetic, Russian Federation

Alexandre Marletta, Universidade Federal de Uberlândia, Brazil

Manuel Marques, FCUP, Portugal

Paulo Marques, FCUP/INESC Porto, Portugal

Nicolas Martin, FEMTO-ST, France

Rodrigo Martins, Departamento de Ciências dos Materiais, Faculdade de Ciências e

Tecnologia, Universidade Nova de Lisboa, Portugal

Francisco Medina, University of Seville, Spain

Andrea Melloni, Politecnico di Milano, Italy

Roberto Morandotti, Institut National de la Recherche Scientifique—Énergie,

Matériaux et Télécommunications, Canada

Bill Munro, NTT Basic Research Laboratories, Japan

Phyllis R. Nelson, California State Polytechnic University Pomona, United States

André Nicolet, Institut Fresnel, AIX Marseillle Université, CNRS, France

Rogério N. Nogueira, Institute of Telecommunications—Aveiro, Portugal

Pál Ormos, Biological Research Centre, Hungarian Academy of Sciences, Hungary

Wolfgang Osten, Universität Stuttgart, Germany

Aydogan Ozcan, University of California—Los Angeles, United States

Ayca Yalcin Ozkumur, Massachusetts Institute of Technology Department of Chemical Engineering, Turkey

Krassimir Panajotov, Free University of Brussels, Belgium

Jisha Chandroth Pannian, Centro de Física da Universidade do Porto, Portugal

Seoung-Hwan Park, Catholic University of Daegu, Korea, Republic of

YongKeun Park, Department of Physics, KAIST, Korea, Republic of

Organization xi

Emmanuel Paspalakis, University of Patras, Greece

Lorenzo Pavesi, University of Trento, Italy

Johannes Pedarnig, Johannes Kepler University Linz, Austria

Gang-Ding Peng, University of New South Wales, Australia

Alfons Penzkofer, Universität Regensburg, Germany

João Pinto, Aveiro University, Portugal

Alexander N. Pisarchik, Centro de Investigaciones en Optica, Mexico

Edwin Yue Bun Pun, City University of Hong Kong, Hong Kong

Weiping Qin, Jilin University, China

Jianrong Qiu, South China University of Technology, China

Fabrice Raineri, Laboratory for Photonics and Nanostructures, France

Roberta Ramponi, Politecnico di Milano, Campus Milano Leonardo, Italy

Maria Raposo, CEFITEC/FCT/UNL, Portugal

Alessandro Restelli, Joint Quantum Institute, United States

Paulo Ribeiro, CEFITEC/FCT/UNL, Portugal

Mauricio Rico, Centro de Láseres de Pulsados (CLPU), Spain

Alessandro Rizzi, Università di Milano, Italy

Ana Rocha, Instituto de Telecomunicações Aveiro, Portugal

Luis Roso, Centro de Laseres Pulsados, Spain

Ali Rostami, University of Tabriz, Iran, Islamic Republic of

Carlos Saavedra, Center for Quantum Optics and Quantum Information, Chile

Svilen Sabchevski, Institute of Electronics, Bulgarian Academy of Sciences, Bulgaria

Bouchta Sahraoui, University of Angers, UFR of Sciences, France

Marco Salerno, Italian Institute of Technology, Italy

Elisa Sani, INO-Istituto Nazionale di Ottica, CNR, Italy

Luís Santos, Instituto Superior Técnico, Portugal

Manuel Pereira dos Santos, Centro de Física e Investigação Tecnológica, Faculdade de Ciências e Tecnologia, Universidade Nova de Lisboa, Portugal

David Schmool, University of Perpignan/Laboratoire PROMES, UPR 8521 CNRS, France

Alan Shore, Bangor University, UK

K. Alan Shore, Bangor University, UK

Josmary Silva, Universidade Federal do Mato Grosso-Campus Universitário do Araguaia, Brazil

Stefan Sinzinger, Technische Universität Ilmenau, Germany

Peter G.R. Smith, University of Southampton, UK

Feng Song, Nankai University, China

Nara de Souza, Universidade Federal do Mato Grosso, Brazil

Viorica Stancalie, National Institute for Laser, Plasma and Radiation Physics, Romania

Iuliana Stoica, "Petru Poni" Institute of Macromolecular Chemistry, Romania

Xiao Wei Sun, Nanyang Technological University, Singapore

Takenobu Suzuki, Toyota Technological Institute, Japan

xii Organization

João Manuel R.S. Tavares, FEUP—Faculdade de Engenharia da Universidade do Porto, Portugal

Roy Taylor, Imperial College London, UK

António Teixeira, Instituto de Telecomunicações, Portugal

Ladislav Tichy, IMC ASCR, Czech Republic

Swee Chuan Tjin, Nanyang Technological University, Singapore

Ioannis Tomkos, Athens Information Technology, Greece

José Roberto Tozoni, Universidade Federal de Uberlandia, Brazil

Alessandro Tredicucci, Università di Pisa, Italy

Valery V. Tuchin, Saratov State University, Russian Federation

Graham A. Turnbull, University of St Andrews, UK

Pasi Vahimaa, University of Eastern Finland, Finland

Rui Vilar, Instituto Superior Técnico, Portugal

Naoya Wada, National Institute of Information and Communications Technology, Japan

Ruikang K. Wang, University of Washington, United States

Lech Wosinski, KTH-Royal Institute of Technology, Sweden

Jingshown Wu, Networked Communications Program (NCP), Taiwan

Jiangtao Xi, University of Wollongong Northfields, Australia

Preecha Yupapin, King Mongkut's Institute of Technology Ladkrabang, Thailand

He-Ping Zeng, East China Normal University, China

Lin Zhang, Aston University, UK

Xin-Liang Zhang, Huazhong University of Science and Technology, China

Chao Zhou, Lehigh University, United States

Lei Zhou, Fudan University, China

#### **Invited Speakers**

Ludger Wöste, Freie Universität Berlin, Germany Orlando Frazão, INESC Porto, Portugal Klaus Petermann, Technische Universität Berlin, Germany João Magueijo, Imperial College London, UK Wolfgang Schade, Clausthal University of Technology, Germany

### **Contents**

Pai	1 I myneu raper	
1	Fiber Microstructure Sensors Based on Focused  Ion Beam Technology	3
Par	t II Optics	
2	Focus on the Distal Assembly of a Nonlinear Endomicroscope: A Gradient Index Lens Coupled with a Piezoelectric Scanner for Fluorescence Lifetime Measurements	19
3	Improvement of Transverse Offset-Based Single-Mode-Multimode-Single-Mode-Fiber Structure for DPSK Signal Demodulation Xiaoyong Chen and Paloma R. Horche	35
4	Application of Laser Photoacoustic Spectroscopy and Chemometrics in Homeland Security	53
5	Fibre Bragg Grating Sensor Signal Post-processing Algorithm: Crack Growth Monitoring in Fibre Reinforced Plastic Structures	63

xiv Contents

Part	Ш	Phot	onics

6	Free-Space Millimeter-Wave Electro-optic Modulators Using Quasi-Phase-Matching Gap-Embedded-Patch-Antennas on Low Dielectric Constant Substrate	83
7	An Efficient Optimization Problem for Modal Reflectivity at Optical Waveguide End-Facet Based on the Formulation of Characteristic Green's Function Technique	105
8	Effect of Exponentially Graded Material on Photonic and Omni-Directional Band Gaps in 1-D Photonic Crystals Bipin Kumar Singh and Praveen Chandra Pandey	119
9	Smith-Purcell Based Terahertz Frequency Multiplier: Three Dimensional Analysis	145
10	Stochastic Resonances and Gated Detection in Photon Number Resolving Detectors.  Shree Krishnamoorthy, Harish Ravi, Pradeep K. Kumar and Anil Prabhakar	157
11	Design Optimization of Silicon-on-Insulator Slot-Waveguides for Electro-optical Modulators and Biosensors	173
Aut	chor Index	189
Ind	ex	191

#### **Contributors**

**Darine Abi Haidar** Laboratoire IMNC, Orsay, France; Université Paris 7-Paris DIDEROT, Paris, France

**Ricardo Melo André** INESC TEC and Faculty of Sciences of the University of Porto (FCUP), Porto, Portugal

**Mauro Casalboni** Department of Industrial Engineering, University of Rome "Tor Vergata", Rome, Italy

Stella Nunziante Cesaro ISMN-CNR c/o Department of Chemistry, Rome, Italy

**Xiaoyong Chen** Departamento de Tecnología Fotónica y Bioingeniería, Universidad Politécnica de Madrid, Madrid, Spain

**Mahboubeh Dolatyari** OIC Research Group, School of Engineering-Emerging Technologies, University of Tabriz, Tabriz, Iran

**Orlando Frazão** INESC TEC and Faculty of Sciences of the University of Porto (FCUP), Porto, Portugal

Gianfranco Giubileo ENEA, FSN-TECFIS-DIM, Frascati, Italy

Hussein Hamzeh Laboratoire IMNC, Orsay, France

**Paloma R. Horche** Departamento de Tecnología Fotónica y Bioingeniería, Universidad Politécnica de Madrid, Madrid, Spain

**Atsushi Kanno** National Institute of Information and Communications Technology, Koganei, Tokyo, Japan

**Tetsuya Kawanishi** National Institute of Information and Communications Technology, Koganei, Tokyo, Japan; Waseda University, Shinjuku, Tokyo, Japan

**Shree Krishnamoorthy** Department of Electrical Engineering, Indian Institute of Technology Madras, Chennai, India

Pradeep K. Kumar Indian Institute of Technology, Kanpur, India

xvi Contributors

Claire Lefort Laboratoire XLIM, Limoges, France

**Manuel J.B. Marques** INESC TEC and Faculty of Sciences of the University of Porto (FCUP), Porto, Portugal

**M. McGugan** Department of Wind Energy, Technical University of Denmark, Roskilde, Denmark

**L.P. Mikkelsen** Department of Wind Energy, Technical University of Denmark, Roskilde, Denmark

Hiroshi Murata Osaka University, Toyonaka, Osaka, Japan

Yasuyuki Okamura Osaka University, Toyonaka, Osaka, Japan

Frédéric Pain Laboratoire IMNC, Orsay, France

Antonio Palucci ENEA, FSN-TECFIS-DIM, Frascati, Italy

**Praveen Chandra Pandey** Department of Physics, Indian Institute of Technology (Banaras Hindu University), Varanasi, India

**G. Pereira** Department of Wind Energy, Technical University of Denmark, Roskilde, Denmark

**Anil Prabhakar** Department of Electrical Engineering, Indian Institute of Technology Madras, Chennai, India

Adriana Puiu ENEA, FSN-TECFIS-DIM, Frascati, Italy

**Silvio Pulwer** Faculty of Engineering and Natural Sciences, University of Applied Sciences Wildau, Wildau, Germany

Harish Ravi Indian Institute of Science, Bangalore, India

**Ali Rostami** Photonic and Nanocrystal Research Lab. (PNRL), Faculty of Electrical and Computer Engineering, University of Tabriz, Tabriz, Iran; OIC Research Group, School of Engineering-Emerging Technologies, University of Tabriz, Tabriz, Iran

**Ghassem Rostami** OIC Research Group, School of Engineering-Emerging Technologies, University of Tabriz, Tabriz, Iran

**Sigurd Schrader** Faculty of Engineering and Natural Sciences, University of Applied Sciences Wildau, Wildau, Germany

**Amir Ahmad Shishegar** Department of Electrical Engineering, Sharif University of Technology, Tehran, Iran

**Bipin Kumar Singh** Department of Physics, Indian Institute of Technology (Banaras Hindu University), Varanasi, India

Contributors xvii

**Patrick Steglich** Faculty of Engineering and Natural Sciences, University of Applied Sciences Wildau, Wildau, Germany; Department of Industrial Engineering, University of Rome "Tor Vergata", Rome, Italy

**Alireza Tavousi** Photonic and Nanocrystal Research Lab. (PNRL), Faculty of Electrical and Computer Engineering, University of Tabriz, Tabriz, Iran

**Abdorreza Torabi** Faculty of Engineering Science, School of Engineering, University of Tehran, Tehran, Iran

**Claus Villringer** Faculty of Engineering and Natural Sciences, University of Applied Sciences Wildau, Wildau, Germany

Liu Wei Laboratoire IMNC, Orsay, France

**Yusuf Nur Wijayanto** National Institute of Information and Communications Technology, Koganei, Tokyo, Japan; Indonesian Institute of Sciences, Cisitu, Bandung, Indonesia

**Naokatsu Yamamoto** National Institute of Information and Communications Technology, Koganei, Tokyo, Japan

## Part I Invited Paper

# **Chapter 1 Fiber Microstructure Sensors Based on Focused Ion Beam Technology**

Ricardo Melo André, Manuel J.B. Marques and Orlando Frazão

**Abstract** Optical fiber sensors have evolved over the years in many different directions. One particular direction dictated by necessity is miniaturization and the creation of micro- and nano- optical fiber sensors. Many techniques now exist that allow the micro-structuring of optical fiber. One in particular is focused ion beam technology. This chapter aims to introduce this technique and present the latest work on the application of focused ion beam to optical fiber micromachining, more specifically, the fabrication of optical fiber microstructure sensors such as micro-gratings and micro-cavities.

#### 1.1 Introduction

Optical fiber sensors are fiber devices used to detect different external parameters such as temperature, strain, pressure, acceleration, humidity, chemical concentrations, presence of biological species, and many more [1]. The general principal is that light from a source, such as a laser or a broadband source, is sent down a fiber through the sensing region where it will experience changes in its properties (e.g. wavelength) or propagation conditions (e.g. optical path). This altered light then reaches a detector that measures these changes and correlates them to the respective changes in the external conditions.

Among the most common optical fiber sensors are fiber Bragg gratings (FBGs) [2], which are based on the temperature and mechanical strain dependence of the Bragg wavelength (maximum reflectivity wavelength) of the FBG itself; distributed

3

R.M. André ( ) · M.J.B. Marques · O. Frazão

INESC TEC and Faculty of Sciences of the University of Porto (FCUP),

Rua do Campo Alegre, 687, 4150-179 Porto, Portugal

e-mail: rmeloandre@gmail.com

M.J.B. Marques

e-mail: mbmarque@fc.up.pt

O. Frazão

e-mail: ofrazao@fc.up.pt

4 R.M. André et al.

fiber sensors based on Rayleigh [3], Raman [4], or Brillouin [5, 6] scattering, not dependent on any additional structuring of the fiber; and Fabry-Perot interferometers, which are generally composed of two parallel reflecting surfaces, where interference occurs from light reflected at both interfaces [7]. Many other sensors exist that depend on microstructured optical fibers [8], long period gratings [9], tapers [10], combinations of different fiber types such as SMF-MMF-SMF structures that work as MMI devices [11], and others. What all these devices have in common is that they are mostly based on standard-diameter optical fiber. This is small when compared to conventional electric sensors but sometimes not small enough for specific applications where smaller volumes, shorter lengths, or even difficult access regions are involved. For example, when considering biological applications such as optogenetics [12] or intra-organism and intracellular sensing [13], typical FBGs are too long.

Fabrication of optical fiber sensors with reduced dimensions—micro- and nanosensors and devices—relies on the adoption of novel techniques that were not previously used in optical fiber sensor fabrication or on the use of costumized tested techniques. These can be loosely divided in two categories: low and high resolution techniques. Low resolution techniques allow the rapid decrease in volume of the optical fiber and/or quick access to the light guiding region. These are generally fast but provide a low resolution in the sense that structures with details only down to few tens of microns can be created. They include chemical etching and tapering. Tapering can itself be achieved with the aid of CO<sub>2</sub> lasers [14], filament heating [15], electric arc [16], flame brushing [17], or even chemical etching [18, 19]. High resolution techniques allow the creation of fine details in structures in the order of a few microns or even tens or hundreds of nanometers. Since these allow such a high resolution, they are inherently much slower and can only be applied, in a timely fashion, in small sections of fiber. They include femtosecond laser micromachining [20, 21] and FIB milling [22–25].

In most cases, the most efficient method of fabricating micro- and nano- fiber devices and sensors, is combining both high and low resolution techniques. First, with the aid of a low resolution technique, reduce the dimensions of the optical fiber down to a few microns or allow easy access to the light guiding region (e.g. core) and then use a high resolution technique to create a truly micro-/nano- structure on the fiber.

This chapter will focus on the high resolution technique called Focused Ion Beam (FIB) and its combination with low resolution techniques such as chemical etching and tapering for the fabrication of optical fiber sensors. Structures such as Fabry-Perot micro-cavities, fiber-top cantilevers, fiber Bragg micro-gratings among others will be explored and detailed.

#### 1.2 Focused Ion Beam Technology

Focused Ion Beam (FIB) is a technology that uses a focused ion beam (usually gallium-ion) to image or ablate/mill the substrate on which it is focused or even aid the deposition of another material on the substrate. Focused Ion Beam technology is

very similar to scanning electron microscopy. The main difference is that the electron beam that scans the sample is replaced by an ion beam. It was developed mainly in the semiconductor industry and for the preparation of transmission electron microscope samples.

#### 1.2.1 Focused Ion Beam System

#### 1.2.1.1 **Sources**

Most ion beam equipment uses liquid-metal ion sources (LMIS), generally gallium-ion sources. The ion beam is generated from the LMIS through a very strong electric field. A tungsten needle is used to heat-up the gallium and take it to its liquid state. The superficial tension and electric field forces lead to the formation of a gallium cone on the needle tip. This cone has a tip with a very small radius of curvature (ca. 5 nm) [26]. As the tip gets sharper, the electric field gets stronger until ions are ejected by evaporation. Gallium ion (Ga<sup>+</sup>) emission occurs at a typical voltage of 7000 V [27].

#### 1.2.1.2 FIB Column and Chamber

The produced ions go through a series of apertures, electrostatic lenses and possibly a mass spectrometer in order to select the ions in a specific range of energies and to reduce the ion beam diameter (Fig. 1.1). At the bottom of the column, an electrostatic deflector controls the final trajectory of the beam and the point of impact on the substrate. A supporting system of vacuum pumps is necessary to maintain vacuum inside the column and the working chamber. A typical vacuum of  $1 \times 10^{-7}$  mbar is maintained inside the chamber.

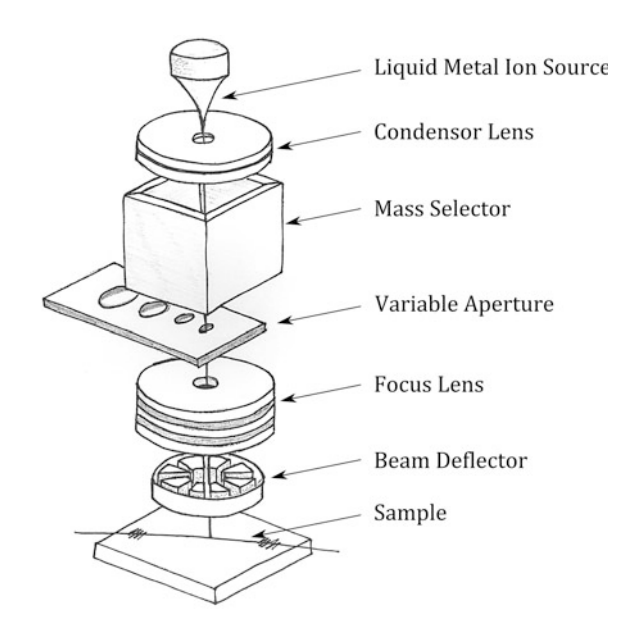
#### 1.2.2 Ion-Substrate Interaction

When an ion from the beam hits the substrate surface, it loses energy that is transferred to the electrons and atoms of the substrate. Depending on the ion energy, it can interact with the surface in several ways [27, 28]. The following physical processes are just some interactions that can result from bombarding the surface with ions:

- sputtering of the substrate material with atom and ion emission;
- emission of electrons:
- atom dislocation in the substrate;
- phonon emission and consequent heating;

6 R.M. André et al.

**Fig. 1.1** Diagram of a focused ion beam system



- ion implantation inside the substrate; and
- redeposition of sputtered material.

Focused ion beam can also be used for the deposition of certain materials and in this case, the ion beam is used to break chemical bonds and dissociate gaseous molecules.

#### 1.2.3 Focused Ion Beam Operation

Focused Ion Beam systems have three main operation modes: imaging, deposition, and milling.

#### **Imaging**

At low currents, very little material is sputtered and therefore an image of the substrate surface can be obtained without inducing much damage. By scanning the surface, secondary particles will be generated in the substrate; namely atoms, ions and electrons will be ejected from the surface. As they leave the substrate, secondary electrons and sputtered ions are collected by positively and negatively polarized detectors, respectively. The resulting ions can also be guided to a Secondary Ion Mass Spectrometer (SIMS) to obtain the atomic composition of the substrate or even a composition map of the surface of the substrate. Recent FIB systems can easily achieve a 5 nm resolution limited only by the beam diameter on the substrate and the local sputtering of the surface [26, 27].

Obtaining an image with FIB always leads to damage on the surface. During the process, gallium ion implantation and sputtering is inevitable. These two processes can be minimized by reducing beam diameter and current.

#### **Deposition**

Depositing several types of materials from metals to insulators is possible using FIB. The principle behind FIB deposition is Chemical Vapor Deposition (CVD). The main difference is the higher resolution obtained with FIB. This higher resolution comes at the cost of a lower deposition rate. The precursor gases are sprayed to the surface and the molecules are adsorbed onto it. The ion beam will then decompose the precursors and the vacuum system will remove the volatile products that are desorbed from the surface while the desired products of decomposition remain on the surface. The most commonly deposited materials using focused ion beam are tungsten, silver and silicon dioxide [27, 28]. Structures with lateral dimensions of 100 nm and thickness of 10 nm can be deposited.

#### Milling

Milling designates the process of removing material from the substrate with the aid of the focused ion beam (Fig. 1.2). Physically, it is the combination of two processes: physical sputtering and material re-deposition. It is possible to remove material from the substrate using a high current ion beam. Structures can be created on the substrate by scanning the high current ion beam. The high energy density of the ion beam combined with its small diameter allows the creation of submicron structures. The sputtering yield depends not only on the substrate material but also on the ion energy, incidence angle, and machining conditions. Nonetheless, this yield cannot be considered the etching yield because material re-deposition always occurs reducing the effective etching rate. To accelerate the milling process, a gas may be introduced inside the chamber in order to increase the etching rate. The gas

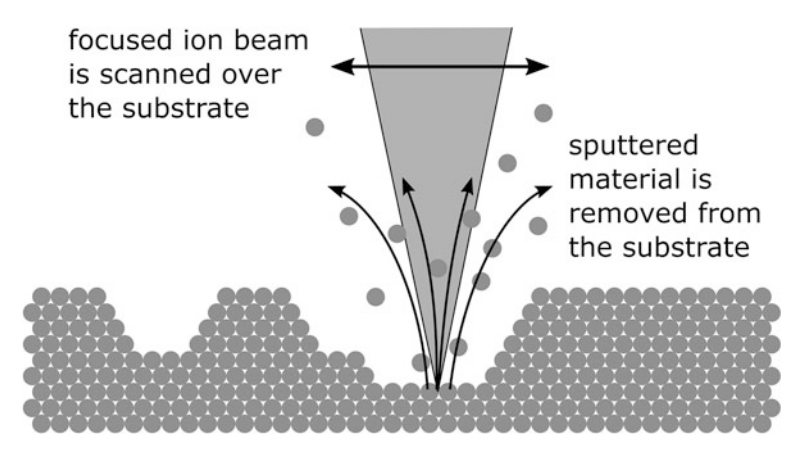


Fig. 1.2 Focused ion beam milling

8 R.M. André et al.

will many times increase the etching selectivity and chemically facilitate the removal of reaction products. One of the most developed applications of FIB is the micro-milling of Transmission Electron Microscope (TEM) samples [29].

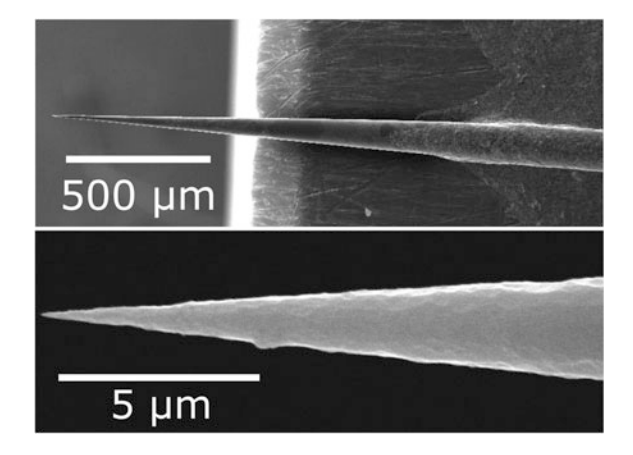
#### 1.3 Focused Ion Beam Optical Fiber Applications

#### **Tapered Fiber Tips**

Of the many structures that can be created using low resolution techniques, the tapered fiber tips are one of the most interesting to use as a base to work with FIB milling. They are important optical devices without any further post-processing but the use of focused ion beam to further develop them can introduce new uses and applications.

A Tapered Fiber Tip (TFT) is a very interesting fiber optic device for sensing. It consists of a microfiber with a taper region that only has one input/output (see Fig. 1.3). Since the input/output of the fiber has a standard diameter of  $125 \mu m$ , connecting this device to other optical components is an easy task. The fabrication of this device is relatively simple. Several different techniques can be used such as chemical etching, tapering by  $CO_2$  laser heating, tapering by filament heating, etc. When fabricating a taper by heating methods, tension is applied until the fiber is separated into two, not necessarily equal, tips. Too short tips have very large losses due to their non-adiabaticity. This leads to coupling of light to non-confined radiation modes. Too long tips also introduce unwanted problems related to an intrinsic lack of stiffness. Therefore, the length of the tip is a very important factor and must be related to the tip's final application. One other technique used to create tapered fiber tips is denominated dynamic chemical etching. In this technique, a hydrofluoric acid solution is used to chemically etch a cleaved fiber tip into a tapered tip [30]. By controlling the relative position between the acid level and the

Fig. 1.3 Micrographs of tapered fiber tips fabricated by dynamic chemical etching [31]



fiber tip, it is possible to control the length, radius, and shape of the TFT. In Fig. 1.3, two examples of tapered fiber tips fabricated by this method are shown.

#### 1.3.1 Fabry-Perot Micro-Cavity

One of the simplest structures that one can mill on a tapered fiber tip using FIB is a *Fabry-Perot* cavity. Using focused ion beam, the cavities are always created removing material in such a way that an open cavity forms. This will result in two surfaces open to the surrounding medium that form the *Fabry-Perot* cavity.

In literature, several different approaches to cavity creation have been reported. A cavity was created using FIB where a rectangular hole near the cleave of a commercial SMF was milled [22]. As the hole is milled near the cleave, two cavities are created, one in-fiber cavity and one open cavity. This structure is then used for the simultaneous measurement of salinity and temperature. A micro-cavity on a slightly tapered fiber was also explored [32]. The cavity was milled at a diameter of 32  $\mu$ m and used as a refractive index sensor. FIB-milled Fabry-Perot cavities for refractive index sensing were also investigated in polished fibers [24]. A SMF was polished at a very oblique angle to gain access to the core of the fiber, where the cavity was then milled.

More interesting is the milling of microcavities in tapered fiber tips. These can be much smaller than in standard-diameter SMF and due to the point-like design, much more versatile. These structures were applied as temperature [25] and refractive index sensors [33]. In this case, to fabricate the tapered fiber tips, a micropipette puller was used. This basically consists of two micrometric translation stages that stretch the fiber while a CO<sub>2</sub> laser is scanned along the fiber to heat it up. For FIB milling, the tip was covered with an aluminum film through evaporation to avoid charge accumulation. In other FIB configurations, a secondary electron beam is used to neutralize the sample and, in this case, the deposition of a conducting film is not necessary. This is an essential step in FIB milling of non-conductive samples (e.g. optical fiber). If the fiber is not in some way prepared to conduct charge out of the milling region, it will inevitably start to charge which will cause the beam to deviate from the desired position. This can cause small deviations in the outcome of the milled structure or even render the milling impossible.

A micro-cavity milled in a TFT is shown in Fig. 1.4. Here, the tip is also cleaved and polished using FIB to create a second silica cavity besides the open cavity. Since the silica cavity is insensitive to external index variations, this structure can be used for the simultaneous measurement of both temperature and refractive index or for temperature-compensated index measurements.

Fabry-Perot cavities have also been milled in exposed core microstructured optical fibers (ECF). The Fabry-Perot cavities were milled directly into the core of ECF [34]. Due to the easy access to the core, it was possible to directly create the cavity on the fiber core without making previous use of any low resolution technique. Two types of cavities where created: one where the milled cavity extends all

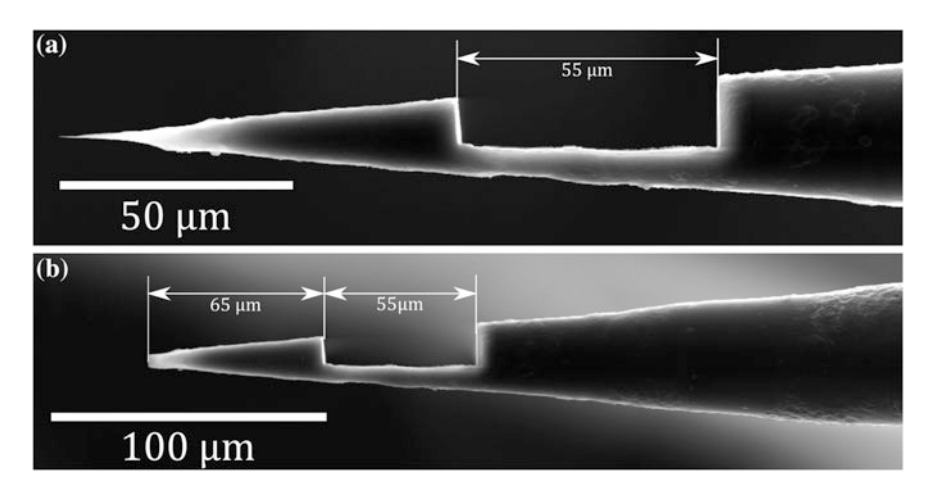


Fig. 1.4 SEM micrograph of **a** a FIB machined micro-cavity on a TFT and **b** the same tip with a polished top

the way through the core and allows access to the inner holes of the ECF and a slot cavity that does not reach deep enough and keeps the holes intact. These structures have been proposed for microfluidic sensing. Others had previously applied FIB to photonic crystal fibers but only for accessing specific holes and not sensing [35].

#### Fiber Cantilevers

Cantilever structures are devices that rely on the possibility to measure the mechanical deformation of the cantilever itself as a response to a certain external stimulus. The deflection of the cantilever can then be read by electronic or optical methods. Electronic methods may not always be suitable if analyzing conductive liquids, explosive gases and in extreme temperatures for example. Optical methods have a larger range of applicability as long as the medium is optically transparent [36–38].

Fiber top cantilever systems, micro-machined with FIB, have an integrated optical readout—the optical fiber itself. The deflection of the cantilever can be determined by analyzing the signal of the reflected light at the fiber-to-air interface and at the cantilever [36–38]. This is effectively a cavity created between the cantilever and the fiber top. When this cavity is altered, a change in the optical signal is detected. In this case, the readout is done making use of the change in optical power reflected by the fiber-top cantilever. Fiber-top cantilevers are interesting devices that due to their monolithic structure and absence of electronics on the sensing head are ideally suitable for operation in small volumes and also in harsh conditions.

Another cantilever-based system is shown in Fig. 1.5. In this structure, hydrofluoric acid is used to etch special structure forming fibers to create 15 µm-diameter microwires that are suspended between the input fiber and the fiber top as shown in Fig. 1.5 [39]. Using FIB, the microwire is cleaved and polished close to one end resulting in a suspended microwire—the cantilever. The obtained

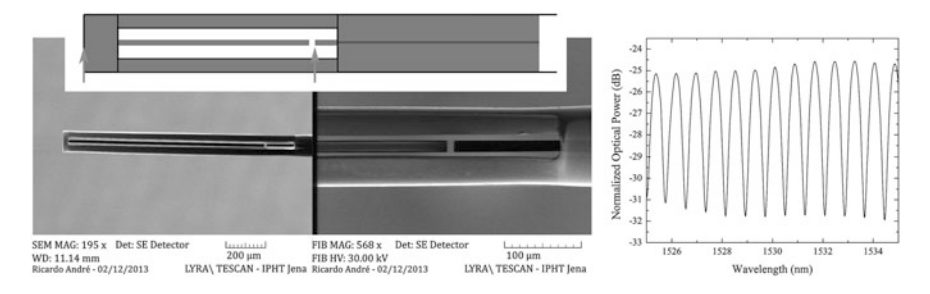


Fig. 1.5 Cantilever Fabry-Perot structure and respective optical spectrum [39]

spectrum is that of a two-wave interferometer. The two surfaces that give rise to this cavity are indicated in Fig. 1.5 by two red arrows.

When the cantilever becomes misaligned with the input fiber, the power reflected by the structure greatly decreases. This inherent property of the structure was used for the creation of a vibration sensor. When a certain vibration frequency is applied to the cantilever structure, the power is modulated accordingly. This can be seen in Fig. 1.6, where the power measured in reflection by a photodiode is represented beside its respective fast Fourier transform for three different applied frequencies.

In the fabrication of this structure, focused ion beam was used to selectively cleave the microwire. This appears to be a simple process but could not be achieved with such a high optical quality with other processing techniques.

#### 1.3.2 Bragg Micro-grating

Creating Bragg gratings on standard diameter fibers by the usual core index modulation is certainly the easiest method. But, due to the weak index modulation,

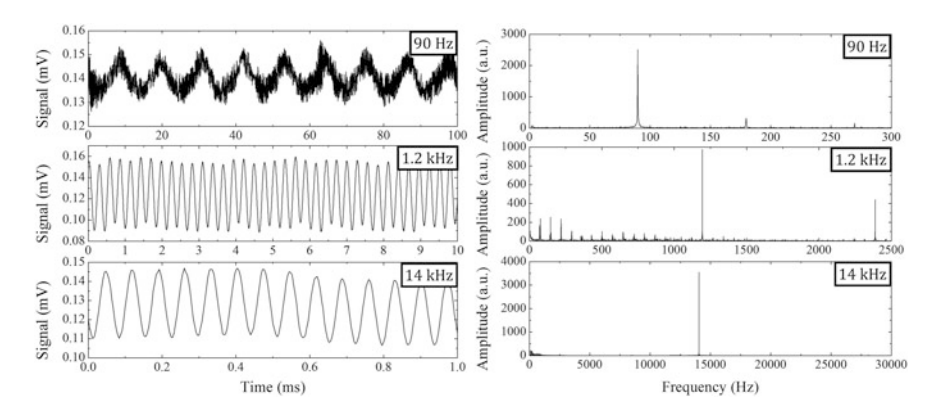


**Fig. 1.6** Cantilever Fabry-Perot structure: time responses (*left*) and respective fast Fourier transforms (*right*) when an external frequency is applied [39]

12 R.M. André et al.

a length of at least several millimeters is necessary. To reduce the length of the grating, a stronger modulation is necessary. This can be done by creating alternate layers of two materials with a high index difference such as silica and air. This would be very difficult to reproduce in standard fibers as it would be necessary to remove large quantities of material just to access the fiber core, where light propagates. In tapers and TFTs such problem does not exist, only small quantities need to be removed to create a grating since light is confined by the silica-air interface. FIB is then the adequate technique for this job. It can easily mill the fiber tips and create a micro-grating. It becomes possible to reduce the grating size from a few millimeters to few tens of micrometers [40].

One example of a micro-grating created with focused ion beam is composed of just 61, 600 nm-periods totaling a length of 36.6  $\mu$ m [40]. This grating has a corrugation depth of 200 nm and was milled in a region with an approximate radius of 3.25  $\mu$ m. This micro-grating was characterized as a temperature sensor and was subjected to temperature variations from room-temperature (21 °C) to 440 °C and a mean sensitivity of approximately 20 pm/K was obtained [40]. An example of even smaller dimensions a micro-grating with a length of just 12  $\mu$ m, composed of just 11 indentations created on a TFT [41].

A Bragg micro-grating on a TFT is shown in Fig. 1.7. This grating has a total of 50 periods with corrugations 270 nm-long and 1.3  $\mu$ m-deep, totaling a length of 27  $\mu$ m [31]. The grating is created in a section with a diameter range of [2.7, 5.1]  $\mu$ m. Using a current of just 115 pA, this grating takes ca. 50 min to structure (TESCAN LYRA FIB-SEM dual-beam system).

This grating is highly sensitive to the external medium where it is placed because the index modulation changes completely from, for example, air-silica modulation (1–1.44) to isopropanol-silica modulation (1.3–1.44) (see Fig. 1.8).

One of the great advantages of this Bragg grating configuration is its small length. Since it is much smaller than usual, it is much easier to manipulate without inducing curvature or stress that would lead to undesired effects when measuring temperature. Furthermore, as opposed to gratings produced by UV exposure where the index modulation is weak and degrades at temperatures higher than 200 °C due to germanium diffusion, these FIB milled gratings can withstand much higher temperatures as the modulation is geometric in nature and only temperatures close to the fusion of silica can lead to its degradation.

**Fig. 1.7** SEM micrograph of a Bragg grating created on a TFT [31]

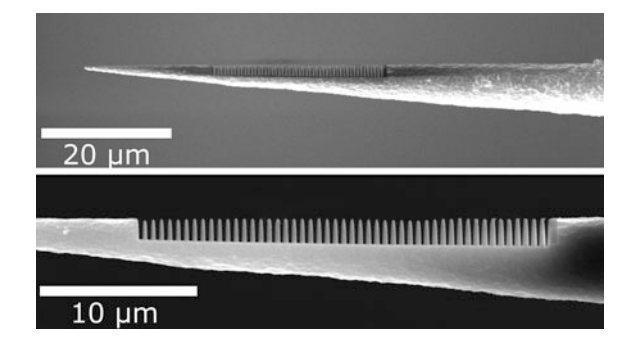
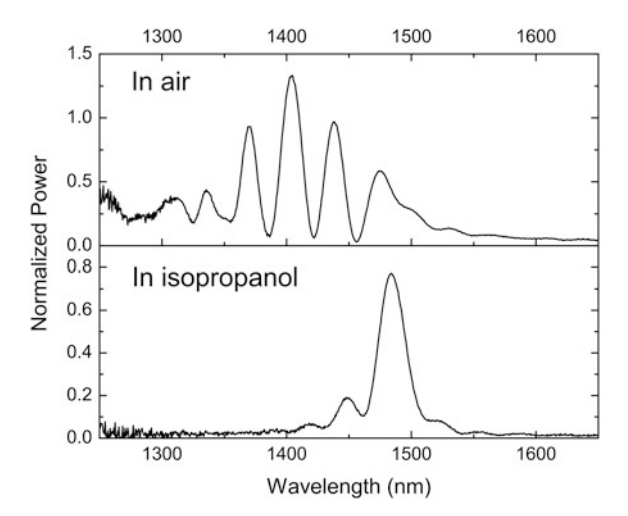


**Fig. 1.8** Bragg micro-grating spectra when dipped in air (*top*) and in isopropanol (*bottom*) [31]



#### 1.4 Concluding Remarks

It was shown that focused ion beam technology has a large potential when it comes to the fabrication of optical fiber sensor microstructures. The tendency is to use focused ion beam in the fabrication of an increasing number of new micro- and nanostructures. The push towards smaller devices into the nanometer range is still active but other areas will start being explored. Presently one can already see focused ion beam being combined with microstructured optical fibers, tapers, and chemically etched structures for the sensing of physical parameters such as temperature and refractive index but soon many others will follow due to the huge potential of this technology in fiber sensing. In the near future, combining focused ion beam post-processing and the functionalization of the milled structures and surfaces will be essential for biosensing. This combination has a large potential as it takes the advantages of miniaturization: smaller devices, faster responses, higher sensitivities and adds biospecificity to create novel micro- and nano-sensors in the ever-expanding field of biosensing.

#### References

- 1. Santos, J.L., Farahi, F.: Handbook of optical sensors. CRC Press, USA (2014)
- Kersey, A.D., Davis, M.A., Patrick, H.J., LeBlanc, M., Koo, K.P., Askins, C.G., Putnam, M. a., Friebele, E.J.: Fiber grating sensors. J. Light. Technol. 15, 1442–1463 (1997)
- 3. Barnoski, M.K., Rourke, M.D., Jensen, S.M., Melville, R.T.: Optical time domain reflectometer. Appl. Opt. 16, 2375 (1977)
- 4. Dakin, J.P., Pratt, D.J., Bibby, G.W., Ross, J.N.: Distributed optical fibre Raman tempera-ture sensor using a semiconductor light source and detector. Electron. Lett. 21, 569 (1985)

14 R.M. André et al.

5. Horiguchi, T., Kurashima, T., Tateda, M.: Tensile strain dependence of Brillouin frequency shift in silica optical fibers. IEEE Photonics Technol. Lett. 1, 107–108 (1989)

- 6. Kurashima, T., Horiguchi, T., Tateda, M.: Distributed-temperature sensing using stimulated Brillouin scattering in optical silica fibers. Opt. Lett. 15, 1038 (1990)
- Kersey, A.D., Jackson, D.A., Corke, M.: A simple fibre Fabry-Perot sensor. Opt. Commun. 45, 71–74 (1983)
- 8. André, R.M., Marques, M.B., Roy, P., Frazao, O.: Fiber loop mirror using a small core microstructured fiber for strain and temperature discrimination. IEEE Photonics Technol. Lett. **22**, 1120–1122 (2010)
- 9. Bhatia, V., Vengsarkar, A.M.: Optical fiber long-period grating sensors. Opt. Lett. 21, 692 (1996)
- 10. Birks, T.A., Li, Y.W.: The shape of fiber tapers. J. Light. Technol. 10, 432-438 (1992)
- 11. André, R.M., Biazoli, C.R., Silva, S.O., Marques, M.B., Cordeiro, C.M.B., Frazao, O.: Strain-temperature discrimination using multimode interference in tapered fiber. IEEE Photonics Technol. Lett. **25**, 155–158 (2013)
- 12. Deisseroth, K.: Optogenetics. Nat. Methods 8, 26–29 (2011)
- Tan, W., Shi, Z.Y., Smith, S., Birnbaum, D., Kopelman, R.: Submicrometer intracellular chemical optical fiber sensors. Science 258, 778–781 (1992)
- Ozcan, L.E., Treanton, V., Guay, F., Kashyap, R.: Highly symmetric optical fiber tapers fabricated with a CO<sub>2</sub> laser. IEEE Photonics Technol. Lett. 19, 656–658 (2007)
- André, R.M.: High birefringence triangular optical nanowire in suspended-core fiber for temperature sensing. J. Nanophotonics 7, 073088 (2013)
- 16. Rego, G.: Fibre optic devices produced by arc discharges. J. Opt. 12, 113002 (2010)
- 17. Kenny, R.P., Birks, T.A., Oakley, K.P.: Control of optical fibre taper shape. Electron. Lett. 27, 1654 (1991)
- Kbashi, H.J.: Fabrication of Submicron-diameter and taper fibers using chemical etching.
   J. Mater. Sci. Technol. 28, 308–312 (2012)
- 19. Dong, L., Cruz, J.L., Reekie, L., Tucknott, J.A.: Chirped fiber bragg gratings fabricated using etched tapers. Opt. Fiber Technol. 1, 363–368 (1995)
- Wei, T., Han, Y., Li, Y., Tsai, H.-L., Xiao, H.: Temperature-insensitive miniaturized fiber inline Fabry-Perot interferometer for highly sensitive refractive index measurement. Opt. Express 16, 5764 (2008)
- Liao, C.R., Hu, T.Y., Wang, D.N.: Optical fiber Fabry-Perot interferometer cavity fabricated by femtosecond laser micromachining and fusion splicing for refractive index sensing. Opt. Express 20, 22813–22818 (2012)
- Nguyen, L.V., Vasiliev, M., Alameh, K.: Three-wave fiber fabry-pérot interferometer for simultaneous measurement of temperature and water salinity of seawater. IEEE Photonics Technol. Lett. 23, 450–452 (2011)
- Yuan, L., Yang, J., Liu, Z., Sun, J.: In-fiber integrated Michelson interferometer. Opt. Lett. 31, 2692 (2006)
- Wieduwilt, T., Dellith, J., Talkenberg, F., Bartelt, H., Schmidt, M.A.: Reflectivity enhanced refractive index sensor based on a fiber-integrated Fabry-Perot microresonator. Opt. Express 22, 25333–25346 (2014)
- Kou, J., Feng, J., Ye, L., Xu, F., Lu, Y.: Miniaturized fiber taper reflective interferometer for high temperature measurement. Opt. Express 18, 14245–14250 (2010)
- Volkert, C.A., Minor, A.M.: Focused ion beam micromachining. Mater. Res. Soc. Bull. 32, 389–399 (2007)
- 27. Reyntjens, S., Puers, R.: A review of focused ion beam applications in microsystem technology. J. Micromech. Microeng. 11, 287–300 (2001)
- Tseng, A.A.: Recent developments in micromilling using focused ion beam technology.
   J. Micromech. Microeng. 14, R15–R34 (2004)
- Giannuzzi, L.A., Stevie, F.A.: A review of focused ion beam milling techniques for TEM specimen preparation. Micron 30, 197–204 (1999)

- Nikbakht, H., Latifi, H., Amini, T., Chenari, Z.: Controlling cone angle of the tapered tip fiber using dynamic etching. In: OFS2014 23rd International Conference on Optical Fiber Sensors (2014)
- 31. André, R.M., Becker, M., Dellith, J., Rothhardt, M., Zibaii, M.I., Latifi, H., Marques, M.B., Bartelt, H., Frazão, O.: Bragg grating fabrication on tapered fiber tips based on focused ion beam milling. In: OFS2015 24th International Conf. on Optical Fiber Sensors (2015)
- 32. Yuan, W., Wang, F., Savenko, A., Petersen, D.H., Bang, O.: Note: Optical fiber milled by focused ion beam and its application for Fabry-Pérot refractive index sensor. Rev. Sci. Instrum. 82, 076103 (2011)
- 33. Kou, J., Feng, J., Wang, Q., Xu, F., Lu, Y.: Microfiber-probe-based ultrasmall interferometric sensor. Opt. Lett. **35**, 2308 (2010)
- 34. Warren-Smith, S.C., André, R.M., Perrella, C., Dellith, J., Rothhardt, M., Bartelt, H.: Direct core structuring of microstructured optical fibers using focused ion beam milling. Opt. Express. 24, 378–387 (2016)
- 35. Wang, F., Yuan, W., Hansen, O., Bang, O.: Selective filling of photonic crystal fibers using focused ion beam milled microchannels. Opt. Express 19, 17585 (2011)
- Iannuzzi, D., Deladi, S., Schreuders, H., Slaman, M., Rector, J.H., Elwenspoek, M.: Fiber-top cantilevers: a new generation of micromachined sensors for multipurpose applications—OSA technical digest (CD). In: Optical Fiber Sensors. p. TuB2. Optical Society of America, USA (2006)
- Iannuzzi, D., Deladi, S., Gadgil, V.J., Sanders, R.G.P., Schreuders, H., Elwenspoek, M.C.: Monolithic fiber-top sensor for critical environments and standard applications. Appl. Phys. Lett. 88, 053501 (2006)
- 38. Iannuzzi, D., Heeck, K., Slaman, M., de Man, S., Rector, J.H., Schreuders, H., Berenschot, J. W., Gadgil, V.J., Sanders, R.G.P., Elwenspoek, M.C., Deladi, S.: Fibre-top cantilevers: design, fabrication and applications. Meas. Sci. Technol. 18, 3247–3252 (2007)
- André, R.M., Pevec, S., Becker, M., Dellith, J., Rothhardt, M., Marques, M.B., Donlagic, D., Bartelt, H., Frazão, O.: Focused ion beam post-processing of optical fiber Fabry-Perot cavities for sensing applications. Opt. Express 22, 13102–13108 (2014)
- 40. Kou, J., Qiu, S., Xu, F., Lu, Y.: Demonstration of a compact temperature sensor based on first-order Bragg grating in a tapered fiber probe. Opt. Express 19, 18452 (2011)
- 41. Feng, Jing, Ding, Ming, Kou, Jun-Long, Fei, Xu, Yan-Qing, Lu: An optical fiber tip micrograting thermometer. IEEE Photon. J. 3, 810–814 (2011)

### Part II Optics

# Chapter 2 Focus on the Distal Assembly of a Nonlinear Endomicroscope: A Gradient Index Lens Coupled with a Piezoelectric Scanner for Fluorescence Lifetime Measurements

Claire Lefort, Hussein Hamzeh, Liu Wei, Frédéric Pain and Darine Abi Haidar

Abstract Today, prototypes of nonlinear endomicroscopes are appearing in order to transfer technics of multiphoton characterization of biological samples to humans in vivo in situ. But they require several optical optimizations to be adapted for a clinical use. Among them, the ideal distal lens, coupled with the ideal scanning system is not yet highlighted. In this paper, we are using a gradient index (GRIN) lens coupled with a piezoelectric scanning system (PZT). The main part is dedicated to a spectral analysis in the context of fluorescence lifetime measurements (FLIM), a well-known technic used to complete multiphoton characterization and discriminate healthy and tumors cells. We spectrally highlight the presence of a background fluorescence perturbing the spectral measurement through the GRIN lens in specific conditions of image space working distance. In a second part, we evaluate the resolution available with the GRIN lens and numerically determine the optimal object working distance depending on the position of the fiber imposed by the PZT.

C. Lefort

Laboratoire XLIM, UMR 7252, CNRS, Limoges 87060, France

H. Hamzeh · L. Wei · F. Pain · D. Abi Haidar (⊠) Laboratoire IMNC, UMR 8165, CNRS, Orsay, France e-mail: abihaidar@imnc.in2p3.fr

D. Abi Haidar Université Paris 7-Paris DIDEROT, Paris 75012, France C. Lefort et al.

#### 2.1 Introduction

Nowadays, cancer is a disease becoming more and more widespread in the world. Cancer treatments are a ticklish issue, depending on the way of development of the cancerous tumour and its localisation in the patient's body. Currently, the main hope of curing this illness lies in surgery, often completed by chemical treatments or radiotherapy [1]. It is now admitted that if this global process is applied in the early stages of the disease, the chances to heal a patient and extends his hope of life considerably increase. Nevertheless, surgery is a very invasive operation for patients and a risk of relapse associated with a new proliferation of cancerous cells in the treated area still exists. This is often mainly due to a non-complete removal of the cancerous cells in their whole, despite the use of combined modality therapies.

Starting from these alarming observations, mainly true in the case of cancers where it is not possible to remove a large part of the tissues around the cancer area like the brain cancer, there is an need for a tool enabling a fast and accurate discrimination between cancerous and healthy cells.

In this context, a way to achieve this goal has been proposed in recent years. It consists in the development of an endoscope with a microscopic resolution. The first endomicroscopes developed were based on the confocal principle with an excitation source in the visible range [2]. It allows to image endogenous tissue components like elastin, in vivo and in real time. This solution is now clinically used. However, some drawbacks are highlighted, such as an imaging depth limited to at a few tens of micrometres inside the target tissues, mainly due to the strong scattering properties of biological tissues, as well as the small number of mean contrasts available from endogenous fluorescent proteins under linear excitation.

To overcome these restrictions, the current research on endomicroscopy aims at developing multiphoton microscopy through an optical fibre. The main modification compared to confocal endomicroscope stays in the excitation source. Indeed, multiphoton processes are obtained thanks to a near infrared (NIR) excitation with femtosecond pulse (150 fs) having a high repetition rate (80 MHz) [3–5]. The interest of multiphoton imaging techniques compared to the confocal one is not only justified by an increase in imaging depth due to NIR excitation [6] but also by the availability of a new mean of contrast thanks to the second harmonic generation emitted by non-centrosymmetric structures as collagen. This, combined to the absence of confocal pinhole due to the intrinsic localisation of the nonlinear phenomenon in the focal plane of the focusing device, promote a deeper imaging depth within a few hundreds of micrometres.

While nonlinear microscopy is now a very well-known and essential tool for biological tissues characterization, its transposition to endomicroscopy remains problematic. Indeed, endomicroscopy requires several miniaturized elements like scanning system or distal lens of focalization [7]. The laser excitation, coming from a Ti: Sapph oscillator is classically delivered through an optical fibre, flexible and with a small diameter providing access to the internal hollow organs (alveoli, kidney...). The choice of the optimal fibre proves to be complex and must be

realized taking into account all other parameters of the global system. The fibre has to be associated in its upstream by a shaping module for the compensation of linear and nonlinear effects occurring inside this material medium [8].

For the instance, all the parts of the endomicroscope requiring to be miniaturized are problematic and prevent the multiphotonic endomicroscope commercialisation. This is particularly true considering the distal lens of focalization. A recent miniaturized technology, named "GRIN lenses" for gradient index lenses, is based on the gradient of negative refractive index of its material from the centre to its outskirts, glued inside a stainless cylinder steel [9]. Dimensions of classical GRIN lenses range between 0.35 and 2 mm in diameter and between 5 mm and few cm in length, with a numerical aperture (NA) of the object space between 0.2 and 0.8.

In this paper we are studying GRIN lenses for the development of a multiphoton endomicroscope. The first part of this publication is dedicated to the experimental study of a GRIN lens alone. Background fluorescence induced in the GRIN lens is studied under classical UV excitation beam, mimicking the emitted multiphoton fluorescence or second harmonic generation coming from biological samples. Then, the impact of the background fluorescence of the GRIN lens on its imaging ability, spectral detection and fluorescence lifetime measurements is evaluated. The 2D lateral resolution is experimentally measured using 1 um diameter gold beads. The second part of the paper is dedicated to numerical simulations of the GRIN lens coupled to a specifically designed double clad fibre (DCF) ideal for the assembly of a multiphotonic endomicroscope [4] using Zemax program. Both geometric ray tracing and Gaussian beam approach are considered and compared. Furthermore, the influence of the relative position between the GRIN lens and the DCF tip on the magnification, field of view (FOV), axial and lateral resolutions are evaluated. Finally, choosing a piezoelectric (PZT) stage as scanning device [10], the coupling of the DCF with the PZT and the GRIN lens is characterized through the variation of the image working distance, the coupling efficiency of the fluorescence beam inside the DCF, the size of the FOV and the axial and lateral resolutions.

#### 2.2 Experimental Characterization of the GRIN Lens

#### 2.2.1 Definition of the GRIN Lenses

All the manufactured GRIN lenses have a continuously variable index of refraction between the periphery and the centre of the lens. This optic is glued to a biocompatible stainless steel ring.

In this study, we have characterized a commercial GRIN lens with a total length of 7.53 mm and a diameter of 1.4 mm (GT-MO-080-018-810, Grintech, Jena, Germany). The definitions of the image and object space and their WD are presented in Fig. 2.1. The object space contains the target biological sample and in the image space lies the DCF delivering the laser and collecting the multiphoton signal emitted by the sample.

C. Lefort et al.

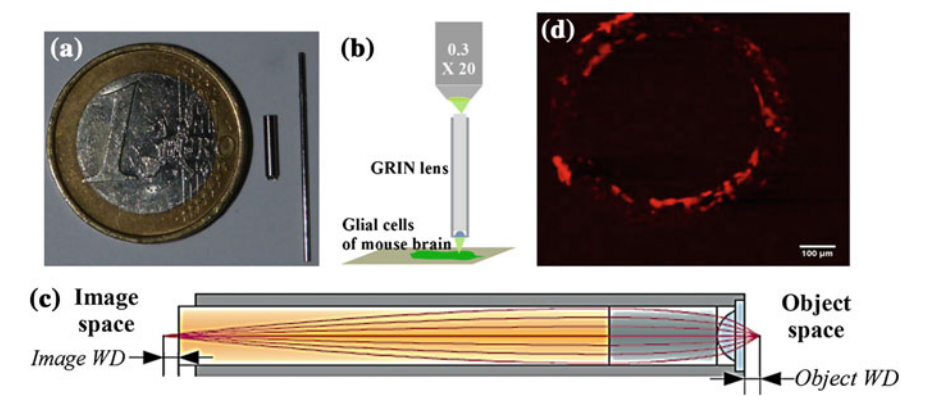


Fig. 2.1 a Two GRIN lenses used in this study. b Experimental setup for the characterization of GRIN lenses. c Definitions of the image and object spaces and the corresponding WD. d Fluorescence image of the glue between the GRIN lens and the stainless steel of protection by confocal imaging

# 2.2.2 Analysis of the Background Fluorescence

# 2.2.2.1 Background Fluorescence Highlighted

Confocal imaging with a GRIN lens needs an initial step for the characterization of the parasite fluorophores emitting a background. The confocal microscope is focusing a krypton argon laser inside the GRIN lens placed under the objective (Fig. 2.1b). An image of the image face of the GRIN lens is thus shown. Figure 2.1d presents the resulting observation of the image space of the GRIN lens where an inhomogeneous fluorescent signal is visible on Fig. 2.1d and probably results from fluorescent components in the glue fixing the GRIN lens to the steel ring. In a first approach, no impact of the intrinsic fluorescence of the glue on fluorescence images of biological samples is visible.

# 2.2.2.2 Spectral Analysis of the Background Fluorescence

We have analysed spectrally the background fluorescence of the GRIN lens thanks to the experimental setup presented in Fig. 2.2a.

This experiment involves a pulsed diode laser at  $405 \pm 10$  nm (LDHP-C-405B, Picoquant) injected into one of the two fibres of a bifurcated fibre (Fig. 2.2b). The average power of the laser can be managed, as well as the repetition rate, which can be set between 2.5 and 40 MHz. The excitation source is guided through the fibre to the image space of the GRIN lens. A solution of Rhodamine B (RhB) is placed in

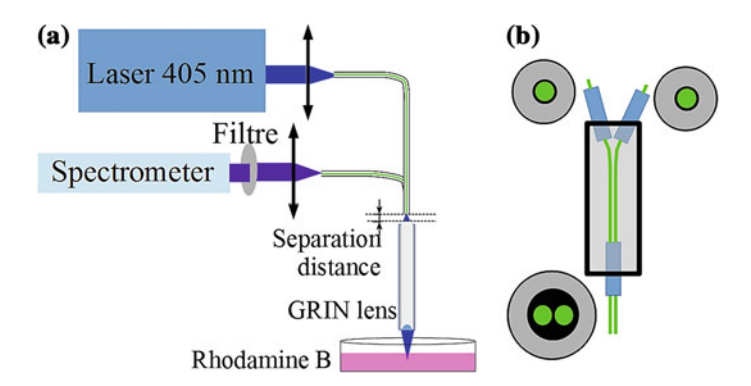


Fig. 2.2 a Experimental setup for the spectral characterization of the background fluorescence of the GRIN lens. b Structure of the bifurcated fibre

the object space of the GRIN lens. The backward fluorescence, emitted by both the RhB and the GRIN lens, is collected by the second core of the bifurcated fibre. A spectrometer, preceded by a long pass filter to reject the excitation laser beam analyses the result. First of all, the GRIN lens is excited at 405 nm without any sample and without any filter. The idea is to measure the background fluorescence emitted by the GRIN lens alone. The graph of Fig. 2.3a shows the spectrum of the emitted background fluorescence from the GRIN lens. This spectrum covers a wide spectral range of 300 nm in the visible range.

The solution of RhB is then illuminated and its fluorescence emission spectrum collected by the GRIN lens with a separation distance between the lens and the fibre of 2 mm and less than 200  $\mu m$  (Fig. 2.3b, c, respectively). Figure 2.3d, e resumes the spectra of all the components by comparison with the sum of all the spectrum obtained: glue of the GRIN lens and the RhB solution. The latter was measured using the bifurcated fibre alone so as to eliminate its possible contribution to the fluorescence signal.

The contribution of the fluorescence from the glue around the GRIN lens is now spectrally characterized (Fig. 2.3a, b and d). From comparison between Fig. 2.3b, c, it can be shown that depending on the separation distance between the fibre tip and the GRIN lens, the contribution of the fluorescence of the glue is variable. At a large separation distance between the GRIN lens and the fibre tip (2 mm, Fig. 2.3b), the RhB spectrum is significantly altered by the background fluorescence, while the background fluorescence is hardly noticeable when this separation distance is very short, below 200  $\mu$ m. This can be explained if one considers the very short image space WD of the GRIN lens (below 100  $\mu$ m in air at 405 nm). It is also remarkable from Fig. 2.3d that the RhB spectrum in blue recovers successfully the measured spectrum using the GRIN lens corroborated by Fig. 2.3e.

C. Lefort et al.

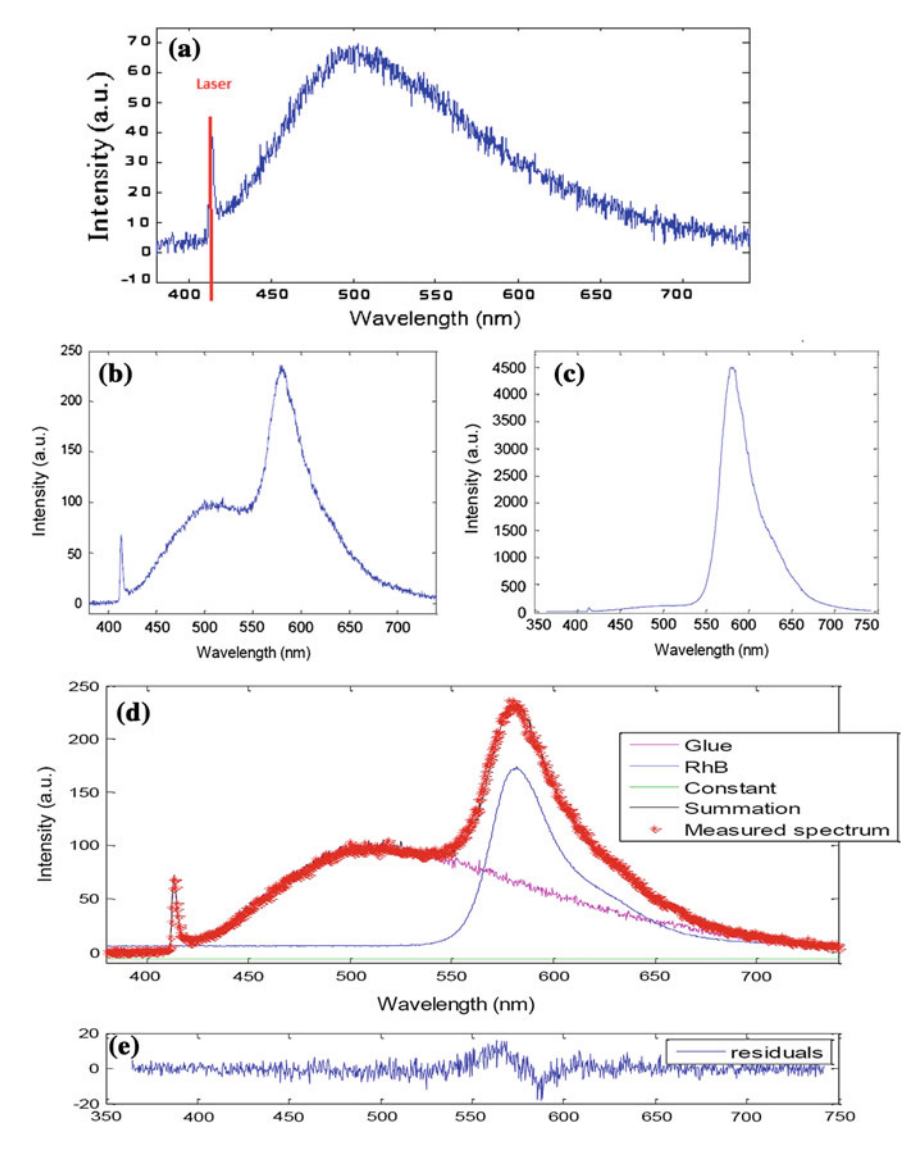


**Fig. 2.3** a Emission spectrum of the background fluorescence from the GRIN lens alone with at 405 nm. **b** RhB spectrum measured with a separation distance between the fibre and the GRIN lens of 2 mm and  $\bf c$  of less than 200  $\mu$ m.  $\bf d$  Summary of the measured emission spectra and the sum of the RhB and glue emission spectra.  $\bf e$  Calculation of the difference between the sum of each spectral component and the effective measured spectrum

### 2.2.2.3 GRIN Lens for Lifetime Measurements

We have shown that background fluorescence is perturbing the spectral measurement through the GRIN lens in specific conditions. In this section, considering ideal conditions of object and image WD, the effect of the GRIN lens position is evaluated on the measurement of fluorescence lifetime of the RhB.

To do so, the spectrometer in Fig. 2.2 is replaced by a photomultiplier tube (PMT) and a Time-Correlated Single Photon Counting (TCSPC) module synchronized with the excitation source. This method detects the exponential decay of fluorescence based on an accurate record of a single photon using a highly sensitive photon detector. The delay time of emission of a photon relative to the laser excitation pulse corresponds to the time spent in the excited state. Then, excitation is repeated several times to maintain the condition that only one photon per molecule is detected at each pulse. A photon counting histogram is generated which represents the fluorescence decay time and the instrument response function (IRF), a Time Harp 200 acquisition card (Pico Quant, Berlin Germany). The timing precision of TCSPC system is characterized by the IRF and should be infinitely narrow for an ideal system. Experimentally, the laser emission is rejected using a 410 nm high pass filter in order to detect fluorescence. The lifetime decays is fitted to an exponential model in order to extract the lifetime information with a reasonable fit quality, assessed by the residuals of the fitting. An exponential model is chosen because it gives a good description of the physics involved in the lifetime decay. Two exponential models have been tested to extract the lifetime information: the multi-exponential tail fit without considering the IRF and the exponential reconvolution considering the IRF. These equations are detailed in (2.1) and (2.2).

$$I(t) = \sum_{i=1}^{n} A_i e^{-\frac{t}{\tau_i}}$$
 (2.1)

$$I(t) = \int_{-\infty}^{t} IRF(t') \sum_{i=1}^{n} A_i e^{-\frac{t-t'}{\tau_i}} dt'$$
(2.2)

where:

I(t) is the measured decay data,

A<sub>i</sub> the amplitude of the *i*th component, in counts,

 $\tau_i$  the lifetime of the *i*th component that has to be calculated.

IRF was measured using a mirror instead of the RhB sample and the filter was replaced by an optical density filter in order to let the attenuated laser beam pass to the PMT for IRF detection. The IRFs measurements of the fibre alone, the fibre coupled to a  $10\times$  microscope objective and the fibre coupled to the GRIN lens are shown and compared in Fig. 2.4.

The IRFs around 0.65 ns at the full width half maximum (FWHM) are similar for the three conditions. As a result, the GRIN lens does not affect lifetime measurements.

C. Lefort et al.

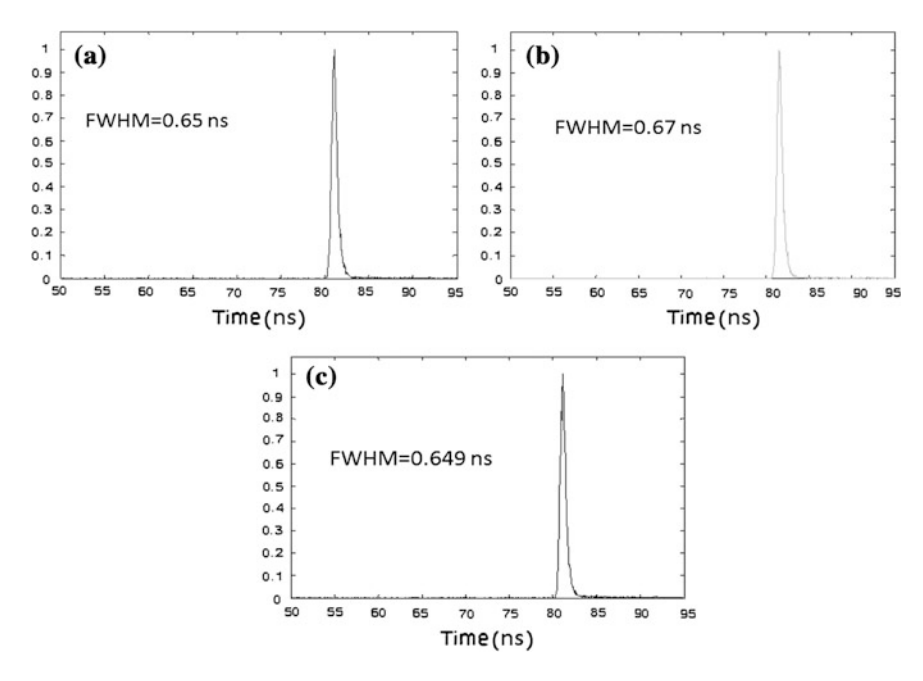
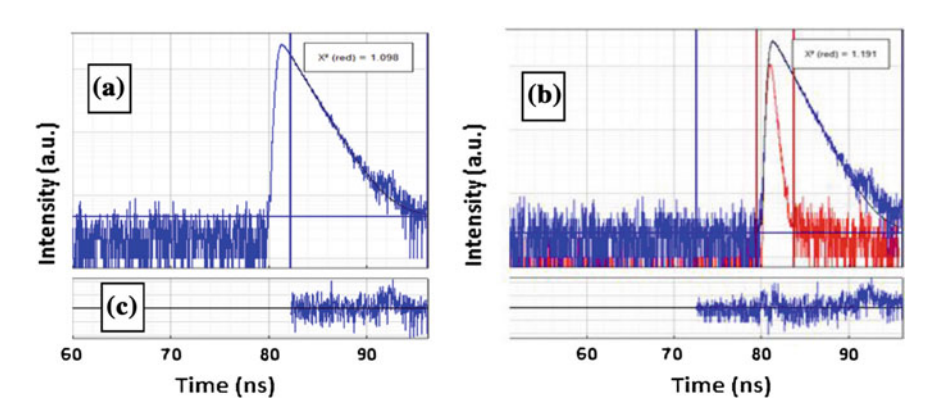


Fig. 2.4 Measurement of the lifetime of the experimental setup. a Fibre alone. b Fibre and  $10 \times$  objective. c Fibre and GRIN lens



**Fig. 2.5** Measured fluorescence decay (*blue*) coupled with the fitting model (*black*). **a** Lifetime of RhB without considering the IRF. **b** Lifetime fitting by reconvolution, IRF deconvoluted with the decay data (*red*). **c** Residuals randomly distributed across the fitting range

Secondly, lifetime measurements using the two fitting methods previously detailed and decay fits of the fluorescence signal of the RhB solution were realized. Figure 2.5a, b displays the fluorescence lifetime of RhB superimposed with the fitting curves.

Element of the setup	A (counts)	τ (ns)	Fit method
Fibre	$1872.4 \pm 20.9$	$1.72 \pm 0.02$	Tail
	$14,046 \pm 94.7$	$1.67 \pm 0.01$	Reconv
Objective	$1638.5 \pm 19.3$	$1.705 \pm 0.015$	Tail
	$3345.3 \pm 40.4$	$1.703 \pm 0.014$	Reconv
GRIN lens	$252.5 \pm 9.41$	$1.628 \pm 0.049$	Tail
	$1835 \pm 29.6$	$1.616 \pm 0.019$	Reconv

**Table 2.1** Lifetime decay fitting through the setup elements using tail fitting without the IRF and reconvolution fitting with the IRF

All the lifetime decays of RhB through the different elements of the setup are summarized in Table 2.1.

In the literature [11], the mean lifetime data of the fluorescence lifetime of a solution of RhB in water at 20 °C is  $\tau_{RhB, ref} = 1.72 \pm 0.02$  ns. The fluorescence lifetime is therefore not affected by the presence of the fibre considering the tail fitting method, while the reconvolution method is less relevant. Furthermore, the fluorescence lifetime is not significantly disturbed by the microscope objective if one takes the experimental incertitude into account. Finally, it can be seen that for the GRIN lens, both fitting methods, lead to a decrease of the fluorescence lifetime from 1.7 ns to about 1.62 ns. This may be explained by the detection of fluorescence signal of the glue of the GRIN lens, leading to an average measurement of the lifetime of the RhB and the glue. That point corroborates the previous conclusions in Sects. 2.2.1 and 2.2.2 on the significant perturbation of the signal collected by the GRIN lens due to the background fluorescence of the glue.

# 2.2.3 GRIN Lens Resolution Measurement

The confocal microscope is used to evaluate the resolution of the imaging system as a whole ( $10 \times$  microscope objective combined with the GRIN lens). Gold beads having a diameter of 1  $\mu$ m are assumed to be point sources. A Gaussian function depicted in Fig. 2.6a, b and c fits the axial and lateral profiles of their images allowing to calculate the FWHM, equivalent to the optical resolution of the system.

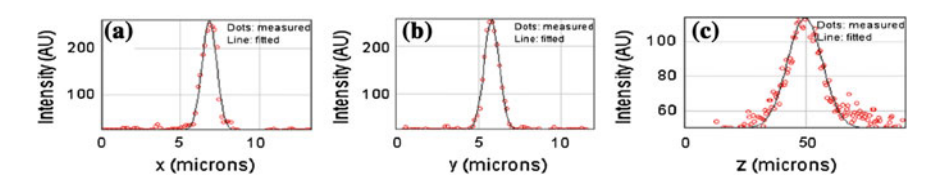


Fig. 2.6 Gaussian fits and beads profile measurements. Resolutions: a Lateral in x ( $\mu m$ ), b Lateral in y ( $\mu m$ ), and c Axial in z ( $\mu m$ )

28 C. Lefort et al.

The lateral resolution in x and y are both 1  $\mu$ m, in agreement with the best performances described in the literature [3]. This system consequently equals the state of the art of the resolution of a fibred endomicroscope, adding the huge advantage of the miniaturized sizes.

# 2.3 Numerical Analysis of the Global Endomicroscope

A numerical simulation of the distal end of an optimized nonlinear endomicroscope is proposed, coupling a GRIN lens with a PZT scanner. These simulations are led simultaneously for NIR nonlinear excitation and collection of the multiphotonic signal emitted by the target. The GRIN lens is coupled to the scanning system and the optical fibre. The simulated fibre, a DCF, delivers the nonlinear excitation by the core and collects the multiphotonic emission by the inner cladding. This DCF is simulated with ideal parameters for delivering the multiphotonic excitation through a small core diameter (5  $\mu$ m) single mode at 800 nm with a small NA (0.04) and a large inner cladding diameter (200  $\mu$ m) to collect the maximum of multiphotonic signal from the GRIN lens thanks, to a large NA (0.3).

# 2.3.1 PZT Scanning System

The scanning system is a tubular PZT. The important advantage of such a scanner stays in its small size not yet equalled by another technology. It consists in a small tubular piezoelectric actuator governed by four electrodes grouped in two pairs, with an optical fibre positioned inside the actuator and electrically glued at its tip. This layout allows driving the fibre tip, exceeding the PZT for several tens of millimetres by application of an arbitrary waveform (triangular or sinusoidal) with a chosen frequency, for each pair of electrodes. This results in a well-defined movement of the fibre tip. The adapted one in the context of endomicroscopy is a circular scanning pattern of the extremity of the fibre. The amplitude is adjustable until a limit depending on the electrical parameters of the PZT, so that the position of the fibre tip can be set on all the surface of a defined circle. The position of the focal point of the excitation beam on different parts of the target relies on the relative position of the fibre with the GRIN lens, as illustrated in Fig. 2.7.



Fig. 2.7 Scheme of the distal end of the endomicroscope containing the DCF, the PZT and the GRIN lens

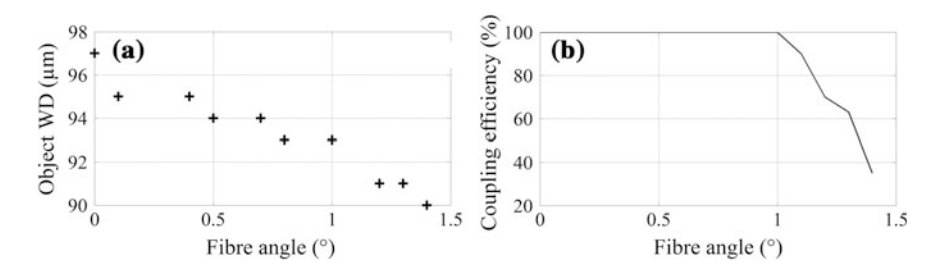


Fig. 2.8 Consequences of the use of a PZT scanner. Evolution of **a** the object WD. **b** the coupling efficiency of the excitation beam with the DCF angle

Several consequences are arising from the use of the PZT scanning system on the fibre tip resulting from the angle between the fibre tip and the GRIN lens: (i) the object WD, (ii) the coupling efficiency between the GRIN lens and the excitation laser, also related to the DCF core diameter and its NA which are necessarily modified by the tilt angle of the fibre. This observation are the subject of this part of numerical simulation realized with Zemax program. Figure 2.8a, b resume the related results.

A decrease of the object WD with the fibre angle is shown in Fig. 2.8a, revealing a fibre tip is not really a plan, but describing a semi-sphere. This parameter is not a major drawback but it should be considered for the interpretation of the obtained images or taken in consideration for the numerical reconstruction of the images. An increase of the fibre angle leads to an important decrease of the coupling efficiency between the excitation beam and the GRIN lens (Fig. 2.8b). Indeed, 10 % of the excitation beam is lost for an angle of 1.1° and more than 60 % are not coupled for 1.4°. This results in the fluctuation of the incident average power in the target, involving a proportional fluctuation of the emitted fluorescence. To limit this problem, a reduction of the amplitude of scan is necessary resulting in the reduction of the field of view in the object space.

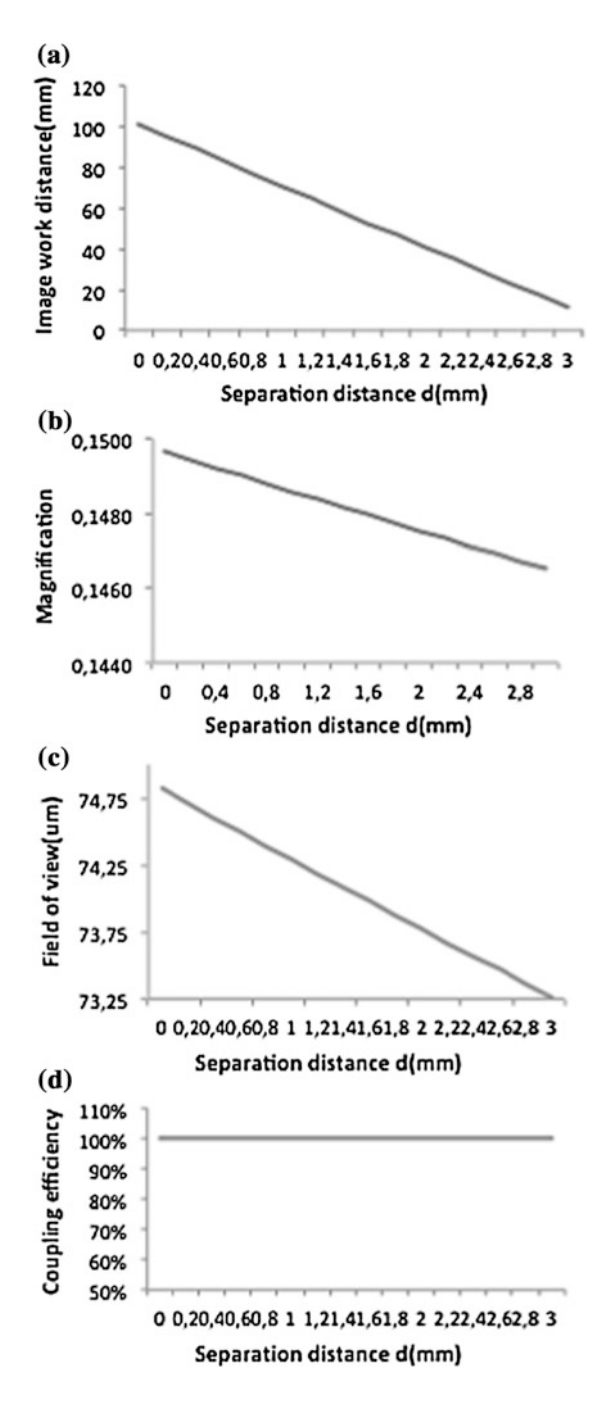
To conclude, PZT scanning system is interesting by its small diameter ideal for the miniaturization of the distal end, but several alteration of the detected image must be considered to interpret the observed images.

# 2.3.2 Simulation of the Optimal Distance Between the DCF and the GRIN Lens

Several parameters are varying with the distance between the DCF and the GRIN lens (Fig. 2.2a): (i) the focal point position and thus (ii) the object WD, (iii) the magnification properties, (iv) the coupling efficiency and (v) the FOV. The impact of these parameters was numerically simulated and the results are summarized in Fig. 2.9. A distance ranging between 0 and 3 mm between the DCF and the GRIN lens has been tested.

C. Lefort et al.

Fig. 2.9 Calculated influence of the separation distance between the GRIN lens and the fibre tip on several parameters. a Object WD. b Magnification. c FOV. d Coupling efficiency



The object WD decreases when the separation distance between the fibre and the GRIN lens increases, as expected. And thus, the focal point is under control of this parameter and can be adjusted between 10 and 100  $\mu$ m, the highest penetration depth reachable by the excitation beam. The magnification and the FOV decrease slowly when the separation distance increases. For example, the FOV, which is very small at the origin (less than 75  $\mu$ m) declines to about 73.25  $\mu$ m at 3 mm. In this distance ranges, we can consider these parameters can be considered negligible.

In Fig. 2.9d it is shown that whatever the distance between the fibre and the GRIN lens, after the collection by the GRIN lens, the coupling efficiency of the multiphotonic signal emitted by the sample is not modified. The big inner cladding diameter of 200  $\mu$ m with the highest possible NA of 0.3 is responsible for this result, justifying the choice of the inner cladding dimension. Consequently, that optimized parameter is crucial for the efficient collection of very weak multiphoton endogenous signals.

In conclusion, if an axial scanning is required, moving the separation distance GRIN lenses are now commonly used in the context of the miniaturization of a. Nevertheless, severals modifications must be considered: an important decrease of the object WD as well as a modification of the magnification and the FOV are modifying the resulting images.

# 2.4 Conclusions

GRIN lenses are now commonly used towards the miniaturization of a distal head of an endomicroscope. In This article, we have consequently characterized a commercial GRIN lens in the context of imaging brain tissues under a confocal microscope. We have identified a potential parasite signal of fluorescent coming from the outlying glue all around the effective area of the lens. Starting from this observation, we have analysed the imaging of glial cells of mouse brain and no influence on the resulting fluorescent image of the sample has been observed. To evaluate the importance of this background fluorescence, spectral analysis and fluorescence lifetime measurements were managed. A non-negligible part of this fluorescence that can be easily identified by its spectrum and by its lifetime were shown for both of them.

In a second step, the GRIN lens lateral and axial resolutions were then established to around respectively 1 and 16  $\mu m,$  in agreement with the values usually presented in the literature.

Finally, we have numerically simulated the global endomicroscope including this GRIN lens coupled to a homemade DCF fixed with a PZT scanning system. We have highlighted limitations of the use of this scanning device: (i) the focal plan is necessarily not plan but curved and (ii) the coupling efficiency of the excitation beam between the DCF and the GRIN lens is hugely reduced to less than 40 % of coupling when the fibre angle exceeds 1.4°. More, the separation distance between the GRIN lens and the DCF influenced the position of the focal point in the object

32 C. Lefort et al.

plan, presenting a way to perform an axial scanning system, which is still a limiting point for obtaining 3D images. We have nevertheless noticed that a modification of the separation distance is inducing a reduction of the FOV and of the magnification. The best simulated FOV obtained with the GRIN lens is  $75 \times 75 \ \mu m^2$ , which is a very small and far from the ideal situation usually asked by the surgeons of  $1 \times 1 \ mm^2$ .

For an ideal development of an endomicroscope, all these limitations must be carefully thought for the experimental use of the GRIN lens. Globally, GRIN lens technology remains the only one allowing a distal lens having a diameter smaller than 0.5 mm, being a fundamental importance in nonlinear endomicroscopy in a clinical application.

Acknowledgements This work has been highly supported by INCA Plan Cancer with Physicancer program grants "MEMBO" & "MEVO" and the Institut National de Physique Nucléaire et de Physique des Particules (IN2P3). This work was supported by the L'Oreal Foundation, thanks to the French National Program "For Woman in Science", distinguishing Claire Lefort for her work on endomicroscopy.

# References

- 1. Miller, A.B., Hoogstraten, B., Staquet, M., Winkler, A.: Reporting results of cancer treatment. Cancer **47**(1), 207–214 (1981)
- Salaün, M., Roussel, F., Hauss, P.-A., Lachkar, S., Thiberville, L.: In vivo imaging of pulmonary alveolar proteinosis using confocal endomicroscopy. Eur. Respir. J. 36(2), 451–453 (2010)
- 3. Gu, M., Bao, H., Kang, H.: Fibre-optical microendoscopy. J. Microsc. 254(1), 13–18 (2014)
- Lefort, C., Hamzeh, H., Louradour, F., Pain, F., Abi Haidar, D.: Characterization, comparison and choice of a commercial double-clad fiber for nonlinear endomicroscopy. J. Biomed. Optics 19(7), 076005 (2014)
- Peyrot, D.A., Lefort, C., Steffenhagen, M., Mansuryan, T., Ducourthial, G., Abi-Haidar, D., Sandeau, N., Vever-Bizet, C., Krulik, S.G., Thiberville, L., Louradour, F., Bourg-Heckly, G.: Devlelopment of a nonlinear fiber-optic spectrometer for human lung tissue exploration. Biomed. Optics Expr. 3(5), 840–853 (2012)
- Cosignani, V., Dvornikov, A., Aguilar, J.-S., Stingari, C., Edwards, R., Mantulin, W.W., Gratton, E.: Deep tissue fluorescence imaging and in vivo biological applications. J. Biomed. Optics 17(11), 116023 (2012)
- Ducourthial, G., Lefort, C., Peyrot, D.A., Mansuryan, T., Kruglik, S.G., Vever-Bizet, C., Thiberville, L., Lacombe, F., Bourg-Heckly, G., Louradour, F.: Label free multiphoton imaging of human pulmonary tissues through two-meter-long microstructured fiber and multicore image-guide. In: Progress in Biomedical Optics and Imaging—Proceedings of SPIE, 85750H (2013)
- Lelek, M., Suran, E., Louradour, F., Barthelemy, A., Viellerobe, B., Lacombe, F.: Coherent femtosecond pulse shaping for the optimization of a non-linear micro-endoscope. Opt. Expr. 15(16), 10154–10162 (2007)
- Hamzeh, H., Lefort, C., Pain, F., Abi Haidar, D.: Optimization and characterization of nonlinear excitation and collection through a gradient-index lens for high-resolution nonlinear endomicroscopy. Opt. Lett. 40(5), 808–811 (2015)

- Myaing, M.T.M., MacDonald, D.J., Li, X.: Fiber-optic scanning two-photon fluorescence endoscope. Opt. Lett. 31(8), 1076–1078 (2006)
- Boens, Noel, Qin, Wenwu, Basaric, Nikola, Hofkens, Johan, Ameloot, Marcel, Pouget, Jacques: Fluorescence lifetime standards for time and frequency domain fluorescence spectroscopy. Anal. Chem. 79, 2137–2149 (2007)

# Chapter 3 Improvement of Transverse Offset-Based Single-Mode-Multimode-Single-ModeFiber Structure for DPSK Signal Demodulation

Xiaoyong Chen and Paloma R. Horche

**Abstract** In this work, we develop a novel all-fiber Mach-Zehnder interferometer (MZI), which is based on a commercial graded-index multimode fiber mismatch spliced between two single-mode fibers. Compared to the common single-mode-multimode-single-mode-fiber (SMS) structure with all fibers aligned perfectly, theoretical analysis shows that more power is coupled into the LP<sub>11</sub> mode while less power is coupled into the LP<sub>01</sub> mode, resulting in power balance between these two modes and high interference extinction ratio (ER). Experiments were also carried out to evaluate the performance of the proposed MZI, and results of transmission spectra showed that interference ER as high as 18 dB can be obtained. Finally, we demonstrate, through simulation, that our proposed MZI can be used for DPSK signal demodulation. Receiver performances are evaluated through back-to-back sensitivity, narrowband optical filtering and differential group delay, with results showing that our proposed DPSK receiver can provide comparable performance as the conventional receiver.

# 3.1 Introduction

Differential Phase Shift Keying (DPSK) signal, which encodes the binary data as either a 0 or  $\pi$  optical phase shift between the adjacent bits, has been proposed for optical transmission systems, since it exhibits superior optical signal to noise ratio (OSNR) sensitivity, high tolerance to chromatic dispersion and high robustness to fiber nonlinear effects [1, 2]. Compared with the on-off keying (OOK), the most obvious benefit of DPSK is the  $\sim$ 3 dB OSNR improvement to reach a given BER.

X. Chen (⋈) · P.R. Horche

Departamento de Tecnología Fotónica y Bioingeniería, Universidad Politécnica de Madrid, Avda. Complutense 30, Madrid, Spain

e-mail: xiaoyong.chen@tfo.upm.es

P.R. Horche

e-mail: phorche@tfo.upm.es

Such advantage can be used to extend the transmission distance, reduce optical requirements, and relax component specifications. Note, however, that this  $\sim 3$  dB benefit can only be obtained using balanced detection.

A delay interferometer (DI), like a conventional Mach-Zehnder interferometer (MZI), is usually used for DPSK signal demodulation [1], due to the simple structure and easy implementation. However, the conventional MZIs have one obvious drawback: the performance is easily affected by the environment, such as temperature, since the two separated light goes through two different physical paths. In order to improve the MZI performance, an all-fiber MZI, which is based on a single-mode-multimode-single-mode-fiber (SMS) structure, is proposed to take place of the conventional MZI in recent years. The main advantage of all-fiber SMS-based MZI, compared to the conventional one, is low-cost, easy manufacture, and performance improvement due to the two arms share the same hardware. Given to these advantages, it has been studied and developed to act as novel optical devices, e.g., a temperature sensor [3], a strain sensor [4], a refractive index sensor [5], a fiber lens [6], and a bandpass filter [7].

Although the all-fiber SMS-based MZI shows advantages in some aspects, it has an obvious drawback: the interference extinction ratio (ER) is very low, since the power coupled into  $LP_{01}$  mode is much higher than that coupled into the  $LP_{02}$  mode. Moreover, the other high-order modes like  $LP_{03}$  and  $LP_{04}$  exited and propagating in the multimode fiber (MMF) will also affect the interference ER. To improve the interference ER, some schemes, through using a special fiber to replace the commercial graded-index MMF in the SMS structure, have been proposed, including a bi-mode fiber [8], a photonic crystal fiber (PCF) [9], a graded-index MMF with a central dip [10], a double cladding fiber [11], and a thin-core fiber [12]. Because of the high interference ER, Some of these schemes [8–10] have also been proposed for DPSK signal demodulation.

In this work, we propose an alternative all-fiber MZI, which is based on a graded-index MMF mismatch spliced between two SMFs. With a transverse offset, more power is coupled into the first non-circular symmetrical mode LP<sub>11</sub>, while less power is coupled into fundamental mode LP<sub>01</sub>, resulting in balancing the power difference between these two beating modes, and thus improving the interference ER. This improvement makes it possible to use as a DPSK demodulator and we will also demonstrate this application in this work. Like other all-fiber MZI-based DPSK receivers [8–10], our proposed DPSK receiver also shows merits of low-cost, easy manufacture and good performance.

The paper is organized as follows: the theory of the proposed all-fiber MZI is presented in Sect. 3.2; Experimental setup and experimental results are presented and discussed in Sect. 3.3; DPSK receiver based on the proposed all-fiber MZI for 40 Gbps DPSK signal demodulation is presented, and simulation results, including back-to-back sensitivity, receiver performances under narrowband optical filtering and differential group delay, are commented in Sect. 3.4; Finally, conclusions are drawn in Sect. 3.5.

# 3.2 The Design of the Proposed All-Fiber MZI

# 3.2.1 Coupling Modes in the Proposed SMS Structure

Modal interference is a well-known phenomenon and it had been studied by many authors [13–16]. In the normal SMS structure, as shown in Fig. 3.1a, due to the perfect alignement of all fibers, only the circular symmetrical modes will be excited and most of the power from the input-SMF is coupled into the  $LP_{01}$  and  $LP_{02}$  modes. These two modes propagate along the MMF with different propagation constants and interfere with each other when they transmit from the MMF to the output-SMF. Therefore, the  $LP_{01}$  and  $LP_{02}$  modes can be seen as the two different optical paths,  $T_1$  and  $T_2$ , in a conventional MZI, as shown in Fig. 3.1b, and the SMS structure can be seen as a quasi-MZI. However, since the large power difference between the  $LP_{01}$  and  $LP_{02}$  modes, the interference ER of this structure is very low.

In order to improve the interference ER, we propose an alternative SMS structure, where the MMF is spliced between two SMFs with a certain transverse offset. Unlike the SMS structure with all fibers aligned perfectly, in our proposed SMS structure, not only the circular symmetrical modes will be excited, but also the non-circular symmetrical modes, such as LP<sub>11</sub> and LP<sub>21</sub> modes. All these excited modes propagate along the propagation direction and interfere with each other.

Based on the concept of transverse offset between the SMFs and the MMF, our proposed structure can be divided into three types, as shown in Fig. 3.2a-c: (a) input-SMF and output-SMF are on the same propagation axis but offset from the center of the MMF; (b) the input-SMF is aligned with the MMF while the

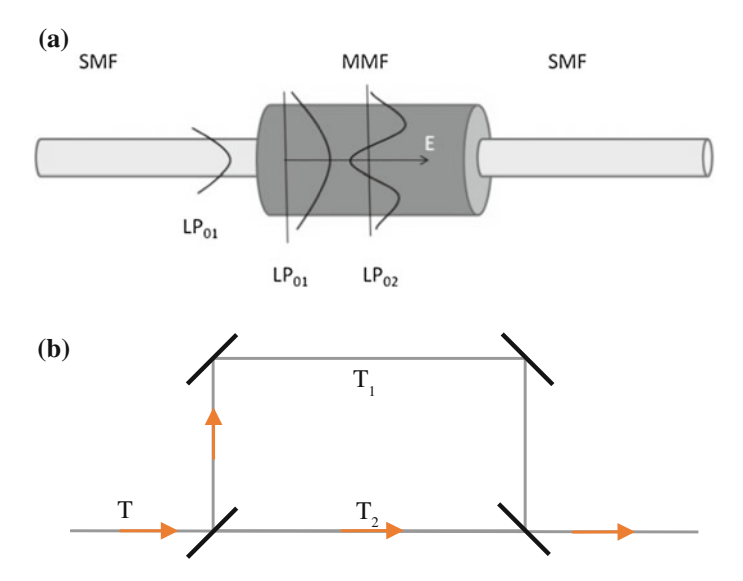


Fig. 3.1 SMS structure with all fibers aligned perfectly (a); principle of the conventional MZI (b)

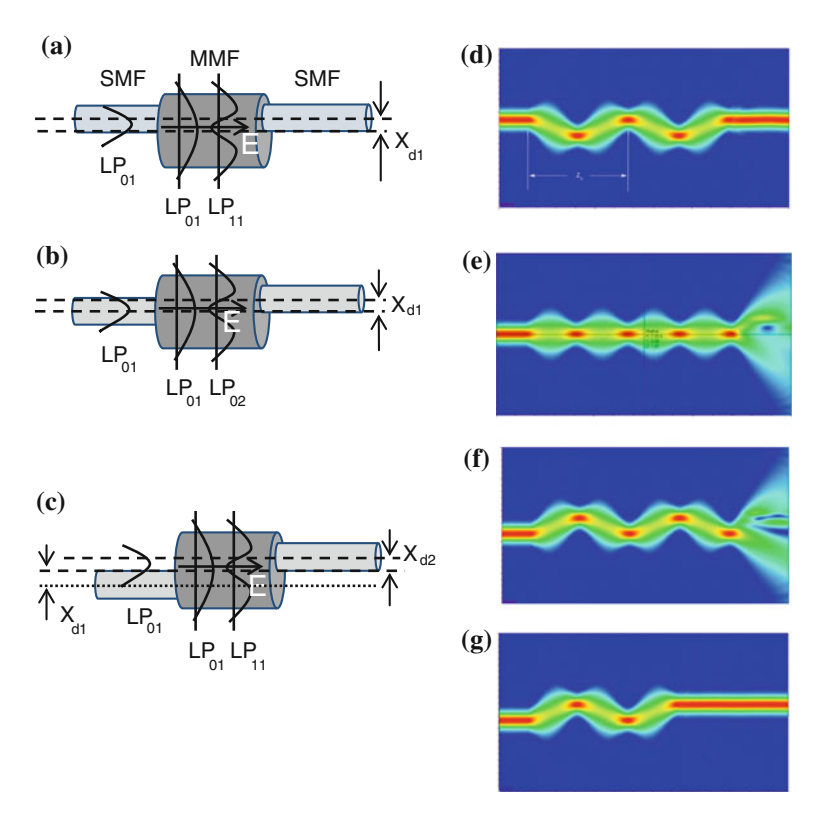


Fig. 3.2 Structure of all-fiber MZI based on an MMF mismatch spliced between two SMFs:  $\bf a$  the input-SMF and the output-SMF are in the same propagation axis,  $\bf b$  the input-SMF is aligned to the center while the output-SMF deviates from the center,  $\bf c$  the input-SMF and the output-SMF are randomly spliced with the MMF;  $\bf d$ - $\bf g$  are the corresponding power distribution in the along the fibers. Note that ( $\bf f$ ) and ( $\bf g$ ) correspond to structure ( $\bf c$ )

output-SMF is misaligned; (c) both the input-SMF and the output-SMF are randomly misaligned with the MMF and they will not be on the same propagation axis. In the third structure, it can be subsequently divided into two sub-types, depending on whether the input-SMF and the output-SMF are aligned with regarding to the center of the MMF or not.

Assuming that the transverse offset between the input-SMF and the MMF is  $x_{\rm d1}$ , whilst that is  $x_{\rm d2}$  between the MMF and the output-SMF, the coupling coefficient based on the overlap integral method at z=0 and z=L can be, respectively, written as follows [6]:

$$c_{nk}^{(0)} = \frac{\left|\int_0^\infty E_{in}(r - x_{d1})\psi_{nk}^*(r)rdr\right|^2}{\int_0^\infty |E_{in}(r)|^2 rdr \int_0^\infty |\psi_{nk}(r)|^2 rdr}$$
(3.1)

$$c_{nk}^{(L)} = \frac{\left| \int_0^\infty \psi_{nk}(r) E_{out}^*(r - x_{d2}) r dr \right|^2}{\int_0^\infty \left| E_{in}(r) \right|^2 r dr \int_0^\infty \left| \psi_{nk}(r) \right|^2 r dr}$$
(3.2)

where  $E_{in}$  and  $E_{out}$  are respectively represented the field distribution of the inputand output-SMF. Because the MMF used in these SMS structures (Fig. 3.2a–c) is the commercial graded-index MMF, the field distribution of each excited mode in the MMF can be described using expressions (3.3) and (3.4). The field distribution at z = L and power coupled into the output-SMF can be written as (3.5) and (3.6).

- Field distribution of each excited mode [17]:

$$\psi_{nk}(r) = N_{nk}r^n \exp\left[-\frac{1}{2}\gamma^2 r^2\right] L_{k-1}^n(\gamma^2 r^2)$$
 (3.3)

with

$$N_{nk} = \gamma^{n+1} \left[ \frac{2(n-1)!}{\Gamma(n+k)} \right]^{1/2}$$
 (3.4)

- Field distribution at z = L,

$$\psi(r,L) = \sum_{n=0}^{N} \sum_{k=1}^{K} \sqrt{c_{nk}^{(0)}} \psi_{nk}(r) \exp(-i\beta_{nk}L)$$
 (3.5)

Output power,

$$P_{\text{out}} = \sum_{n=0}^{N} \sum_{k=1}^{K} c_{nk}^{(0)} c_{nk}^{(L)} + 2 \sum_{n=0}^{N} \sum_{k=1}^{K} \sum_{q=0}^{Q} \sum_{p=1}^{P} \sqrt{c_{nk}^{(0)} c_{nk}^{(L)} c_{qp}^{(0)} c_{qp}^{(L)}} \cos(\varphi_{nk,qp})$$

$$lm \neq qp$$
(3.6)

where  $N_{nk}$  represents the normalization constant of each excited  $LP_{nk}$  mode. The parameter  $\gamma$  is determined by the radius  $a_M$  and the V-parameter of the MMF,  $\gamma = \sqrt{V_M}/a_M$ , where  $V_M = \frac{2\pi a_M}{\lambda_0} \sqrt{n_1^2 - n_2^2}$ .  $L_k^n(x)$  is the Laguerre polynomials,  $L_k^n(x) = \frac{e^x}{n!} \frac{d^n}{dx^n} (e^{-x} x^n)$ .  $\Gamma(k)$  is the gamma function,  $\Gamma(n+k) = (n+k-1)!$ .  $\varphi_{nk,qp} = L\Delta\beta_{nk,qp}$ , is the phase difference between the  $LP_{nk}$  and  $LP_{qp}$  modes, and L is the length of the MMF.

According to (3.1)–(3.6), the power distribution along the MMF and the power coupled into the output-SMF can be calculated, as shown in (d)–(g), corresponding to the three types of transverse offset-based SMS structures. As can be seen, in the first type, (a), where the input- and output-SMFs are on the same propagation axis, the power oscillates in the MMF at a fixed period and most of the power is coupled into the output-SMF when the length of the MMF is integer multiples of the beating length z<sub>b</sub>. In the second type, (b), where the input-SMF is aligned to the MMF while the output-SMF is misaligned, the power distribution along the MMF is the same as the normal SMS structure, but only a little power is coupled into the output-SMF, because most of the power is concentrated nearby the central axis. In the third type, (c), where both input- and output-SMFs are randomly misaligned with the MMF, two cases appear in the output power. Only a little power is coupled into the output-SMF in the first case (f) while most of the power can be recovered in the second one (g). In the second case, the SMS structure should satisfy two conditions: (1) the length of the MMF is odd times the halved beating length,  $z_b/2$ ; (2) the center of the input- and output-SMFs is symmetrical with regard to the center of the MMF.

Therefore, it can be seen that only the first and the third structures have the possibility of being used as an MZI. To simplify the structure and reduce the implementation difficulty, only the first structure is looked into in this work. In this structure, because  $x_{\rm d1} = x_{\rm d2} = x_{\rm d}$ , it can be derived, based on (3.1) and (3.2), that  $c_{nk}^{(0)} = c_{nk}^{(L)} = c_{nk}$ , and the output power of (3.6) can be simplified as:

$$P_{\text{out}} = \sum_{n=0}^{N} \sum_{k=1}^{K} c_{nk}^{2} + 2 \sum_{n=0}^{N} \sum_{k=1}^{K} \sum_{q=0}^{Q} \sum_{p=1}^{P} \sqrt{c_{nk}^{2} c_{qp}^{2}} \cos(\varphi_{nk,qp})$$

$$lm \neq qp$$
(3.7)

# 3.2.2 Design of the Proposed SMS Structure Working as an MZI

Assuming that the transverse offset in our proposed SMS structure is 5  $\mu$ m, the coupling coefficient of each excited mode in the MMF can be calculated according to (3.1), as shown in Fig. 3.3. The MMF model and the corresponding parameters of MMF and SMF used for calculation can be seen in Fig. 3.4 and Table 3.1, respectively. Although many modes are excited and propagate in the MMF, most of the power is coupled into LP<sub>01</sub> and LP<sub>11</sub> modes. From the calculation results, we can see that, the sum power coupled into the LP<sub>01</sub> and LP<sub>11</sub> modes is  $\sim$ 90 %, which is a little less than that coupled into the LP<sub>01</sub> and LP<sub>02</sub> modes ( $\sim$ 98 %) in the SMS structure with all fibers perfectly aligned ( $x_d = 0$ ), but the power difference between them is only  $\sim$ 10 %, which is far smaller than that in the perfectly aligned SMS structure. This means, the interference ER between the two beating modes

**Fig. 3.3** Coupling coefficient of the LP<sub>01</sub>, LP<sub>02</sub>, LP<sub>11</sub> and LP<sub>21</sub> modes when  $x_d = 5 \mu m$  by comparing them to the case of all fibers being perfectly aligned

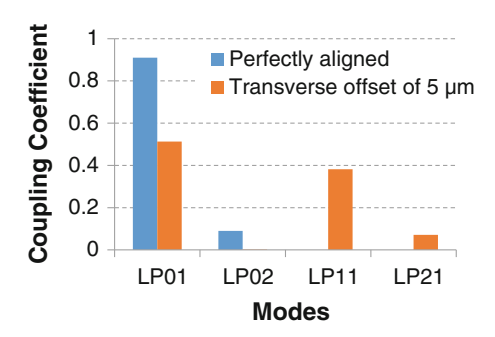


**Fig. 3.4** The model of the MMF used in our proposed SMS structure

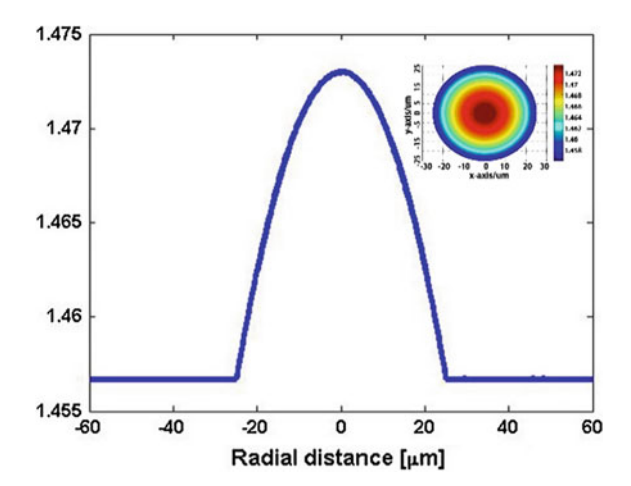


**Table 3.1** Parameters of the SMF and MMF

Parameter	MMF	SMF
Radius (µm)	25	4.5
Core index	1.4730	1.4610
Cladding index	1.4567	1.4570

can be improved greatly using the SMS structure with  $x_{\rm d}$  = 5  $\mu$ m. Hence, our proposed SMS structure cannot only be seen as an MZI, but also improve the interference ER.

Despite a little power is coupled into some high-order modes, they not seriously affect the transmission spectrum of our proposed all-fiber MZI. They only slightly change the interference ER, leading to the outline of transmission spectrum periodically oscillating with the wavelength (or frequency), which is verified in Sect. 3.3. If we ignore the high-order modes excited in the MMF, the transmission function (3.7) of our proposed all-fiber MZI can be simply expressed as (3.8), the transmission function of a conventional MZI. In this case, the LP<sub>01</sub> and LP<sub>11</sub> modes can be seen as the two different physical paths in the conventional MZI (Fig. 3.1b). Because both arms share the same hardware, our proposed all-fiber MZI performs

more stable compared with the conventional MZI built with two fiber couplers. The resultant intensity will be:

$$T = T_1 + T_2 + 2\sqrt{T_1 T_2} \cos(\varphi)$$
 (3.8)

where  $T_1$  and  $T_2$  represent the intensity of modes LP<sub>01</sub> and LP<sub>11</sub>, respectively and  $\varphi$  is the phase difference between these two modes, which can be written as:

$$\varphi = \int_{0}^{L} \Delta \beta(z) dz = L \Delta \beta \tag{3.9}$$

where L is the MMF length,  $\Delta\beta$  is the propagation constants difference between modes LP<sub>01</sub> and LP<sub>11</sub>. From (3.8) and (3.9), we can see that the power coupled into the output-SMF is only decided by the length of the MMF, L.

To concentrate the power on the axis location of the output-SMF at the end of the MMF, the phase difference between these two dominated modes should be equal to an integer multiple of  $2\pi$ . In other words, the MMF length should be an integer multiple of beat length  $z_b$ , which can be written as:

$$z_b = \frac{2\pi}{|\beta_{01} - \beta_{11}|} \tag{3.10}$$

where  $\beta_{01}$  and  $\beta_{11}$  are the propagation constants of LP<sub>01</sub> and LP<sub>11</sub> modes, respectively.

The transmission spacing  $\Delta \lambda$  between the adjacent constructive peaks (or destructive valleys) can be written as [18]:

$$\Delta \lambda = \frac{\lambda^2}{|n_{01} - n_{11}|L} = \frac{2\pi\lambda}{|\beta_{01} - \beta_{11}|L} = \frac{\lambda z_b}{L}$$
 (3.11)

where  $n_{01}$  and  $n_{11}$  are the effective index of LP<sub>01</sub> and LP<sub>11</sub> modes, respectively. We can see that, the spacing  $\Delta\lambda$  is inversely proportional to MMF length. In addition, the difference in propagation constants between the two beating modes can be approximately written as:

$$\beta_{01} - \beta_{11} = \frac{\lambda}{4\pi a^2 n_{\text{core}}} \left( U_{01}^2 - U_{11}^2 \right) \tag{3.12}$$

with

$$egin{aligned} U_{01} &= 2.405\,e^{-1/V} & \mbox{for the mode $\it LP$}_{01} \ U_{11} &= 3.83\,e^{-1/V} & \mbox{for the mode $\it LP$}_{11} \end{aligned}$$

$$V = \frac{2\pi a}{\lambda} \sqrt{n_{core}^2 - n_{clad}^2}$$

where a is the radius of the core of the MMF.  $\lambda$  is the wavelength in vacuum.  $n_{core}$  is the maximum refractive index of the core and  $n_{clad}$  is that of the cladding of the MMF.

Combining with (3.10), the time delay between two beating modes can be defined as:

$$\Delta t = \frac{L}{c/n_{01}} - \frac{L}{c/n_{02}} = \frac{\Delta nL}{c} = \frac{\lambda^2}{c\Delta\lambda}$$
 (3.13)

This shows that the delay time only depends on the effective index difference,  $\Delta n$ , and the MMF length, L. In order to evaluate the delay efficiency of our proposed all-fiber MZI, we also define another parameter called delay coefficient,  $\Delta d$ , corresponding to the time delay in a one-meter MMF:

$$\Delta d = \frac{\Delta t}{L} = \frac{\Delta n}{c} = \frac{\lambda^2}{cL\Delta\lambda} \tag{3.14}$$

We can see that the delay coefficient only depends on the effective index difference  $\Delta n$ , which is determined by the refractive index profile of the MMF.

# 3.3 Experiment

According to the theoretical analysis in Sect. 3.2, we built an experimental setup, as shown in Fig. 3.5, for observing the transmission spectrum of our proposed all-fiber MZI. A white source with almost a flat spectrum in the range from 1 to 1.62  $\mu$ m, as shown in Fig. 3.6a, was used as the light source. The SMFs (9  $\mu$ m/125  $\mu$ m) were the commercial standard SMFs compliant with ITU-T G.652, and the MMF (50  $\mu$ m/125  $\mu$ m) was also a commercial graded-index MMF, with maximum core

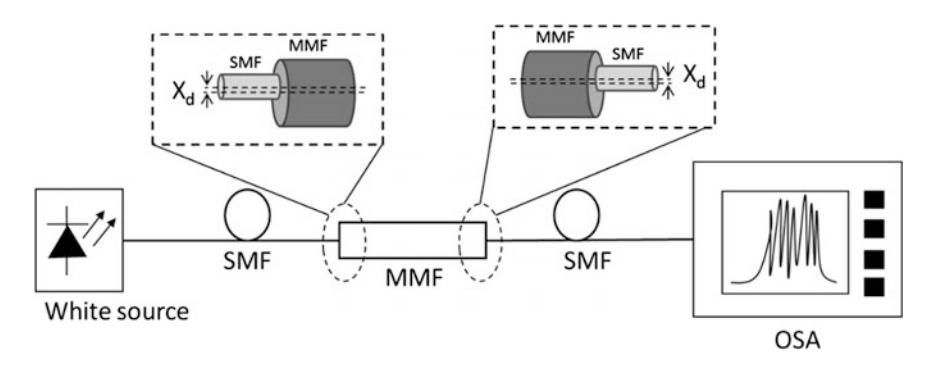


**Fig. 3.5** Experimental setup. *LED* light emitting diodes; *MMF* multimode fiber; *SMF* single-mode fiber; *OSA* optical spectrum analyzer

44 X. Chen and P.R. Horche

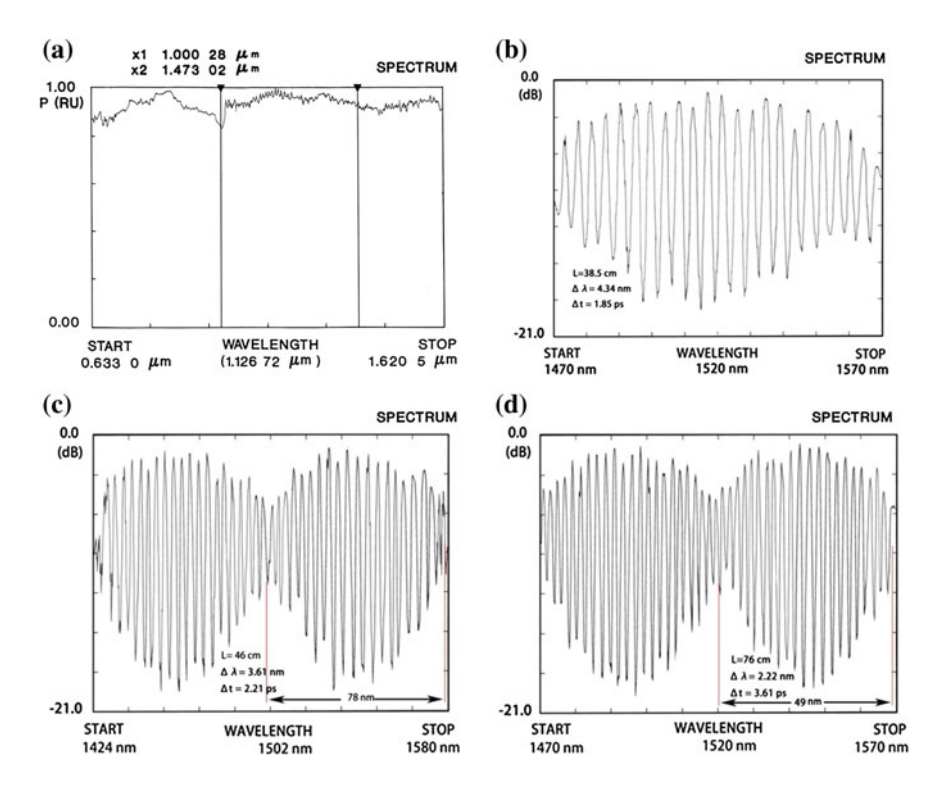


Fig. 3.6 Transmission spectra of the light source (a), and the proposed all-fiber MZI device with different MMF lengths of 38.5 cm (b), 46 cm (c), and 76 cm (d)

refractive index of 1.473 and cladding refractive index of 1.4567. In the experiment, the MMF was spliced between two SMFs by two micro-positioners, for accurately adjusting the transverse offset. Note that the micro-positioners are not shown in Fig. 3.5. Finally, the output-SMF was directly connected to an optical spectrum analyzer (OSA) for observing and recording the transmission spectrum.

The experimental results of transmission spectra are shown in Fig. 3.6, with different MMF lengths of 38.5, 46 and 76 cm. As can be seen, interference ER as high as 18 dB is obtained in the experiment. These results agree with the theory presented in Sect. 3.2: most power is coupled into modes  $LP_{01}$  and  $LP_{11}$ , and power difference between these two modes is small. Also, comparison between Fig. 3.6b, d indicates that the transmission spacing  $\Delta\lambda$  is inversely proportional to the MMF length: increasing MMF length from 38.5 to 76 cm results in a decrease of wavelength spacing  $\Delta\lambda$  from 4.34 to 2.22 nm.

Figure 3.6b also shows that a relative time delay  $\Delta t$  of 1.85 ps, which is got through (3.7), is obtained when the MMF length is 38.5 cm. According to (3.8), it can be calculated that the delay coefficient  $\Delta d$  is 4.81 ps/m. This value is larger than that of the bi-mode MMF-based MZI [8] and the birefringent fiber-based loop mirror [19], which possesses delay coefficients of 3.48 and 0.91 ps/m, respectively.

It implies that the required MMF length for generating a certain time delay is much shorter. However, the delay coefficient of our proposed all-fiber MZI device is much smaller than that of the all-fiber MZIs proposed by Chen [10] and Du [9], which possesses delay coefficients of 8.7 and 30.4 ps/m, respectively.

The transmission spectra in Fig. 3.6c, d reveal the periodic nature on the change of the interference ER. This phenomenon agrees with the theoretical analysis mentioned in Sect. 3.2: some high-order modes, such as  $LP_{02}$  and  $LP_{21}$  modes, are excited and propagate in the MMF. Note, however, that the transmission spectrum is mainly determined by the phase difference between the  $LP_{01}$  and  $LP_{11}$  modes at the end of MMF. At a certain wavelength, the output power reaches the minimum due to the destructive interference, when the phase difference is equal to odd time of  $\pi$ ; the output power reaches the maximum owing to the constructive interference, when the phase difference is equal to even times of  $\pi$ . In theory, the spectral period should be inversely proportional to MMF length, which agrees with the experimental results: increasing MMF length from 46 to 76 cm leads to a decrease of spectral period from 78 to 49 nm.

# 3.4 Proposed MZI for DPSK Signal Demodulation

As mentioned in Sect. 3.1, interference ER is a very important parameter for demodulating DPSK signals, when an all-fiber MZI is used as a DPSK demodulator. The high interference ER obtained in the experiment make our proposed all-fiber MZI device possible for use as a DPSK demodulator. In this section, we verify, through simulation, that our proposed all-fiber MZI can be used for DPSK signal demodulation.

The MMF model, as shown in Fig. 3.4, used in the simulation is almost the same as the graded-index MMF used in the experiment. It can be theoretically calculated that the delay coefficient is 4.93 ps/m, which is very close to the results obtained in the experiment. The required MMF length, thus, is 5.068 m for demodulating a 40 Gbps DPSK signal. Figure 3.7 shows the transmission spectrum of the proposed all-fiber MZI with MMF length of 5.068 m. It can be seen that high interference ER is obtained in the simulation.

Simulation design of a back-to-back 40 Gbps DPSK system, including a conventional transmitter and a receiver based on our proposed all-fiber MZI, is depicted in Fig. 3.8. At the transmitter, a 1550 nm continuous-wave source was modulated by a LiNbO<sub>3</sub> Mzch-Zehnder modulator (MZM), driven by a 40 Gbps precoded data stream, which is a pseudo random bit sequence of length 2<sup>15</sup>–1, to generate a 40 Gbps DPSK signal. At the receiver, the signal was first amplified by an erbium-doped fiber amplifier (EDFA), and then the noise-loaded signal was filtered by a bandpass filter with an 85-GHz 3-dB bandwidth. After that, the signal was demodulated by our proposed all-fiber MZI, followed by a photodetector. Finally, a bit error rate (BER) analyzer was used to analyze the quality of the received signal. Note that the simulations were carried out through OptiSystem.

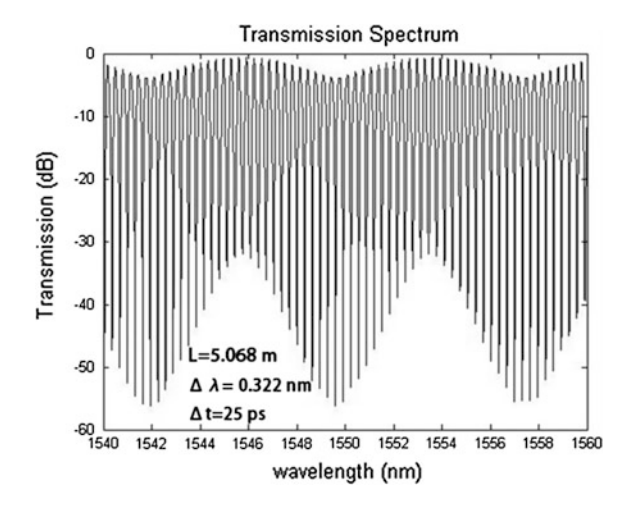
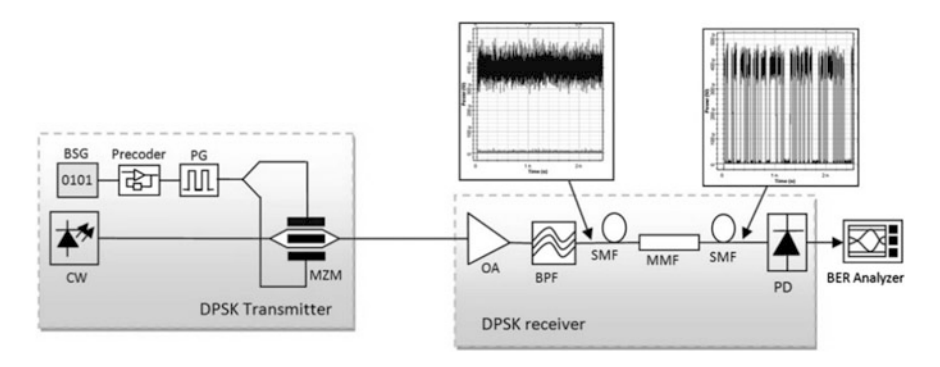


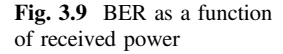
Fig. 3.7 Transmission spectrum of the proposed all-fiber MZI with MMF length of 5.068 m

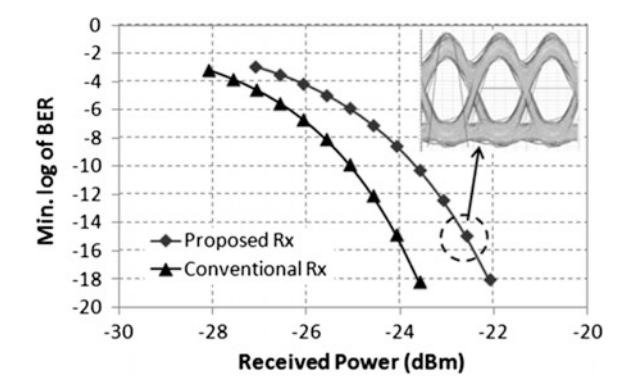


**Fig. 3.8** Simulation setup. *CW* continuous wave; *BSG* bit sequence generator; *PG* pattern generator; *MZM* Mach-Zehnder modulator; *OA* optical amplifier; *BPF* bandpass filter; *BER* bit error rate; *PD* photodetector

# 3.4.1 Back-to-Back Sensitivity

The simulation results of back-to-back sensitivity are shown in Fig. 3.9. The sensitivity of our proposed receiver is about -22.5 dBm at a BER of  $10^{-15}$  and about -23.9 dBm at a BER of  $10^{-9}$ . Compared with the conventional DI-based DPSK receiver [1], our proposed receiver has  $1.3 \pm 0.2$  dB sensitivity penalty. This penalty is mainly caused by the imbalanced detection, since the output-SMF in our proposed MZI only provides one output port. This problem can be solved by splicing a dual-core fiber at the output end of the proposed MZI, thus, detecting the demodulated signals in the two cores. However, it should be noted that this design is at the expense of increasing the complexity of the receiver. In addition, the MMF





induced signal impairment can also lead to sensitivity penalty. The relatively open intensity eye shown in the inset demonstrates that the proposed receiver can provide error-free operation.

# 3.4.2 Narrowband Optical Filtering

Reconfigurable optical add-drop multiplexers (ROADMs) and optical cross-connects (OXCs) nodes are widely used in optical networks for keeping signals within the optical domain for as long as possible [20]. These components usually contain many optical filters, such as multiplexers, demultiplexers, wavelength blockers and wavelength selective switches, which will reduce the effective bandwidth of the channel, resulting in the signal spectrum being clipped in the frequency domain and signal distortion in time domain. Moreover, different types of receiver will lead to different tolerance to narrowband optical filtering. Thus, in this subsection we will study the receiver performance under narrowband optical filtering, using two types of optical filter: 45 GHz- and 85 GHz-based Butterworth optical filters [21].

The simulation results are shown in Fig. 3.10. As can be seen, when the 45-GHz filters are used in the channel, only one filter is allowed with a 1-dB OSNR penalty. When more than two filters are cascaded in the channel, a very high OSNR is required. This is because the effective channel bandwidth is narrower than the signal bandwidth, and the signal spectrum is clipped severely, leading to serious intersymbol interference (ISI) in the time domain. Therefore, it can be seen that the standard 40 Gbps DPSK signal is not able to work on the 50-GHz ITU grid. Note, however, that the partial-DPSK [22], where the delay between the two arms in the MZI is reduced from 1 to 0.65 bit, can work on the 50-GHz ITU grid. We do not discuss this case in this work.

When the 85-GHz filters are used in the channel, about 8 filters are allowed to be cascaded, with a 1-dB OSNR penalty. This is because the filter-induced ISI is

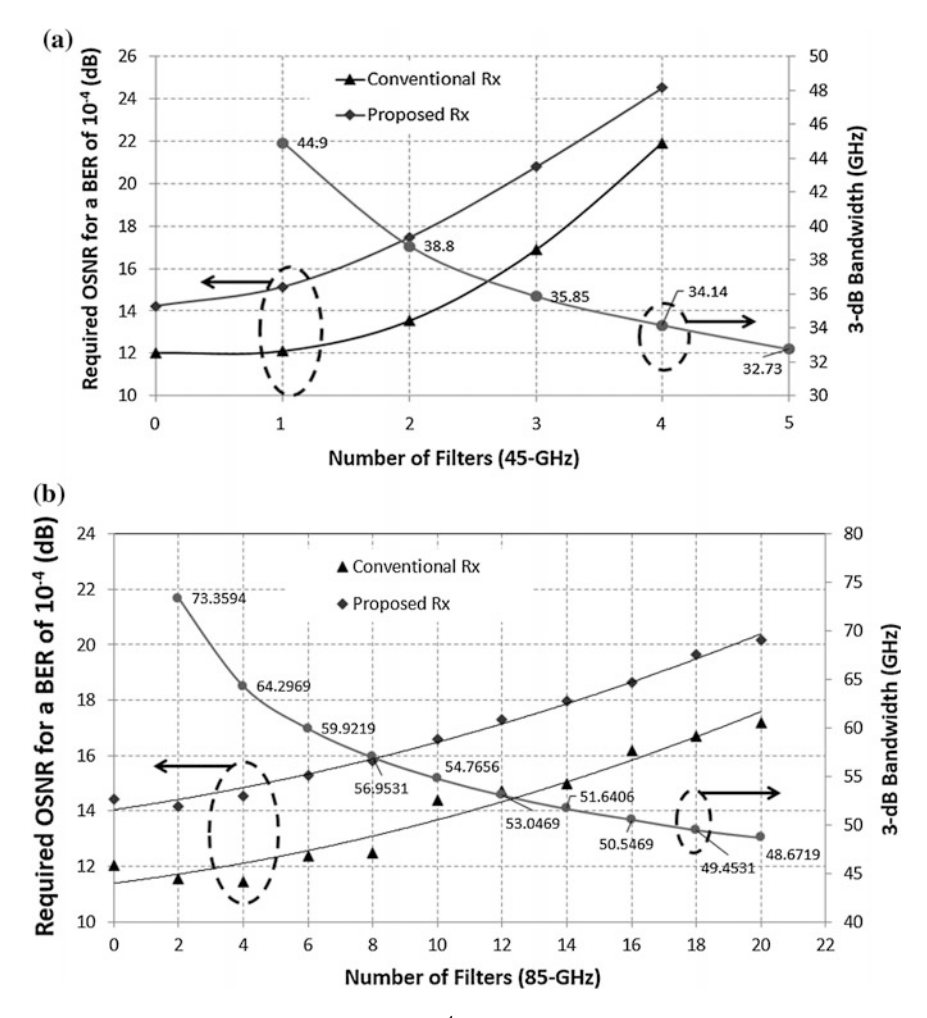
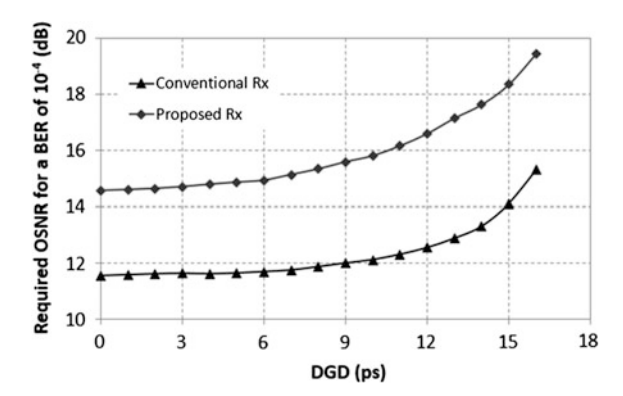


**Fig. 3.10** Required OSNR for a BER of  $10^{-4}$  as a function of the number of filters, with filter bandwidth of 45-GHz (a) and 85-GHz (b)

mitigated. The simulation results demonstrates that  $2.5-4~\mathrm{dB}$  more OSNR is required using our proposed receiver, compared to the conventional one. This can be understood from the single-branch detection. As mentioned in Sect. 4.1, this problem can be solved by balanced detection, but at the price of increasing the receiver complexity. Here it should be pointed out that the required BER of  $10^{-4}$  applied in our simulations can be improved to  $10^{-15}$ , if a forward error correction (FEC) technique is used.

**Fig. 3.11** Required OSNR for a BER of  $10^{-4}$  as a function of the accumulated DGD



# 3.4.3 Differential Group Delay (DGD) Tolerance

Polarization mode dispersion (PMD) can have adverse effects on data transmission in fiber-optic links over long distances at very high data rates [23], because portions of the transmitted signals in different polarization modes will arrive at slightly different times. This can cause some levels of pulse broadening, leading to ISI, and thus a degradation of the received signal. PMD has been studied extensively because it limits the performance of modern lightwave systems, especially high-symbol rate systems. In this subsection, the tolerance to the first-order PMD, which is also called DGD, is studied using our proposed receiver.

In the simulation, a tunable polarization-maintaining fiber (PMF) was used as the DGD element and a different DGD can be obtained by changing the length of the PMF. A polarization controller (PC), placed in front of the PMF was used to launch at 45° to the principle state of polarization axes of the PMF, leading to the worst-case conditions.

The simulation results, as shown in Fig. 3.11, detail that the DGD tolerance is  $\sim 9$  ps using our proposed receivers, with 1-dB OSNR penalty. This value is in agreement with the theory [2]: a 1-dB OSNR penalty occurs at a DGD of between 30 % and 40 % of the symbol duration. The required OSNR increases quickly when the DGD is higher than 9 ps. Moreover, due to single-branch detection, 3–4 dB more OSNR is required by our proposed receiver compared to the conventional DPSK receiver. However, this OSNR penalty can be solved using balanced detection in our proposed receiver.

# 3.5 Conclusion

We have, theoretically and experimentally, demonstrated an all-fiber MZI device, which is based on a commercial graded-index MMF mismatch spliced between two SMFs. In this structure, most of the power from the input-SMF is coupled into

50 X. Chen and P.R. Horche

excited LP<sub>01</sub> and LP<sub>11</sub> modes in the MMF. These two modes interfere with each other along the propagation direction, and the light power coupled into the output-SMF only depends on the relative phase difference at the end of the MMF. Thus, interference pattern can be obtained at the exit of the output-SMF. Interference ER as high as 18 dB was obtained in the experiment, and a delay coefficient of 4.81 ps/m was achieved. Finally, simulations carried out in a 40 Gbps DPSK system have demonstrated that our proposed all-fiber MZI can be used as a DPSK demodulator. Receiver performances under back-to-back sensitivity, narrowband optical filtering and DGD, have shown that our proposed receiver can provide similar performance as the conventional one.

Since the design of our proposed all-fiber MZI is low-cost and ease of manufacture, it may be used widely in many optical applications in future, such as a bandpass filter or a temperature sensor. Furthermore, with the proper design, it can also be applied as a WDM multiplexer/demultiplexer.

**Acknowledgements** The authors would like to acknowledge support from the China Scholarship Council (CSC). The authors would also like to dedicate this work to the memory of Prof. Alfredo Martín Mínguez.

# References

- Gnauck, A.H., Winzer, P.J.: Optical phase-shift-keyed transmission. J. Lightwave Technol. 23, 115–130 (2005)
- 2. Winzer, P.J., Essiambre, R.-J.: Advanced optical modulation formats. Proc. IEEE **95**, 952–985 (2006)
- Kumar, M., Kumar, A., Tripathi, S.M.: Acomparison of temperature sensing characteristics of SMS structures using step and graded index multimode fibers. Opt. Comumn. 312, 222–226 (2014)
- 4. Tripathi, S.M., Kumar, A., Varshney, R.K., Kumar, Y.B.P., Marin, E., Meunier, J.-P.: Strain and temperature sensing characteristics of single-mode-multimode-single-mode structures. J. Lightwave Technol. 27, 2348–2355 (2009)
- Shao, M., Qiao, X., Fu, H., Li, H., Jia, Z., Zhou, H.: Refractive index sensing of SMS fiber structure based Mach-Zehnder interferometer. IEEE Photon. Technol. Lett. 26, 437–439 (2014)
- Mohammed, W.S., Mehta, A., Johnson, E.G.: Wavelength tunable fiber lens based on multimode interference. J. Lightwave Technol. 22, 469–477 (2004)
- Tripathi, S.M., Kumar, A., Marin, E., Meunier, J.-P.: Single-multi-single mode structure based band pass/stop fiber optic filter with tunable bandwidth. J. Lightwave Technol. 28, 3535–3541 (2010)
- Lize, Y.K., Gomma, R., Kashyap, R.: Low-cost multimode fiber Mach-Zehnder interferometer for differential phase demodulation. In SPIE 2006, San Diego, USA (2006)
- 9. Du, J., Dai, Y., Lei, G.K.P., Tong, W., Shu, C.: Photonic crystal fiber based Mach-Zehnder interferometer for DPSK signal demodulation. Opt. Express 18, 7917–7922 (2010)
- Chen, X., Horche, P.R., Minguez, A.M.: DPSK signals demodulation based on a multimode fiber with a central dip. In: 19th European Conference on Networks and Optical Communications (NOC), 2014, pp. 18–22 (2014)

- 11. Fufei, P., Wenbin, L., Wenchao, X., Na, C., Xianglong, Z., Zhenyi, C., Tingyun, W.: Temperature-insensitivity bending sensor based on cladding-mode resonance of special optical fiber. IEEE Photon. Technol. Lett. **21**, 76–78 (2009)
- Jing-Jing, Z., Zhang, A.P., Tian-Hao, X., Sailing, H., Wei, X.: Fiber-optic high-temperature sensor based on thin-core fiber modal interferometer. IEEE Sens. J. 10, 1415–1418 (2010)
- Horche, P.R., López-Amo, M., Muriel, M.A., Martin-Pereda, J.A.: Spectral behavior of a low-cost all-fiber component based on untapered multifiber unions. IEEE Photon. Technol. Lett. 1, 184–187 (1989)
- 14. Soldano, L.B., Pennings, E.C.M.: Optical multi-mode interference devices based on self-imaging: principles and applications. J. Lightwave Technol. 13, 615–627 (1995)
- Rota-Rodrigo, S., Lopez-Amo, M., Kobelke, J., Schuster, K., Santos, J., Frazao, O.: Multimodal interferometer based on a suspended core fiber for simultaneous measurement of physical parameters. J. Lightwave Technol. (2014)
- Xue, L.-L., Yang, L.: Sensitivity enhancement of RI sensor based on SMS fiber structure with high refractive index overlay. J. Lightwave Technol. 30, 1463–1469 (2012)
- 17. Ghatak, A., Thyagarajan, K.: Introduction to Fiber Optics, pp. 173–183, Cambridge University Press, Cambridge (1997)
- 18. Horche, P.R., Muriel, M.A., Martin-pereda, J.A.: Measurement of transmitted power in untapered multifibre unions: oscillatory spectral behaviour. Electron. Lett. 25, 843–844 (1989)
- 19. Chow, C.W., Tsang, H.K.: Polarization-independent DPSK demodulation using a birefringent fiber loop. IEEE Photon. Technol. Lett. 17, 1313–1315 (2005)
- Tibuleac, S., Filer, M.: Transmission impairments in DWDM networks with reconfigurable optical add-drop multiplexers. J. Lightwave Technol. 28, 557–568 (2010)
- Chen, X., Horche, P.R., Minguez, A.M.: Analysis of optical signal impairment induced by different types of optical filters in 40Gbps DQPSK and 100 Gbps PM-DQPSK systems. Opt. Fiber Technol. 22, 113–120 (2015)
- Mikkelsen, B., Rasmussen, C., Mamyshev, P., Liu, F.: Partial DPSK with excellent filter tolerance and OSNR sensitivity. Electron. Lett. 42, 1363–1364 (2006)
- Pincemin, E., Karaki, J., Loussouarn, Y., Poignant, H., Betoule, C., Thouenon, G., Bidan, R.
   L.: Challenges of 40/100 Gbps and higher-rate deployments over long-haul transport networks. Opt. Fiber Technol. 17, 335–362 (2011)

# Chapter 4 Application of Laser Photoacoustic Spectroscopy and Chemometrics in Homeland Security

Adriana Puiu, Gianfranco Giubileo, Stella Nunziante Cesaro and Antonio Palucci

**Abstract** In the last decades, the military and Government organizations have an increasing interest in development of field-sensors for homeland security issues. In order to detect explosives (such as DNT, TNT, tetryl, RDX, HMX, TATP, PETN) and some precursors of Improvised Explosive Devices (i.e. potassium sulfate, potassium nitrate, magnesium sulfate, ammonium perchlorate, ammonium nitrate, acetone), we applied laser photoacoustic spectroscopy (LPAS) and a chemometric method (PCA, Principal Component Analysis) to speed up the identification process. The results indicated that the combination of LPAS and PCA is very useful for a rapid identification of these chemicals.

# 4.1 Introduction

The use of explosives and Improvised Explosive Devices (IEDs) by terrorists continue to pose a significant threat for civilians. Explosives are one of the most important threats including many categories of chemicals, whose recognition in combination with the most usual substrates (plastic or jelly) in bombs manufactory is a formidable task from an analytical point of view and might require complex data sampling and time consuming analysis procedures, which are unsuitable to obtain real time results in field applications when using conventional laboratory equipment. Most common explosives utilized in warfare since the World War I (WWI) up to now are nitrogen containing compounds characterized by a peculiar O/N content (e.g. nitro compounds), which favours the explosive ignition, and the presence of an organic matrix (C and H based) as fuel to burn up. As traditional explosives are difficult to obtain, bomb makers search for chemicals commercially available in hardware stores, pharmacies and cosmetics stores to use them as ex-

A. Puiu (⋈) · G. Giubileo · A. Palucci

ENEA, FSN-TECFIS-DIM, Via E. Fermi 45, 00044 Frascati, Italy

e-mail: adriana.puiu@enea.it

S.N. Cesaro

ISMN-CNR c/o Department of Chemistry, P.le A. Moro 5, 00185 Rome, Italy

<sup>©</sup> Springer International Publishing Switzerland 2016

P. Ribeiro and M. Raposo (eds.), Photoptics 2015,

54 A. Puiu et al.

Acetone	Hydrogen peroxide	Potassium sulfate
Ammonium nitrate	Hexamine	Potassium perchlorate
Ammonium perchlorate	Magnesium sulfate	Sodium chlorate
Barium nitrate	Nitric acid	Sodium nitrate
Citric acid	Nitromethane	Sulphuric acid
Guanidine nitrate	Potassium chlorate	Hydrochloric acid
Urea	Potassium nitrate	

Table 4.1 Chemicals used as precursors of IEDs [6, 7]

plosives precursors. In the last years, the most prevalent form of explosive device utilized in the attacks have been the IEDs. These mixtures are homemade. non-conventional explosives, fabricated by combining common chemicals to manufacture a rudimental but efficient bomb. A list of some chemicals used as precursors of IEDs is reported in Table 4.1. The number of explosives which can be home-manufactured is limited by the imagination and knowledge as well as by the cost and availability of these chemicals on the market. Improvised explosives are typically mixtures of an oxidizer and a fuel. The first substance must be rich in Oxygen and the second one must be able to react very fast so that it changes and multiplies its volume [1]. Nowadays, there is a need to develop new efficient methods able to perform sensitive and selective detection of such chemicals during transportation or storing by terrorists. The fight against the increased manufacturing of modern bombs for criminal use is approached by developing fast real-time easy-to-use methods for the detection of IED precursors, such as Infrared Laser Photo-acoustic Spectroscopy (IR-LPAS). IR-LPAS already demonstrated to be promising in the design of an integrated optical system for the real time detection and identification of explosive species in traces to support homeland security [2–5].

In this paper we report the LPAS analysis of some explosives and common chemicals used as IED precursors: trinitrotoluene, dinitrotoluene, triacetonetriper-oxide, Hexogen, Octogen, Nitropenta, potassium sulfate, potassium nitrate, magnesium sulfate, ammonium perchlorate, ammonium nitrate, and acetone. The analyzed chemical species were classified by Principal Component Analysis (PCA) applied to the collected IR spectral data, which facilitate the recognition capability of the adopted method.

# 4.2 Materials and Methods

The experimental work was performed by using a home-made LPAS apparatus equipped with a line tuneable 10 W Continuous Wave stabilized CO<sub>2</sub> laser source and with a home-made 3 cc photoacoustic (PA) cell. System control and Data acquisition were achieved through a specialized card, IEEE488.2—GPIB National Instruments, with signal processed by a lock-in amplifier, SR830 Stanford Research

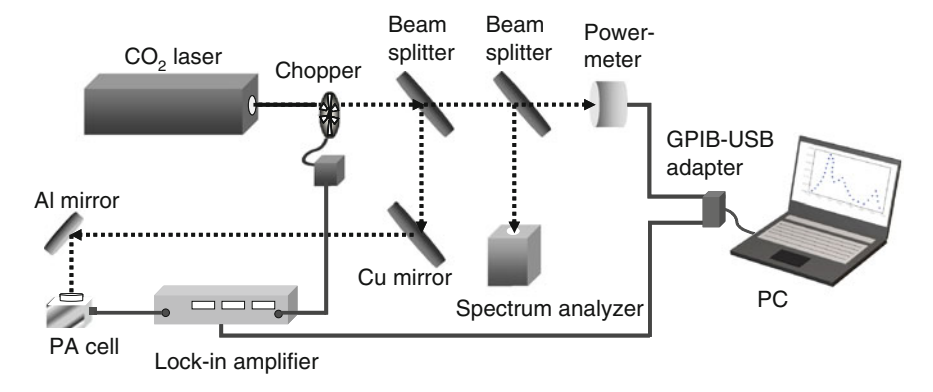


Fig. 4.1 Schematic of the LPAS set-up

Systems, in a LabView environment. A schematic of the LPAS apparatus is shown in Fig. 4.1. More details on the Photoacoustic facility were reported in a previous paper [3]. The PA signal produced by a few hundreds  $\mu$ g/cm² of each chemical was filtered by a low pass pre-amplifier and selectively amplified by a lock-in amplifier. The background signal was negligible when compared to the sample signal.

FT-IR analysis was performed on explosive compounds in the spectral range 9–11  $\mu$ m by using an IFS66 (Bruker) interferometer equipped with a Praying Mantis (Harrick) accessory for DRIFT located in the sample chamber under rotary vacuum.

In this study, military explosives and precursors substances were used. Among military explosives TNT (2,4,6-Trinitrotoluene) is one of the most widely diffused, and has been in use for about the last 100 years, with most of the production during WWI and WWII. RDX (cyclotrimethyltrinitramine, known as Hexogen) and PETN (Nitropenta) are more recent, they were largely produced during WWII and are still widely diffused today, also in plastic explosives. HMX (Octogen) is a very powerful and expensive military explosive, which has been employed in solid-fuel rocket propellants and in military high performance warheads. Different combinations of TNT, RDX, PETN, HMX, etc. are currently used with a number of organic compounds (waxes, plasticizers, stabilizers, oils, etc.). Ammonium nitrate is utilized as the basis for other families of explosives, typically for industrial applications and in solid rocket propellants. To the previous list of high energetic materials, recently has been added also a new category of Improvised Explosive Devices (IEDs), as triacetone triperoxide (TATP), mainly employed in the implementation of homemade explosives that are carried by suicide bombers. The TATP precursors are very cheap and commercially available: acetone and hydrogen peroxide. For this reason we considered necessary to dedicate a part of the study to analyze such substances used as precursors of IEDs. The list of precursors considered in the present experimental work is reported in Table 4.2.

All the pure solid substances were purchased from different suppliers such as Carlo Erba, Sigma and Accucstandard and they were analyzed by LPAS without A. Puiu et al.

<b>Table 4.2</b>	List of LPAS
analyzed II	ED precursors

Precursor	Chemical formula	m.p. (°C)
Acetone	CH3-CO-CH <sub>3</sub>	-95
Ammonium nitrate	NH <sub>4</sub> NO <sub>3</sub>	169
Ammonium perchlorate	NH <sub>4</sub> ClO <sub>4</sub>	200
Magnesium sulfate	MgSO <sub>4</sub>	1124
Potassium sulfate	K <sub>2</sub> SO <sub>4</sub>	1069
Potassium nitrate	KNO <sub>3</sub>	334

any pretreatment in weighted amounts of  $100-300~\mu g$ . The samples were directly warmed by the incident laser beam so that the PA signal was generated without previously warm the sample to bring out vapours. Before each measurement, the PA cell was shortly cleaned by vacuum pumping.

# 4.3 Results

The concept of LPAS recognition of IED precursors has been demonstrated by performing measurements on some conventional explosives and on the selected set of precursors of IEDs reported in Table 4.2. Figure 4.2 reports the PA spectra and FT-IR spectra of common explosives (TNT, DNT, TATP, HMX, RDX, tetryl). It appears well evident the agreement among the data obtained from the two different spectral techniques. Examples of some IEDs PA spectra are shown in Figs. 4.3, 4.4, 4.5, 4.6. The spectra were collected in the 9.2–10.8  $\mu$ m spectral range covered by the adopted laser source. All the considered chemicals underwent the same analytical procedure.

As it can be observed, characteristic absorption peaks distribution was found in the investigated spectral range for each analyzed sample. The error bars in the

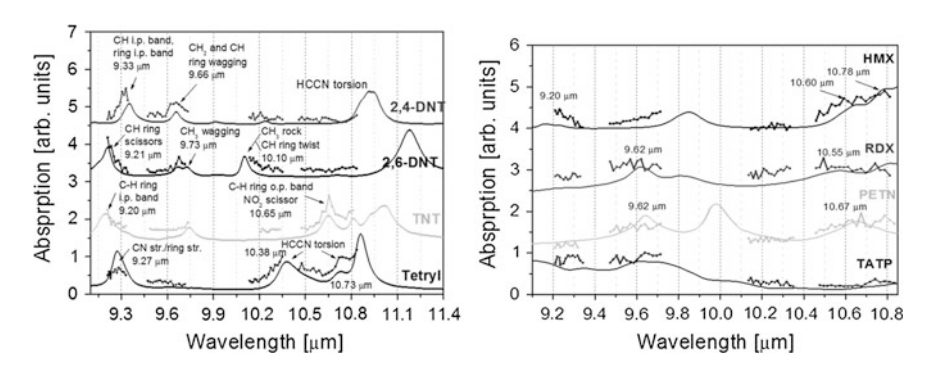
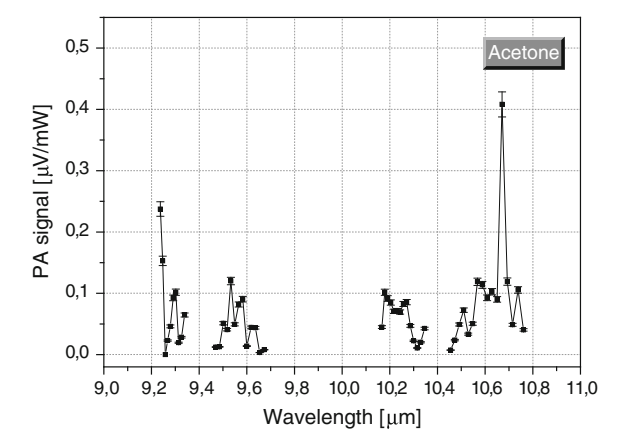
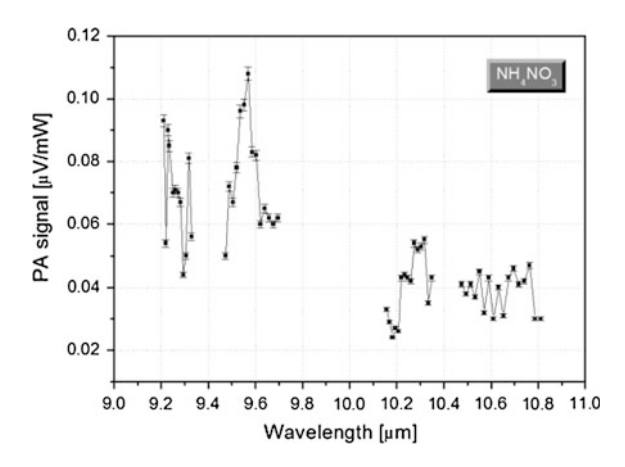


Fig. 4.2 Photoacoustic spectra of explosives analyzed by LPAS technique (*dot lines*) compared to FT-IR spectra (*continuous line*)

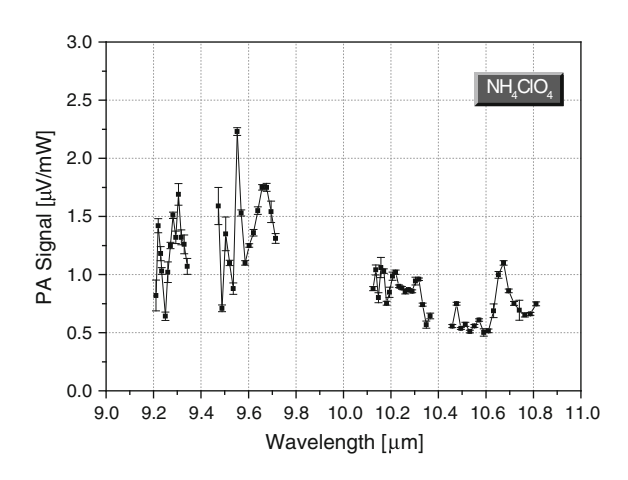
**Fig. 4.3** Photoacoustic spectrum of acetone



**Fig. 4.4** Photoacoustic spectrum of ammonium nitrate

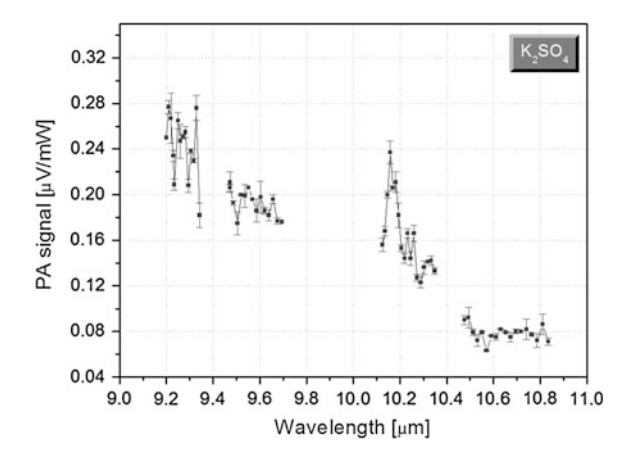


**Fig. 4.5** Photoacoustic spectrum of ammonium perchlorate



58 A. Puiu et al.

**Fig. 4.6** Photoacoustic spectrum of potassium sulfate



graphs represent the standard deviation of ten different PA signal acquisitions on the given laser emission line.

The strong absorption band presented by  $NH_4CIO_4$  (ammonium perchlorate) at 9–10  $\mu$ m determines the relatively higher LPAS signals recorded for this chemical in the mentioned interval. For  $NH_4NO_3$  and  $K_2SO_4$  species, an increasing LPAS signal going from 11  $\mu$ m toward 9  $\mu$ m was recorded, as confirmed also by FTIR data in the literature [8].

Despite the analyzed samples are inorganic substances that do not possess the rich band structure generally found for the organic species in the fingerprint region (6–20  $\mu$ m), the high resolution PA spectroscopy put in evidence different spectral patterns characteristic for each substance in the spectral interval covered by the CO<sub>2</sub> laser (9–11  $\mu$ m), even in the absence of specific absorption bands ascribable to some roto-vibrational motions within the molecule.

# 4.4 Principal Component Analysis

From a first graphs examination it appears that the spectral features of the analyzed substances are sufficiently different from each other to consent a good discrimination. Nevertheless, a direct comparison of the collected spectra is quite difficult in practice. Due to the complex structures of the photoacustic responses of the investigated samples, a unique selection of representative lines of each species, not overlapping each other, is not straightforward achievable. Therefore in order to achieve the unambiguous and rapid recognition of trace explosive compounds and precursors of IEDs, a chemometric approach has been exploited to the experimental results as a whole.

The chemometric approach was based on Principal Component Analysis (PCA) applied to the set of experimental data. PCA gives valuable information

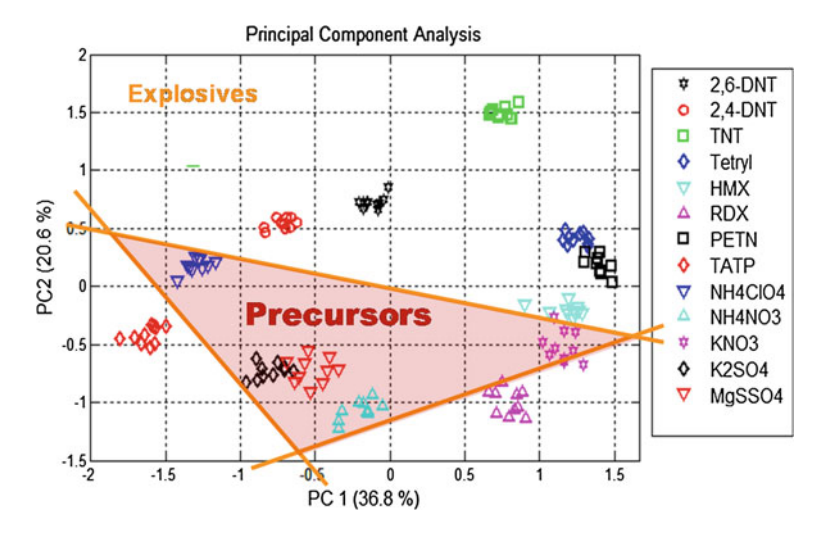


**Fig. 4.7** Graphical presentation of PC1 versus PC2 applied to photoacoustic spectra of different chemicals (explosives and IED precursors)

about the factors which mainly affect the spectral variations among different analyzed samples.

The result of PCA treatment on the investigated samples is shown in Fig. 4.7. Looking at the graph it appears evident the discrimination capability of the LPAS analysis coupled to the PCA chemometric algorithm.

The infrared photoacoustic spectra were previously normalized to the laser power, and then to their maximum peak value. We recorded the PA signal from 55 emission wavelengths of the  $CO_2$  laser. Thus, by using a software developed in MatLab environment, the PCA was applied to a data matrix of 55 datapoints and 60 samples. On a data matrix containing elements  $x_{ik}$ , where index k is used for the experimental measurements and index i for the samples under study, the PCA model is described by (4.1):

$$x_{ij} - \bar{x}_k = e_{ik} + \sum_{i=1}^{N} t_{jk} p_{jk}$$
 (4.1)

where the loadings  $p_{jk}$  depend only on the experimentally measured variables and the scores  $t_{ij}$  only depend on the sample constituents; N is the number of significant components [4].

From the PCA, one can find that the first three principal components are explaining 70.6 % of the overall spectral variation. The corresponding loading plots, which indicate the specific contribution of each absorption line in the total variance of the spectral data, are reported in the Fig. 4.8. The first principal component, PC1, which accounts for the 36 % of spectral variance, has one isolated peak around 9.5 µm that correspond to some vibrations in the two nitro-compounds

A. Puiu et al.

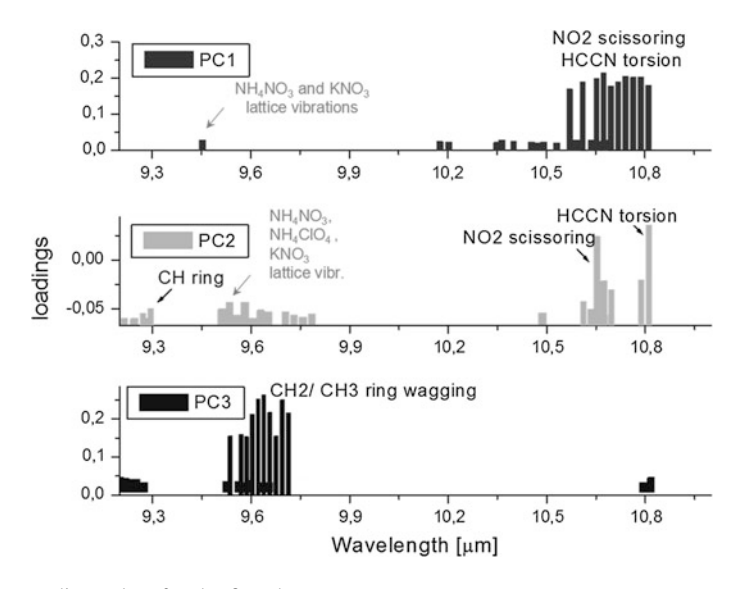


Fig. 4.8 Loadings plots for the first three components

(NH<sub>4</sub>NO<sub>3</sub> and KNO<sub>3</sub>). Generally, the fingerprints of inorganic compounds fall in the region 25  $\mu m^{-1}$  mm (400–10 cm $^{-1}$ ) due to the presence of the lattice modes of vibration which are characteristic of a specific crystal geometry [9]. These modes result from the motion of one polyatomic group relative to another within the unit cell. Thus, there are no absorption peaks in the interval 9–11  $\mu m$  which can be ascribed to a specific mode of vibration of some functional groups inside the IEDs precursor samples. The band in the range 10.5–10.8  $\mu m$  can be assigned to NO<sub>2</sub> scissoring in TNT and HCCN torsion in tetryl.

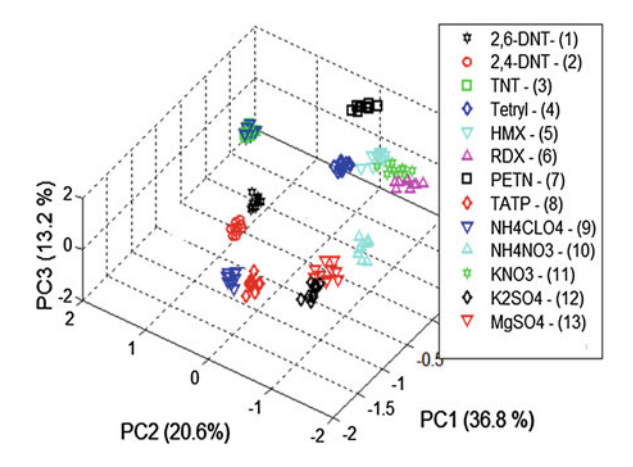
In the second component, PC2, with an explained spectral variance of 22 %, there is a wider band centered around one isolated peak around 9.5  $\mu$ m that correspond to some vibrations in the NH<sub>4</sub>NO<sub>3</sub>, NH<sub>4</sub>ClO<sub>4</sub> and KNO<sub>3</sub>, while the other bands can be ascribed to nitro-explosives with benzene ring.

The loading plot for PC3, which explains the 13.6 % of spectral variance, shows, besides the peaks in position equivalent to those in the PC1 or PC2, a strong band in the 9P branch of the  $CO_2$  laser emission wavelengths, probably due to the ring wagging in DNT and TNT.

In general, a low number of PC able to explain more than 60 % of the spectral variances is correlated with a large spectral difference among the samples. Thus, in our case only two components can be sufficient to describe the data set, as evidenced in Fig. 4.7, which shows the PCA plot for the PC1 and PC2, the two largest principal components of the dataset, which explain 58 % of the spectral variance between the samples. In this plot each sample is represented by a point, and the six groups, each corresponding to a precursor substance, are clearly separated.

In Fig. 4.9 we report the 3D plot of PC1, PC2 and PC3 (70.6 % explained variance), which clearly shows that each compound can be correctly grouped with

**Fig. 4.9** PCA results in the 3D space generated by the first three components (PC1, PC2, and PC3)



no misassignment. Therefore, the application of PCA to the LPAS spectra expressed by 55 different wavelengths allowed to reduce the output to only three components. The score plots indicate that the proposed model is able to correctly group the IED's precursors in spite of the oversimplification of LPAS spectra.

## 4.5 Conclusions

The concept of LPAS recognition of explosives and IED precursors has been demonstrated by performing measurements on the selected set of chemicals reported in Figs. 4.2, 4.3, 4.4, 4.5, 4.6. PA spectroscopy put in evidence different spectral patterns characteristic for each substance in the spectral interval covered by the CO<sub>2</sub> laser. Nevertheless, in order to simplify the daunting task of substance identification, a multivariate statistical analysis tool based on PCA was developed in MatLab. In spite of the fact that inorganic compounds identification by infrared spectroscopy is considered somewhat less successful in the middle infrared (MIR) region, the recognition ability of MIR-LPAS technique coupled with a PCA data treatment was demonstrated by the reported results. Applying PCA to the LPAS spectra of thirty compounds, it was found that 70.6 % of the spectral variation was accounted for by the first three principal components. This percentage obtained with only a few number of components indicates a large spectral difference among the samples. Even if no spectral features attributable to specific vibrational modes of a certain functional group are present in the LPAS spectra of IEDs precursors, analysis of the score and loadings plot showed that the samples can be well identified due to the presence of lattice modes of vibration.

62 A. Puiu et al.

In conclusion, LPAS coupled with PCA could provide an useful detection method to support the fight to the increased realization of modern bombs for criminal use. Moreover, an integration with complementary methods such as Raman spectroscopy may further increase the specificity of detection, especially for the chemicals exhibiting poor infrared absorption profiles.

**Acknowledgements** The authors acknowledge the financial support of the EU projects ISOTREX, BONAS and EDEN.

## References

- Australian Explosives Manufacturers Safety Committee Report: Code of Good Practice, Precursors for Explosives, 1st edn. (1999)
- Chaudhary, A.K., Bhar, G.C., Das, S.: Low-limit photo-acoustic detection of solid RDX and TNT explosives with carbon dioxide laser. J. Appl. Spectrosc. 73, 123–129 (2006)
- 3. Giubileo, G., Puiu, A.: Photoacoustic spectroscopy of standard explosives in the MIR region. Nucl. Instrum. Methods A **623**, 771–777 (2010)
- Giubileo, G., Colao, F., Puiu, A.: Identification of standard explosive traces by infrared laser spectroscopy: PCA on LPAS data. Laser Phys. 22, 1033–1037 (2012)
- Puiu, A., Giubileo, G., Nunziante Cesaro, S.: Vibrational spectrum of HMX at CO<sub>2</sub> laser wavelengths: a combined DRIFT and LPAS study. Int. J. Spectr. (2012). Article ID 953019. doi:10.1155/2012/953019
- Rostberg, J.I.: Naval Postgraduate School Thesis, Common Chemicals as Precursors of Improvised Explosive Devices: The Challenges of Defeating Domestic Terrorism. Monterey, California (2005)
- 7. Singapore Police Force: New Control Measures: Available at http://www.spf.gov.sg (2007)
- 8. Miller, F.A., Wilkins, C.H.: Infrared spectra and characteristic frequencies of inorganic ions. Anal. Chem. **24**, 1253–1294 (1952)
- 9. Nyquist, R.A., Kael, R.O.: Infrared Spectra of Inorganic Compounds, Vol. 4. Academic Press Inc (1997)

# Chapter 5 Fibre Bragg Grating Sensor Signal Post-processing Algorithm: Crack Growth Monitoring in Fibre Reinforced Plastic Structures

## G. Pereira, L.P. Mikkelsen and M. McGugan

**Abstract** A novel method to assess a crack growing/damage event in fibre reinforced plastic, using conventional single mode Fibre Bragg Grating sensors embedded in the host material is presented in this article. Three different damage mechanisms that can change the sensor output, longitudinal strain  $\varepsilon_{xx}$ , transversal stress  $\sigma_{yy,zz}$ , and non-uniform strain  $\varepsilon_{xx}(xx)$ , were identified. These damage mechanisms were identified during the experimental testing and linked with the sensor output using a digital image correlation technique. A dedicated algorithm to extract information from the reflected spectrum that enables crack detection was developed. Double Cantilever Beams specimens made with glass fibre and bonded with structural adhesive, were instrumented with a Fibre Bragg Grating array embedded in the host material, and tested using an experimental fracture procedure. This method was successfully validated in three different loading conditions, where were obtained very promising results that enable crack growth monitoring.

## 5.1 Introduction

## 5.1.1 Fibre Reinforced Polymer Materials

Fibre Reinforced Polymer (FRP) materials, or as often called composite materials, have been extensively used in aerospace, automotive, naval, civil engineering and

G. Pereira ( $\boxtimes$ ) · L.P. Mikkelsen · M. McGugan

Department of Wind Energy, Technical University of Denmark,

Frederiksborgvej 399, 4000 Roskilde, Denmark

e-mail: gfpe@dtu.dk

URL: http://www.vindenergi.dtu.dk/english

L.P. Mikkelsen e-mail: lapm@dtu.dk

M. McGugan

e-mail: mamc@dtu.dk

wind energy applications. The main difference with FRP materials compared to metals is that they have an isotropic behaviour, which means that it shows different mechanical properties in different directions. These FRP materials consist of two macroscopic phases, a stiff fibre phase usually glass or carbon fibre, and a polymer matrix usually polyester or epoxy. The main advantage of this material is its capability to be tailored for a specific application, enabling an enhancement, and a high level of customization of mechanical properties, such as light-weight, thermal expansion, chemical/corrosion resistance, fatigue behaviour, etc. [1].

## 5.1.2 FRP Failure and Damage Mechanism

Many structures made of FRP material, such as aerospace structures, ships, air-crafts and wind turbine blades, are constructed using multi-directional laminates that are bonded together using structural adhesives. Therefore, the most common failures in this type of structures are delamination, by crack growth along interfaces between layers inside the laminates, or adhesive joint failure, by cracking along the interface of the laminate and structural adhesive, as shown in Fig. 5.1.

In both failure situations a fibre crack bridging is often created, where intact fibres connect the crack faces behind the crack tip, as shown in Fig. 5.2. This fibre crack bridging creates an extra resistance that the crack has to overcome to grow, meaning that the energy required for the crack to grow is higher than that the energy required to initiate it. However, this damage mechanism can't be analysed by classic linear elastic fracture mechanics. Instead, a cohesive law can be used to describe the fracture mechanism, as described by some authors [2, 3]. The cohesive

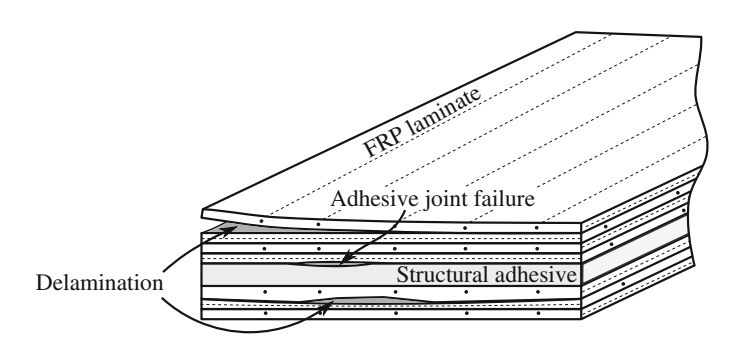
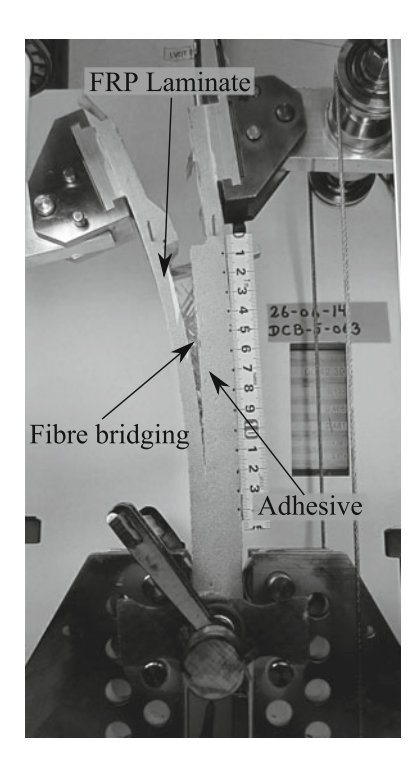


Fig. 5.1 Most common type of failure in FRP laminate structures: delamination and adhesive joint failure

**Fig. 5.2** Fibre bridging phenomenon during adhesive joint failure of a FRP specimen



law,  $\sigma(\delta)$ , is a traction-separation relation that represents the stress transmitted between crack faces in the active cohesive zone (active fracture process zone).

To develop a monitoring system capable of detecting cracks/delamination, the stress distribution around the crack and the active cohesive zone needs to be analysed. A Finite Element Method Model (FEM) that simulates the delamination of a FRP structure bonded with structural adhesive was developed, based on the material/structure tested in this study.

The stress distribution along the active fracture process zone is shown in Fig. 5.3, and can be divided in two distinct contributions:

- near the crack tip (x = 0), where the material strength was reduced, and due to the proximity with the stress singularity (crack tip) the stress tends to infinite, creating a high stress gradient region;
- in the fibre bridging zone (x < 0), the fibres connecting the crack faces behind the crack tip will act like cables, forcing the faces to close, which creates a traction stress in that area. However, to maintain a force equilibrium, a compression field is formed ahead the crack tip.

These two crack/fracture phenomena, stress gradient and compression field, will move as the crack grows.

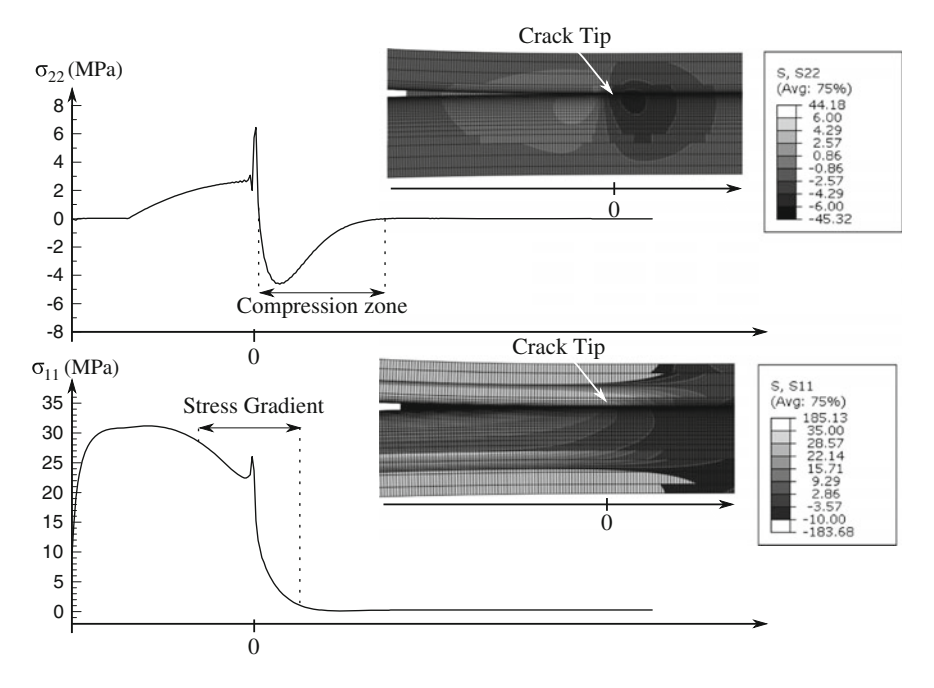


Fig. 5.3 Finite element method simulation: stress  $\sigma_{11}$  and  $\sigma_{22}$  distribution along the crack surface

# 5.1.3 Crack/Delamination Detection in Fibre Reinforced Polymer Materials

Sensing technology has been implemented in FRP materials to track delamination. Acoustic emission [4] that measures the stress waves generated by the crack front growing, vibration [5] that detects changes in the specific damping capacity of the structure, model analysis [6] by monitoring the material natural frequencies and mode shapes, piezo-electric actuators/sensors and wavelet analysis [7] based on the energy variation of the structural dynamic. However, these measurement systems have several limitations, among these the need for qualified operators, expensive hardware and impractical to use under operation. Also, to detect delamination in FRP materials the sensor must be embedded in the laminate layers or in the interface between the FRP and the structural adhesive.

Fibre Bragg Gratings (FBG) have the capability to be embedded in the FRP material, even in an operational structure, without compromising its structural resistance. This is due to the FBG reduced size, with a diameter of 125  $\mu$ m, it is virtual non-intrusive to the material. Also, FBG sensors present other interesting features, such high resolution, multiplexing capability, immunity to electromagnetic fields, chemical inertness and long term stability.

# 5.1.4 Crack/Delamination Detection by Embedded Fibre Bragg Gratings

During a crack/delamination event different fracture features will be present near the crack tip, as such as a stress gradient and a compression field. Thus, being able to identify and measure this specific phenomena with a FBG sensor is a key factor to correctly determine the presence of damage and it growth.

Different FBG response stages under a crack growth event are presented in Fig. 5.4. First, before the crack reaches the proximity of the grating, Fig. 5.4a, the material will build up uniform strain (considering structure loading or geometric singularities distant enough from the grating), which will make a uniform wavelength shift in the FBG reflected peak. Next, the compression field formed ahead the crack tip due to the the fibre bridging will reach the grating area, creating a splitting of the FGB reflected wave, as shown in Fig. 5.4b. Then, when the grating is near the influence of the crack singularity, the non-uniform strain field will change the

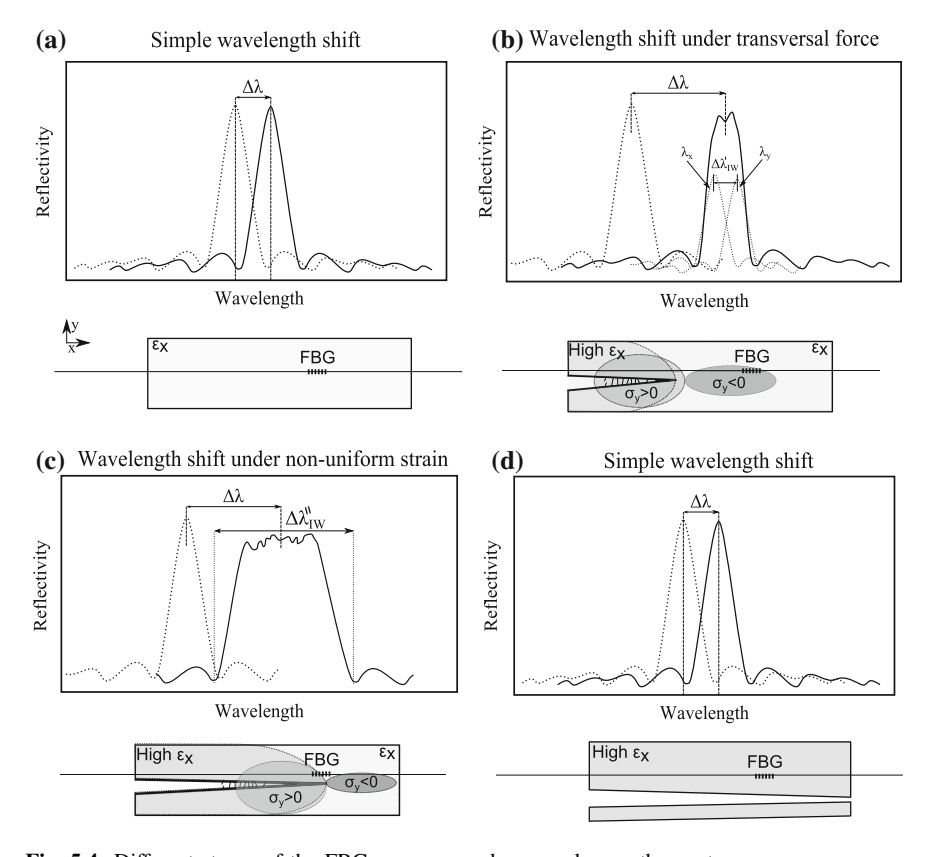


Fig. 5.4 Different stages of the FBG response under a crack growth event

shape of the reflected peak increasing the width of the reflected wave, as shown in Fig. 5.4c. At last, after the crack passes the FBG sensor, the shape of the reflected wave will return to its original shape, and the sensor response will be again a simple wavelength shift, because at this stage only uniform strains will be acting in the FBG, as shown in Fig. 5.4d.

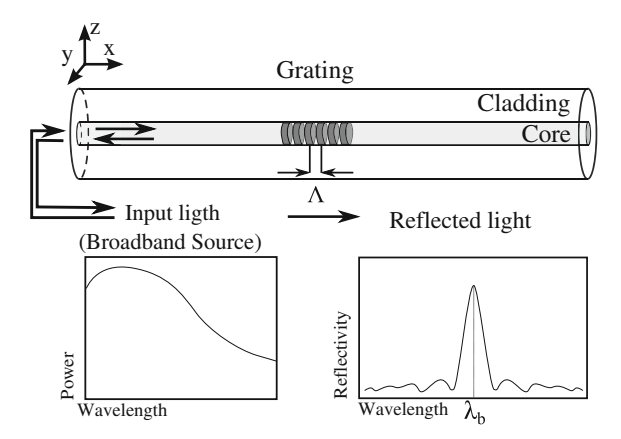
## 5.2 Fibre Bragg Grating Working Principle

A Fibre Bragg Grating (FBG) is formed by a permanent periodic modulation of the refractive index along a section of an optical fibre, by exposing the optical fibre to an interference pattern of intense ultra-violet light [8]. The photosensitivity of the silica exposed to the ultra-violet light is increased, so when the optical fibre is illuminated by a broadband light source, a very narrow wavelength band is reflected back. The spectral response of a homogeneous FBG is a single peak centred at the wavelength  $\lambda_b$ , as shown in Fig. 5.5. The wavelength  $\lambda_b$  is described by the Bragg condition,

$$\lambda_B = 2n_{eff,0}\Lambda_{.0} \tag{5.1}$$

where  $n_0$  is the mean effective refractive index at the location of the grating, the index 0 denotes unstrained conditions (initial state). The parameter  $n_{eff}$  is the effective refractive index and  $\Lambda$  is the constant nominal period of the refractive index modulation [9].

**Fig. 5.5** Fibre Bragg grating response working principle



# 5.2.1 Fibre Bragg Grating Response to Uniform Variation of Strain and/or Temperature

The wavelength shift  $\Delta \lambda_b$  of an embedded FBG under a uniform variation of strain  $\varepsilon_{xx}$ , and temperature  $\Delta T$  is given by the (5.2),

$$\frac{\Delta \lambda_b}{\lambda_b} = (1 - p_e)\varepsilon_{xx} + \left[ (1 - p_e)(\alpha_s - \alpha_f) + \xi \right] \Delta T \tag{5.2}$$

where  $p_e$  is a photoelastic coefficients,  $\alpha_s$  and  $\alpha_f$  are the thermal expansion coefficients of the host material and the optical fibre, respectively, and  $\xi$  is the thermo-optic coefficient.

# 5.2.2 Fibre Bragg Grating Response Under Transverse Force: Birefringent Effect

An optical fibre can present a birefringent behaviour, defined by the change of the refractive index  $n_{eff}$  in the two directions  $n_{effy}$  and  $n_{effx}$ , when the grating is subjected to a transverse force. The variation of the refractive index in the two directions  $n_{effy}$  and  $n_{effz}$  is given by the (5.3) and (5.4) [10–13].

$$\Delta n_x = -\frac{n_0^3}{2E_f} \left\{ (p_{11} - 2v_f p_{12})\sigma_z + \left[ (1 - v_f)p_{12} - v_f p_{11} \right] (\sigma_y + \sigma_x) \right\}$$
 (5.3)

$$\Delta n_{y} = -\frac{n_{0}^{3}}{2E_{f}} \left\{ (p_{11} - 2v_{f}p_{12})\sigma_{y} + \left[ (1 - v_{f})p_{12} - v_{f}p_{11} \right] (\sigma_{x} + \sigma_{z}) \right\}$$
 (5.4)

 $\sigma_{y,z}$  is the transverse stress,  $E_f$  is the elastic modulus of the optical fibre,  $v_f$  is the Poisson's ration,  $n_0$  is the initial refractive index,  $p_{11}$  and  $p_{12}$  are the photo-elastic coefficients of the optical fibre.

Rewriting the (5.3) and (5.4), it is possible to determine the increase in the width of the reflected wave,  $\Delta \lambda'_{IW} = ||\lambda_x - \lambda_y||$ , caused only by a transverse stress.

$$\Delta \lambda'_{IW} = 2\Lambda |\Delta n_{effz} - \Delta n_{effx}|$$

$$= \frac{\Lambda n_o^3}{E_f} \left[ (1 + v_f) p_{12} - (1 + v_f) p_{11} \right] |\sigma_z - \sigma_y|$$
(5.5)

# 5.2.3 Fibre Bragg Grating Response Under Non-uniform Strain

When an FBG sensor is near a defect, a crack, a material change or a geometric variation, this can create a stress concentration that will lead to an abrupt variation of strain. This non-uniform strain, or strain gradient, can change the periodicity of the grating along the sensor length, modifying the grating pattern configuration from "uniform" to "chirped" [14, 15].

As demonstrated by Peters [16], in a uniform grating the applied strain will induce a change in both grating period and the mean index. These two effects can be superimposed by applying an effective strain of " $(1 - p_e)\varepsilon_{xx}(x)$ ", similar to the first part of (5.2) but taking into account the strain variation along the x direction. Then it is possible to rewrite the grating period as:

$$\Lambda(z) = \Lambda_0[1 + (1 - pe) \times \varepsilon_{xx}(x)] \tag{5.6}$$

where the parameter  $\Lambda_0$  is the grating period with zero strain. The non-uniform strain effect can be approximated by using the maximum and minimum strain values along the grating. So, the maximum grating period  $\Lambda_{\rm max}$  and minimum  $\Lambda_{\rm min}$  can be calculated using the (5.6). Thus, an approximated increase of the width of the reflected wave due to a non-uniform strain,  $\Delta\lambda''_{IW}$ , is given by combining (5.6) and (5.1).

$$\Delta \lambda_{IW}^{"} = 2n_{eff} \Lambda_{\text{max}} - 2n_{eff} \Lambda_{\text{min}}$$
 (5.7)

## 5.3 Crack Detection Algorithm

Conventional signal processing software, provided by the FBG measurement system manufactures, were developed for simple and reliable strain and temperature measurements. This is made by tracking only the wavelength shift of the reflected wave maximum optical power. However, this software has several limitations for crack detection. It isn't possible to evaluate the shape of the reflected wave or distinguish between a single peak from a multi-peak, which are key features for a reliable crack detection method. Thus, a dedicated algorithm was developed to detect and evaluate the different stages of the FBG response during a crack growth event, as presented in Fig. 5.4.

The FBG signal acquision system used in this work, FS2200 Industrial BraggMeter from FiberSensing<sup>TM</sup>, measures the reflected light coming from the optical fibre every second (1 Hz), where it is outputted the reflected power amplitude for the bandwidth 1500–1600 nm as a 20,000 points file. The algorithm developed computes this raw data at this level, allowing us to extract more information per sensor.

All the different reflected wave spectrum features that the algorithm will detect are schematically shown in Fig. 5.6. The *Grating Band* is a parameter, inputed by the user, which will define the bandwidth boundaries where the algorithm will make the measurements considering only one FBG sensor in that interval. This will allow to detect multi-peaks and connect them with a single FBG sensor, as well as the moment that the peak splitting occurred. The *Peak Height* is the maximum optical power of the reflected wave inside each *Grating Band*. The *Height Threshold* is a percentage of the *Peak Height*, defined by the user, used to determine the number of peaks in each FBG, and consequently determine the correspondent wavelength  $\lambda_{1,2,...}$  for a single peak or multi-peak FBG. The *Peak Width*,  $\lambda_{IW}$ , is the width of the reflected wave that is calculated at half of the peak height for each FBG.

The algorithm is schematically shown in Fig. 5.7. Initially, the user will define the number of FBG sensors per optical fibre, and assign it to a specific *grating band*. The user will define the *height threshold* and register the initial wavelength of each FBG in a free-state (unstrained).

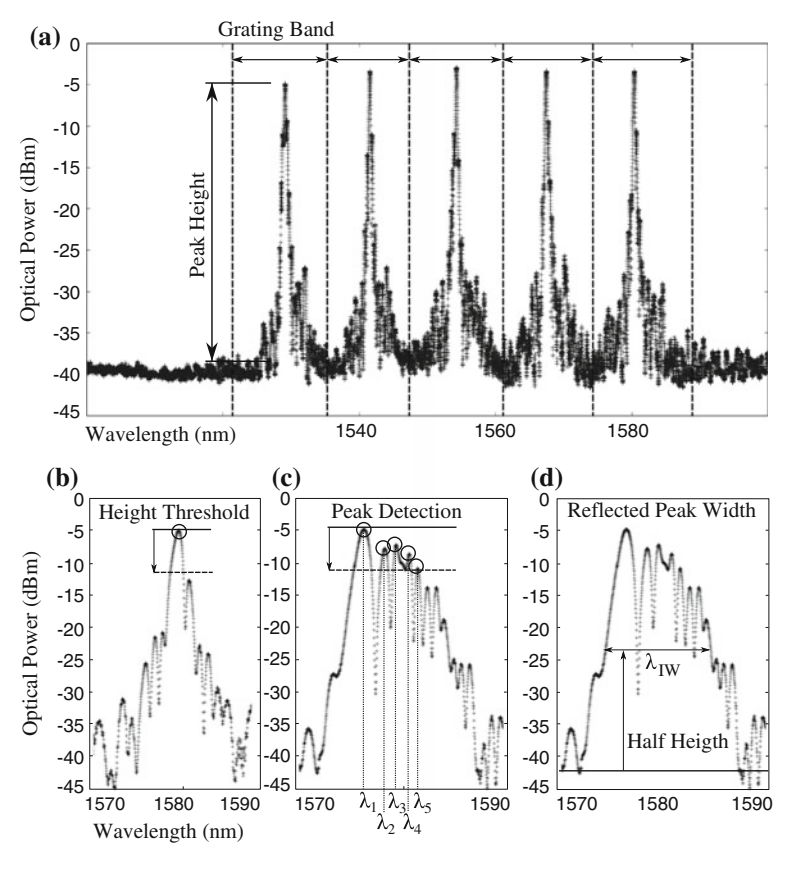
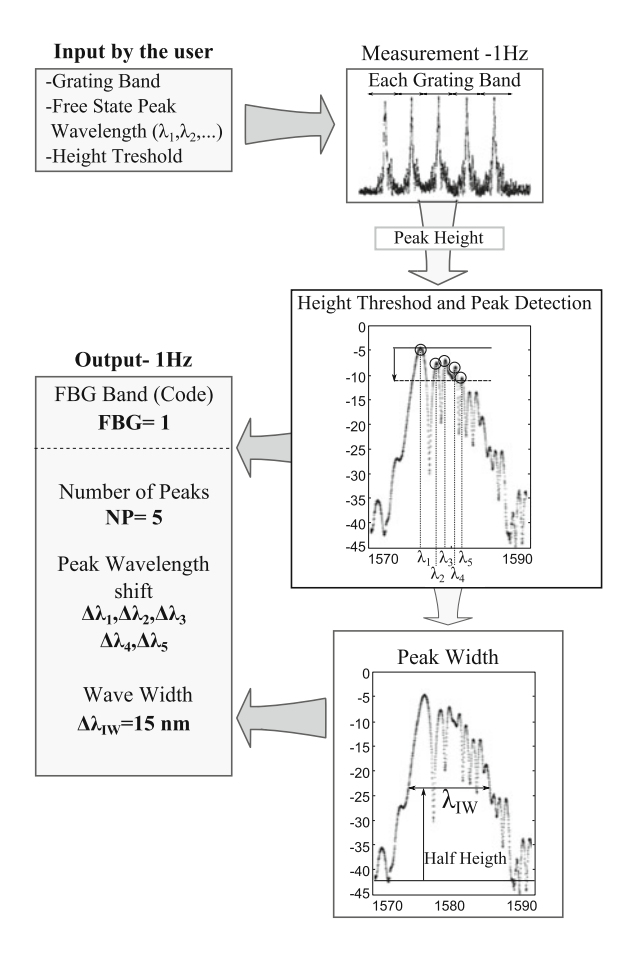


Fig. 5.6 Crack detection algorithm: reflected spectrum features detected

**Fig. 5.7** Schematic of the sensor output algorithm for crack detection



During operation and every second (1 Hz), the algorithm will perform a measurement inside each grating band defined. The maximum height of the reflected wave will be calculated, and the number of peaks detected inside the defined height threshold together with the correspondent wavelength. At this point, the algorithm will output the number of peaks and the wavelength shift, assigned to each grating. Finally, the algorithm will measure the width of the reflected wave at half height.

In summary, every second and for each FBG, the algorithm measures the number of peaks (NP), the wavelength shift  $(\Delta\lambda)$  using the wavelength measured in a free-state as reference, and the peak wave width  $(\Delta\lambda_{IW})$ .

## 5.4 Material and Experimental Procedure

In order to measure all the different features of the damage mechanism and to relate them with the FBG response, experiments were conducted on Double Cantilever Beams (DCB) with embedded FBG sensors, subjected to a fracture testing procedure.

## 5.4.1 Material and Testing Procedure

To correctly evaluate the different stages in the FBG response, a stable and controlled crack growth is required. Eight (8) DCB specimens were tested in a fracture test machine commonly used to determine material fracture properties, developed by *Sørensen* [17]. The DCB specimens were loaded in different conditions at 1 mm/min, ranging pure Mode I (tensile loading) to pure Mode II (shear loading), in order to simulate the different crack/delamination situations. This testing technique allows stable crack growth that makes it possible to correctly evaluate the FBG response at different stages.

The DCB specimens were manufactured using two composite material arms, glued by a commercial epoxy structural adhesive, Epikote MGS BPR 135G/Epikote MGS BPH137G. The geometry of the DCB specimen is presented in Fig. 5.8.

To manufacture the DCB arms two plates of  $700 \times 1000$  mm, and approximately 7 mm of thickness, were produced using multiaxial glass fibre. Ten layers of fabric per plate were used, consisting of two triaxial fabrics, Saertex Triax S32E4590, as skin layers, and eight unidirectional central layers, Saertex S35EU910. The layup stacking of the laminates was:  $[90/+45/-45/0_4/0_4/+45/-45/90]$ , and the backing of the unidirectional layers was facing out-wards, away from the central

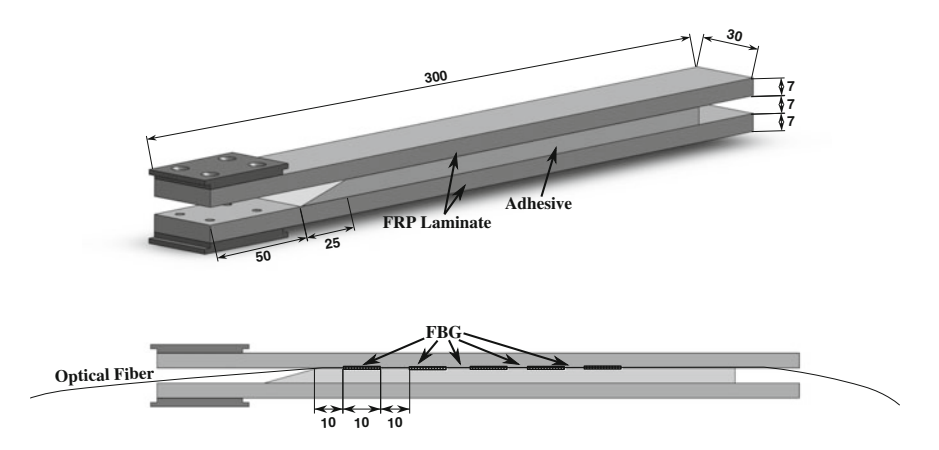


Fig. 5.8 DCB specimen geometry and FBG array Configuration

plane. The plates were made by hand-lay up of dry fibre fabric followed by epoxy impregnation, Momentive-Epikote/Epikure-100:30, by vacuum infusion at 50 °C for 5 h, and post-cured at 80 °C for 3 h. The plates were glued using a commercial structural adhesive, Momentive-Epikote/Epikure MGS BPR 135G/137G, and 7 mm spacers were used to give a well defined specimen thickness and geometry. A thin slip foil was placed in the edge of the structural adhesive, to act as a pre-crack and ease crack initiation. An array of 5 uncoated single mode FBG sensors (5 gratings in one optical fibre), with 10 mm of length, were embedded in the interface of the laminate plate with the structural adhesive. The gratings array were spaced 10 mm from each other, and the first grating was positioned 10 mm from the edge of the adhesive.

Digital image correlation (DIC) technique was applied to the specimens, in order to determine the presence of specific phenomenon caused by the crack and to correlate it with the FBG output. Digital image correlation is an optical method that by tracking changes in a random pattern in the specimen, can correlate this information with deformation/strain in the material. A pattern was painted on the side surface of the DCB specimen and ARAMIS<sup>TM</sup> software was used to calculated the strains from each measurement. All the measurements from the *BraggMeter* and *Aramis* were synchronized with the crack growth.

## 5.5 FBG Response to Crack Growth: Experimental Results

Figure 5.9 shows some measurements from a five FBG array embedded in a DCB specimen under a Mode II fracture testing. The reflected peak at 1580 nm, furthest to the right, corresponds to the grating closest to the crack tip, and consequently the peak at 1530 nm corresponds to the most distant. The table shows the algorithm output for each measurement, where is possible to observe, as the crack propagates, changes in the shape of the reflected wave  $(\Delta \lambda_{IW})$ , in the number of peaks per FBG (NP), and in the wavelength shift $(\Delta \lambda)$ .

As mentioned before and observed here, the crack proximity to the FBG will make a change in the shape of the reflected peak, thus evaluating and tracking this change will permit an accurate determination of the crack.

The shape of the *FBG* 5 reflected wave during Mode II crack growth, and the strain distribution in the DCB surface given by the DIC technique are presented in Fig. 5.10. It can be observed that during propagation of the crack, different damage features can change the shape of the reflected wave. In the left column are the DIC measurement of  $\varepsilon_y$ , where the red area is a compressive stress/strain created ahead the crack tip. As mentioned, the compression stress causes a birefringent effect in the FBG, making a peak separation and an increasing of the reflected wave width, as can be observed in Fig. 5.4. In the center column DIC measurement of  $\varepsilon_x$  are represented, where the gradient of colours represents variation of strain, indication of non-uniform strain acting in the FBG length, and consequently the change in the reflected wave.

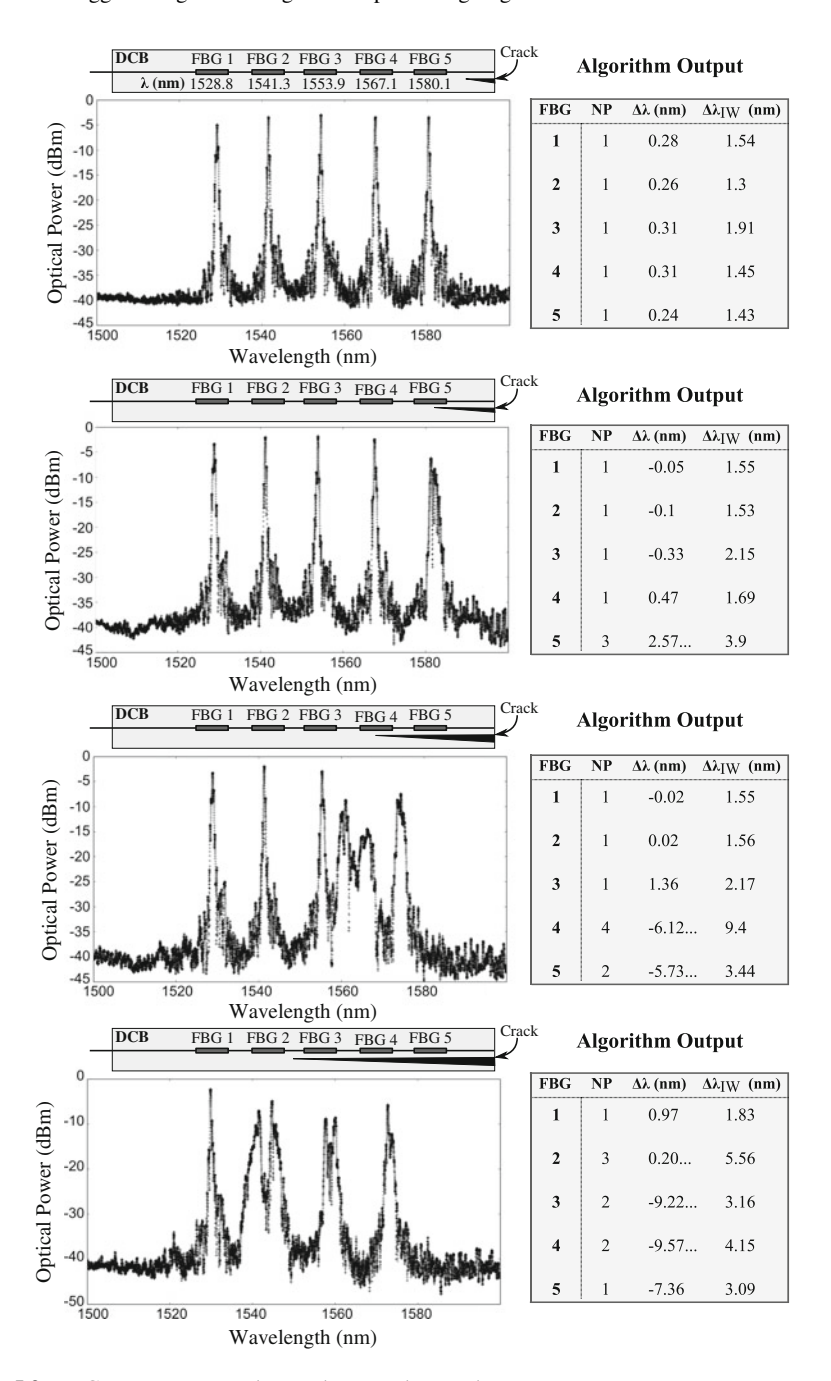


Fig. 5.9 FBG array output under Mode II crack growth

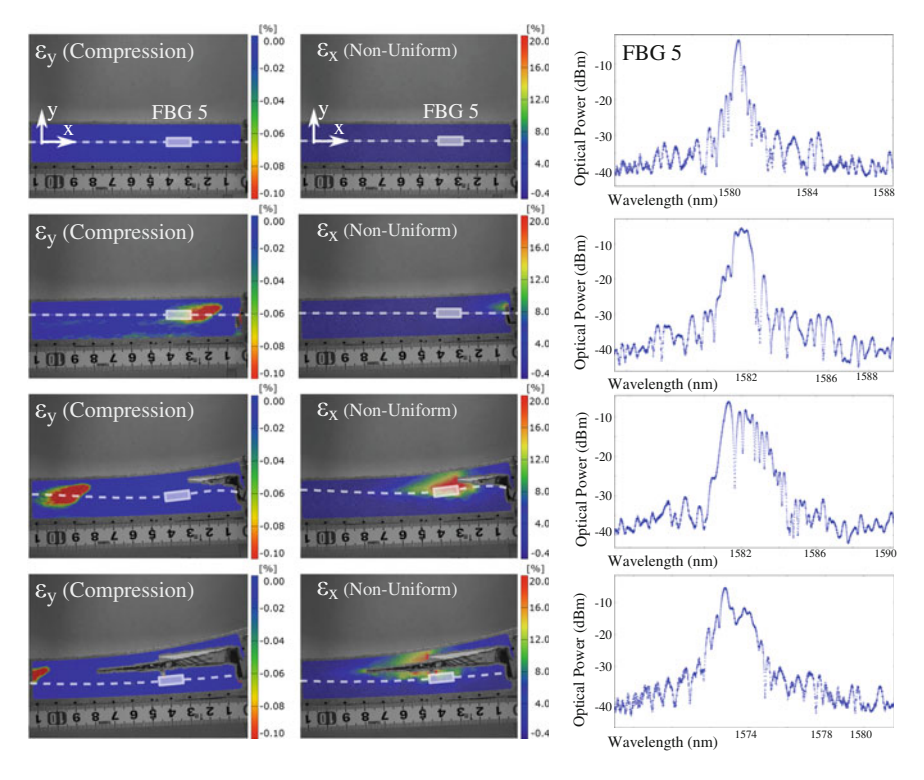


Fig. 5.10 Stages of the FBG output during crack growth: DIC measurement and FBG spectrum

As described in Sect. 1.4, it is possible to identify the different stages of the crack growth from the sensor response, and therefore detect crack growth. Before the crack reaches the proximity of the grating, the material builds up uniform strain, that induces a uniform wavelength shift in the sensor response. Next, the compression field formed ahead of the crack tip reaches the grating area, this creates a peak splitting/increase of the width. Then, when the grating is near the influence of the crack singularity, the non-uniform strain field creates a change in the shape of the reflected wave. Finally, after the crack passes the FBG sensor the shape of the reflected peak gradually recovers its original shape.

## 5.6 Discussion of Results

The wavelength shift  $\Delta\lambda$ , the wave width  $\Delta\lambda_{IW}$ , and the number of peaks per FBG, computed using the algorithm developed in this article, are presented in Figs. 5.11, 5.12 and 5.13, for three different loading conditions. Each symbol represents each FBG in the sensor array, FBG5 being the sensor closest to the adhesive edge (initiation of the crack), and FBG1 the sensor most distant. The crack growth in the

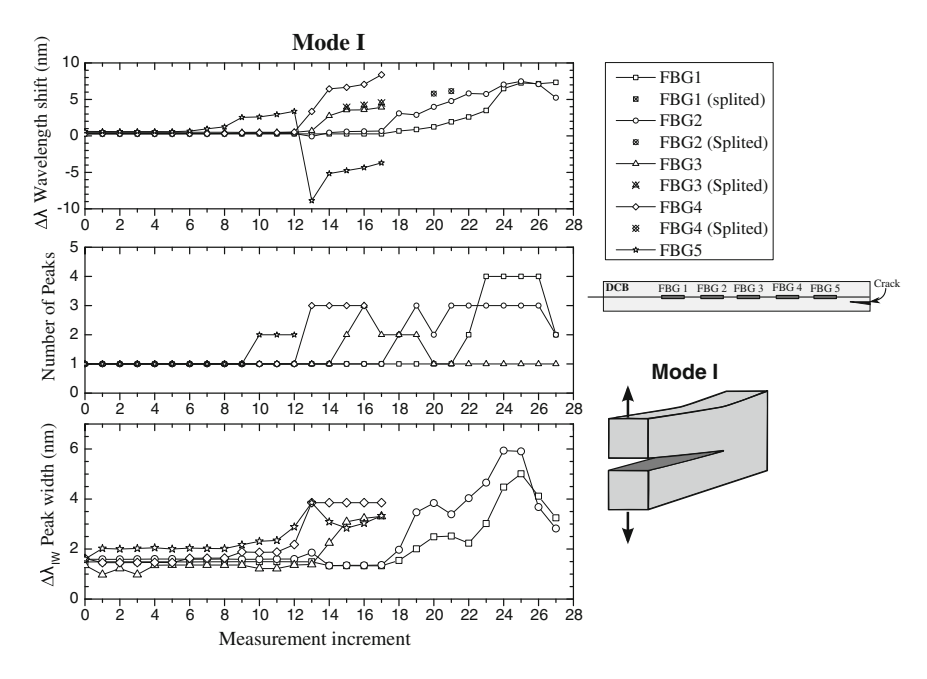


Fig. 5.11 FBG sensor array output: Mode I crack growth

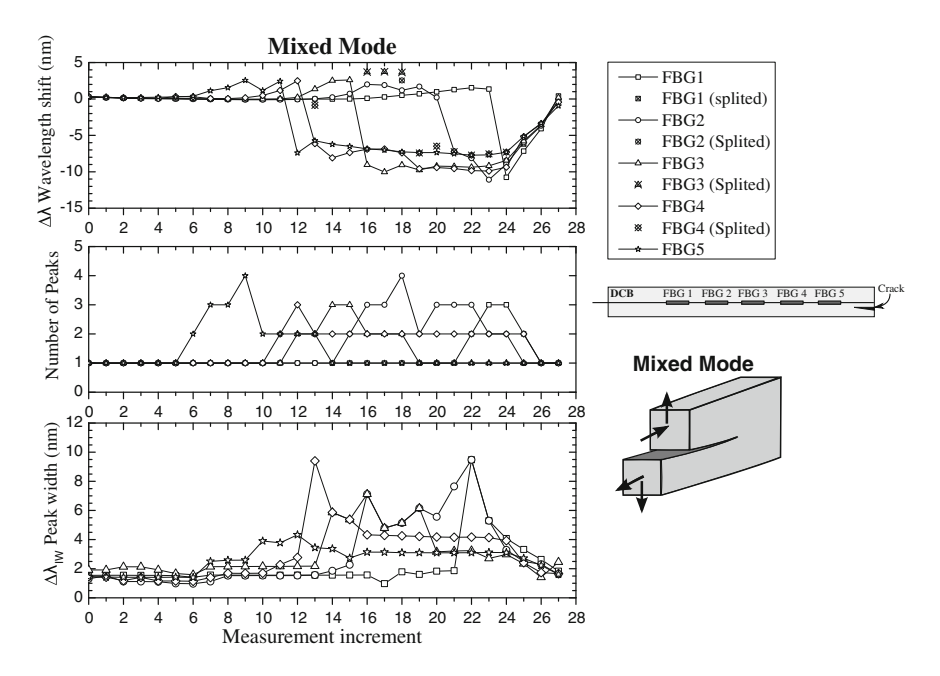


Fig. 5.12 FBG sensor array output: mixed mode crack growth

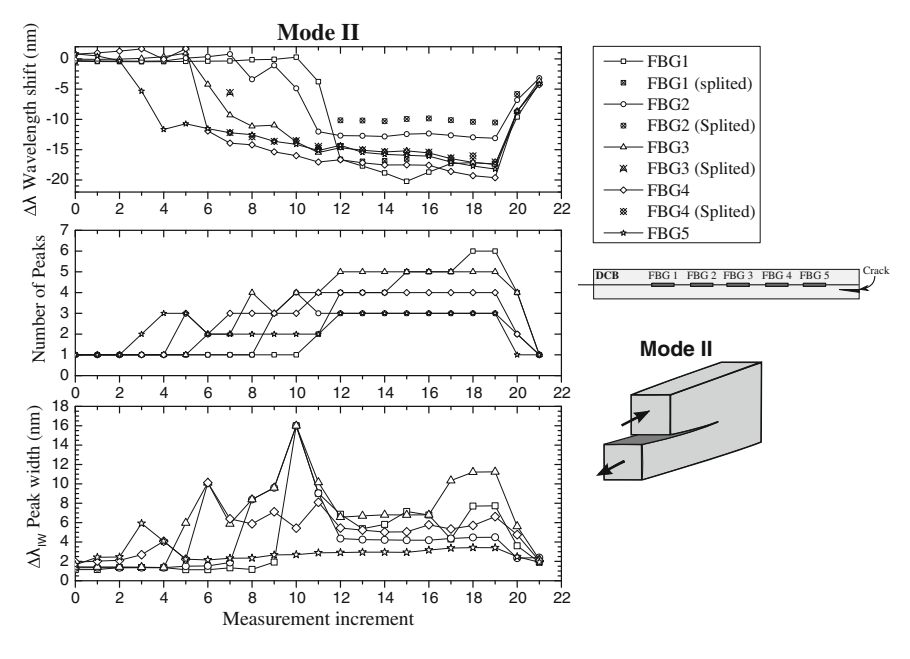


Fig. 5.13 FBG sensor array output: Mode II crack growth

order: FBG  $5 \rightarrow 4 \rightarrow 3 \rightarrow 2 \rightarrow 1$ . During Mode I loading, three FBG sensors were lost during the test, because the crack path crossed the fibre optic cutting the connection with the measurement equipment. However, the system was capable to record the growth of the crack.

The wavelength shift  $\Delta\lambda$ , is a direct indication of strain  $\varepsilon_x$  along the specimen. By analysing the graphs, it was observed that the magnitude of the  $\Delta\lambda$ , measured by each FBG, increases after the crack passes the grating area. This is because the structure loses compliance and it becomes easier to deform the material surrounding the FBG sensor. However, the evolution of the wavelength shift  $\Delta\lambda$  is different for the three loading types. For Mode I, the location where the fibre optic was embedded is under traction loading, therefore a positive  $\Delta\lambda$  was measured. For Mode II and Mixed Mode, the location is under compression loading, resulting in a negative  $\Delta\lambda$  value. Bases on this, it can be concluded that an abrupt change of  $\Delta\lambda$  is an indication that the structure is losing compliance, probably due to crack growth.

The number of peaks and the reflected wave width  $\Delta \lambda_{IW}$  are a direct indication of the presence of the crack. By analysing the graphs, it is observed that these values increase when the crack is near the FBG sensor, in all loading cases, returning to its original values after the crack passes. Thus, we can conclude that the wavelength shift is dependent on the loading type, but the increase in the width and number of peaks is related to the presence of a crack. Using this information it is possible to track the crack independently of the loading conditions or geometry of the specimen.

## 5.7 Conclusions

In this article the capability of Fibre Bragg Gratings embedded in composite material to detect and track cracks cracks/delamination was demonstrated. Three different damage mechanisms that can change the sensor output, longitudinal strain  $\varepsilon_{xx}$ , transversal stress  $\sigma_{yy,zz}$  and non-uniform strain  $\varepsilon_{xx}(xx)$ , were identified. By the use of digital image correlation technique, these damage mechanisms were identified during the experimental testing and linked with the sensor output. Thus, it is possible to extract information from the sensor that is independent of the loading type, geometry and boundary conditions, and only depends on the proximity of the crack.

A dedicated algorithm was developed to extract more information from the reflected spectrum when compared to conventional FBG signal processing software. The algorithm presented is a tool to detect and evaluate all the different stages in the FBG response during a crack growth event. This technique was successfully validated in three different loading conditions, and very promising results were obtained that enables crack growth monitoring.

The authors vision is that this monitoring method can be implemented into operational structures, enabling the design of structures in fibre reinforced materials that can operate safely, even when in damaged condition.

**Acknowledgements** The authors acknowledges the Seventh Framework Programme (FP7) for funding the project MareWint (Project reference: 309395) as Marie-Curie Initial Training Network, Fibersensing for providing the FBG sensors and hardware, and SSP-Technology for providing the material tested.

## References

- Jones, R.M.: Mechanics of Composite Materials. Taylor & Francis, Abingdon (1999). ISBN:156032712x,9781560327127
- Sørensen, B.F.: Cohesive Laws for Assessment of Materials Failure: Theory, Experimental Methods and Application. Risø DTU, Roskilde (2010). ISBN:9788755038271
- 3. Suo, Z., Bao, G., Fan, B.: Delamination R-curve phenomena due to damage. J. Mech. Phys. Solids **40**, 1–16 (1992)
- Silversides, I., Maslouhi, A., Laplante, G.: Interlaminar fracture characterization in composite materials by using acoustic emission. In: 5th International Symposium on NDT in Aerospace, Singapore (2013)
- Kyriazoglou, C., Le Page, B., Guild, F.J.: Vibration damping for crack detection in composite laminates. Compos. Part A Appl. Sci. Manuf. 35(7–8), 945–953 (2004)
- Huiwen, H., Wang, B-T., Lee, C-H., Su, J-S.: Damage detection of surface cracks in composite laminates using modal analysis and strain energy method. In: Composite Structures, vol. 74, no. 4, pp. 399

  –405, (2006)
- Yan, Y.J., Yam, L.H.: Online detection of crack damage in composite plates using embedded piezoelectric actuators/sensors and wavelet analysis. Compos. Struct. 58(1), 29–38 (2002)
- 8. Hill, K., Meltz, G.: Fiber Bragg grating technology fundamentals and overview. J. Lightwave Technol. **15**(8), 1263–1276 (1997)

 Morey, W., Meltz, G., Glenm, W.: Fiber optic Bragg grating sensors. In: Fiber Optic and Laser Sensors VII. vol.1169, (1989)

- Sørensen, L., Botsis, J., Gmr, T., Cugnoni, J.: Delamination detection and characterisation of bridging tractions using long FBG optical sensors. In: Composite Part A: applied science and manufacturing, vol. 38, no. 10, pp. 2087–2096, (2007)
- 11. Zhang, W., Chen, W., Shu, W., Lei, X., Liu, X.: Effects of bonding layer on the available strain measuring range of fiber Bragg gratings. In: Applied Optics, vol. 53, no. 5, p. 885, (2014)
- Julich, F., Roths, J.: Comparison of transverse load sensitivities of fibre Bragg gratings in different types of optical fibres. In: Optical Sensing and Detection, vol. 7726, no. 0, p. 77261N-77261N-9, (2010)
- Bosia, F., Giaccari, P., Botsis, J., Facchini, M., Limberger, H.G.: Characterization of the response of fibre Bragg grating sensors subjected to a two-dimensional strain field. Smart Mater. Struct. 925(12), 925–934 (2003)
- 14. Yashiro, S., Okabe, T., Toyama, N., Takeda, N.: Monitoring damage in holed CFRP laminates using embedded chirped FBG sensors. Int. J. Solids Struct. **44**(2), 603–613 (2007)
- Zhang, X., Max, J-J., Jiang, X., Yu, L., Kassi, H.: Experimental investigation on optical spectral deformation of embedded FBG sensors. In :Proceedings of SPIE, vol. 6478, pp. 647808–647808-7, (2007)
- Peters, K., Studer, M., Botsis, J., Iocco, A., Limberger, H., Salath, R.: Embedded optical fiber bragg grating sensor in a nonuniform strain field: measurements and simulations., In: Kluwer Academic Publishers, vol. 41, pp. 19–28, (2001). doi:10.1007/BF02323100
- 17. Sørensen, B.F., Jørgensen, K., Jacobsen, T., Østergaard, R.C.: DCB-specimen loaded with uneven bending moments. In:International Journal of Fracture, vol. 141, pp. 163–176, (2006). doi:10.1007/s10704-006-0071-x

## Part III Photonics

## Chapter 6 Free-Space Millimeter-Wave Electro-optic **Modulators Using Quasi-Phase-Matching Gap-Embedded-Patch-Antennas on Low Dielectric Constant Substrate**

Yusuf Nur Wijavanto, Atsushi Kanno, Hiroshi Murata, Tetsuva Kawanishi, Naokatsu Yamamoto and Yasuvuki Okamura

**Abstract** Conversion devices between free-space microwave/ millimeter-wave and lightwave signals are required in Fiber-Wireless (Fi-Wi) links. In this paper, we propose a free-space millimeter-wave Electro-Optic (EO) modulator using Quasi-Phase-Matching (QPM) gap-embedded-patch-antennas on a low dielectric constant substrate. Free-space millimeter-wave signals can be received and converted directly to lightwave signals using the proposed device. It can be operated passively with no external power supply and operated with extremely low millimeter-wave losses. The QPM array structure can be adopted for improving modulation efficiency by considering the transit-time effects. The proposed device is easy connected to optical fiber, therefore Fi-Wi can be realized using the proposed device. Basic structure, analysis, and experimental results of the proposed device are discussed and reported for 40 GHz operational millimeter-wave bands.

#### 6.1 Introduction

Free-space (wireless/mobile) communication has been implemented and used recently for transferring data to mobile devices. Microwave bands are used widely for carrying data through air medium with several free-space communication

Y.N. Wijayanto (⋈) · A. Kanno · T. Kawanishi · N. Yamamoto National Institute of Information and Communications Technology, 4-2-1 Nukui-Kitamachi, Koganei, Tokyo 184-8795, Japan e-mail: ynwijayanto@nict.go.jp

Y.N. Wijayanto

Indonesian Institute of Sciences, Jl. Sangkuriang, Cisitu, Bandung 40135, Indonesia

H. Murata · Y. Okamura

Osaka University, 1-3 Machikaneyama, Toyonaka, Osaka 560-8531, Japan

T. Kawanishi

Waseda University, 3-4-1 Ohkubo, Shinjuku, Tokyo 169-8555, Japan

<sup>©</sup> Springer International Publishing Switzerland 2016

P. Ribeiro and M. Raposo (eds.), Photoptics 2015,

standards such as Wi-Fi, WiMAX, LTE, [1, 2]. Since demand of high quality data transfers using mobile devices is always increase time by time, the microwave bands will be saturated in the near future due to large data size and increasing mobile users. Scientists and researchers are looking for solving the problems by minimizing the data size, saving used frequency spectra, increasing transfer capacity, enlarging operational bandwidth, [3–6].

In order to increase transfer capacity and enlarge the operational bandwidth, high operational microwave frequency into millimeter-wave or sub-millimeter-wave bands are promising to use for carrying large data with high transfer speed. Naturally, the millimeter-wave bands have relatively large propagation loss in air and metal cables than microwave bands [7–9]. Therefore, short distance free-space millimeter-wave communication in pico/femto-cells can be developed for indoor free-space communication, personal area network (PAN), local area networks (LAN). Since coverage area of pico/femto-cells is small, networking of pico/femto-cells can be adopted for enlargement of the coverage area. The pico/femto-cell networks can be connected using low propagation loss optical fibers as backhaul networks by adopting microwave-photonic technology as illustrated in Fig. 6.1 [10, 11].

Microwave-photonic technology is a combination technology where microwave and lightwave bands are operated simultaneously by considering their advantages such as high mobility, large bandwidth, no induction, [12, 13]. The technology can be implemented on Fiber-Wireless (Fi-Wi) links since free-space microwave and optical fiber communication are used together. In order to realize the Fi-Wi link, converters between microwave and lightwave signals are required highly. A high-speed photo-detector can be used for converting lightwave signals to microwave signals [14]. As the other one, microwave signals can be converted to lightwave signals by use of a high-speed optical modulator [15].

In general for Fi-Wi links, a converter from free-space microwave/millimeter-wave to lightwave signals is composed of free-space microwave/millimeter-wave antennas and optical modulators [16, 17]. The antennas are used for receiving free-space microwave/millimeter-wave signals. Then, the received microwave/millimeter-wave signals are transferred to the optical modulators by a connection

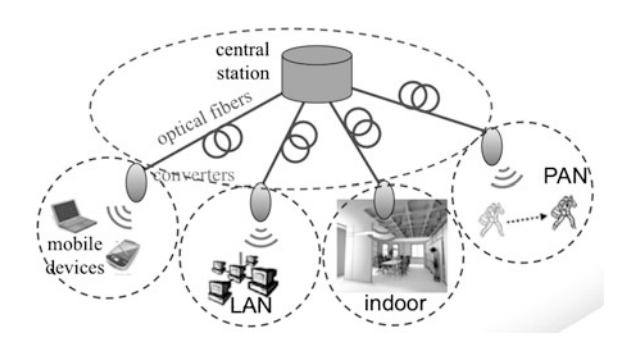


Fig. 6.1 Microwave-photonic technology for pico/femto-cell free-space communication

line, such as a coaxial cable. Therefore, the microwave/millimeter-wave signals are modulated in lightwave signals propagated on optical fibers. However, microwave/millimeter-wave signal distortion and decay might occur in the connection line when an operational frequency becomes high.

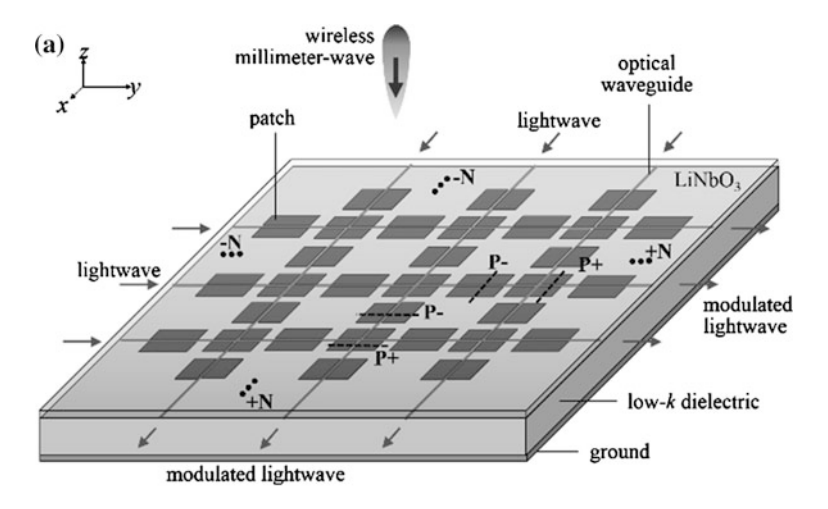
Integration of microwave/millimeter-wave antennas and optical modulators fabricated on an electro-optic (EO) crystal are also developed for reducing microwave/millimeter-wave signal distortion and decay [18–20]. They are composed of planar antennas, connection lines, and resonant electrodes with simple and compact device structures. Since several microwave/millimeter-wave planar electrodes on the substrate, completely impedance matching is required to obtain effective microwave/millimeter-wave resonance. The tuning of them is rather difficult and low microwave/millimeter-wave losses might be still induced along the connection line and their coupling.

New fusion of microwave/millimeter-wave antennas and EO modulators were proposed [21–23]. Patch-antennas embedded with a narrow-gap were fabricated on an EO crystal substrate. Displacement current and microwave/millimeter-wave electric field across the gap can be used for EO modulation. Precise tuning is not required since patch-antennas takes place at the substrate. Therefore, extremely low microwave/millimeter-wave signal distortion can be achieved using the fusion structures with a simple and compact structure. EO modulators using the fusion structures in an array structure were also reported for enhancing modulation efficiency by considering transit-time effect [24]. In high operational frequency, the patch-antennas become small. Therefore, antenna gain becomes small and microwave/millimeter-wave-lightwave electric field interaction length becomes short. The reported devices are operated effectively for a linear microwave/millimeter-wave polarization.

In this paper, a free-space millimeter-wave electro-optic (EO) modulator using Quasi-Phase-Matching (QPM) gap-embedded-patch-antennas on a low dielectric constant substrate is proposed. By using low dielectric constant material as the antenna substrate, a large patch-antenna size can be realized for increasing antenna gain and enhancing millimeter-wave electric field strength across the gaps and enlarging interaction length between millimeter-wave and lightwave electric fields. Therefore, modulation efficiency enhancement can be obtained. Further enhancement of the modulation efficiency can be achieved using the QPM array structure by considering transit-time effect.

## **6.2** Device Proposal and Operational Principle

Figure 6.2 shows a structure of the proposed device. It consists of a QPM array of patch-antennas with orthogonal-gaps fabricated on a low dielectric constant material stacked with a thin LiNbO<sub>3</sub> optical modulator. The patch electrodes are inserted between the LiNbO<sub>3</sub> optical crystal and low dielectric constant material. The patch electrode length, L, is set at a half wavelength of the designed millimeter-wave. The



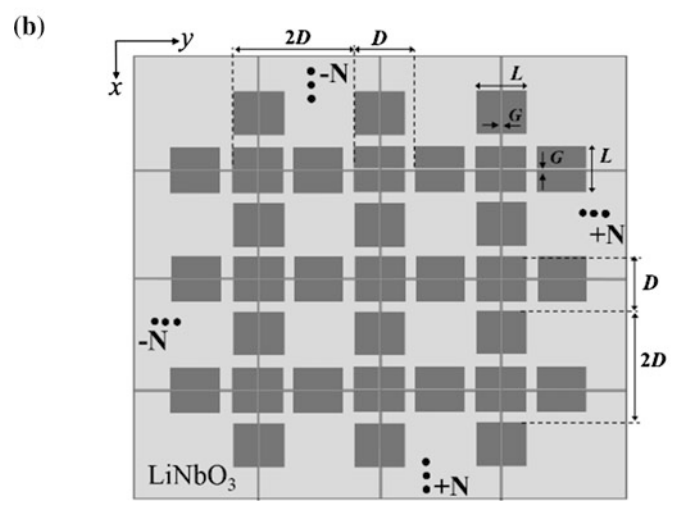


Fig. 6.2 Structure of QPM array of patch-antennas with orthogonal-gaps on low dielectric constant material stacked with EO modulator, **a** whole and **b** top views

gap width, G, is set in micrometer order ( $\sim10~\mu m$ ). The patch electrodes are set in an array structure by considering a QPM method with a distance of D. Since a z-cut LiNbO3 optical crystal is used, optical waveguides are located on a one side of the gap edge as shown in cross-sectional view of Fig. 6.3. The gap position refer to the optical waveguide are slightly shifted for satisfying the QPM method. A buffer layer is also inserted between the LiNbO3 optical crystal and patch electrodes. The reverse side of the low dielectric constant material is covered with a ground electrode.

When a free-space millimeter-wave signal is irradiated to the device, standing-wave currents are induced on the patch electrode surface [25, 26]. By

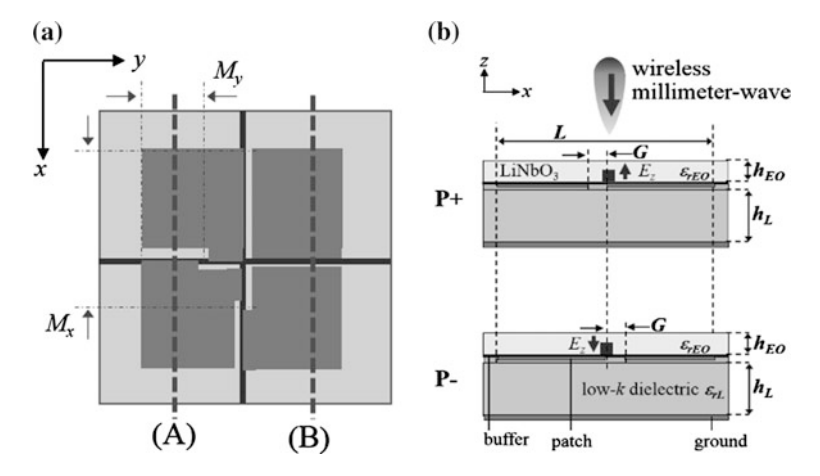


Fig. 6.3 Structure of meandering gaps for polarization inversed structure, **a** top and **b** cross-sectional views

embedding orthogonal-gaps at the center of the patch electrodes, millimeter-wave displacement current and strong electric field are induced across the orthogonal-gaps due to current flow continuity [27]. The induced millimeter-wave electric field can be used for optical modulation through the Pockels EO effect of LiNbO<sub>3</sub> optical crystal. When lightwave propagating in the orthogonal optical waveguides located on the orthogonal-gaps are modulated by the radiated free-space millimeter-wave signal. Since the gap width is relatively much smaller than the electrode patch size, the patch-antenna characteristics are not changed.

Generally, modulation efficiency improvement can be obtained using an array structure. However, the spacing between patch electrodes is required relatively large owing to the transit-time effect [24]. New patch-antennas can be added in the large spacing of the previous antennas by considering QPM methods. The QPM methods can be adopted to reduce the spacing of about half. Therefore, twice modulation efficiency can be obtained using QPM array structure in the same device length, since the patch electrodes number becomes double.

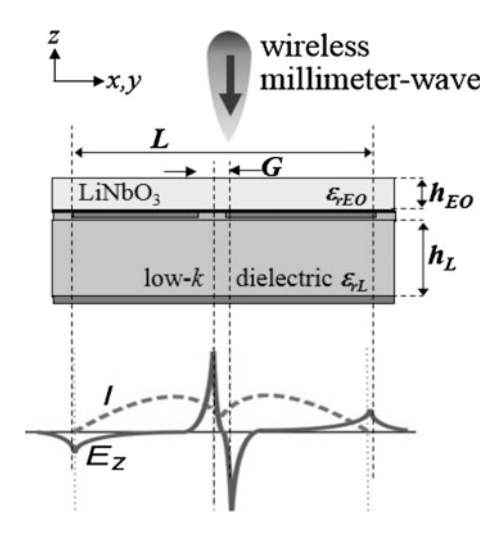
## 6.3 Device Analysis and Design

## 6.3.1 Millimeter-Wave Analysis

## **6.3.1.1** Displacement Current

When a free-space millimeter-wave signal is irradiated to the standard patch-antennas with no gap, a standing-wave millimeter-wave surface current is induced on the patch electrodes. Then, orthogonal narrow gaps are introduced at the

**Fig. 6.4** Millimeter-wave current and electric field profiles of the proposed device



center of the patch electrode as shown in Fig. 6.4. Owing to the requirement of current continuity on the patch electrode, millimeter-wave displacement current and strong electric field are induced across the gap. The induced millimeter-wave electric field across the gap is obtained by time integration of the displacement current. Therefore, it can be expressed as

$$E_m(t) = E_0 \cos(\omega_m t) \tag{6.1}$$

The millimeter-wave current and electric field profiles of the proposed device are also illustrated in Fig. 6.4.

## 6.3.1.2 Patch-Antenna Size

In order to consider for obtaining large antenna gain, it can be achieved by enlarging patch electrode fabricated on a low dielectric constant material as the antenna substrate. In general, a patch electrode size is inversely proportional to the designed operational frequency of free-space millimeter-wave signals. It is also inversely proportional to square root of substrate effective dielectric constant [26].

The patch size can be enlarged using reduction of the effective dielectric constant of the antenna substrate. In order to reduce the effective dielectric constant of the substrate, it can be realized using a thin high-k EO crystal bonded with a low dielectric constant material as shown in Fig. 6.2. By using a bonded material structure with a thin EO crystal, the effective dielectric constant becomes low.

## 6.3.1.3 EO Crystal Types

The EO crystal orientation, the distribution of the millimeter-wave electric field across the orthogonal-gaps, and position of the optical waveguide must be taken into account for achieving effective operation. The orthogonal optical waveguides should be set on one side of the gap edge as shown in Fig. 6.3, since a z-cut LiNbO $_3$  optical crystal is used in the analysis.

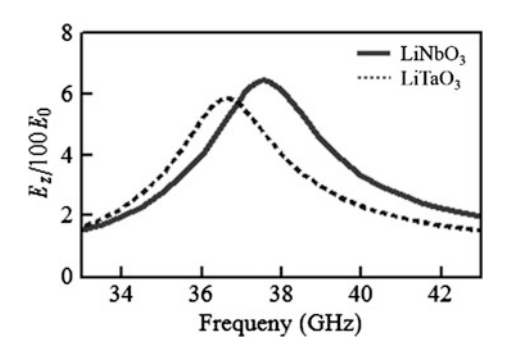
The induced millimeter-wave electric field across the gaps was calculated using electromagnetic software analysis. The optical crystal thickness was set  $80~\mu m$  and low dielectric constant material thickness was set  $130~\mu m$  with dielectric constant of 3.5. The length and width of the patch electrodes with gold metal were set 1.6~mm. A gap with  $10~\mu m$ -wide was located at the center of the patch electrodes. Ultraviolet adhesive glue as a buffer layer was also inserted between the bonded structures. The calculated electric fields across the gap are shown in Fig. 6.5~for~z-cut LiNbO $_3~(solid-line)$  and LiTaO $_3~(dashed~line)$ .

The millimeter-wave operational frequencies are shifted due to different effective dielectric constant of the devices with bonded structure between anisotropic  $\text{LiNbO}_3/\text{LiTaO}_3$  crystal and low-k material. Based on the result, we expected that the proposed device using z-cut  $\text{LiNbO}_3$  crystal can be used for enhancing modulation efficiency.

## **6.3.1.4** EO Crystal Thickness

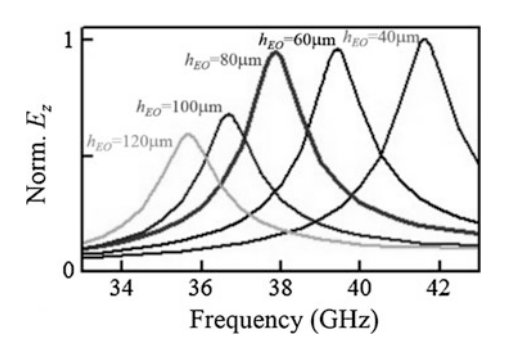
Figure 6.6 shows the calculated millimeter-wave electric field magnitude across the gap as a function of operational frequency for several *z*-cut LiNbO<sub>3</sub> optical crystal thicknesses. The peak frequency is shifted due to different effective dielectric constant of the proposed device by changing the LiNbO<sub>3</sub> optical crystal thickness. When the *z*-cut LiNbO<sub>3</sub> crystal thickness becomes thin, operational frequency becomes high and millimeter-wave electric field strength becomes large. It is promising also for obtaining large modulation efficiency.

Fig. 6.5 The calculated millimeter-wave electric field across the gap for z-cut LiNbO<sub>3</sub> (solid-line) and LiTaO<sub>3</sub> (dashed line)



90 Y.N. Wijayanto et al.

**Fig. 6.6** The calculated millimeter-wave electric field across the gap for *z*-cut LiNbO<sub>3</sub> crystal dependences



## **6.3.1.5** Millimeter-Wave Polarization

Figure 6.7 shows the calculated electric field distributions in the *z*-component for the top view. We can see that the strong millimeter-wave electric field is induced across the gaps. The strongest millimeter-wave electric field is induced when the millimeter-wave polarization is perpendicular to the gaps. Almost no millimeter-wave electric field is induced, when the millimeter-wave polarization is parallel to the gaps. When the millimeter-wave polarization is not completely perpendicular or parallel to one of the gap, the millimeter-wave electric field is induced across the two orthogonal-gaps. The magnitude of millimeter-wave electric field across the gap depends on the millimeter-wave polarization condition.

## 6.3.2 Optical Modulation

#### 6.3.2.1 Transit-Time Effect

For an array of gap-embedded patch electrodes, the temporal phases of the millimeter-wave signal supplied to the gap-embedded patch electrodes are changed according their distance, D, and the free-space millimeter-wave irradiation angle,  $\theta_x$  and  $\theta_y$ . When a lightwave propagates in the optical waveguide, the millimeter-wave electric field as would be observed by the lightwave can be expressed by following

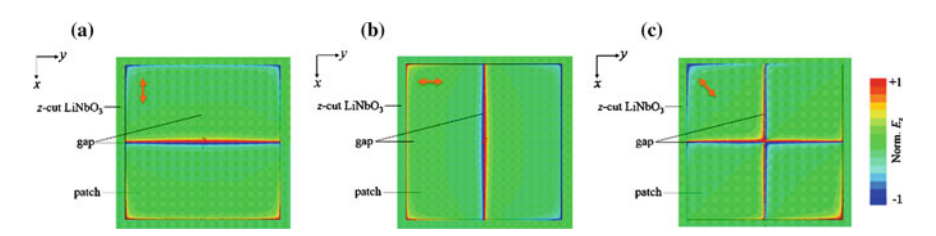


Fig. 6.7 Calculated millimeter-wave electric field distribution in the z-component for  $\mathbf{a}$  x-,  $\mathbf{b}$  y-, and  $\mathbf{c}$  xy-polarizations (diagonal)

equation with taking into account the transit-time of the lightwave along x- and y-axes,

$$E_{m-light}^{h}(x,\theta_{x}) = E_{0}\cos(k_{m}n_{g}y) + 2Dh(k_{m}n_{0}\sin\theta_{x} + \varphi)$$
(6.2)

$$E_{m-light}^{h}(y,\theta_{y}) = E_{0}\cos(k_{m}n_{g}y) + 2Dh(k_{m}n_{0}\sin\theta_{y} + \varphi))$$
 (6.3)

where  $k_m$  is the wave number of the millimeter-wave,  $n_g$  is the group refractive index, h denotes the number of the gap-embedded patch electrodes, D is a distance of the patch electrodes ( $D = \Lambda_m/2n_g$ ),  $n_0$  is the refractive index of the millimeter-wave in air (=1), and  $\varphi$  is an initial phase of the lightwave ( $\varphi = k_m n_g y'$ ). The millimeter-wave electric fields as would be observed by the lightwave are shown by the sinusoidal-curve in Fig. 6.8 with QPM and with no QPM structures.

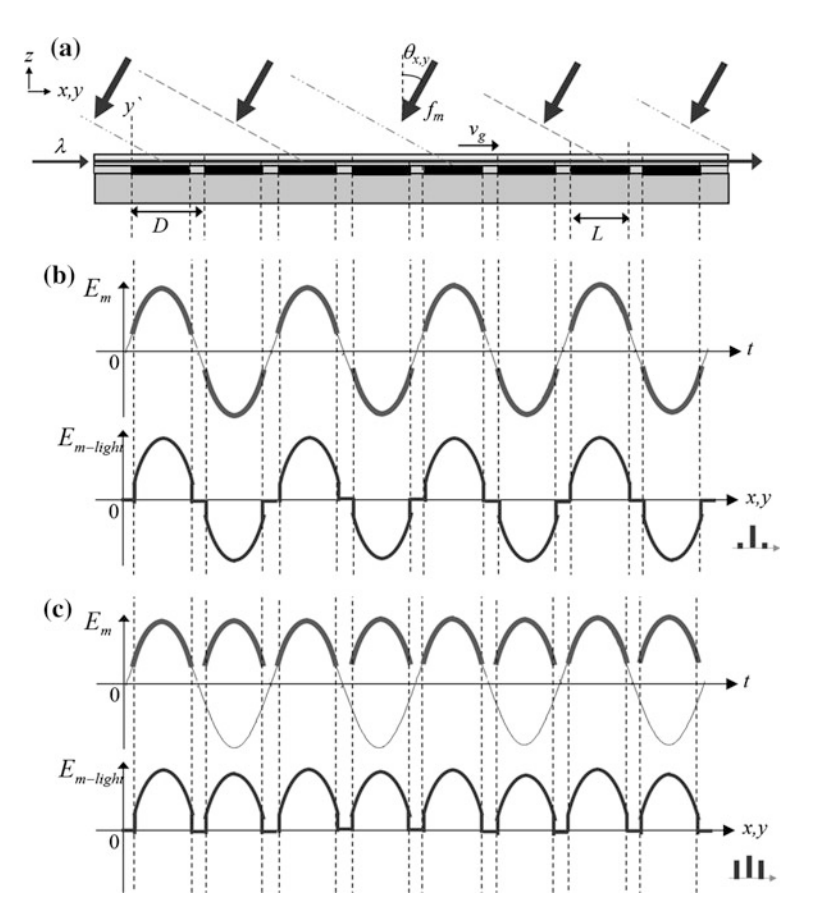


**Fig. 6.8** Operational principle of QPM EO modulators under irradiation of a free-space millimeter-wave signal angle of  $\theta_{x,y}$  degrees. Modulation efficiency corresponds to the integration of the millimeter-wave electric field observed by lightwave

The proposed QPM device is an optical phase modulator, therefore the modulation efficiency,  $\Delta\phi$  from the free-space millimeter-wave signal to the optical signal is proportional to power ratio between lightwave carrier and sidebands, when  $\Delta\phi\ll 1$ . The modulation efficiency is calculated by the integration of millimeter-wave electric field as would be observed by the lightwave along the gap-embedded patch electrodes, it can be expressed as following equation for optical waveguide along a- and y-axes,

$$\Delta\phi(\theta_x) = \frac{\pi r_{33} n_e^3}{\lambda} \Gamma \sum_{h=-N}^{N} \int_{0}^{W} P(y) E_{m-light}^h(x, \theta_x) dx$$
 (6.4)

$$\Delta\phi(\theta_{y}) = \frac{\pi r_{33} n_{e}^{3}}{\lambda} \Gamma \sum_{h=-N}^{N} \int_{0}^{W} P(y) E_{m-light}^{h}(y, \theta_{y}) dy. \tag{6.5}$$

where  $\lambda$  is the wavelength of lightwave propagating in the optical waveguides,  $r_{33}$  is the EO coefficient,  $n_e$  is the extraordinary refractive index of the substrate,  $\Gamma$  is a factor expressing the overlapping between the induced millimeter-wave and the lightwave electric field, W are the width of the patch electrodes as the interaction length of the millimeter-wave and lightwave electric field, and N is the number of gap-embedded patch electrodes in an array structure. P(y) expresses the polarization of the millimeter-wave electric field in the z-component under the gap edge along the optical waveguide. The modulation index of the QPM structure corresponds to the sum of the integration of the millimeter-wave electric field observed by lightwave in Fig. 6.8. Since the modulation index is also a function of free-space irradiation angle,  $\theta$ , the directivity in the modulation efficiency can be also calculated using (6.4) and (6.5).

## **6.3.2.2 QPM Array**

The millimeter-wave electric fields in the *z*-component between two-edges of gaps have different polarities [27]. The different polarities enable us to obtain the polarization-inversed structure for the QPM condition. The polarization-inversed structures on a *z*-cut EO crystal are obtainable by switching spatial relationship between the gap edge and optical waveguide along the gap-embedded patch electrodes.

In order to obtain polarization-inversed structure, meandering gaps can be adopted as shown in Fig. 6.3. The gaps are meandered on straight optical

waveguide by considering transit-time effect. Therefore, it can be used for recovering optical modulation degradation due to miss-matching between millimeter-wave and lightwave electric fields.

## **6.3.2.3** Free-Space Irradiation Angle

The meandering-gaps are promising for free-space irradiation angle or beam-steering controls. Several patterns of meandering gaps are designed as shown in Fig. 6.9. The designed meandering gaps are set by considering transit-time effect for receiving several irradiation angles of free-space signals.

The directivity of free-space millimeter-wave signals in the proposed device can be calculated using (6.3). The calculated directivities in the designed device for several patterns of meandering gaps are shown in Fig. 6.10. Clearly, the meandering gaps can be used for controlling irradiation angle or beam-steering of free-space millimeter-wave signals.

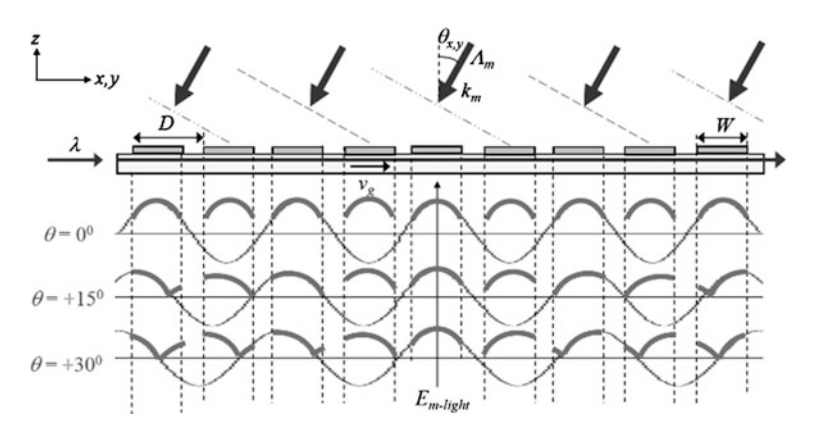
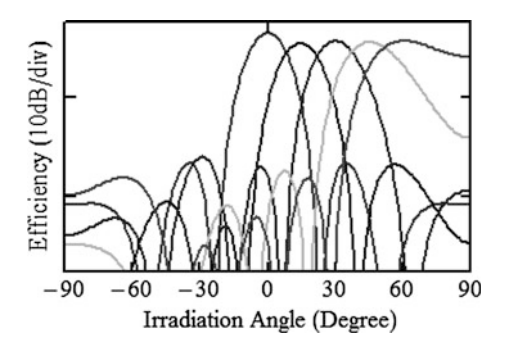


Fig. 6.9 Typical patterns of patch electrodes with meandering gaps

Fig. 6.10 Calculated irradiation angle dependence of the designed QPM EO modulator for several patterns of meandering-gaps



## 6.4 Device Realization and Characterization

## 6.4.1 Realization Process

The designed device was fabricated as illustrated in Fig. 6.11a. First, a z-cut LiNbO<sub>3</sub> crystal with a thickness of 300 µm was prepared. Then, single-mode

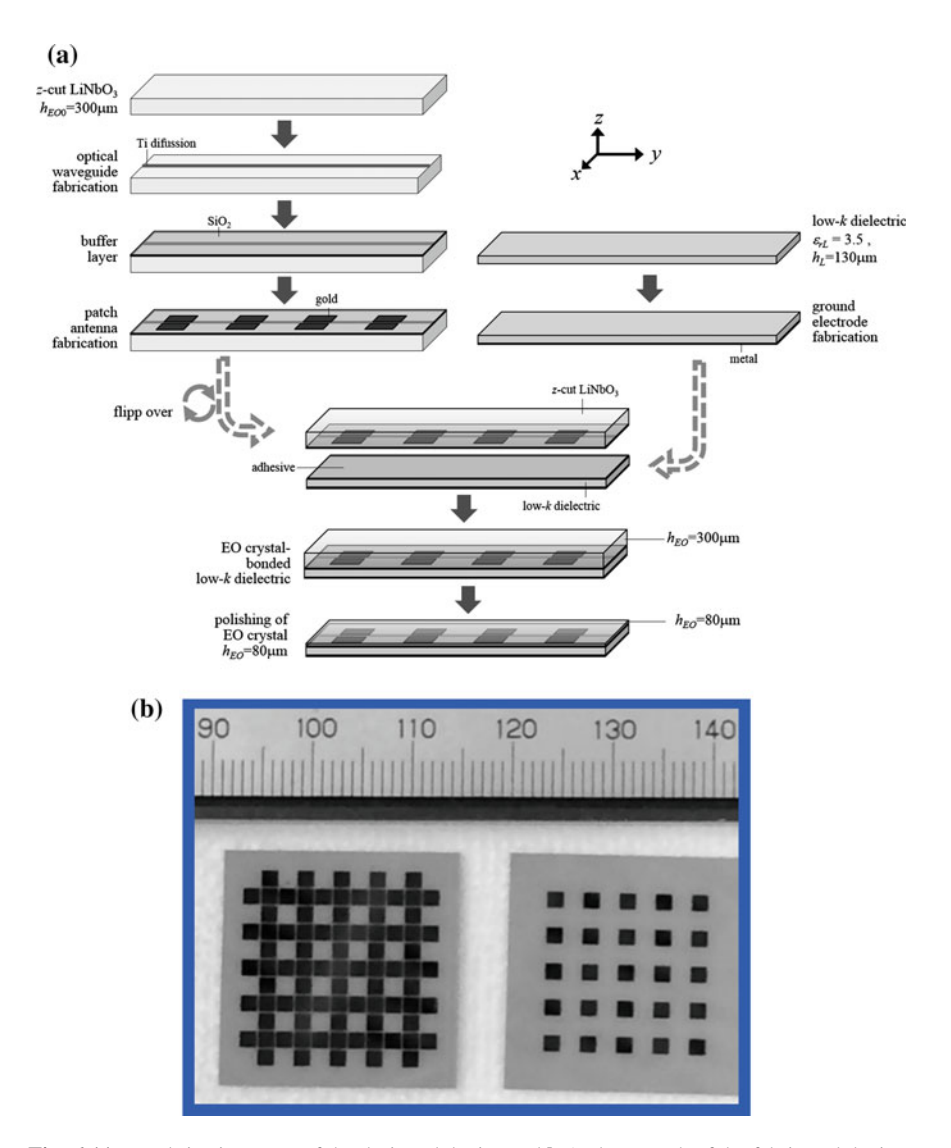


Fig. 6.11 a Fabrication steps of the designed device and  $\mathbf{b}$  A photograph of the fabricated devices with an array of gap-embedded patch-antennas, with QPM structures ( $\mathit{left}$ ) and with no QPM structure ( $\mathit{right}$ )

orthogonal channel optical waveguides were fabricated on the EO crystal using titanium diffusion method [28]. The titanium were diffused with 1100 °C for 10 h. After that, a 0.2  $\mu m$ -thick SiO $_2$  buffer layer was deposited on the EO crystal. An array of patch electrodes embedded with orthogonal-gaps was also fabricated on the EO crystal. The patch electrodes were fabricated using a 2  $\mu m$ -thick gold film on the EO crystal through thermal vapor deposition, standard photo-lithography, and a lift-off technique. The optical waveguides were aligned onto one side of the gap edge.

A ground metal was deposited to the bottom surface of a low dielectric constant material. Then, the top surface of a low dielectric constant material was covered with an optical adhesive for next bonding process.

In bonding process, the EO crystal was flipped over with  $180^{\circ}$ . So as the metal antennas become on the bottom surface of the EO crystal. Then, the flipped EO crystal was bonded to the low dielectric constant material by exposing ultraviolet (UV) light to the UV-cured optical adhesive [29]. Finally, the  $300~\mu$ m-thick EO crystal was polished to the designed thickness of  $80~\mu$ m using a polishing machine with diamond slurry. A photograph of the fabricated device is shown in Fig. 6.11b.

## 6.4.2 Characterization

Performances of the fabricated device were measured experimentally with a measurement setup as shown in Fig. 6.12. Lights of 1.55 µm wavelength from laser were propagated to optical fibers and coupled to the fabricated device. Millimeter-wave signal in 40 GHz bands from a signal generator was amplified and irradiated to the fabricated device using a horn antenna with an irradiation power of 20 mW. The output lightwave signals were measured using an optical spectrum analyzer (OSA).

Typical of the measured output light spectra from two orthogonal waveguides are shown in Fig. 6.13, where a 34 GHz free-space millimeter-wave signal was irradiated at the device at a normal irradiation angle and polarization of 45°. The optical sidebands were observed clearly. The intensity ratio between the sidebands and optical carrier were about 37 dB.

**Fig. 6.12** Measurement setup for characterization of the fabricated devices

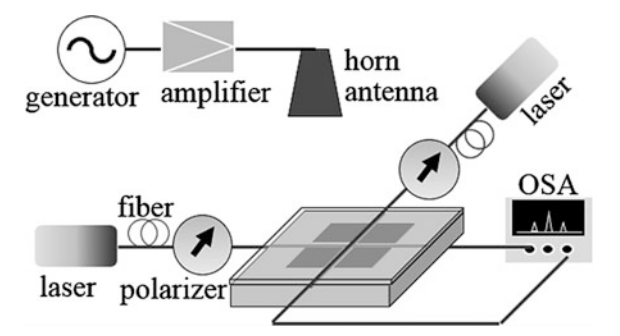
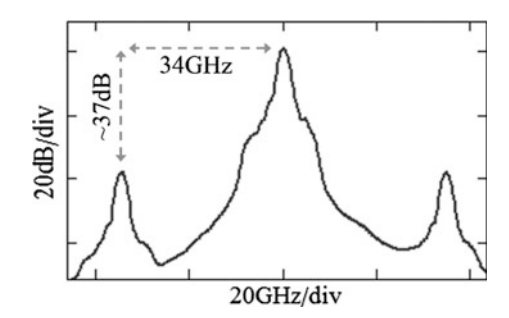
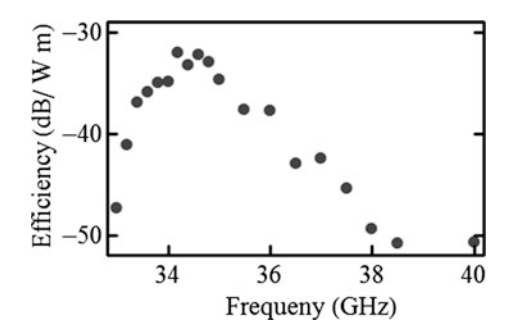


Fig. 6.13 Typical measured output light spectra from the orthogonal waveguides



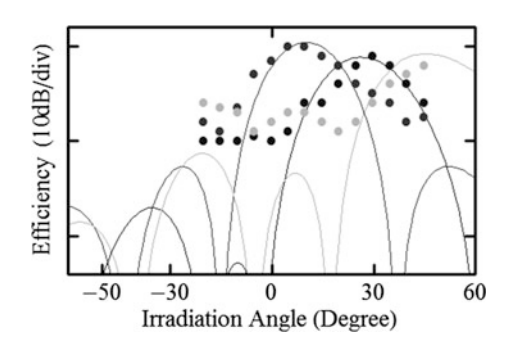
**Fig. 6.14** Measured modulation efficiency as a function of the millimeter-wave operational frequency



The measured modulation efficiency as a function of millimeter-wave frequency is shown by the dots in Fig. 6.14, when the irradiation angle of the free-space millimeter-wave signal was set to be normal to the device. The unit is expressed for power ratio between carrier and sidebands per millimeter-wave irradiation power and distance between the horn antenna and fabricated device. The measured peak frequency was about 34 GHz. It is slightly shifted than the designed operational frequency due to fabrication error such as EO crystal thickness, UV-adhesive glue thickness, and other parameters.

The dots in Fig. 6.15 show the measured modulation efficiency as a function of free-space irradiation angle in the yz-plane, when the frequency of the free-space

**Fig. 6.15** Measured modulation efficiency as a function of free-space millimeter-wave irradiation angles



millimeter-wave signal was set at 34 GHz. The largest modulation efficiency for certain free-space irradiation angle depends on meandering-gap patterns. The measured directivities are in good agreement with the calculation results.

#### 6.5 Fiber-Wireless Links

Figure 6.16 shows setup of Fi-Wi links using the LiNbO<sub>3</sub> modulators stacked to orthogonal-gap-embedded patch-antennas on low-k dielectric substrate. Millimeter-wave signal was generated by a signal generator, amplified by an amplifier, and irradiated to the devices by a horn antenna. The horn antenna was set with 45° rotation to the devices for generating dual linear polarization of free-space millimeter-wave signals. lightwave from lasers were coupled to the orthogonal optical waveguides using optical fibers directly. Optical polarizers were set for controlling polarization of lightwave since a z-cut LiNbO<sub>3</sub> optical crystal is used. Lightwave output were coupled with optical fibers and connected to an optical filter and amplifier. The optical filters were used for cutting one sideband and reducing ratio between optical carrier and sideband. Optical sidebands can be measured using optical spectrum analyzer. The filtered lightwave signals were amplified using optical amplifiers. The modulated lightwave were detected by high-speed photo-detectors for reconverting them to millimeter-wave signals. The reconverted millimeter-wave signals were measured using millimeter-wave spectrum analyzer or oscilloscope.

Typical measured optical sideband after pass through the optical filter is shown in Fig. 6.17 for 36 GHz millimeter-wave operational frequency. Clear optical single sideband was observed clearly with sideband and carrier power ratio of about 10 dB. Additionally, Fig. 6.18 shows the measured reconverted lightwave signals by high-speed photo detectors and the lightwave signals were observed using microwave spectrum analyzer. We can see that, about 30 dB carrier-to-noise ratio (CNR) was obtained in the Fi-Wi links using the fabricated device.

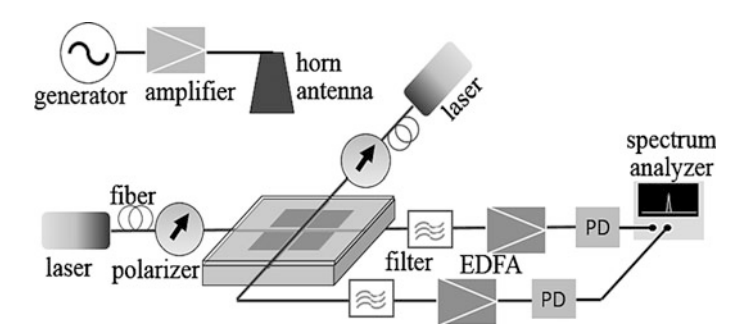


Fig. 6.16 Illustration of measurement setup for Fi-Wi links using the proposed device

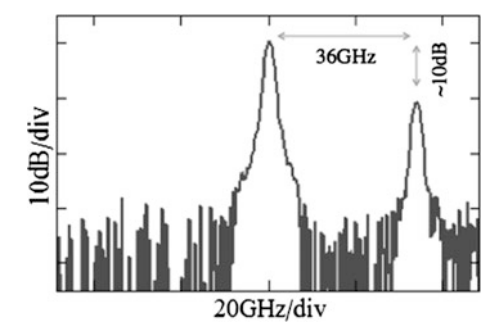


Fig. 6.17 Typical measured single sidebands passed through optical filters

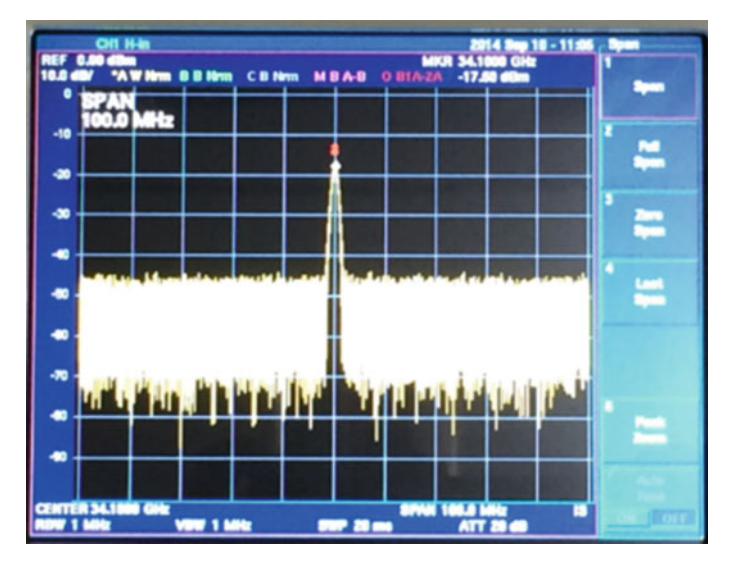
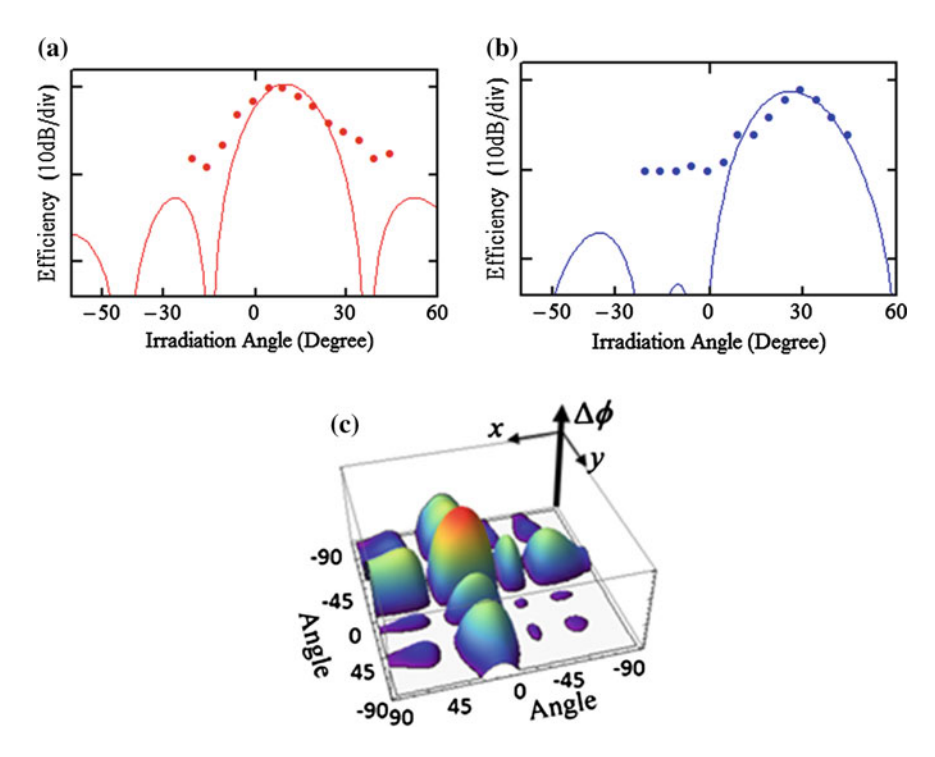


Fig. 6.18 The measured reconverted millimeter-wave signals using millimeter-wave spectrum analyzer

#### 6.6 Promising Device Functions and Applications

Optical millimeter-wave beam-steering using the proposed device was verified experimentally for 1-D in single plane (*xz*- or *yz*-planes). Based on that, 2-D beam-steering of the millimeter-wave in *xyz*-space can be obtained by considering the two orthogonal modulated lightwave. The 2-D beam-steering is analyzable by multiplying or comparing the modulated orthogonal lightwave from orthogonal optical waveguides [30].

Figure 6.19 shows the typical calculated 2-D optical millimeter-wave beam-steering for several variation of meandering gaps. 2-D beam-steering of the



**Fig. 6.19** Typical calculated 2-D millimeter-wave beam-steering using the designed device by considering two orthogonal 1-D millimeter-wave beam-steering

millimeter-wave can be discriminated for certain angles by considering designed patterns of the meandering-gaps. Furthermore, the 2-D beam-steering can be anacontinuously from each orthogonal optical waveguides. meandering-gap patterns of N along orthogonal optical waveguides in the x- and yaxes are set, N-square combinations of 2-D beam-steering can be obtained according the  $N \times N$  orthogonal modulated lightwave in N-patterns of the meandering-gaps. Therefore, the proposed device can be used for millimeter-wave beam-steering in 1-D or 2-D. Furthermore, the light inputs and outputs in the proposed device can be connected and integrated with low loss optical dividers and combiners, respectively [31, 32]. As results, the integrated devices with simple and compact structure can be realized for easy implementation.

Additionally, the proposed device is promising for application in directed free-space millimeter-wave communication such as MIMO, free-space backhaul, [33, 34]. It is illustrated in Fig. 6.20 where free-space millimeter-wave front-ends are connected by optical fibers. In the front-ends, the proposed device can be used for receiving millimeter-wave from free-space. It can be used for protection of optical fiber networks due to unwanted disaster or troubles as shown in Fig. 6.11a. The directed free-space communication for Multi-Input Multi-Output (MIMO) and Space-Division-Multiplexing-Access (SDMA) can be also realized using the

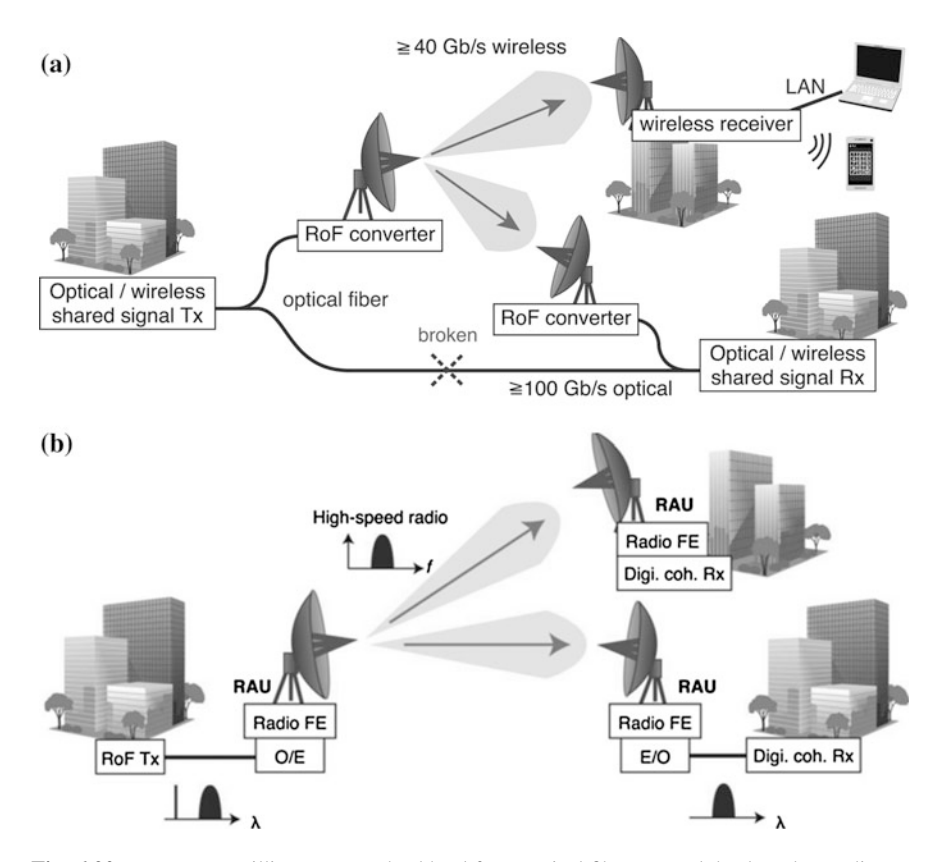


Fig. 6.20 Free-space millimeter-wave backhaul for a optical fiber network backup due to disaster and b MIMO free-space millimeter-wave links [33, 34]

proposed device as shown in Fig. 6.11b. In additional by considering requirement of the millimeter-wave beam-steering, the proposed device can be operated for 1-D or 2-D millimeter-wave beam-steering.

#### 6.7 Conclusion

We have proposed a free-space millimeter-wave electro-optic (EO) modulator using Quasi-Phase-Matching (QPM) gap-embedded-patch-antennas on a low dielectric constant substrate. A free-space millimeter-wave signal can be received and converted directly to a lightwave signal with the proposed device through EO modulation using the Pockels effect. Performance of the proposed device for operation in the millimeter-wave band was demonstrated experimentally. Double modulation efficiency can be obtained also since a QPM array structure is used. The proposed

device has a compact structure and can be operated with a low millimeter-wave signal loss and no external electrical power supply. Additionally, the proposed device can be operated for dual linear polarization or circular polarization of free-space millimeter-wave signals since orthogonal-gaps are used.

The proposed device is promising for broadband free-space (wireless/mobile) communication such as for MIMO and SDMA. It can be used also for precise measurement/sensing applications such as high-frequency Electromagnetic Compatibility (EMC) chamber and Radio Detecting and Ranging (RADAR). Additionally, the device performance for optical modulation can be enhanced using EO polymer and new structure with metamaterial [35, 36]. In the future, it is promising for application to integrated optical circuit and optical interconnect [37, 38].

**Acknowledgements** The authors would like thanks to Dr. T. Umezawa and Mr. S. Nakajima from National Institute of Information and Communications Technology (NICT) Japan and Dr. H. Shiomi from Osaka University Japan for their constructive comments and suggestions during discussion. Thanks to Dr. Y. Ogawa from NICT Japan for his helpful supports during device fabrication.

This research activity was partly supported financially by the Ministry of Internal Affairs and Communications, Japan, for the financial support partly thru the project entitled "Research and Development of high-precision imaging technology using 90 GHz band linear cells" funded by the "Research and Development to Expand Radio Frequency Resources."

#### References

- Abichar, Z., Peng, Y., Chang, J.: WiMAX: the emergence of wireless broadband. In: IEEE Computer Society, Vols. July–August, pp. 44–48 (2006)
- 2. Akyildiz, I.F., Gutierrez-Estevez, D.M., Reyes, E.C.: The evolution to 4G cellular systems: LTE-advanced. Phys. Commun. **3**, 217–244 (2010)
- 3. Lu, X., Wang, P., Niyato, D., Hossain, E.: Dynamic spectrum access in cognitive radio networks with RF energy harvesting. In: IEEE Wireless Communications, pp. 102–110 (2014)
- Mendeiros, H.P., Maciel, M.C., Sauza, R.D., Pellenz, M.E.: Lightweight data compression in wireless sensor networks using human coding. Int. J. Distrib. Sens. Netw. 2014(672921) (2014)
- Pi, Z., Khan, F.: An introduction to millieter-wave mobile broadband systems. IEEE Commun. Mag., 101–107 (2011)
- Armi, N., Arshad, M., Rizvi, A., Safdar, S., Yusoff, M.Z., Saad, M., Naufal, M.: Performance of opportunistic spectrum access with sensing error in cognitive radio ad hoc networks. J. Eng. Sci. Technol. 1–15 (2011)
- 7. Rec. ITU-R.: Attenuation of atmospheric gases, pp. 676–5 (2001)
- 8. Iezekiel, S.: Microwave photonics: devices and applications. Wiley, Chichester, UK (2009)
- 9. Nanzer, J.A.: Microwave and millimeter-wave remote sensing for security applications. Artech House (2012)
- 10. Shi, J., Huang, C., Pan, C.: Millimeter-wave photonic wireless links for very high data rate communication. NPG Asia Mat. 3, 41 (2011)
- Vidal, B., Nagatsuma, T., Gomes, N., Darcie, T.: Photonic technologies for millimeter- and submillimeter-wave signals. Adv. Opt. Technol. 2012, 925065 (2012)
- 12. Seeds, A.J.: Microwave photonics. IEEE Trans. Microw. Theory Tech. 50(3), 877–887 (2002)

- 13. Yao, J.: A tutorial on microwave photonics. IEEE Photon. Soc. Newlett., pp. 5-12 (2012)
- Watanabe, I., Nakata, T., Tsuji, M., Makita, K., Torikai, T., Taguchi, K.: High-speed, high-reliability planar-structure superlattice avalanche photodiodes for 10-Gb/s optical receivers. J. Lightwave Technol. 18(12), 2200–2207 (2000)
- Shinada, S., Kawanishi, T., Izutsu, M.: A resonant type LiNbO<sub>3</sub> optical modulator array with micro-strip antennas. IEICE Transac. Electron. E90-C(5), 1090–1095 (2007)
- Sheehy, F.T., Bridges, W.B., Schaffner, J.H.: 60 ghz and 94 ghz antenna-coupled linbo<sub>3</sub> electrooptic modulators. IEEE Photon. Technol. Lett. 5(3), 307–310 (1993)
- 17. Waterhouse, R.B., Novak, D.: Integrated antenna/electro-optic modulator for RF photonic front-ends. In: Proceedings of the IMS2011, WE2C-4, Baltimore-MD (2011)
- Bridges, W.B., Sheehy, F.T., Schaffner, J.H.: Wave-coupled LiNbO<sub>3</sub> modulator for microwave and millimeter-wave modulation. IEEE Photon. Technol. Lett. 3(2), 133–135 (1991)
- Murata, H., Miyanaka, R., Okamura, Y.: Wireless space-division-multiplexed signal discrimination device using electro-optic modulator with antenna-coupled electrodes and polarization-reversed sructures. Int. J. Microwave Wireless Technol. 4, 399–405 (2012)
- Murata, H., Kohmu, N., Wijayanto, Y.N., Okamura, Y.,: Integration of patch antenna on optical modulators. IEEE Photon. Soc. News., 28(2) (2014)
- Wijayanto, Y.N., Murata, H., Okamura, Y.: Novel electro-optic microwave-lightwave converters utilizing a patch-antenna embedded with a narrow gap. IEICE Electron. Exp. 8 (7), 491–497 (2011)
- 22. Wijayanto, Y.N., Murata, H., Kawanishi, T., Okamura, Y.: X-cut LiNbO<sub>3</sub> optical modulators using gap-embedded patch-antennas for wireless-over-fiber systems. Adv. Optical Technol. **2012**(Article ID 383212), 8 (2012)
- Wijayanto, Y.N., Kanno, A., Murata, H., Kawanishi, T. and Okamura, Y.: Millimeter-wave radar receiver using Z-cut LiNbO<sub>3</sub> optical modulator with orthogonal-gap-embedded patch-antennas on low-k dielectric material. IEICE Transac. Electron. E98-C(8), 783–792, (2015)
- 24. Yariv, A.: Quantum electronics, 3rd edn. Wiley, New York (1989)
- 25. Lefort, G., Razban, T.: Microstrip antennas printed on lithium niobate substrate. Electron. Lett. 33(9), 726–727 (1997)
- Gupta, V.R., Gupta, N.: Characteristics of a compact microstrip antenna. Microw. Optical Technol. Lett. 40(2), 158–160 (2004)
- Rodriguez-Berral, R., Mesa, F., Jackson, D.R.: Gap discontinuity in microstrip lines: an accurate semi analytical formulation. IEEE Trans. Microw. Theor. Tech. 59(6), 1441–1453 (2011)
- 28. Hu, H., Ricken, R., Sohler, W.: Low-loss ridge waveguides on lithium niobate fabricated by local diffusion doping with titanium. Appl. Phys. B **98**, 677–679 (2010)
- Uddin, M.A., Chan, H.P., Tsun, T.O., Chan, Y.C.: Uneven curing induced interfacial delamination of UV adhesive-bonded fiber array in V-Groove for photonic packaging. J. Lightwave Technol. 24(3), 1342–1349 (2006)
- Wijayanto, Y.N., Murata, H., Okamura, Y.: Electro-optic beam forming device using a two-dimensional array of patch-antennas embedded with orthogonal-gaps for millimeter-wave signals. In: IEEE Photonic Conference 2013, Seattle (2013)
- 31. Tao, S.H., Fang, Q., Song, J.F., Yu, M.B., Lo, G.Q., Kwong, D.L.: Cascade wide-angle Y-junction 1 × 16 optical power splitter based on silicon wire waveguides on silicon-on-insulator. Optics Exp. **16**(26), 21456–61 (2008)
- 32. Mahmudin, D., Maulana, Y.Y., Oktafiani, F., Daud, P., Wijayanto, Y.N.: Photonic beam-former based on micro-ring resonators for phased array antennas in radar applications. In: Proceeding on International Conference on Radar, Antenna, Microwave, Electronics and Telecommunications (ICRAMET), pp. 84–85, JW Marriott Hotel, 27–28 March 2013

- 33. Kanno, A., Inagaki, K., Morohashi, I., Sakamoto, T., Kuri, T., Iwao, H., Kawanishi, T., Yoshida, Y., Kitayama, K.: 40 Gb/s W-band (75–110 GHz) 16-QAM radio-over-fiber signal generation and its wireless transmission. Opt. Expr. 19, B56–B63 (2011)
- Kanno, A., Kuri, T., Hosako, I., Kawanishi, T., Yoshida, Y., Yasumura, Y., Kitayama, K.: Optical and millimeter-wave radio seamless MIMO transmission based on a radio over fiber technology. Opt. Expr. 20, 29395–29403 (2012)
- 35. Park, D.H., Pagán, V.R., Murphy, T.E., Luo, J., Jen, A.Y., Herman, W.N.: Free space millimeter wave-coupled electro-optic high speed nonlinear polymer phase moudlator with in-plane slotted patch antennas. Optical Expr. 23(7), 232525 (2015)
- 36. Wijayanto, Y.N., Kanno, A., Nakajima, S., Daud, P., Mahmudin, D. and Kawanishi, T.: Electrical-optical converter using electric-field-coupled metamaterial antennas on electro-optic modulator. In: Proceeding of PIERS 2015, Prague, Czech Republic, p. 2A8 (2015)
- 37. Marpaung, D., Roeloffzen, C., Heideman, R., Leinse, A., Sales, S., Capmany, J.: Integrated microwave photonics. Laser & Photon. Rev. 7(4), 506–538
- Malacarne, A., Gambini, F., Faralli, S., Klamkin, J., Poti, L.: High-speed silicon electro-optic microring modulator for optical interconnects. Photon. Technol. Lett., IEEE, 26(10) (2014)

# Chapter 7 An Efficient Optimization Problem for Modal Reflectivity at Optical Waveguide End-Facet Based on the Formulation of Characteristic Green's Function Technique

Abdorreza Torabi and Amir Ahmad Shishegar

Abstract A novel method to compute guided mode reflectivity from optical waveguide end-facet is presented in this paper. First, rational function fitting method (RFFM) is applied in characteristic Green's function (CGF) technique to find an approximate closed-form analytic expression for spatial Green's function of abruptly truncated slab waveguide. Then, derived closed-form relation along with the exact results of spatial Green's function, obtained by full wave solution, are incorporated in an efficient optimization problem. The fast Newton reflective method with trust region algorithm are utilized for optimized reflection coefficients of guided modes. The main advantage of the proposed CGF-RFFM method in comparison with the previous presented method based on CGF technique is its high accuracy and speed. Simple implementation of CGF-RFFM is also makes it superior to other approaches reported. Excellent agreements with rigorous are illustrated in several examples.

#### 7.1 Introduction

Optoelectric devices such as laser amplifier, optical modulator and coupler are widely used in integrated optics (IO) circuits. In these applications, facet reflectivity typically deviates the performance of the integrated system from its original designed target. The oldest accepted model for computation of facet reflectivity is Ikegami's model [1], which was introduced for double-heterojunction

A. Torabi (⊠)

School of Engineering, Faculty of Engineering Science, University of Tehran, Tehran, Iran e-mail: torabi@ee.sharif.edu

A.A. Shishegar

Department of Electrical Engineering, Sharif University of Technology, Tehran, Iran e-mail: shishegar@sharif.edu

<sup>©</sup> Springer International Publishing Switzerland 2016

P. Ribeiro and M. Raposo (eds.), Photoptics 2015,

(DH) GaAs-AlGaAs lasers. In this approach, with the use of eigenmode expansion, electric and magnetic fields are matched at the facet. In [2], an approximate modal reflectivity is developed by means of a plane wave Fresnel reflectivity expansion. Derived expressions are utilized in some other works related to two-dimensional (2-D) buried DH lasers [3]. These results are quite accurate but are just useful for low refractive index contrast. Gelin [4] extended Rozzi's variational treatment [5] for end-facet modal reflectivity and proposed an efficient numerical computation. The main challenge of mode matching based approach is the computation of time-consuming integrals which usually have singular integrands to contribute radiation modes. Moreover, finite window Fourier transform could be combined with perturbation series for fast computation of end-facet reflectivity [6]. An efficient way to regard the continuous spectrum contribution in mode matching method is using appropriate set of modes achieved by closing the desired structures with perfectly matched layers (PMLs) [7]. The main disadvantage of PML method is the considerable number of discrete modes must be considered to obtain for an appropriate accuracy. A different approach is utilizing iterative based methods. In [8], split-operator method is utilized and the interface of facet is divided into segments in such a way that within each segment the refractive index is nearly constant. The resulting contribution of each segment to the total reflected field is superimposed. Finally a linear iterative equation is obtained which can be solved by classical Neumann series or more stably by bi-conjugate gradient method [9]. In other iterative approach, reflection operator is diagonalized completely or partially [10] using the known eigenmodes and eigenvectors of square root operator. A separate class of solution methods employ Padé or complex Padé approximations to rational approximation of the square root operator [11–13]. Stability and convergence problem are the main challenges in this approach. For more rigorous solution, integral equation can be used. Parsa and Paknys [14] used equivalence principle and image theory and model the truncated semi-infinite dielectric slab waveguide by an infinite dielectric slab with unknown current density on a plane just at truncating surface of the end-facet which is solved by the method of moments (MoM). Coupling of the guided modes are incorporated in this method in the form of coupling matrix of end-facet.

In this paper a novel method for computation of guided modes reflectivity at the waveguide end-facet is presented. The proposed method is based on the characteristic Green's function (CGF) technique combined with rational function fitting method (RFFM) [15, 16]. Spatial Green's function of finite dielectric planar waveguide is obtained by separation of the structure into infinite 1-D layered media. For nonseparable structure like typical finite dielectric slab waveguide (i.e. DH laser), using separability assumption, an approximate and closed-form expression for spatial Green's function is achieved. The final formulation is utilized in an efficient optimization problem to find the exact facet reflection coefficients of guided modes. In contrary to previous reported CGF-complex images (CI) based method [17], in the formulation of CGF-RFFM continuous spectrum contribution are presented by some poles similar to guided modes part. Then unlike CGF-CI, in CGF-RFFM both discrete and continuous spectrum contributions are efficiently

incorporated in the optimization problem. Therefore more exact results of guided modes reflectivity can be obtained. This fact is shown in several examples. Simplicity of implementation as well as precision is the main advantage of the proposed method. Moreover, this method can be used for any planar dielectric waveguides with abrupt termination and also for any refractive index contrasts.

#### 7.2 CGF-RFFM Formulation

#### 7.2.1 CGF Technique and Separability Assumption

The 2-D Helmholtz's equation should be solved for Green's function of magnetic vector potential,  $A_z$ , for a line source surrounded by layered media as it is shown in Fig. 7.1a. Here for simplicity the derivations are developed for truncated dielectric slab waveguide shown in Fig. 7.1b for simplicity while the implementation for multilayered media (Fig. 7.1a) is straightforward. The 2-D Helmholtz's equation can be separated into two 1-D equations if [18, 19]

$$\varepsilon_r(x, y) = \varepsilon_x(x) + \varepsilon_y(y).$$
 (7.1)

By the assumption of (7.1), the original structure has been decomposed into two layered media denoted by  $N_x$  and  $N_y$  layered media (Fig. 7.2a, b,  $N_\gamma$  called *normal* to  $\gamma$  where  $\gamma = x, y$ ), which their relative dielectric constants are  $\varepsilon_x(x)$  and  $\varepsilon_y(y)$  respectively. If this separation is rigorously possible, it means that the original structure, Fig. 7.1b, can be exactly reproduced by crossing two 1-D  $N_x$  and  $N_y$  layered media which is shown in Fig. 7.2c. The solutions to the 1-D Helmholtz's equations are denoted by  $G_x$  (for Fig. 7.2a) and  $G_y$  (for Fig. 7.2b) and can be obtained analytically using usual spectral techniques [20]. We will have,

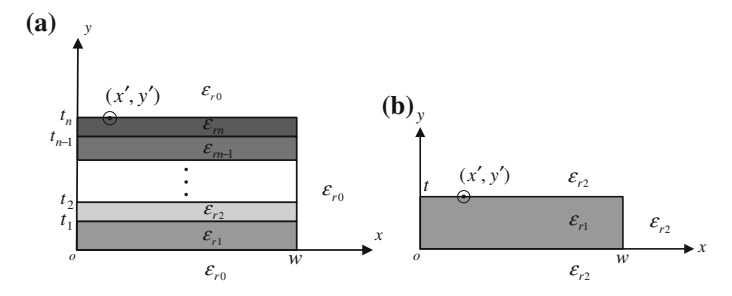


Fig. 7.1 A line source on a truncated a multilayered b slab waveguide

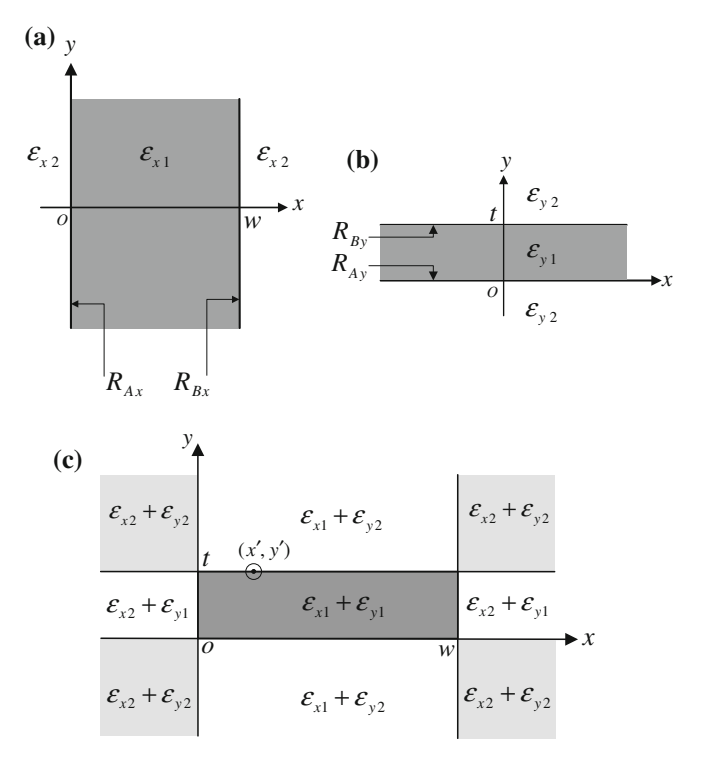


Fig. 7.2 a  $N_x$  and b  $N_y$  layered media, c separable structure analyzed instead of original structure in CGF technique

$$G_{\gamma}(\gamma, \gamma') = \frac{\left(1 + R_{\gamma}e^{-j2\beta_{\gamma 1}\gamma_{<}}\right)\left(1 + R_{\gamma}e^{-j2\beta_{\gamma 1}\left(\mathbf{d}_{\gamma} - \gamma_{>}\right)}\right)e^{-j\beta_{\gamma 1}(\gamma_{>} - \gamma_{<})}}{(2j\beta_{\gamma 1})\left(1 - R_{\gamma}^{2}e^{-j2\beta_{\gamma 1}\mathbf{d}_{\gamma}}\right)}, \tag{7.2}$$

$$R_{\gamma} = \frac{\beta_{\gamma 1} - \beta_{\gamma 2}}{\beta_{\gamma 1} + \beta_{\gamma 2}},\tag{7.3}$$

where  $d_{\gamma}$  is equal to w and t for  $\gamma = x$  and y respectively.  $\gamma_{>}$  and  $\gamma_{<}$  are greater and smaller values of  $\gamma$  and  $\gamma'$  respectively and  $\beta_{\gamma i} = \sqrt{\epsilon_{\gamma i}k_0^2 + \lambda_{\gamma}}$  (i = 1, 2).  $R_x$  and  $R_y$  are the reflection coefficients of a TE wave at the interfaces (due to the symmetry  $R_{Ax} = R_{Bx} = R_x$  and  $R_{Ay} = R_{By} = R_y$  in Fig. 7.2). Then having  $G_x$  and  $G_y$ , the solution of  $A_z$  for separable structure of Fig. 7.2c is given by [18, 19]

$$A_{z}(x,y;x',y') = \left(\frac{-1}{2\pi i}\right) \oint_{C_{\lambda}y} G_{x}(x,x',-\lambda_{y}) G_{y}(y,y',\lambda_{y}) d\lambda_{y}, \tag{7.4}$$

where the contour  $C_{\lambda}y$ , encloses only the singularities of  $G_y$ , (including branch cut, branch point and discrete poles singularities), in counterclockwise sense. For the structure at hand, Fig. 7.1b, it can be shown that the separation of 1, is not rigorously possible [19]. If one ignore (7.1) in four exterior regions in Fig. 7.2c, then an infinite number of solutions for  $\varepsilon_{x1}$ ,  $\varepsilon_{x2}$ ,  $\varepsilon_{y1}$  and  $\varepsilon_{y2}$  could be found. It must be noted that the solutions are not physically available relative dielectric constants. They are just mathematical quantities. One can choose  $\varepsilon_{x1} = 0$ ,  $\varepsilon_{x2} = \varepsilon_{r2} - \varepsilon_{r1}$ ,  $\varepsilon_{y1} = \varepsilon_{r1}$ ,  $\varepsilon_{y2} = \varepsilon_{r2}$  for  $N_x$  and  $N_y$  media. For all possible solutions, the corner regions of the original structure are replaced by  $\varepsilon_x 2 + \varepsilon_y 2 = 2\varepsilon_r 1 - \varepsilon_r 2$  [19]. This deviation makes the CGF result in (7.4) an approximate Green's function for original structure (Fig. 7.1b). It should be noted that for multilayered truncated waveguide (with n layers) of Fig. 7.1a, after separation, the  $N_y$  layered media would be a 1-D infinite layered media (with n layers) while  $N_x$  media would be the same as Fig. 7.2a. So it is just sufficient that  $G_y$  of related  $N_y$  layered media is computed analytically and incorporated in integral representation of (7.4).

#### 7.2.2 *CGF-RFFM*

In common optical waveguide structures, t is much smaller than w. So, with acceptable approximation, guided modes (surface wave poles) of CGF  $G_y$  (Fig. 7.2b) denote the guided modes of the original structure in Fig. 7.1b. Furthermore, the integration of (7.4) in CGF technique is so time consuming and expensive due to highly oscillatory nature of its integrand. To circumvent the numerical integration of (7.4), rational function fitting method can be used. In CGF-RFFM the  $G_y$  is first approximated by appropriate set of discrete poles via modified VECTFIT algorithm [16]. Like,

$$G_{y}(y, y', \lambda_{y}) \approx \sum_{m=1}^{N_{p}} \frac{\text{Res}_{m}}{\lambda_{y} - \lambda_{ym}}$$
 (7.5)

where  $\operatorname{Res}_m$  is the residue of  $G_y$  at the mth pole.  $N_p$  is the number of poles used in RFFM for rational fitting. It should be noted that the set of extracted poles in (7.5) includes guided modes of the structure. Moreover, some other poles are also extracted that are responsible to construct the continuous spectrum contribution. Therefore, these poles have similar characteristic to leaky wave poles and so we may call them quasi leaky wave poles [16]. Then by substituting (7.5) in (7.4) and applying residue theorem, a closed form series representation for  $A_z$  will be obtained and can be found by (7.6). In (7.6),  $k_{xm} = \sqrt{\varepsilon_{x1}k_0^2 - \lambda_{ym}}$  is the propagation constant of the mth mode in the x-direction. Since the rational function fitting of 5 would have excellent accuracy, therefore a closed form relation of 6 can approximate the integral of 4 very well.

$$A_{z} = \sum_{m=1}^{N_{p}} -\text{Res}_{m} \frac{\left(1 + R_{x} m e^{-j2k_{x} m x_{<}}\right) \left(1 + R_{x} m e^{-j2k_{x} m (w-x_{>})}\right) e^{-jk_{x} m (x_{>} - x_{<})}}{(2jk_{x} m) \left(1 - R_{xm}^{2} e^{-j2k_{x} m w}\right)}, \quad (7.6)$$

$$A_{z} = A_{z}^{g} + A_{z}^{r},$$

$$A_{z}^{g} = \sum_{m=1}^{N_{SW}} -\text{Res}_{m} \frac{\left(1 + R_{x}me^{-j2k_{x}mx_{<}}\right)\left(1 + R_{x}me^{-j2k_{x}m(w-x_{>})}\right)e^{-jk_{x}m(x_{>}-x_{<})}}{(2jk_{x}m)\left(1 - R_{xm}^{2}e^{-j2k_{x}mw}\right)},$$

$$A_{z}^{r} = \sum_{m=1}^{N_{qLW}} -\text{Res}_{m} \frac{\left(1 + R_{x}me^{-j2k_{x}mx_{<}}\right)\left(1 + R_{x}me^{-j2k_{x}m(w-x_{>})}\right)e^{-jk_{x}m(x_{>}-x_{<})}}{(2jk_{x}m)\left(1 - R_{xm}^{2}e^{-j2k_{x}mw}\right)},$$
(7.7)

We can separate  $A_z$  of (7.6) in two terms like (7.7) where  $A_z^g$  denotes the guided modes part (or discrete spectrum contribution) and is in series form of (7.6) in which just guided modes (with number  $N_{SW}$ ) contributes while  $A_z^r$  related to radiation modes part (or continuous spectrum contribution) and is in series form of (7.6) in which the non surface wave poles (quasi leaky wave poles with number  $N_{qLW}$ ) contributes.

In (7.6),  $R_{xm}$  is the reflection coefficient of modes at the  $N_x$  interface shown in Fig. 7.3a. But actually, these modes are reflected from truncated surface of the substrate shown in Fig. 7.3b. This discrepancy arises from the separability approximation of the original structure which also makes the refractive index of four exterior corners deviate from its exact value. For low refractive index contrast,  $\varepsilon_{r1} \approx \varepsilon_{r2}$ , as is common in optical buried waveguides, the error in  $A_z$  due to approximate modeling of the corner regions is ignorable because  $2\varepsilon_{r2} - \varepsilon_{r1} \approx \varepsilon_{r2}$ . But in high refractive index contrasts, considerable deviation may be imposed on the Green's function especially for source and field points close to the corners. Therefore to have exact  $A_z$  for truncated dielectric slab waveguide of Fig. 7.1b both terms  $A_z^g$  and  $A_z^r$  should be corrected. Although having enough distance from corners for source and field point makes the deviation in  $A_z^r$  part small but for more

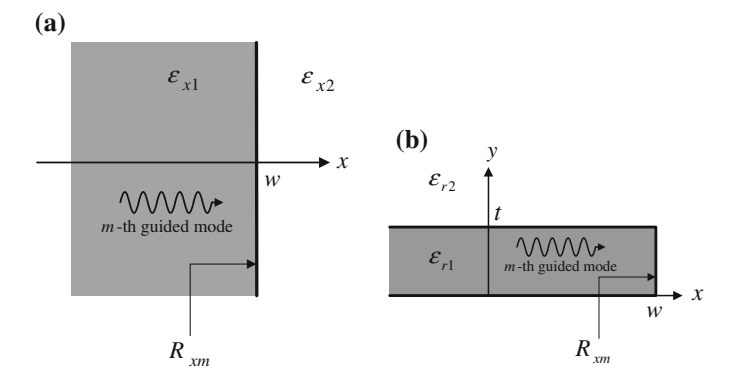


Fig. 7.3 Reflection of mth SW at the a interface of  $N_x$  structure, and b end-facet

accurate results of reflection coefficients of guided modes, correction of  $A_z^r$  part along with  $A_z^g$  part should be considered. Before defining the optimization problem, it should be noted that the main difference between proposed CGF-RFFM and CGF-CI method [17] is in the approximation form of  $G_y$ . In CGF-CI the surface wave poles are first extracted from  $G_y$  in a similar form of (7.5) and the remaining part is approximated exponentially by GPOF approach [21]. In fact by CGF-RFFM, unlike CGF-CI, a uniform representation of  $G_y$  as well as  $A_z$  can be achieved and it will be shown that it leads to more accurate results of reflection coefficients.

#### 7.3 Optimization Problem

Exact values of  $A_z$  for field points  $(x_i, y_i)$ ,  $i = 1, 2, ..., N_f$  can be achieved by CAD tools like COMSOL which is fast and accurate and are capable of solving 2-D problem like Fig. 7.1. Moreover, exterior-interior method of moments (MoM) can be used for problem of Fig. 7.1 to find exact  $A_z$  [18]. Consider the field distribution on the upper surface of the waveguide, y = t, in Fig. 7.1b. The line source is located at x' = w/2 and y' = t. Suppose that the exact result of  $A_z$  is denoted by  $A_z^{exact}$ . If we consider  $R_{xm}$ ,  $m = 1, 2, ..., N_p$  in (7.6) as unknowns, then a following optimization problem can be defined for computation of the exact  $R_{xm}$  at the end-facets of truncated slab shown in Fig. 7.1

$$\min_{\substack{R_{xm},\\m = 1, 2, ..., N_p.}} f_{\text{error}}(R_{x1}, R_{x2}, ..., R_{xN_p}), \tag{7.8}$$

$$f_{\text{error}} = \sum_{i=1}^{N_f} |A_z(x_i, y_i; x', y'; R_{x1}, R_{x2}, \dots, R_{xN_p}) - A_z^{exact}(x_i, y_i; x', y')|^2.$$
 (7.9)

To solve the optimization problem, subspace trust-region algorithm is used which is based on the interior-reflective Newton method described in [22]. By increasing the number of field points,  $N_f$ , more exact  $R_{xm}$ s will be obtained. For initial values of  $R_{xm}$ s, one can use  $\frac{\beta_{x1}-\beta_{x2}}{\beta_{x1}+\beta_{x2}}|_{\lambda_y=\lambda_{ym}}$  for  $R_{xm}$ , obtained in CGF method (7.3). More rapid convergence and rigorous results can be obtained by using modified initial values of  $R_{xm}$  such as Marcateli's approximation  $R_{xm}=\frac{n_m-n_2}{n_m+n_2}$  where  $n_2=\sqrt{\varepsilon_{r2}}$  and the effective index  $n_m$  is calculated from the propagation constant of  $N_y$  guided mode. i.e.  $n_m=\frac{k_{xm}}{k_0}$ . More accurate closed-form expression for  $R_{xm}$  can be found in [2].

The main advantage of using CGF-RFFM is that all extracted poles can incorporate in the optimization problem of (7.7). While in CGF-CI method [17] the part of continuous spectrum contribution ( $A_z^{CS}$  in [15]) which is related to approximate separable structure of Fig. 7.2c is first subtracted by exact  $A_z$  and the remained part

is used to optimized discrete spectrum contribution to find  $R_{xm}$  of guided modes. Therefore in (7.8) both discrete and continuous spectrum parts would be corrected by optimizing all the  $R_{xm}$  of extracted poles including guided and quazi-leaky wave poles. This is in fact due to the capability of the rational function fitting method to obtain uniform expansion of  $A_z$  in (7.5). So it is expected that more accurate  $R_{xm}$  of guide modes could be found by CGF-RFFM than CGF-CI method. Although the time of optimization process would be increased due to more poles incorporated in 8 but results of next section shows that this is ignorable in comparison with the gained accuracy.

#### 7.4 Numerical Results

To show the efficiency and versatility of the proposed approach rigorous methods such as mode matching is utilized [4]. More, CGF-CI-optimization [17] results are also provided. RFFM step which includes poles extraction from  $G_{\nu}$  can be so fast. Then, to have exact reflection coefficients, optimization step should be run for  $N_f$ sample field points [0, w] where the exact  $A_z$  are available there. We place the source far from the corners to have more exact results from CGF-RFFM in (7.6). More it should be noted here that in CGF-CI based method a guard  $d_s$  is considered and the samples are chosen in  $[d_s, w - d_s]$ . This is due to the fact that contribution of continuous spectrum of separable structure, Fig. 7.2c, largely deviates from its original value for nonseparable structure, Fig. 7.1b, especially near the corners. But in CGF-RFFM there is no need for any guard because continuous spectrum contribution is also incorporated and corrected in the optimization process along with discrete spectrum contribution. It should be noted that Green's function  $A_z$  includes only TE guided modes of the Fig. 7.1b. Therefore by using and incorporating  $A_z$  in defined optimization problem, reflection coefficients of TE guided modes can be obtained. To have results for TM guided modes one can easily use Green's function of scalar or vector electric potential and follow the similar steps.

At first, let us consider low refractive index contrasts. Results for reflection coefficient of guided mode for structure 1 and 2 with parameters ( $n_1 = 1.46$ ,  $n_2 = 1.45$ ,  $t = 0.1\lambda$ ) and ( $n_1 = 2.6$ ,  $n_2 = 2.5$ ,  $t = 0.1\lambda$ ) respectively, are shown in Table 7.1.

Simulation results for higher refractive index contrast are also reported in Table 7.1 for structures 3, 4, 5 which have single guided mode. We can find excellent agreement between proposed method and rigorous mode matching method [4]. For single guided mode supported waveguide considered in Table 7.1, mean simulation time for optimization is less than 4 s. Disregarding the time for preprocessing of the structure to find the exact  $A_z$ , our method is much faster than mode matching method. Furthermore, by adding required time of step 1 (which is approximately 8 s in COMSOL for high accuracy), total CPU-time would still be less than mode matching method. moreover, it can be seen from Table 7.1 that

	100	$n_1$	$n_2$	CGF-RFFM-optimization	CGF-CI-optimization	Reference [4]
Structure 1	0.1	1.46	1.45	-0.760 + j0.038	-0.735 + j0.088	-0.761 + j0.039
Structure 2	0.1	2.6	2.5	-0.468 - j0.372	-0.472 - j0.379	-0.468 - j0.372
Structure 3	0.1	4.472	1	0.688 + j0.232	0.672 + j0.228	0.688 + j0.231
Structure 4	0.166	4.472	1	0.716 + j0.151	0.711 + j0.142	0.718 + j0.155
Structure 5	0.08	5.477	1	0.651 + j0.396	0.649 + j0.391	0.651 + j0.399
Mean time	-	_		\$ \$ \times \$ \$ \times \$ \$ \$ \$ \$ \$	\$ 2 s	> 8 min

CGF-RFFM leads to more accurate results in comparison with CGF-CI results. For rational function fitting step of (7.5),  $N_p = 14$  poles are used in modified VECTFIT algorithm.

The number of observation points  $N_f$  may be an important parameter in controlling the speed and accuracy of the method. In Table 7.2, amplitude of optimized  $R_{xm}$  for two of considered structures in Table 7.1 can be found for different  $N_f$ . Small changes in optimized reflection coefficient can be seen, by increasing  $N_f$ . It can be concluded that with small  $N_f$ , quite exact reflection coefficient with high speed can be obtained. In Table 7.3, Reflection coefficients for a structure with parameter  $(n_1 = 5.477, n_2 = 1, t = 0.19\lambda)$  that has three guided TE modes are reported. Excellent match between the results of CGF-RFFM-optimization and IE-MoM can be found [14]. Required simulation time for optimization is near to 8 s which is much less than exact IE-MoM based method.

To search the versatility of the proposed method let us consider a problem of modal reflectivity at end-facet of of three-layer media of Fig. 7.4. The refractive

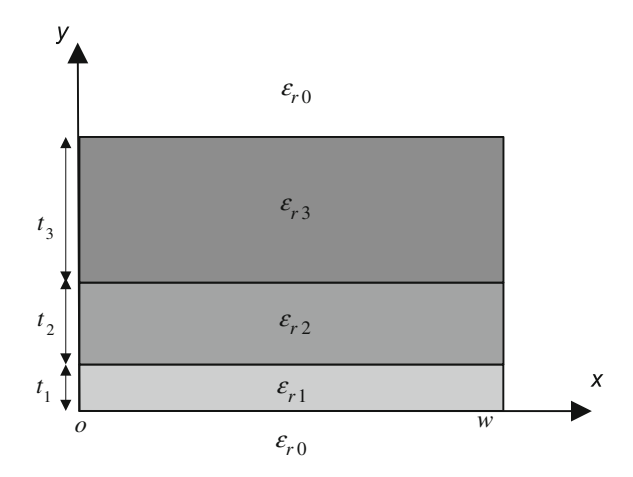
**Table 7.2** Amplitude of optimized  $R_{x1}$  for structure 4 and 5 for different number of observation points  $N_f$ 

$N_f$	$ R_{x1} $ of Structure 4	$ R_{x1} $ of Structure 5
150	0.723	0.759
200	0.726	0.762
250	0.728	0.764
300	0.728	0.765

**Table 7.3** Reflection coefficients for structure shown in Fig. 7.1 with  $n_1 = 5.477$ ,  $n_2 = 1$ ,  $t = 0.19\lambda$ ,  $w = 2\lambda$ ,  $N_f = 200$ 

$R_{xm}$	CGF-RFFM-optimization	IE-MoM [14]
$R_{x1}$	-0.263 + j0.654	-0.263 + j0.752
$R_{x2}$	0.443 + j0.758	0.443 + j0.759
$R_{x3}$	0.315 + j0.841	0.315 + j.841
Time	<8 s	>6 min

**Fig. 7.4** Three layer truncated dielectric slab waveguide



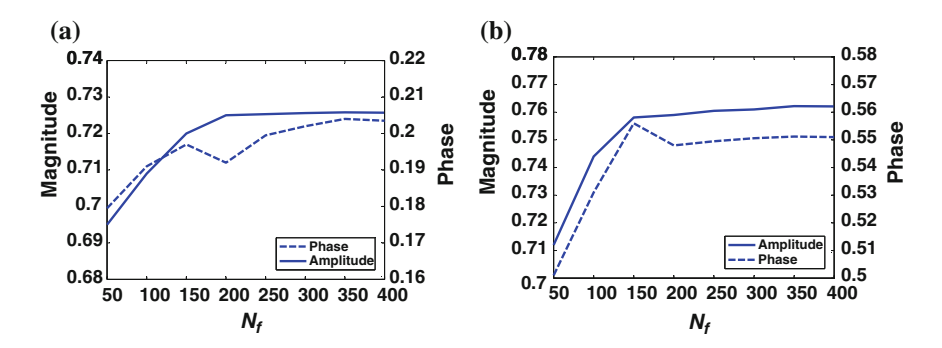


Fig. 7.5 Convergence of magnitude and phase of optimized a  $R_{x1}$  and b  $R_{x2}$ , for different  $N_f$  for structure of Table 7.4

**Table 7.4** Reflection coefficients for structure shown in Fig. 7.4 with  $n_1 = 1.132$ ,  $n_2 = 2.449$ ,  $n_3 = 3.162$ ,  $n_0 = 1$ ,  $t_1 = 0.1\lambda$ ,  $t_2 = 0.2\lambda$ ,  $t_3 = 0.4\lambda$ ,  $w = 2\lambda$ , for  $N_f = 200$  observation points using CGF-RFFM-optimization, CGF-CI-optimization [17] with  $d_s = w/10$ , and mode matching methods [4]

$R_{xm}$	CGF-RFFM-optimization	CGF-CI-optimization	Reference [4]
$R_{x1}$	0.295 + j0.717	0.286 + j0.722	0.293 + j0.716
$R_{x2}$	0.753 + j0.107	0.721 + j0.085	0.755 + j0.109
Time	<10 s	<5 s	>10 min

Mean time for computation of  $A_{\tau}^{exact}$  by COMSOL is less than 8 s

indices of layers are  $n_1 = 1.132$ ,  $n_2 = 2.449$ ,  $n_3 = 3.162$ ,  $n_0 = 1$ , with thickness of  $t_1 = 0.1\lambda$ ,  $t_2 = 0.2\lambda$ ,  $t_3 = 0.4\lambda$  that leads to two supporting guided modes. Results for reflection coefficient of guided modes obtained by CGF-RFFM-optimization are reported in Table 7.4 along with the results of CGF-CI-optimization and mode matching method are also given.  $N_p = 16$  poles are considered for rational function fitting step of (7.5). In comparison with CGF-CI-optimization results excellent match between CGF-RFFM results and exact mode matching method [4] is evident. Moreover, from Table 7.1 and Table 7.2, increasing in simulation time of CGF-RFFM due to incorporation of more poles in optimization step is ignorable. The number of observation points  $N_f$  has marginal effects on the speed and accuracy of the method. In Fig. 7.5a, b magnitude and phase of the optimized  $R_{x1}$  and  $R_{x2}$  for structure of Fig. 7.4 (described in Table 7.4) are depicted for  $N_f$ . Good convergence can be seen in the optimized reflection coefficients, by increasing  $N_f$ .

#### 7.5 Conclusion

A novel method for reflection of guided mode at the end-facet of optical waveguide is presented. The method is based on the formulation of characteristics Green's function which is combined with rational function fitting method. In the

closed-form derivation for spatial Green's function of finite dielectric slab waveguide, discrete and continuous spectrum contribution are expressed in appropriate forms which can be imported in optimization problem to obtain an exact reflection coefficients of guided modes. The main advantages of this method lie in its rapidity as well as accuracy. By using COMSOL for exact results of spatial Green's function for optimization, total CPU-time is much less than rigorous methods. In general, for all planar multilayered waveguide the formulation can be easily derived for all components of dyadic Green's function to have reflection coefficients of guided modes at the end-facet of truncation.

#### References

- Ikegami, T.: Reflectivity of mode at facet and oscillation mode in double-heterostructure injection lasers. IEEE J. Quantum Electron. 8(6), 470–476 (1972). doi:10.1109/JQE.1972. 1077091
- Lewin, L.: A method for the calculation of the radiation-pattern and mode-conversion properties of a solid-state heterojunction laser. IEEE Trans. Microw. Theory Techn. 23(7), 576–585 (1975). doi:10.1109/TMTT.1975.1128629
- 3. Hardy, A.: Formulation of two-dimensional reflectivity calculations for transverse-magnetic-like modes. J. Opt. Soc. Am. A 1(7), 760–763 (1984)
- Gelin, P., Petenzi, M., Citerne, J.: Rigorous analysis of the scattering of surface waves in an abruptly ended slab dielectric waveguide. IEEE Trans. Microw. Theory Techn. 29(2), 107– 114 (1981). doi:10.1109/TMTT.1981.1130304
- Rozzi, T., Veld, G.: Variational treatment of the diffraction at the facet of d.h. lasers and of dielectric millimeter wave antennas. IEEE Trans. Microw. Theory Techn. 28(2), 61–73 (1980). doi:10.1109/TMTT.1980.1130012
- Chen, Y., Lai, Y., Chong, T.C., Ho, S.T.: Exact solution of facet reflections for guided modes in high-refractive-index-contrast sub-wavelength waveguide via a fourier analysis and perturbative series summation: derivation and applications. J. Lightw. Technol. 30(15), 2455–2471 (2012). doi:10.1109/JLT.2012.2200876
- Derudder, H., Olyslager, F., De Zutter, D., van den Berghe, S.: Efficient mode-matching analysis of discontinuities in finite planar substrates using perfectly matched layers. IEEE Trans. Antennas Propag. 49(2), 185–195 (2001). doi:10.1109/8.914270
- 8. Yevick, D., Bardyszewski, W., Hermansson, B., Glasner, M.: Split-operator electric field reflection techniques. IEEE Photon. Technol. Lett. **3**(6), 527–529 (1991). doi:10.1109/68.
- 9. Wei, S.H., Lu, Y.Y.: Application of Bi-CGSTAB to waveguide discontinuity problems. IEEE Photon. Technol. Lett. 14(5), 645–647 (2002). doi:10.1109/68.998712
- Yevick, D., Bardyszewski, W., Hermansson, B., Glasner, M.: Lanczos reduction techniques for electric field reflection. J. Lightw. Technol. 10(9), 1234–1237 (1992). doi:10.1109/50. 156874
- El-Refaei, H., Betty, I., Yevick, D.: The application of complex Pade approximants to reflection at optical waveguide facets. IEEE Photon. Technol. Lett. 12(2), 158–160 (2000). doi:10.1109/68.823502
- Jamid, H., Khan, M.: 3-D full-vectorial analysis of strong optical waveguide discontinuities using Pade approximants. IEEE J. Quantum Electron. 43(4), 343–349 (2007). doi:10.1109/ JQE.2007.893007
- 13. Yu, C., Yevick, D.: Application of the bidirectional parabolic equation method to optical waveguide facets. J. Opt. Soc. Am. A **14**(7), 1448–1450 (1997)

- Parsa, A., Paknys, R.: Interior Green's function solution for a thick and finite dielectric slab. IEEE Trans. Antennas Propag. 55(12), 3504–3514 (2007). doi:10.1109/TAP.2007.910367
- Torabi, A., Shishegar, A.A., Faraji-Dana, R.: Application of the characteristic Green's function technique in closed-form derivation of spatial Green's function of finite dielectric structures. Computat. Electromagnet. Workshop (CEM) 2013, 54–55 (2013). doi:10.1109/ CEM.2013.6617132
- Torabi, A., Shishegar, A.A., Faraji-Dana, R.: An efficient closed-form derivation of spatial Green's function for finite dielectric structures using characteristic Green's function-rational function fitting method. IEEE Trans. Antennas Propagat. 62(3) (2014)
- Torabi, A., Shishegar, A.A., Faraji-Dana, R.: Analysis of modal reflectivity of optical waveguide end-facets by the characteristic Green's function technique. J. Lightw. Technol. 32 (6), 1168–1176 (2014)
- 18. Faraji-Dana, R.: An Efficient and Accurate Green's Function Analysis of Packaged Microwave Integrated Circuits. Ph.D. thesis, University of Waterloo (1993)
- Shishegar, A.A., Faraji-Dana, R.: A closed-form spatial Green's function for finite dielectric structures. Electromagnetics 23(7), 579–594 (2003)
- Michalski, K., Mosig, J.: Multilayered media Green's functions in integral equation formulations. IEEE Trans. Antennas Propagat. 45(3), 508–519 (1997). doi:10.1109/8. 558666
- Hua, Y., Sarkar, T.: Generalized pencil-of-function method for extracting poles of an EM system from its transient response. IEEE Trans. Antennas Propag. 37(2), 229–234 (1989). doi:10.1109/8.18710
- 22. Coleman, T.F., Li, Y.: An interior trust region approach for nonlinear minimization subject to bounds. SIAM J. Optim. **6**(2), 418–445 (1996)

#### Chapter 8

# Effect of Exponentially Graded Material on Photonic and Omni-Directional Band Gaps in 1-D Photonic Crystals

Bipin Kumar Singh and Praveen Chandra Pandey

**Abstract** Photonic and Omni-directional band gaps have been obtained for one-dimensional (1-D) photonic crystal consists of exponential graded index material and constant refractive index material in range 150–750 THz of electromagnetic radiation. Transfer matrix method has been used for calculation of reflectance. The number of photonic band gaps and their bandwidths has been tuned by changing relative parameters, thickness of exponentially graded material and angle of incidence. This work will be useful in design of filters, optical sensors, reflectors etc., and provide more design freedom for alternative photonic devices.

#### 8.1 Introduction

The propagation of light through a periodic medium has been widely studied since the appearance of photonic crystal (PC) materials [1]. PCs are structures composed of two or more materials with different refractive index and arranged in a periodic configuration that forbids the propagation of electromagnetic waves in certain frequency ranges. This leads to a range of frequency where no electromagnetic mode exists inside of the PCs, is called photonic band gap, which is analogous to the electronic band gap in conventional semiconductors [2]. This property can be utilized to confine, manipulate and control of photons in PCs, and anticipated that would be a key technology for all integrated optical devices [3]. Over the past several years, 1-D PCs have been intensively investigated with different materials such as dielectric, anisotropic, negative refractive index, magnetic materials etc. in periodic or non-periodic arrangements [4–11]. These have numerous potential applications in optical communication and optoelectronics such as reflecting mirrors,

B.K. Singh  $\cdot$  P.C. Pandey  $(\boxtimes)$ 

Department of Physics, Indian Institute of Technology (Banaras Hindu University), Varanasi 221005, India

e-mail: pcpandey.app@iitbhu.ac.in

B.K. Singh

e-mail: bipinksingh.rs.app@iitbhu.ac.in

waveguides, optical switches, filters, detectors, limiters, light emitting diode etc. Moreover, one of the very interesting property of the PCs is Omni-directional reflection by which light within some frequency region from all of the incident angle is totally reflected for both of the TE (Transverse electric) and TM (Transverse magnetic) polarization. The absolute Omni-directional photonic band gap has been demonstrated theoretically and experimentally in 1-D PC structures [12–15]. The Omni-directional band gap has potential applications in reflectors, filters and optical fibers etc.

Recently, several other researchers have been proposed the photonic crystal structures, in which structural parameters changed in the gradual fashion. Such types of structures are called graded photonic crystals (GPCs). In one-dimensional GPC structures, gradual variations of the relative parameters such as refractive index and thickness of layers varies in a gradual fashion along the direction perpendicular to the surface of layer [16–20]. Gradual variation of relative parameters in GPCs makes them very different in behavior from conventional PCs and enhances the ability to mold and control of the light wave propagation. Graded index materials in one dimensional quasi-periodic photonic crystal have great influence on the optical reflectance and localization modes [21–23].

Motivated by the ability to mold, confine and control of the electromagnetic waves by different types of GPCs. Herein, we have studied the photonic and Omni-directional band gap characteristics in 1-D GPCs constituted with exponentially graded dielectric layer. Refractive index in exponentially graded layers varies in the exponential fashion as a function of the depth of graded layer. This paper is arranged as follows. In Sect. 8.2, the theory and calculations of the reflectance and band structure of 1-D GPC structures are provided. In Sect. 8.3, we have investigated the influence of exponentially graded layers on the photonic and Omni-directional band gap properties of 1-D GPC structures. We have also investigated the effect of constituted homogeneous layer on the photonic and Omni-directional band gaps. In this Section, our study has been carried out in three steps. First, we have presented the reflection spectra and band structure of 1-D GPC structures for different layer thicknesses and various refractive index of the constituted normal layer. Second, we have investigated the properties of Omni-directional band gap for quarter-wave and latent type layer stacking arrangements, and demonstrated the effect of constituted homogeneous layer on Omni-directional band gap. Next, we have studied the effect of the contrast of initial and final refractive index of the exponential graded layer on the photonic band gap of the structures. Finally, we have briefly summarized the results in Sect. 8.4.

#### **8.2** Theoretical Description

The considered 1-D GPC multilayer structures is shown in Fig. 8.1. The GPCs considered in our investigation are composed of two types of dielectric layers. One is the graded layer (A or A') with exponential varying refractive index as a function

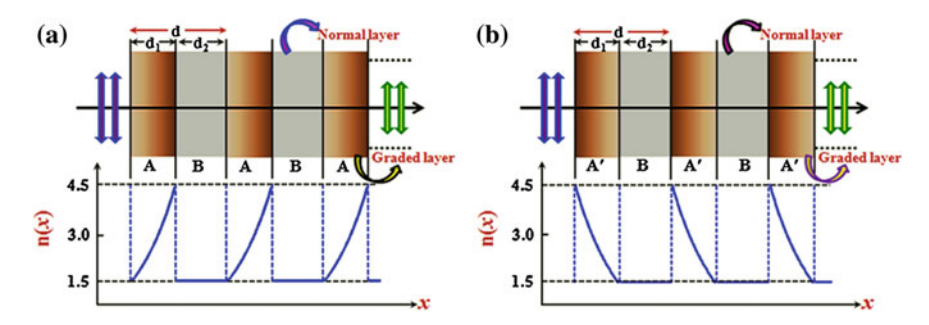


Fig. 8.1 The schematic representation of 1-D graded photonic crystals with exponentially a increasing and b decreasing refractive index along the thickness of exponential graded layer

of the depth of layer and other is homogeneous layer (B) with space independent refractive index. Refractive index profile in the considered exponential graded layers varies in two ways with depth of layer. First, index of refraction increases exponentially from initial to end boundary of the graded layer and is represented as:

$$n(x) = n_i \exp\left(\frac{x}{d_1} \ln \frac{n_f}{n_i}\right) \tag{8.1}$$

Second, when refractive index decreases exponentially from initial to final boundary of the graded layer, it can be expressed as:

$$n(x) = n_f \exp\left(\frac{x}{d_1} \ln \frac{n_i}{n_f}\right) \tag{8.2}$$

where  $n_i$  and  $n_f$  is the lower and higher index of refraction, respectively and  $d_1$  is the layer thickness. In our proposed structures, first case is considered in layer 'A' and second case in layer 'A'. The two representative structures of 1-D GPCs are a multilayer structure composed with layer A and A', and their schematic diagram are illustrated in Fig. 8.1a, b, respectively. Refractive index variation in relative proposed structures is also shown in Fig. 8.1.

The wave equation for light wave propagation in graded layer, which has exponentially varying refractive index along the plane perpendicular to the surface of layer (suppose x-direction) can be written as:

$$\xi^2 \frac{d^2}{d\xi^2} E + \xi \frac{d}{d\xi} E + \frac{\xi^2}{\gamma^2} E = 0$$
 (8.3)

where  $\xi = \frac{2\pi}{\lambda} n(x)$  is the wave propagation vector for exponential graded layers at normal angle of incidence. Refractive index n(x) taken according the exponential graded layers with increasing and decreasing refractive index defined as above (8.1) and (8.2), respectively and  $\lambda$  is the wavelength of light. Grading profile parameter

for exponentially increasing and decreasing refractive index layers to be  $\gamma = \frac{1}{d_1} \ln \left( \frac{n_f}{n_i} \right)$  and  $\gamma' = \frac{1}{d_1} \ln \left( \frac{n_i}{n_f} \right)$ , respectively. Therefore, we can represent the (8.1) and (8.2) for variation of refractive index in the exponential graded layers (A and A') as  $n(x) = n_i e^{\gamma x}$  or  $n_f e^{\gamma x}$  for increasing or decreasing order, respectively [24].

The solution of (8.3) can be expressed for increasing refractive index in the exponential graded layers as:

$$E(x) = A_G J_0 \left(\frac{\xi}{\gamma}\right) + B_G Y_0 \left(\frac{\xi}{\gamma}\right)$$
 (8.4)

where  $A_G$  and  $B_G$  are arbitrary constants for graded layers,  $J_0$  and  $Y_0$  are first and second kind of the zero-order Bessel function, respectively. Subscript G represents a graded layer.

Similarly, the solution for exponential graded layers with decreasing refractive index to be similar as (8.4) only propagation wave vector and grading profile parameter changes according to this layer.

The electric field distribution for a homogeneous layer along x-axis can be written as:

$$E(x) = A_H \exp(-ik_H x) + B_H \exp(ik_H x)$$
(8.5)

where,  $A_H$  and  $B_H$  are the arbitrary constants,  $k_H$  is the wave vector and at normal angle of incidence  $k_H = \frac{2\pi}{\lambda} n_B$ . Subscript H represents a homogeneous layer.

To investigate the propagation properties of the electromagnetic wave in the periodic structures  $(AB)^N$  and  $(A'B)^N$ , where N is the number of periods. We embrace the transfer matrix method to calculate the reflectance and band gap spectra. After applying the transfer matrix approach on the considered structures, if refractive index increases exponentially with depth of graded layers, the electromagnetic wave propagate through the whole structures can be expressed by multiplying the characteristic matrices of the constituent layers as:

$$\begin{pmatrix} \mathbf{A}_0 \\ \mathbf{B}_0 \end{pmatrix} = \mathbf{M}_0^{-1} \cdot (\mathbf{M}_G \cdot \mathbf{M}_H)^N \cdot \mathbf{M}_0 \begin{pmatrix} \mathbf{A}_{N+1} \\ 0 \end{pmatrix}$$
(8.6)

Similarly, for the second case if refractive index decreases exponentially with depth of graded layers:

$$\begin{pmatrix} \mathbf{A}_0 \\ \mathbf{B}_0 \end{pmatrix} = \mathbf{M}_0^{-1} \cdot \left( \mathbf{M}_{\mathbf{G}}' \cdot \mathbf{M}_{\mathbf{H}} \right)^N \cdot \mathbf{M}_0 \begin{pmatrix} \mathbf{A}_{N+1} \\ 0 \end{pmatrix}$$
(8.7)

where N is the number of the period,  $A_0$ ,  $B_0$  and  $A_{N+1}$  are the arbitrary constant for incident (0<sup>th</sup>) media and outgoing (N + 1)<sup>th</sup> media, respectively. Matrix  $M_G$  and  $M'_G$  are the characteristics matrix of exponentially increases and decreases refractive

index with depth of graded layers, respectively. Matrix  $M_H$  and  $M_0$  is the characteristics matrix of homogeneous layers and air media, respectively.

The reflection and transmittance coefficient of the structures, respectively can be written as:

$$\mathbf{R} = \left| \frac{\mathbf{B}_0}{\mathbf{A}_0} \right|^2 \text{And } \mathbf{T} = \left| \frac{\mathbf{A}_{N+1}}{\mathbf{A}_0} \right|^2 \tag{8.8}$$

Naturally, due to our consideration of lossless dielectric material, the transmittance here is just the reflectance's complement.

A periodic layer structure is equivalent to a one-dimensional lattice that is invariant under the lattice translation. Here, refractive indices of layers are unchanged by the translation of the wave vector by a lattice constant d, where d is the total thickness of the periodic system. Using the Floquet's theorem, the solution of the wave equation of a period of the electric field for a periodic layer system can be written as  $E_K(x,z) = E_K(x).e^{-i.\beta.z-i.K.x}$ , where  $E_K$  is periodic with period d i.e.,  $E_K(x+d) = E_K(x)$  and constant K is known as the Bloch wave number. Hence the dispersion relation for a periodic layer medium can be written as:

$$K(\beta, \omega) = \frac{1}{d} \cdot \cos^{-1} \left\{ \frac{1}{2} (M_{11} + M_{22}) \right\}$$
 (8.9)

where d is the total thickness of a period of the periodic system,  $M_{11}$  and  $M_{22}$  is the elements of the optical transfer matrix  $M_{ij}(i,j=1,2)$ . Here, Optical transfer matrix  $(M_{ij})$  of a period equal to  $M_G.M_H$  and  $M'_G.M_H$  for considered structures with exponentially increasing and decreasing of the refractive index between the boundaries of the exponential graded layer, respectively.

The dispersion relation exhibits multiple spectral bands classified into two regimes: First, where  $|(M_{11}+M_{22})/2| \le 1$  corresponds to real K and thus to propagating Bloch waves. Second, spectral bands within which K is complex correspond to evanescent waves that are rapidly attenuated. Defined by the condition  $|(M_{11}+M_{22})/2| > 1$ , these bands correspond to the stop bands also called photonic band gaps/ forbidden gaps since propagating modes do not exist for the systems [24].

#### **8.3** Numerical Results and Discussion

In this section, we present some numerical results to characterize the optical reflection, band structures, phase shift and Omni-directional band due to the relevant structural parameters of considered 1-D GPC structures. We consider the medium B as homogeneous layer with variable refractive index  $n_B$ , while for medium A or A' (Graded layer), we have exponentially varying refractive index

with depth of layer in increasing (for layer A) and decreasing (for layer A') fashion between lower refractive index,  $n_i = 1.5$  and higher refractive index,  $n_f = 4.5$ , as expressed by (8.1) and (8.2), respectively. In this study, we assume that light incident through the air medium and materials are lossless dielectric. The numerical observations for the considered 1-D GPC structures constituting exponentially graded index layers have been carried out in three parts.

### 8.3.1 Effect of Layer Thickness on Photonic Band Gaps in 1-D GPC Structures

We first present the reflection spectra of 1-D GPC structures at different layer thickness for some selected refractive index of homogeneous layer B under normal incident angle. Thickness of the homogeneous and graded layers are chosen as to give,  $n_G d_1 = n_B d_2 = D$ , where  $d_1$  and  $d_2$  are the thickness of the graded and homogeneous layer, respectively and  $n_G$  is the mean value of the initial and final refractive index of the graded layer. For various layer thicknesses, we choose D as  $\lambda_0/8$ ,  $\lambda_0/4$ ,  $\lambda_0/2$  and  $3\lambda_0/4$ , where  $\lambda_0$  is the optical wavelength and equal to wavelength for the mean value (450 THz) of the considered frequency region (150– 750 THz). As is evident from the results shown in Fig. 8.2, there exists number of photonic bands, where electromagnetic waves cannot be transmitted. The number of photonic bands increases with increasing the thickness of the layers for each choosen refractive index of the homogeneous layer B. Because, with increasing the thickness of layers, the rate of change of refractive index in graded layers increases, and the average refractive index over the volume of each graded layer becomes large. Namely, the rate of change of refractive index contrast of the two types of dielectric layers is enhanced and hence influences the Bragg stack effectively. We also observed that formation reflection spectra are same for the structures with both exponential graded layers A and A'. Figure 8.2a, b, c, respectively show the reflection spectra of the considered structures for constituted homogeneous layer refractive index,  $n_B = 2.0$ , 1.5 and 1.0.

For all the chosen refractive index of the homogeneous layer B, the formation of photonic bands is similar under normal angle of incidence, but bandwidth of photonic bands is different. Bandwidths are larger for  $n_B = 1.0$  as compare to other  $n_B$  values. Bandwidths are decreases with increasing  $n_B$  values because the photonic band gap properties are basically affected by the contrast of refractive index of constituted media. Contrast of refractive index of homogeneous layer and graded layer is higher for  $n_B = 1.0$  as compare to other considered values, therefore the Bragg stack is more effective and widths of photonic bands are large.

Now, we examine the confinement effects arising from competition between the structures induced by changing the thickness of layers and magnitude of the total photonic bandwidths in the photonic band gap spectra. Note that, as expected for large layer thickness, we get number of forbidden bands and their bandwidths

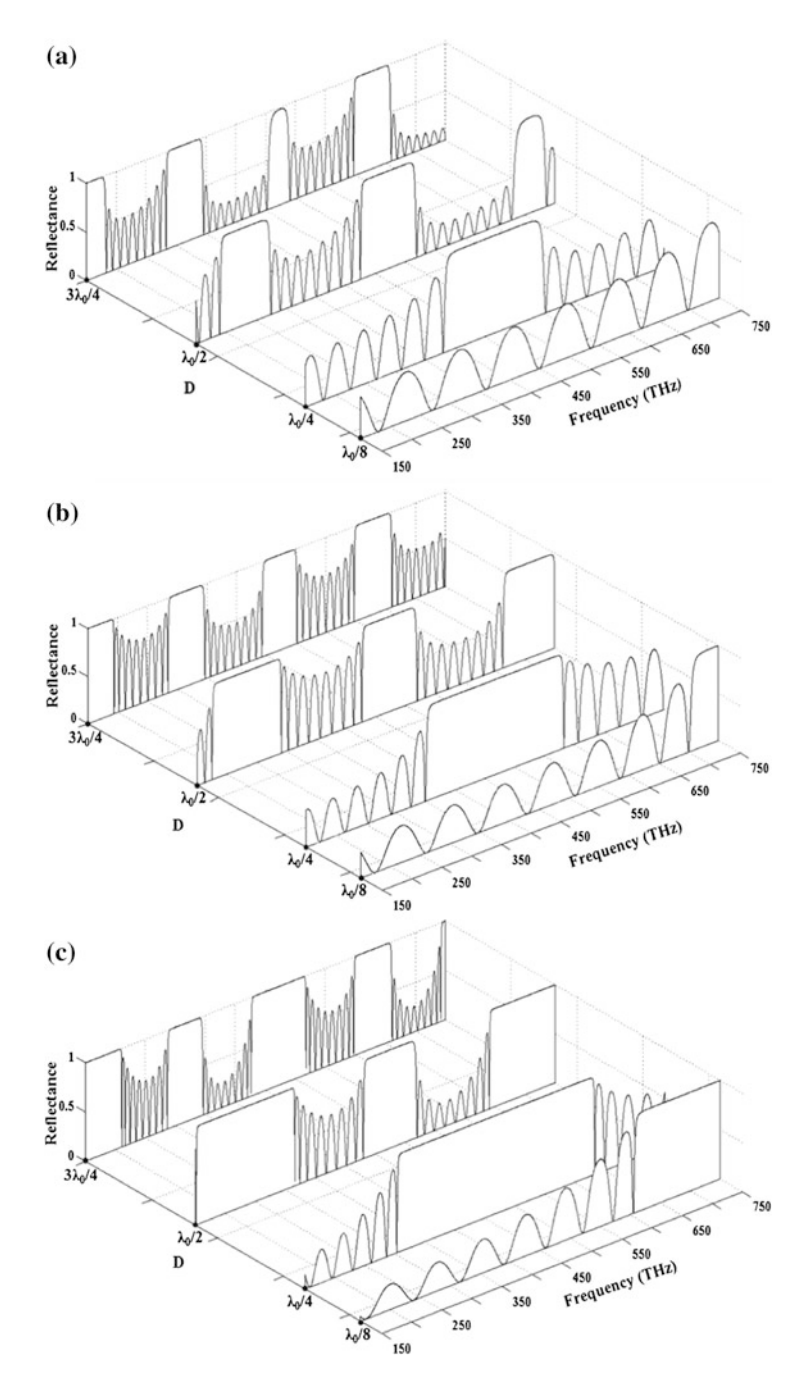


**Fig. 8.2** Reflectance spectra of the considered 1-D graded photonic crystal structures for the constituted homogeneous layer refractive index **a**  $n_B = 2.0$ , **b**  $n_B = 1.5$  and **c**  $n_B = 1.0$ , with various layer thickness constant D

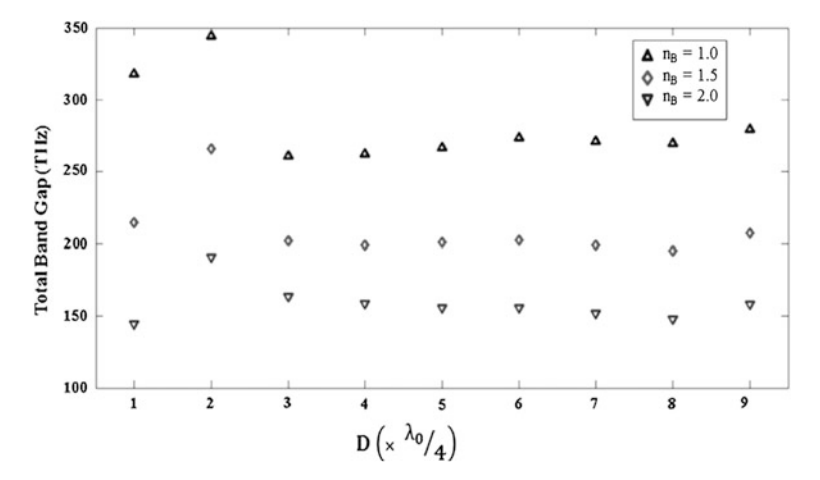
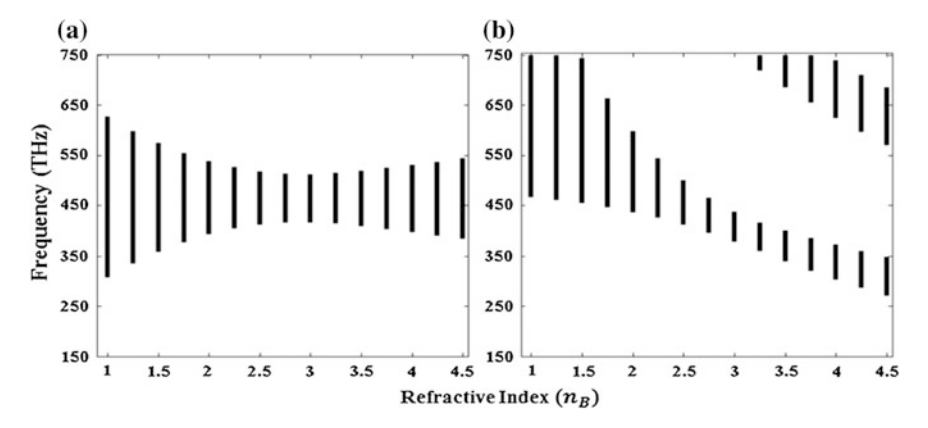


Fig. 8.3 The distribution of the total band gap of the forbidden band regions against the layer thickness constant D

become narrower and narrower as an indication of more photonic band gaps with small bandwidths. We observed that the number of forbidden bands are approximate same for the structures with acceptable  $n_R$ -values but their bandwidths are different.

Total bandwidths in the structures with  $n_B = 1.0$  are maximum as compared to other considered  $n_B$ -values, which is clearly demonstrated in Fig. 8.3. In this figure, we show the total band gap verses the layer thickness constant (D) for the structures with various refractive index  $(n_R)$  of homogeneous layer up to the value of D =  $9\lambda_0/4$ . It reveals that the total band gaps randomly change with increasing the layer thicknesses, but it is extremum for considered structures with latent type layer stacking arrangements. Furthermore, we have emphasized the photonic band gaps as changing of the refractive index of the normal layer B. To do that, we calculate the regions for forbidden (stop bands) frequencies, where  $|(M_{11} + M_{22})/2| > 1$ , as a function of  $n_B$  is depicted in Fig. 8.4a, b, respectively for the structures with quarter wave arrangements and precise layer thickness  $d_1 = 50$  nm and  $d_2 = 75$  nm. These figures show the distribution of the forbidden (black region) and allowed (white region) frequencies region as a function of the  $n_B$  up to 4.5. As shown in Fig. 8.4a, the photonic band gap first decreases with increasing the value of  $n_R$  up to 3.0 and then slowly increases for the higher value of  $n_B$  in the structures with quarter wave arrangements, while for the structure with precise layer thicknesses  $d_1 = 50$  nm and  $d_2 = 75$  nm, behavior of photonic band gap variation is same as above but that shifted toward lower frequency region with increasing the value  $n_B$  as depicted in Fig. 8.4b. Note that new photonic band gaps are also generated at higher values of  $n_B$  for the structure with precise layer thicknesses. Here, we can also clearly see that the values of  $n_B$  in the structures with quarter wave arrangements only influence on the width of the photonic band gap, while in the structures with precise layer thicknesses, the values of  $n_B$  effect on both width and generation of new photonic band gaps.



**Fig. 8.4** The distribution of the bandwidths as a function of the homogenous layer refractive index  $n_B$  for the structures with **a** quarter wave arrangements and **b** precise layer thicknesses  $d_1 = 50$  nm and  $d_2 = 75$  nm

For better understanding the effect of graded layer in the considered 1-D GPCs, we have also calculated the spatial distribution of the square magnitude of the electric field at three selected frequencies impinging under  $\approx 0$ ,  $\approx 50$  and  $\approx 100$  % reflection conditions for the structures (AB)<sup>10</sup> and (A'B)<sup>10</sup>, and demonstrated in Fig. 8.5. The electric field is denoted by E(x). For the sake of clarity, we have chosen the thickness of layers with relative refractive index equal to  $5\lambda_0/4$ , so the effect of electric field can be better appreciated. From the reflection spectra of the structures with  $n_R = 1.0$ , it can be clearly observed that at the spectral band edge positions 635 THz, where close to 0 % reflection is found, reflection is maximum ≈100 % within the band gap region that observed for frequencies 580 THz inside the band gap, and at one of the reflection peak at 628.4 THz where ≈50 % reflection is observed. Therefore, electric field intensity within the considered structures for frequencies 635, 628.4 and 580 THz is demonstrated in Fig. 8.5a, b, c, respectively. Panels (i) and (ii) of the Fig. 8.5 show the distribution of electric field intensity in the periodic structures (AB)<sup>10</sup> and (A'B)<sup>10</sup>, respectively. It is shown that the electric field distributions in exponential graded layers for different grading profiles are quite different, although the volume-average refractive index is same. For exponentially increasing refractive index profile, the electric field intensities in exponential graded layers decrease as propagating depth increases as seen in panels (i), while intensities increase with increasing the propagating depth for exponential decreasing refractive index as depicted in panels (ii). The reason is the effect of the inhomogeneity in the exponential graded layers and the variation of electric field intensities in graded layers changes due to the space dispersive increasing or decreasing refractive index with graded layers depth. On the other hand, the electric field intensities in non-graded layers keep unchanged for both types of periodic structures (AB)<sup>10</sup> and (A'B)<sup>10</sup>.

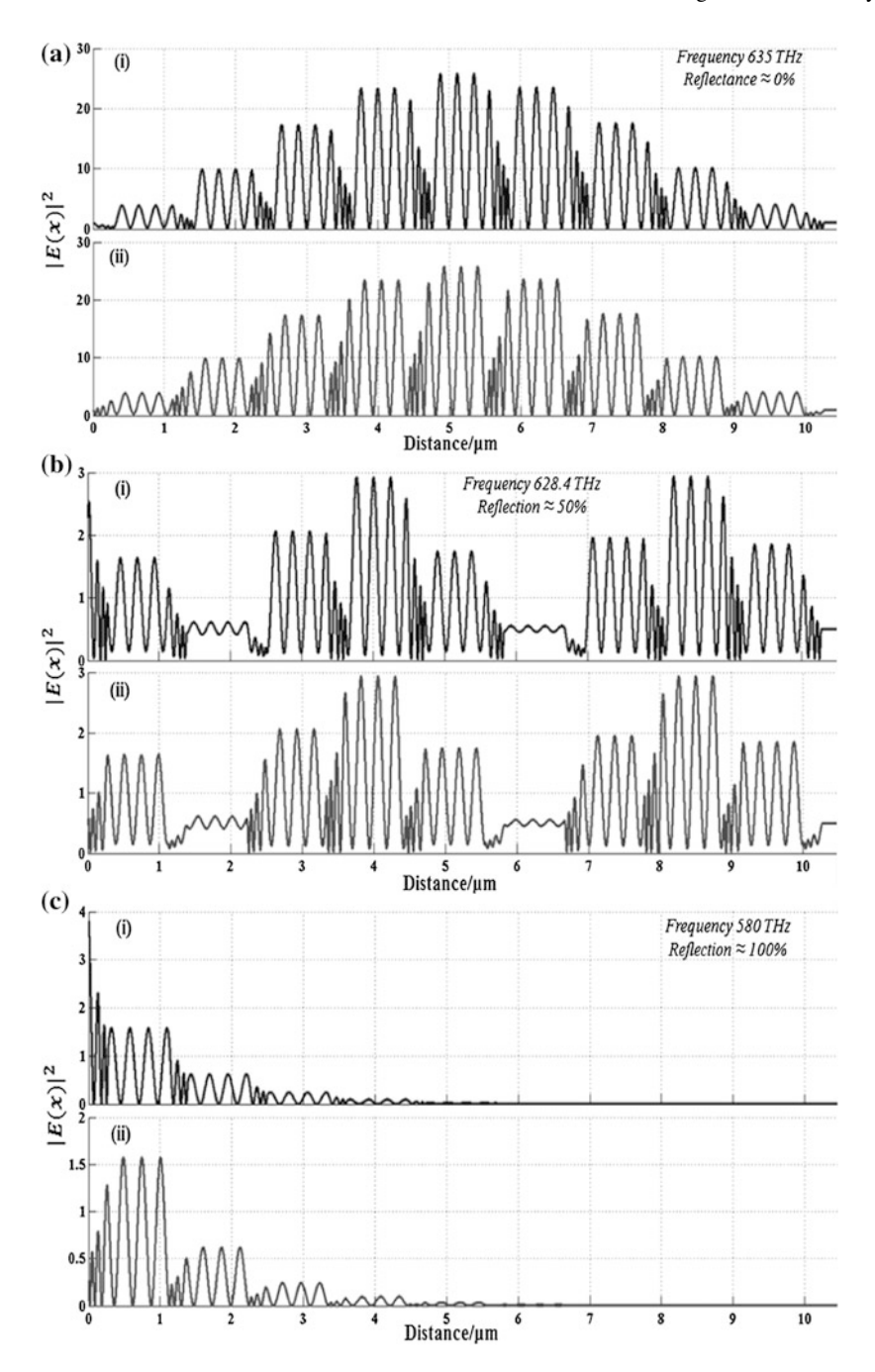


**Fig. 8.5** Panels (i) and (ii), respectively show the spatial distributions of the electric field intensity in the systems type 1 (AB)<sup>10</sup> and type 2 (A'B)<sup>10</sup> at three selected frequencies **a** 580 THz, **b** 628.4 THz and **c** 635 THz, impinging under  $\approx$ 0,  $\approx$ 50 and  $\approx$ 100 %, respectively

Due to the importance of the widespread photonic band gaps for the 1-D GPC structures, we would like to extend the study on the dispersion curves and reflection phase shift associated with the wider photonic band gaps in structures with  $n_B = 1.0$ . For different layer thickness, dispersion curves are calculated from (8.9) for the unbounded periodic structures and shown in panels (i) of the Fig. 8.6 as functions of the reduced Bloch wave vector  $kd/\pi$ , and related reflection phase shifts are likewise illustrated in panels (ii) of the Fig. 8.6. As expected, the band gaps

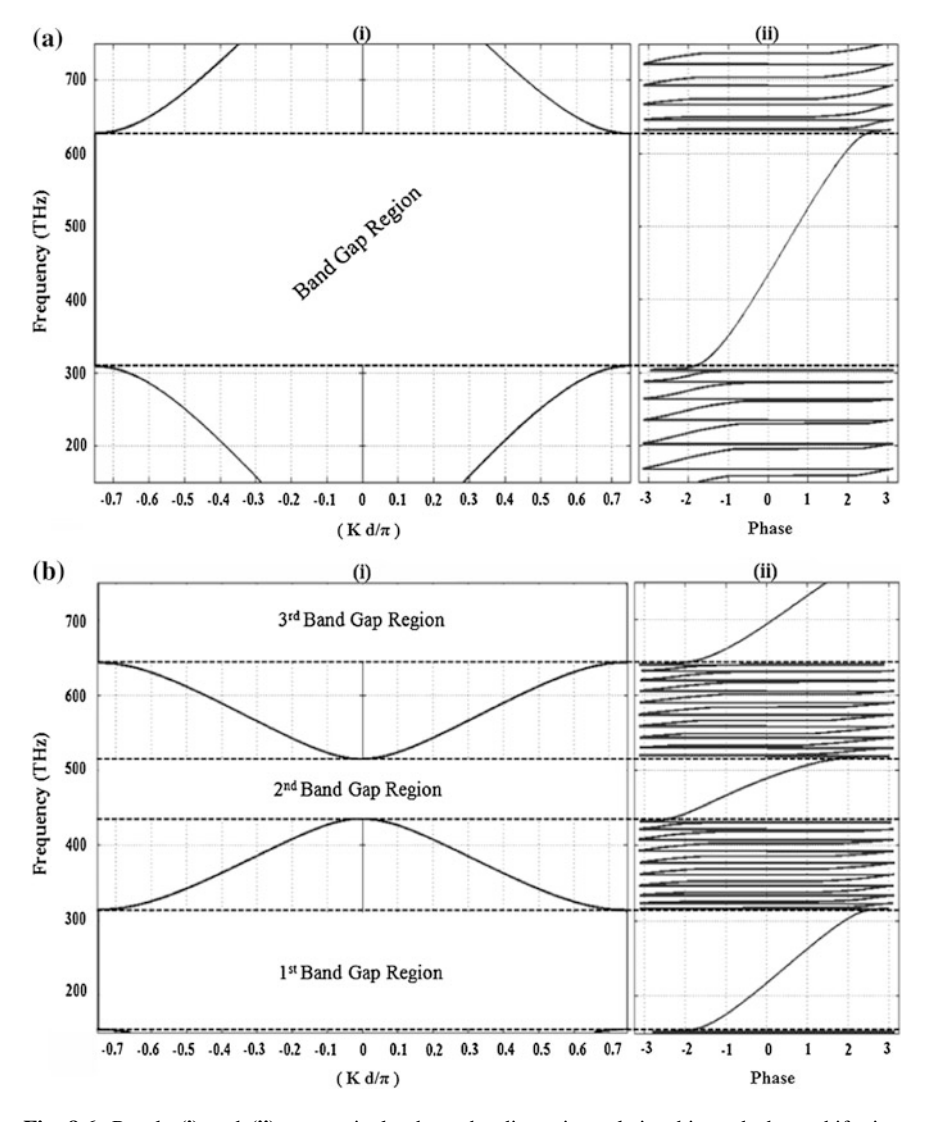


**Fig. 8.6** Panels (i) and (ii), respectively show the dispersion relationship and phase shifts in a photonic crystal with unit cell consisting of one layer of exponentially graded index material  $(n_i = 1.5 \text{ to } n_f = 4.5)$  and other layer of air, for optical layer thicknesses with relative refractive index equal to a  $\lambda_0/4$  and b  $\lambda_0/2$ 

observed at zero transmission intensity range. The corresponding dispersion curves for the finite crystal are depicted in panels (i) of the Fig. 8.6a, b, respectively for layer thickness with relative refractive index proportional to  $\lambda_0/4$  and  $\lambda_0/2$ . Also as seen here, number of bands increases with increase in layer thicknesses, single band formed for layer thickness with relative refractive index equal to  $\lambda_0/4$  and three bands for  $\lambda_0/2$ , but the bandwidths become narrow and narrow with increasing the number of bands.

Moreover, we watch in panels (ii) of the Fig. 8.6 and observe that reflection phase shifts varies from close to  $-\pi$  at one band edge to approximate  $\pi$  at another band edge of the stop bands for the precise arrangement of unit cells in structures. Here, we have investigated reflection phase shifts for one of the specified possible arrangements of layers in period 'BA' of the considered graded photonic crystal structures. For other periodic arrangements such as AB or A'B or BA', reflection phase shifts varies in different ways between  $-\pi$  and  $\pi$ . The explanation for this phenomenon is that, in the stop band, the electric field of the lower band edge is mainly distributed in the non-graded material of the unit cell, while distribution of electric field in graded layer have adequate amplitudes at the upper band edge. In graded layers, distribution of field changes according to the gradation profiles. Therefore, due to the transform of field intensity distribution at the interface boundaries, the phase shifts are change between  $+\pi$  and  $-\pi$  with different values. According to our results, we observed that the reflection, transmission and photonic band gap spectra are independent of the arrangement of graded layers (A or A') in unit cells of the structures, whereas field distributions and reflection phase shifts change with arrangement of graded layers in unit cells of the structures. The forbidden bands region and bandwidths of the structures for different layer thicknesses and various refractive index of the homogeneous layer B are listed in Table 8.1.

**Table 8.1** Reflection bands region and bandwidths in the GPC structures at normal incidence for different layer thickness

Thickness constant (D)	$n_B=2.0$		$n_B = 1.5$		$n_B = 1.0$	
	Band region	Band width	Band region	Band width	Band region	Band width
λ <sub>0</sub> /8			750.0–719.0	31	750.0–617.8	132.2
λ <sub>0</sub> /4	538.0-393.8	144.2	574.0-359.6	214.4	627.0-309.0	318
$\lambda_0/2$	269.0-197.0	72	287.0-179.8	107.2	313.4–154.6	158.8
	512.2-431.2	81	514.0-432.6	81.4	514.8–435.4	79.4
	725.8–688.4	37.4	746.2–669.2	77	750.0–643.6	106.4
3λ <sub>0</sub> /4	179.2–150.0	29.2	191.2–150.0	41.2	209.0-150.0	59
	341.8–287.6	54.2	342.4–289.2	53.2	343.2–290.2	53
	483.8–459.0	24.8	497.4–446.2	51.2	515.6-429.2	86.4
	655.8-601.0	54.8	656.6-601.2	55.4	658.6-601.0	57.6
					750.0–745.0	5

Now, to have a more complete description and a better understanding of the effect of the layer thicknesses on the properties of photonic band gap, it is important to know how layer thickness change the properties of the reflection coefficients and photonic band gap for the structures with specific layer widths. Here, we also show the reflection spectra for different layer thickness of graded layers ( $d_1$ ) and normal layers ( $d_2$ ) in Fig. 8.7a, b for the structures with fixed values of  $d_2 = 75$  nm and  $d_1 = 50$  nm, respectively. The acquired band gap is shifted towards the lower frequency region and their bandwidth also decreases with increasing the values of

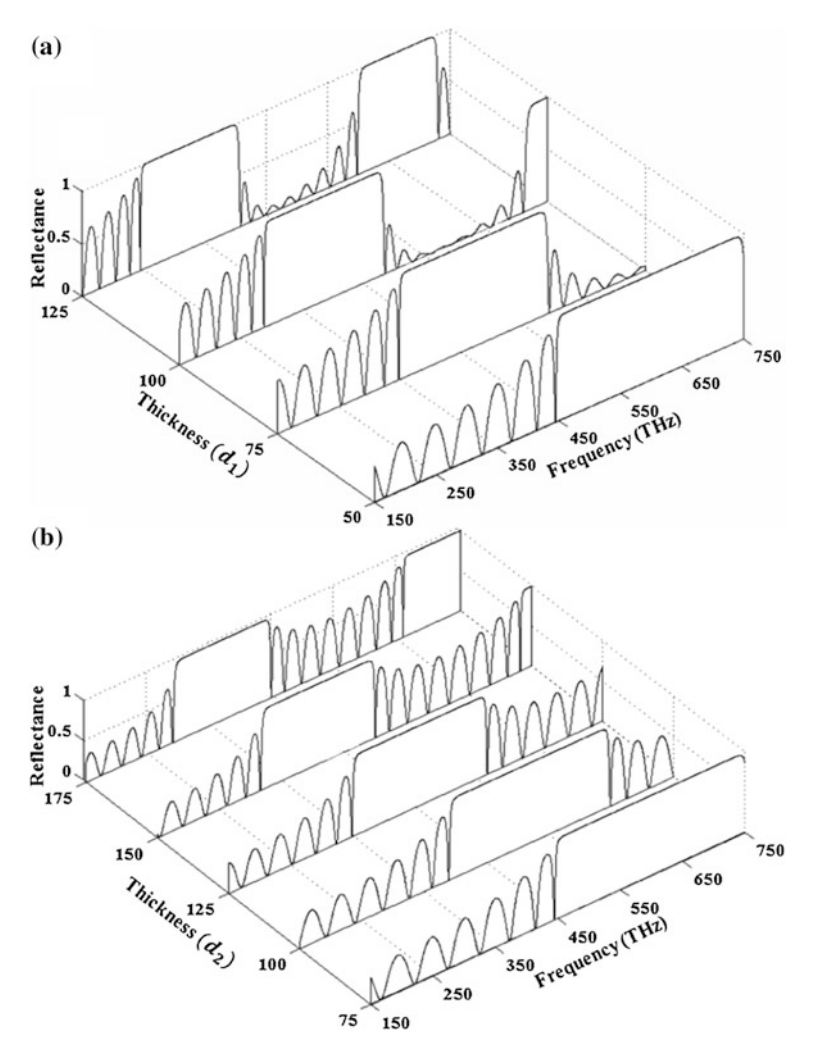


**Fig. 8.7** Reflectance spectra for different precise layer thicknesses of graded layers  $(d_1)$  and normal layers  $(d_2)$  for the structures with fixed values of  $\mathbf{a}$   $d_2 = 75$  nm and  $\mathbf{b}$   $d_1 = 50$  nm, respectively

thickness  $d_1$  and  $d_2$ , it is clearly demonstrated in Fig. 8.7a, b, respectively. Note that, as expected for large layer thicknesses, we get new forbidden bands because with increasing the thickness of layer, effective refractive index of the structure increases. The change of exponential graded layer thickness has great influence on the formation of photonic band gaps as compare to the change of normal layers thicknesses.

## 8.3.2 Study of the Omni-Directional Band Gap in 1-D GPC Structures

In this section, we will discuss the Omni-directional band gap characteristics in the proposed 1-D GPC structures, which have quarter-wave and latent type layer stacking arrangements. An Omni-directional band gap can be obtained within a specific frequency range in photonic crystal as a forbidden band gap that reflects electromagnetic wave at any incident angle for both TE and TM-polarization. The dependence of photonic band gaps on the incident angle in a quarter-wave stacking multilayer structures for TE and TM polarization are shown in Figs. 8.8a, b, 8.9a, b and 8.10a, b for various refractive index;  $n_B = 2.0$ , 1.5 and 1.0, respectively.

These figures are clearly demonstrated that the expansion of photonic band gap in structures with  $n_B = 2.0$  and 1.5 are enhance for both TE and TM-wave, while for  $n_B = 1.0$ , photonic band spreading in frequency range for TE-wave and shrinking in frequency range for TM-wave, when the incident angle increases. In order to discuss the Omni-directional band gap properties of the structures, we have plotted the projection band structures as changing of the incident angle and exhibited in Figs. 8.8c, 8.9c and 8.10c, respectively for the structures with  $n_B = 2.0$ , 1.5 and 1.0.

From these figures, we can clearly inspect the variation of higher and lower band edges as changing of the incident angle. There is an Omni-directional band gap, which exists between higher and lower band edges as prevalent band region for both TE and TM-polarization. The photonic band spectra of the photonic crystals can be usually achieved from the projection of unit reflectance from Figs. 8.8a, b, 8.9a, b and 8.10a, b, and Omni-directional band gap clearly demonstrated in Figs. 8.8c, 8.9c and 8.10c. In Figs. 8.8c, 8.9c and 8.10c, the grey areas represent the forbidden band for relative polarization and the ubiquitous white area between the band edges in both polarizations illustrate the Omni-directional band gap.

It is certified from figures, an Omni-directional band exists for structure with  $n_B = 2.0$  and 1.5, while it is not observed in structure with  $n_B = 1.0$ . But one obvious feature of this structure is that there exist large complete band gap for TE-wave. Therefore, structure with  $n_B = 1.0$  is more suitable for designing TE-polarized photonic devices and structures with  $n_B = 2.0$  and 1.5 can be used for design Omni-directional photonic devices.

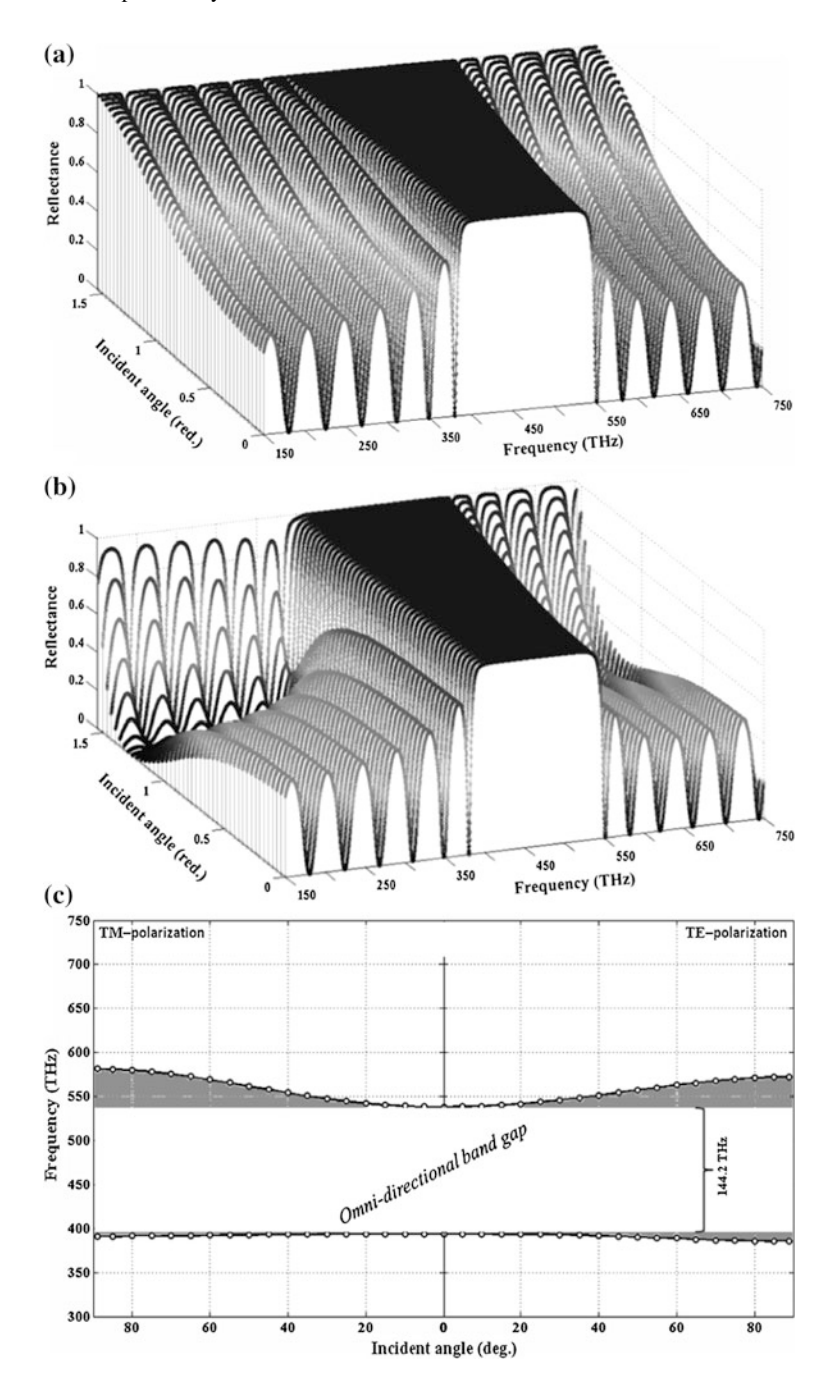


**Fig. 8.8** Reflection spectra for a TE-polarization, **b** TM-polarization and **c** projected band structure as the changing of the incident angle of the quarter-wave structure with  $n_B = 2.0$ 

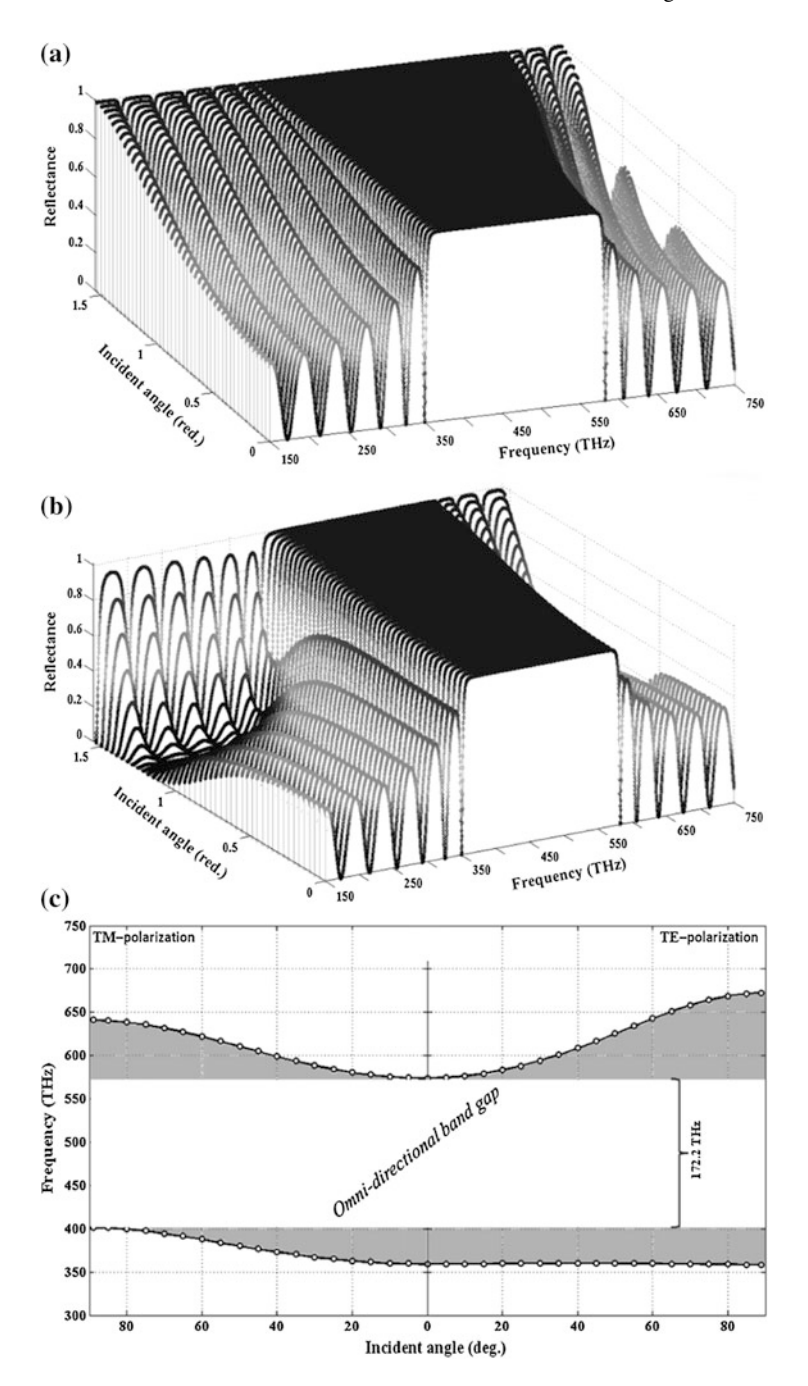


**Fig. 8.9** Reflection spectra for a TE-polarization, **b** TM-polarization and **c** projected band structure as the changing of the incident angle of the quarter-wave structure with  $n_B = 1.5$ 

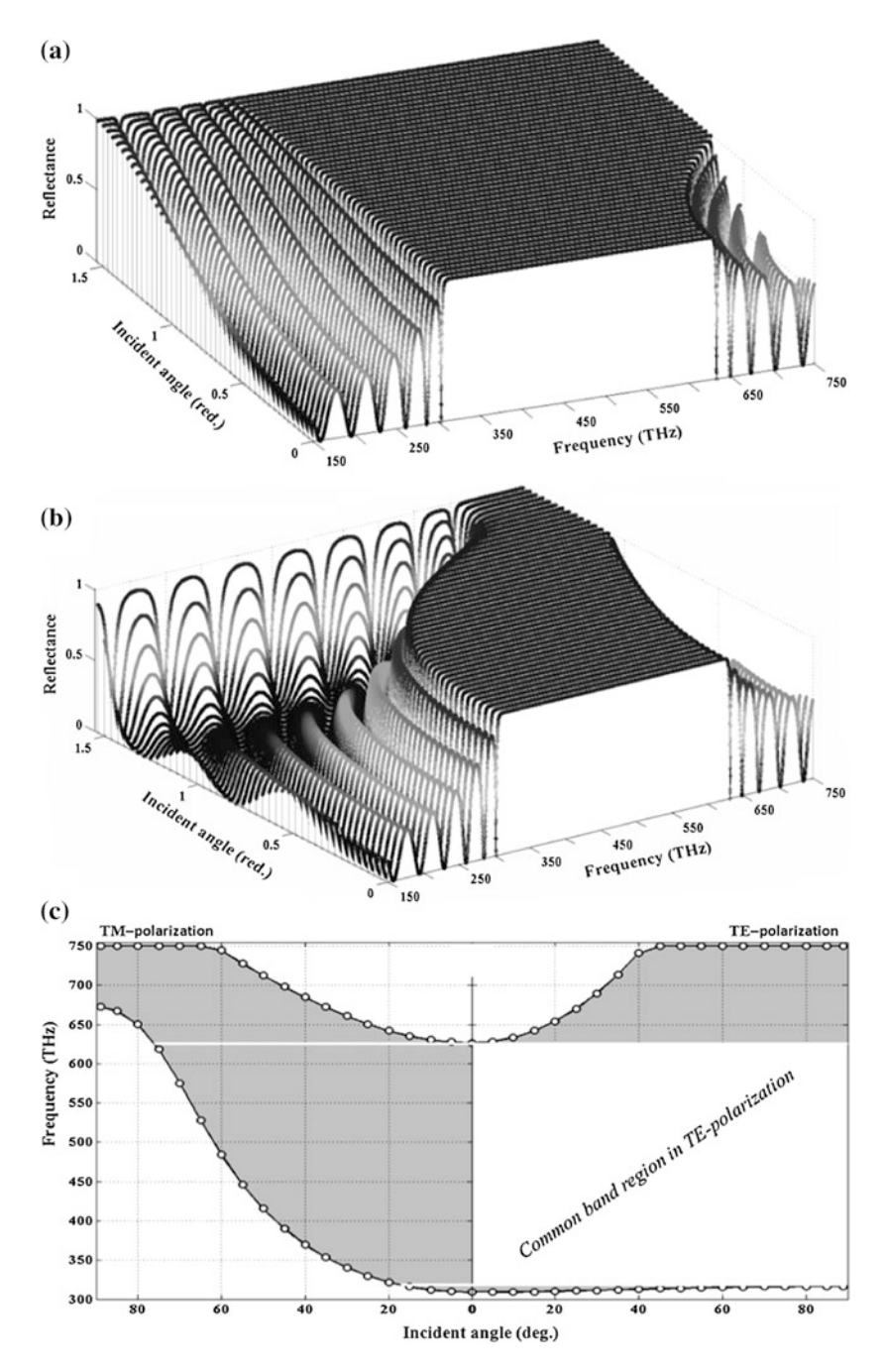


Fig. 8.10 Reflection spectra for a TE-polarization, b TM-polarization and c projected reflection band structure as the changing of the incident angle of the quarter-wave stacking structure with  $n_B = 1.0$ 

Furthermore, we have emphasized the projection band structure as the changing of the incident angle for latent type layer stacking multilayer structures with  $n_B = 2.0$ , 1.5 and 1.0, and shown in the Figs. 8.11a, b and c, respectively. It is clear from the Fig. 8.11, as like a quarter-wave stacking structures, Omni-directional band gap does not exist for structure with  $n_B = 1.0$ , but it is obtained for structure with  $n_B = 2.0$  and 1.5. This implies that occurrence of Omni-directional bands is affected by the contrast of refractive index between homogeneous and graded layer, and it is in absence for the structures with  $n_B = 1.0$ . The number of Omni-directional bands existed for these structures with  $n_B = 2.0$  and 1.5. Therefore, these types of structure can be used in the widespread Omni-directional photonic devices which operate in range 150–750 THz. The Omni-directional bands range and bandwidths for the quarter-wave and latent type layer stacking structures with different  $n_B$ -values are tabulated in Table 8.2.

Accordingly, we find that refractive indices of constituted homogeneous layers greater than one produce the omnidirectional band gaps but increasing the indices band gaps becomes narrow and narrow. Thus the existence of omnidirectional band gaps in graded-homogeneous periodicity approach requires the index contrast  $(n_G - n_B)$  for  $n_B > 1$ . Under this condition, the broader Omni-directional band range demands higher index contrast. In addition, the omnidirectional band gaps can be adjusted by the modifying the layers thickness.

Now, we have emphasized the Omni-directional band gaps as changing of the refractive index of the normal layer B. To do that, we calculate the ubiquitous forbidden (stop bands) frequencies regions for both TE and TM-polarization as a function of  $n_B$  is depicted in Fig. 8.12 for the structures with quarter wave arrangements. This figure shows the distribution of the forbidden (black region) and allowed (white region) frequencies, as a function of the  $n_B$  up to 4.5. As shown in Fig. 8.12, the Omni-directional band gap first decreases with increasing the value of  $n_B$  up to 3.0 and then slowly increases for the higher value of  $n_B$ . We find that the width of Omni-directional band gap is maximum for the refractive index  $n_B$  equal to 1.5.

# 8.3.3 Effect of the Ratio of $n_i$ and $n_f$ on the Photonic Band Gap

Now, we investigate the dependence of the photonic band gap on the ratio of initial and final refractive index i.e.  $(n_f/n_i)$ -value of the exponential graded layers in 1-D GPC structures under normal angle of incidence. Here, we considered initial refractive index  $(n_i)$  is fixed and equal to 1.5, while, final refractive index  $(n_f)$  varies according to contrast values. In the Fig. 8.13a, we have depicted the refractive spectra for the various  $(n_f/n_i)$ -values in a quarter wave stacking multilayer structures with homogeneous layer refractive index  $n_B = 0.1$ . As expected, the photonic bandwidth decreases with decreasing the ratio i.e.,  $(n_f/n_i)$ -values. This phenomenon is that

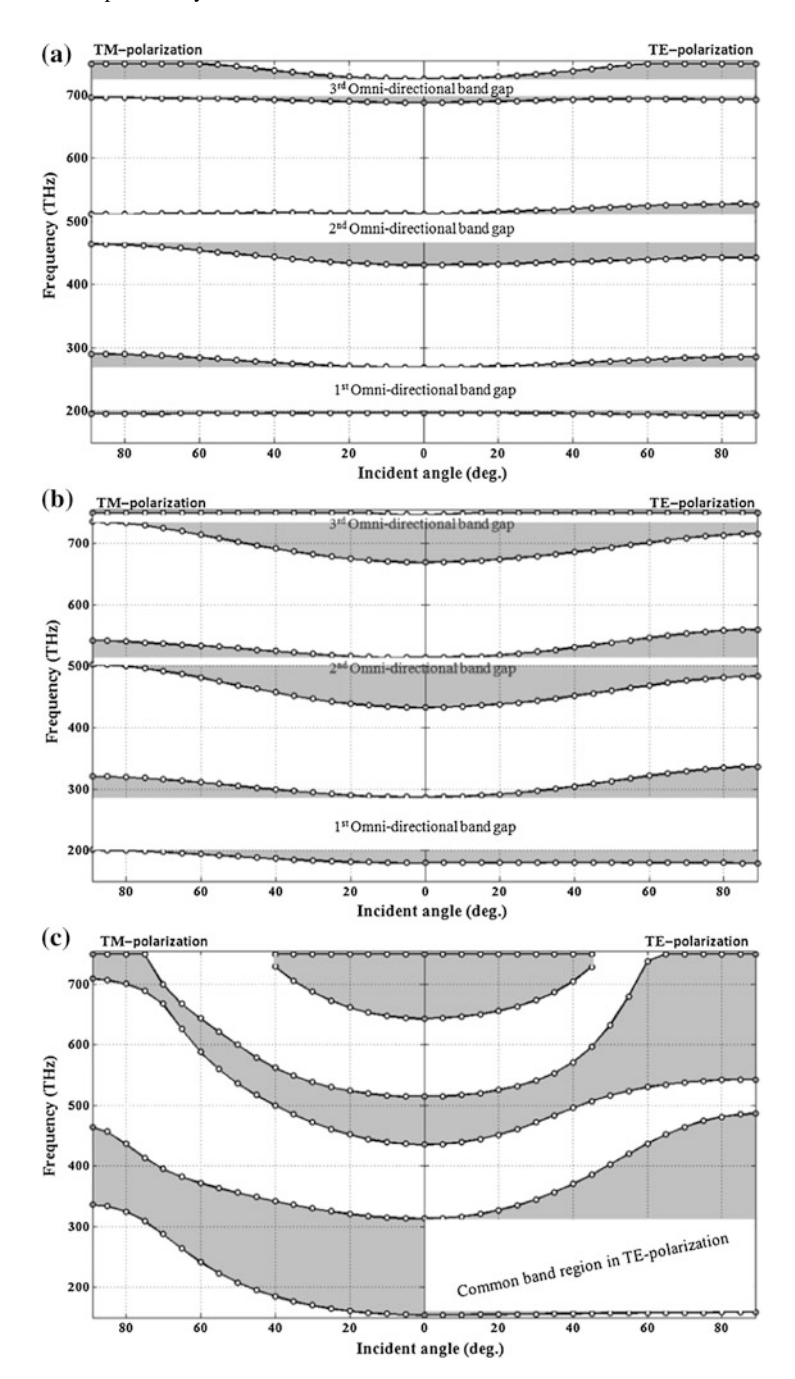
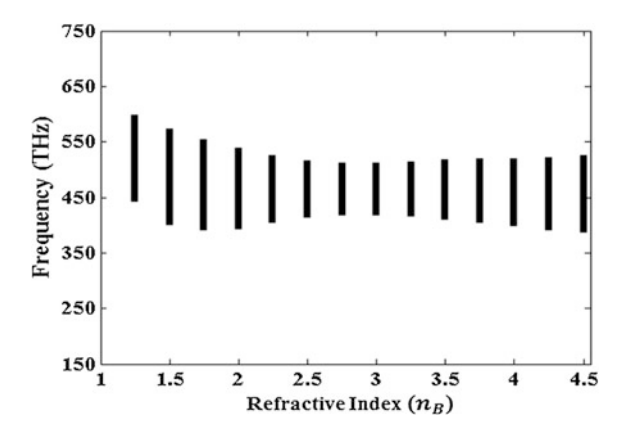


**Fig. 8.11** Projected reflection band spectra as the changing of the incident angle of the latent type structures for the refractive index  $\mathbf{a}$   $n_B = 2.0$ ,  $\mathbf{b}$   $n_B = 1.5$  and  $\mathbf{c}$   $n_B = 1.0$ 

Table 8.2 Omni-directional bands region and bandwidths in the 1-D GPC structures for various n<sub>B</sub>-values

Structures	Layer thickness constant (D)   Complete band region in	Complete band reg	ion in	Omni-directional band	Omni-directional band
with		TE-Polarization TM-Polarization	TM-Polarization	region	width
$n_B = 2.0$	$\lambda_0/4$	538.0–393.8	538.0–393.8	538.0–393.8	144.2
	$\lambda_0/2$	269.0–197.0	269.0-197.0	269.0–197.0	72
		512.2–443.0	512.2–464.6	512.2–464.6	47.6
		725.8–694.0	725.8–696.6	725.8–696.6	29.2
$n_B = 1.5$	$\lambda_o/4$	574.0–360.2	574.0-401.8	574.0-401.8	172.2
	2012	287.0–180.2	287.0-201.0	287.0–201.0	98
		514.0–483.6	514.0–502.6	514.0–502.6	11.4
		746.2–715.6	746.2–735.4	746.2–735.4	10.8
$n_B = 1.0$	$\lambda_0/4$	627.0–316.8			•
	2012	313.4–158.4	:		:
		:	:	::	:

**Fig. 8.12** The distribution of the Omni-directional band gap as a function of the refractive index  $n_B$  for the structure with quarter wave arrangement



decreasing the ratio of initial and final index of refraction of the exponential graded layer, the rate of modification of the grading profile parameter ( $\gamma$  or  $\gamma'$ ) decreases, and corresponding average refractive index over the volume of each graded layer conjointly decreases, hence influence the Bragg stack become less effectively. However, the photonic band gap decreases with decreasing the grading profile parameter while obtained band gap exists around the central frequency and it is obviously exhibited in Fig. 8.13a. To have a more complete description and a better understanding of the effect of the ratio of initial and final refractive index of the exponential graded layer on the properties of photonic band gap, it is important to know how these effects change the properties of the reflection coefficients and photonic band gap for the structures with specific layer widths. Here, we also observe that the photonic band gap diminishes with decreasing the grading profile parameter but here acquired band gap is shifted towards the higher frequency region, and it is clearly demonstrated in Fig. 8.13b. The explanation for this difference between the above-considered structural arrangements is that, in case of quarter-wave stacking arrangements, the graded layers thickness and grading profile parameter change with the ratio of initial and final refractive index, while in case of the structures with set layer widths, the width parameters are independent of the ratio of initial and final refractive index.

Moreover, we have plotted the forbidden bandwidth by changing the ratio  $(n/n_i)$  for a quarter-wave stacking multilayer structure with various relative homogeneous layer refractive indices under normal angle of incidence, which have been illustrated in the Fig. 8.14a. In this figure, we see that for a quarter-wave stacking type structures, photonic bandwidth decreases almost linearly. Diminishing of photonic bandwidths observed for all values of the refractive index ratio greater or equal to the refractive index of the homogeneous layer. But, when the refractive index of the homogeneous layer than forbidden band width increases gradually and it is clear from third graph for  $n_B = 2.0$  in Fig. 8.14a. This is the effect of the increase in contrast of refractive indices of the homogeneous and graded layer. To have a better

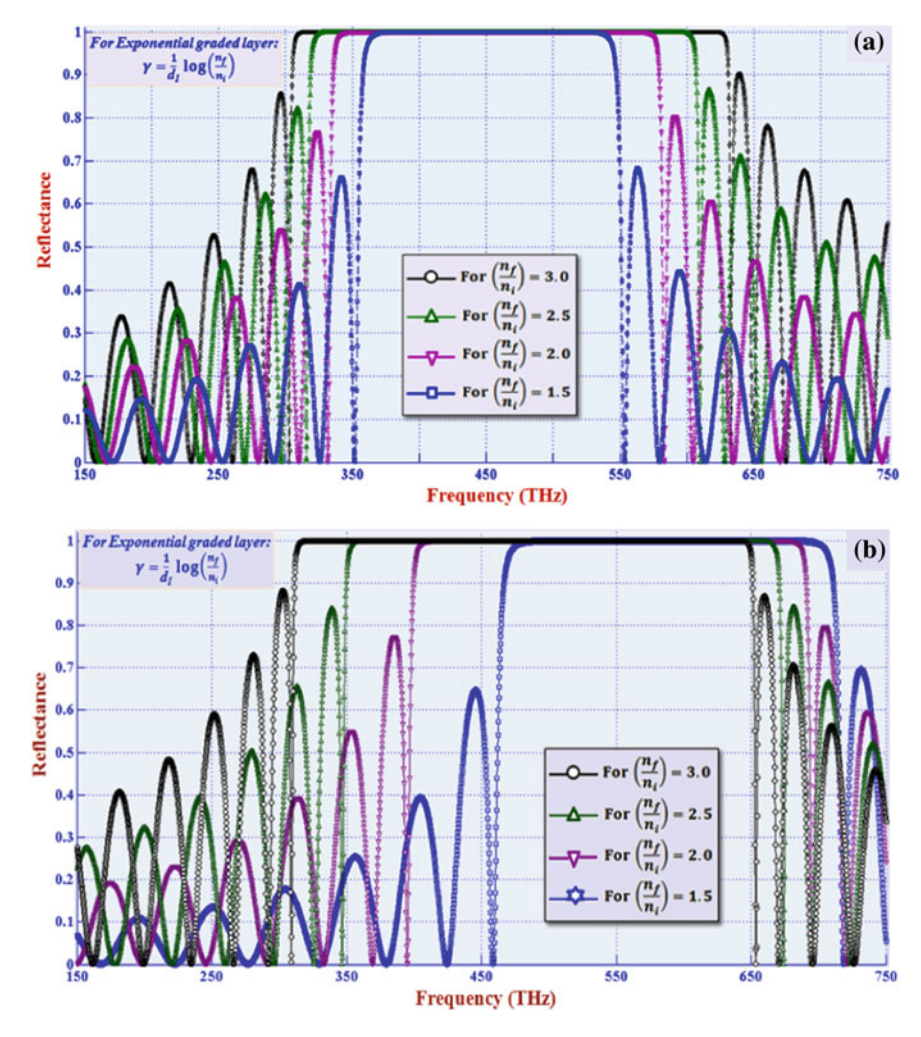
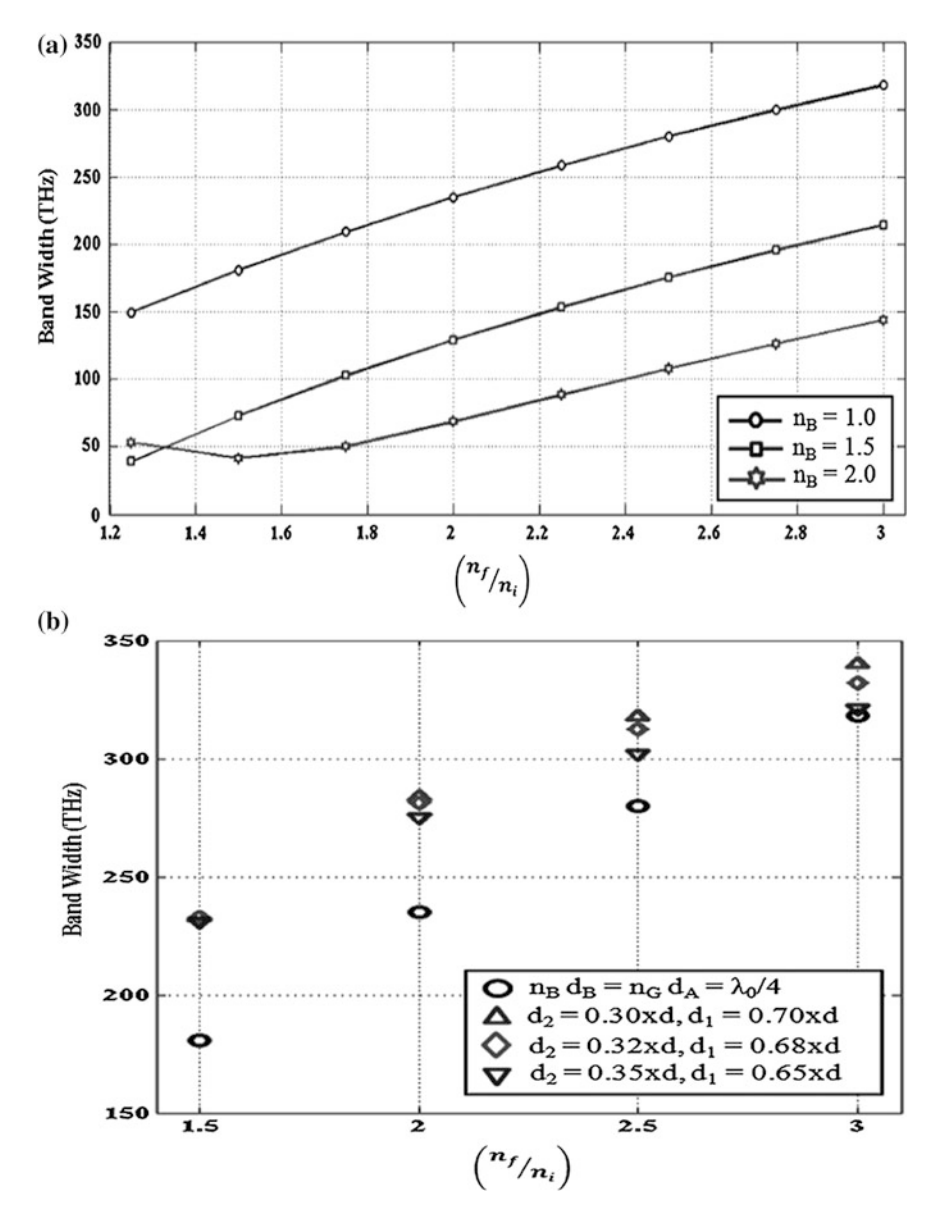


Fig. 8.13 Reflectance spectra for different values of grading parameter  $\gamma$  (or  $\gamma$ ') for the structures with **a** quarter wave stacking and **b** precise layer thickness  $d_1 = 64$  nm and  $d_2 = 136$  nm

understanding of the effect of the refractive index ratio on the photonic bandwidths, we have also demonstrated the photonic bandwidths variation by changing the ratio  $(n_f/n_i)$  for the structures with different precise layer widths, and it is clearly exhibited in Fig. 8.14b. From this figure, we observe that for the structures with set layer widths, photonic bandwidth decreases in a parabolic way with diminishing of the refractive index ratio. In these cases, bandwidth also decreases with increasing the exponential graded layer thickness. Bandwidths are extremum for lower graded layer thickness and at higher refractive index ratio, but in this figure it is clearly



**Fig. 8.14** Panel **a** shows the distribution of the bandwidths as a function of the ratio  $(n/n_i)$  for the quarter wave stacking structures with different considered  $n_B$ -values and **b** exhibits the distribution of the bandwidths as a function of the ratio  $(n/n_i)$  for the specific layer thickness structures with  $n_B = 1.0$  and d = 200 nm

seen that bandwidths are approximately same at lower refractive index ratio for each set graded layer thickness.

Ratio	Quarter-wave		Structure with constant layers thickness					
$(n_f/n_i)$ structure			$d_1 = 60 \text{ ns}$ $d_2 = 140 \text{ s}$		$d_1 = 64 \text{ m}$ $d_2 = 136 \text{ m}$		$d_1 = 70 \text{ nm}$ $d_2 = 130 \text{ m}$	
	Band range	Width	Band range	Width	Band range	Width	Band range	Width
1.5	362.2- 543.0	180.8	479.6– 712.4	232.8	472.2- 705.0	232.8	462.0– 692.8	230.8
2	340.0- 575.0	235	412.2- 695.8	283.6	404.6– 685.6	281	394.4– 669.2	274.8
2.5	322.8- 602.8	280	361.6– 679.4	317.8	354.2- 666.6	312.4	344.4– 646.2	301.8
3	309.0- 627.0	318	322.4– 662.6	340.2	315.4– 647.4	332	305.8- 626.8	321

**Table 8.3** Reflection bands region and bandwidths in the GPC structures for different  $(n_f/n_i)$  values and  $n_R = 1.0$  at normal incidence

The photonic bands range and bandwidths for different  $(n_f/n_i)$ -values in the quarter-wave stacking structures and structures with different specific layer widths are tabulated in Table 8.3.

Accordingly, the average refractive index over the volume of each layer and the different grading profile parameter has great influence on photonic and Omni-directional band gaps. Hence, we can tune and achieve the desirable photonic and Omni-directional band gaps by adjusting and tuning the relative parameters of the GPC structures.

#### 8.4 Conclusion

In this communication, we have presented the effect of exponential graded index material on photonic and Omni-directional band gaps of 1-D GPC structures in frequency region (150–750 THz). The structure is considered of exponential graded index layers and normal homogeneous layers. The variation of refractive index in exponential graded layer has been considered as a function of layer depth along perpendicular direction to the layer surface. We observed that the number of photonic bands increases with increasing the layer thickness irrespective of the refractive index of the constant refractive index layer, but their bandwidths decrease with increase of their refractive index. Widths of the photonic bands are strongly depend on the ratio of initial and final refractive index of the constituted exponential graded layer in the considered 1-D GPC structures. The tunability of bandwidth of photonic bands by adjustment of gradation profile parameters of the layers has been done. In addition, we observed that the Omni-directional band exist when we choose the relative refractive index of homogeneous layer equal to 1.5 and 2.0, while it disappeared for 1.0. We found that 1-D GPC structures with relative

refractive index of the constituted homogeneous layer equal to 1.5 and 2.0 are appropriate to design the widespread Omni-directional band gap mirrors, filters, reflectors, sensors and other optical devices. For TE-polarization, 1-D GPC structures with refractive index of the homogeneous layer equal to 1.0 has widest common reflection band. Therefore, these structures can be utilized especially for configuration of TE-polarized devices.

**Acknowledgements** This work has been supported by Department of Science & Technology DST (INDIA) in the form of project, grant No. 100/IFD2489/2011-12.

#### References

- Yablonovitch, E.: Inhibited spontaneous emission in solid-state physics and electronics. Phys. Rev. Lett. 58, 2059–2062 (1987)
- Joannopoulos, J.D.: Photonic crystals: putting a new twist on light. Nature 386, 143–159 (1997)
- Lipson, R.H., Lu, C.: Photonic crystals: a unique partnership between light and matter. Eur. J. Phys. 30, S33–S48 (2009)
- Tolmachev, V.A., Perova, T.S., Ruttle, J., Khokhlova, E. V.: Design of one-dimensional photonic crystals using combination of band diagram and photonic gap map approaches. J. Appl. Phys. 104, 033536 (2008)
- Negro, L.D., Yi, J.H., Nguyen, V., Yi, Y., Michel, J., Kimerling, L.C.: Spectrally enhanced light emission from aperiodic photonic structures. Appl. Phys. Lett. 86, 261905 (2005)
- 6. Alagappan, G., Sun, X.W., Shum, P., Yu, M.B., Doan, M.T.: One-dimensional anisotropic photonic crystal with a tunable bandgap. J. Optical Soc. Am. B 23, 159–167 (2006)
- Zharov, A.A., Zharova, N.A.: Quasi-guided electromagnetic beam propagation in one-dimensional photonic crystal with a left-handed metamaterial. J. Appl. Phys. 103, 013109 (2008)
- 8. Vasconcelos, M.S., Mauriz, P.W., de Medeiros, F.F., Albuquerque, E.L.: Photonic band gaps in quasiperiodic photonic crystals with negative refractive index. Phys. Rev. B **76**, 165117 (2007)
- Yu, Z., Wang, Z., Fan, S.: One-way total reflection with one-dimensional magneto-optical photonic crystals. Appl. Phys. Lett. 90, 121133 (2007)
- Macia, E.: Exploiting aperiodic designs in nano-photonic devices. Rep. Prog. Phys. 75, 036502 (2012)
- Mishra, R.K., Pandey, P.C.: Study of s-polarized photonic bandgap structure in three component opticalfibonacci multilayers composed of nanoscale materials. Solid State Commun. 149, 946–951 (2009)
- Fink, Y., Winn, J.N., Fan, S., Chen, C., Michel, J., Joannopoulos, J.D., Thomas, E.L.: A dielectric omnidirectional reflector. Science 282, 1679–1682 (1998)
- 13. Yablonovitch, E.: Engineered omnidirectional external-reflectivity spectra fromone-dimensional layered interference filters. Opt. Lett. 23, 1648–1649 (1998)
- Seeser, J.W., Carniglia, C.K., Dowling, J.P.: Perfect mirrors, past and present. Science 283, 938 (1999)
- Xiang, Y., Wen, S., Dai, X., Tang, Z., Fan, D.: Extend the omnidirectional zero-average-index photonic band gap using the band edge formalism: application to the metamaterial with Drude dispersion. J. Appl. Phys. 108, 093105 (2010)
- 16. Rauh, H., Yampolskaya, G.I., Yampolskii, S.V.: Optical transmittance of photonic structures with linearly graded dielectric constituents. New J. Phys. 12, 073033 (2010)

- 17. Sang, Z.F., Li, Z.Y.: Optical properties of one-dimensional photonic crystals containing graded materials. Optics Commun. **259**, 174–178 (2006)
- Pandey, P.C., Thapa, K.B., Ojha, S.P.: Large forbidden band in one-dimensional multi-layered structure containing exponentially graded materials. Optics Commun. 281, 1607–1614 (2008)
- 19. Rauh, H., Yampolskaya, G.I., Yampolskii, S.V.: Optical transmittance of photonic structures with logarithmically similar dielectric constituents. J. Opt. 14, 015101 (2012)
- Singh, B.K., Thapa, K.B., Pandey, P.C.: Optical reflectance and omnidirectional bandgaps in Fibonacci quasicrystals type 1-D multilayer structures containing exponentially graded material. Optics Commun. 297, 65–73 (2013)
- Singh, B.K., Pandey, P.C.: A study of optical reflectance and localization modes of 1-D Fibonacci photonic quasicrystals using different graded dielectric materials. J. Mod. Opt. 61, 887–897 (2014)
- Singh, B.K., Pandey, P.C.: Influence of graded index materials on the photonic localization in one-dimensional quasi-periodic(thue-morse and double-periodic) photonic crystals. Optics Commun. 333, 84–91 (2014)
- Singh, B.K., Kumar, P., Pandey, P.C.: Tunable photonic band-gaps in one-dimensional photonic crystals containing linear graded index material. Appl. Phys. B Lasers Optics 117, 947–956 (2014)
- 24. Yeh, P.: Optical Wave in Layered Media. Wiley, Interscience, New Jersey (1988)

# Chapter 9 Smith-Purcell Based Terahertz Frequency Multiplier: Three Dimensional Analysis

Alireza Tavousi, Ali Rostami, Ghassem Rostami and Mahboubeh Dolatyari

**Abstract** In this paper, we numerically investigate on a three dimensional Smith-Purcell (SP) based terahertz frequency multiplier. Frequency multiplication procedure is proposed via learning of spontaneous SP radiation. At low frequency regions, texturing the metallic surfaces would manipulate the spoof surface plasmons (SSPs). Due to electronically exciting of these SSPs in a one-dimensionally extended metallic grating, a strong electron-plasmon momentum coupling develops and electron bunches arise. The evanescent wave releases from both ends of the structure. At the frequency harmonics of these SSPs, an umklapp process redshifts the SSP momentum beyond the light zone and the SP radiation is generated in the span of 0.466-1.1 THz and detected with a maximum peak around  $90^{\circ}$  (with respect to the grating). The SP radiation center frequency is  $\sim 0.65$  THz. Three dimensional particle-in-cell (PIC) simulations have been performed via finite integral method and the obtained results completely agree with analytic ones.

A. Tavousi · A. Rostami (⊠)

Photonic and Nanocrystal Research Lab. (PNRL), Faculty of Electrical and Computer Engineering, University of Tabriz, 5166614761 Tabriz, Iran

e-mail: rostami@tabrizu.ac.ir

A. Tavousi

e-mail: tavousi@tabrizu.ac.ir

A. Rostami  $\cdot$  G. Rostami  $\cdot$  M. Dolatyari OIC Research Group, School of Engineering-Emerging Technologies, University of Tabriz, 5166614761 Tabriz, Iran e-mail: gh.rostami@tabrizu.ac.ir

M. Dolatyari

e-mail: m.dolatyari@tabrizu.ac.ir

© Springer International Publishing Switzerland 2016 P. Ribeiro and M. Raposo (eds.), *Photoptics 2015*, Springer Proceedings in Physics 181, DOI 10.1007/978-3-319-30137-2\_9 146 A. Tavousi et al.

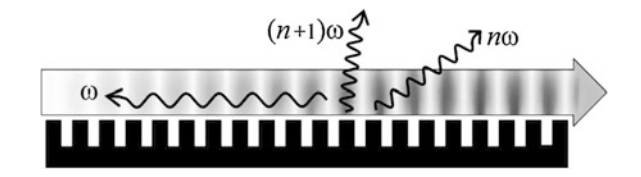
#### 9.1 Introduction

Surface plasmon polariton (SPP) and its low-frequency counterpart, "spoof" surface plasmon (SSP) confine electromagnetic (EM) waves within sub-wavelength dimensions. Researchers [1] have described that one can manipulate the "spoof" surface plasmons at low frequency regions by texturing the metallic surface. With electronically exciting of SSPs in a one-dimensionally extended metallic grating, a strong electron-plasmon momentum coupling develops and electron bunches arise. At the frequency harmonics of these SSPs, an umklapp process redshifts the SSP momentum beyond the light zone, and thus THz waves are created.

The 'terahertz' word has been useful in diverse electromagnetic bands such as for frequency analysis of point contact diode detectors [2], frequency of a Michelson interferometer [3], frequencies beneath the far infrared, the resonant frequency of a water laser, and now terahertz is practical to sub-millimetre wavelengths extent between 100 and 1000  $\mu$ m (0.3–3 THz) [4]. Until recently there were no suitable sources and detectors for THz and thus this portion of the EM spectrum has not been used a lot. In the middle of the most advanced terahertz uses which the scientific enquiries are investigating about, we take along the following examples: medical security, communications, industrial measurements, imaging, chemistry and biochemistry applications, molecular recognition and protein folding, and sub-millimetre astronomy [5].

Smith–Purcell radiation (SPR) [6] mechanism is based on excitation of "surface eigenwaves" [7, 8] above a metallic gratings. This phenomenon is considered to be one of the most interesting methods of generating sub-millimetre waves mainly in THz realm [9–16]. At frequency harmonics of the mentioned surface waves, in which the electron bunches advance, spontaneous SPR develops. This device is abstractly shown in Fig. 9.1 and is frequently studied in electron-beam driven frequency multiplication processes [17] and certainly it is a promising candidate for producing terahertz radiation [7, 18–20]. As discussed in the most of theoretical studies [19] and in experimental ones [21], SPR power is still very low which its origin seems to be from its spontaneous nature. However if an additional cavity is used, one can harness higher power and better selectivity [10]. Due to non-relativistic nature of the device, it neither requires a high operational voltage nor a large focusing magnet. Yet it is able to play the role of a compact THz radiation source in a diverse range of uses such as spectroscopy and diagnostics of different media.

**Fig. 9.1** Conceptual design of an self-excited electron-beam driven THz frequency multiplier [7]



The metallic structures are assumed to be made of perfect conductor and unlike the experimental cases [21] in which pencil-like electron beams are used, a sheet electron beam is implemented as electron source. Through enhancing the interaction of electron beam and surface wave, the operating current and output power will increase. It is known that single-mode operation of the surface wave is possible in the circumstance of a legitimately slim beam [22]. However when the beam size comes to be far larger than the wavelength of the surface mode, different transverse parts of the beam would be capable of excitement of different transverse surface modes. Hence their frequencies and phases are marginally altered and the optical beam diffuses [7]. This is already mentioned for SP backward wave oscillators (BWOs) that they will not operate with an infinitely wide grating [22].

In this paper, we evaluate the incoherent spontaneous SPR emission using CST studio suite, a 3-D particle-in-cell simulator code which simulates the conditions in which the space charge and electromagnetic fields are concurrently acting together.

#### 9.2 Simulation Model

Here, we consider a metallic grating slab having a period L and thus a wave number of K =  $2\pi/L$  (the grating length will differ in each particular case). Generally, due to interaction of electron beam with exponentially decaying evanescent surface wave (i.e. SSP) an evanescent wave can travel above the surface of such grating in the direction in which the slab is periodic (perpendicular to the grooves). Considering c as the travelling speed of light in vacuum, the electron beam's velocity is  $v_e = \beta_e c$ . Thus the relativistic factor  $\beta_e$  is defined as  $\beta_e = \sqrt{1 - (1 + \gamma^2/2)^{-2}}$ , where  $\gamma^2 = E_e/E_0$ ,  $E_0 = m_e c^2/e = 5.11 \times 10^5 \, \text{V} \sim 0.511 \, \text{MV}$ , and  $m_e$  and e are the rest mass and charge of the electron, respectively. Using this equation, the beam kinetic energy is found as  $\eta_e = eE_e(v_e) = eE_0\left(1/\sqrt{1-\beta_e^2}-1\right)$ . The phase velocity is  $v_{\varphi} = \omega/k = c\beta_{\varphi}$ , and the group velocity is  $v_g = d\omega/dk = \beta_g c$  where  $\omega$  is the frequency of the traveling evanescent wave and k is the wave number.

In k space, the dispersion diagram is periodic and for each of its Brillion zones the dispersion curve is symmetric about k/K = 0.5 (surface mode is like a  $\pi$ -type one and is named as the Bragg point). Depending on the position of the synchronous working point which may be positioned on the right-hand side or left-hand side of k/K = 0.5 (for which the group velocity disappears), the operating characteristics of the device fundamentally alter. For k/K > 0.5, the group velocity is negative and for k/K < 0.5 the group velocity is positive. Here we are interested in the earlier case and the negative group velocity regions. If we assume that due to an electron beam, there would be no gain or losses in the structure, then we may use Floquet's theorem for solving Maxwell equations on top of the grating and the dispersion relation  $D_0(\omega, k) = 0$  is obtained for the evanescent waves [23].

148 A. Tavousi et al.

With respect to the operating point, our Smith-Purcell based THz source is a backward wave oscillator in which, if a certain beam current threshold known as start current is reached, the optical intensity grows to saturation even if no feedback mirrors are employed.

The wavelength of radiation  $\lambda$  that is observed at the angle  $\theta$  (which is measured from the direction of travelling electron) is given by:

$$\frac{\lambda}{L} = \frac{1}{|n|} \left( \frac{1}{\beta_{\varphi}} - \cos \theta \right), \tag{9.1}$$

where n indicates the harmonics of the diffraction order. To compare our 3-D simulation results with experiment results, we chose to use grating parameters of Urata et al. [21] summarized in Table 9.1. However, the data provided by them is for 2-D case and we will add the third dimension to it. Figure 9.2 illustrates the simulation model and the placement of detectors.

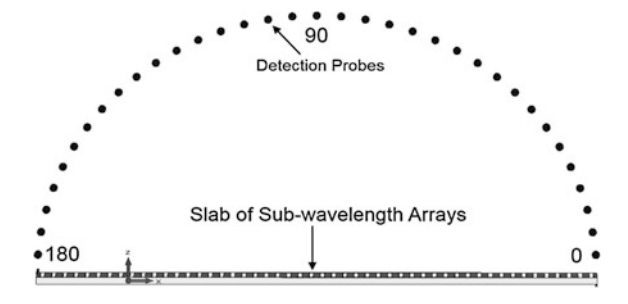
In this SPR based device, the moving electron beam must significantly interact with the fundamental surface mode which is confined very close to the grating. To describe the interaction mechanism and strength between the surface mode and the moving electron beam, we need to numerically solve the coupled Maxwell-Lorentz equations. For this purpose, we used the CST studio suite software for solving these coupled equations via 3-D PIC codes.

Since we have performed our simulations in a 3-D scheme, a variable width from  $400{\text -}1600~\mu\text{m}$  is used for grating. Also, the grating length is variable and arranged to be 20, 40, 60, 80, and 100 periods. The main simulations are performed using a grating with length Ng = 100 periods and S = 800  $\mu$ m and then the results are extended and compared with other grating lengths and widths.

**Table 9.1** Grating profile used in the experiments of Urata et al. [21]

Grating period	173 μm		
Groove width	62 μm		
Groove depth	100 μm		

Fig. 9.2 Conceptual illustration of the simulation model and the placement of detectors

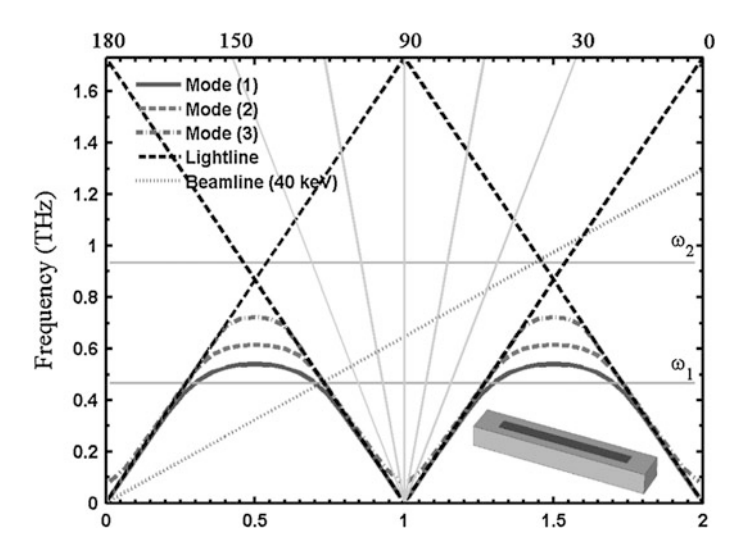


#### 9.3 Simulation Results

The dispersion diagram of the first three modes of a grating with parameters from Table 9.1 is shown in Fig. 9.3. The 40 keV beam negative group velocity region i.e. k/K > 0.5, thus the synchronous point frequency would be calculated as 0.466 THz. For a device operating in positive group velocities, higher beam energies is required.

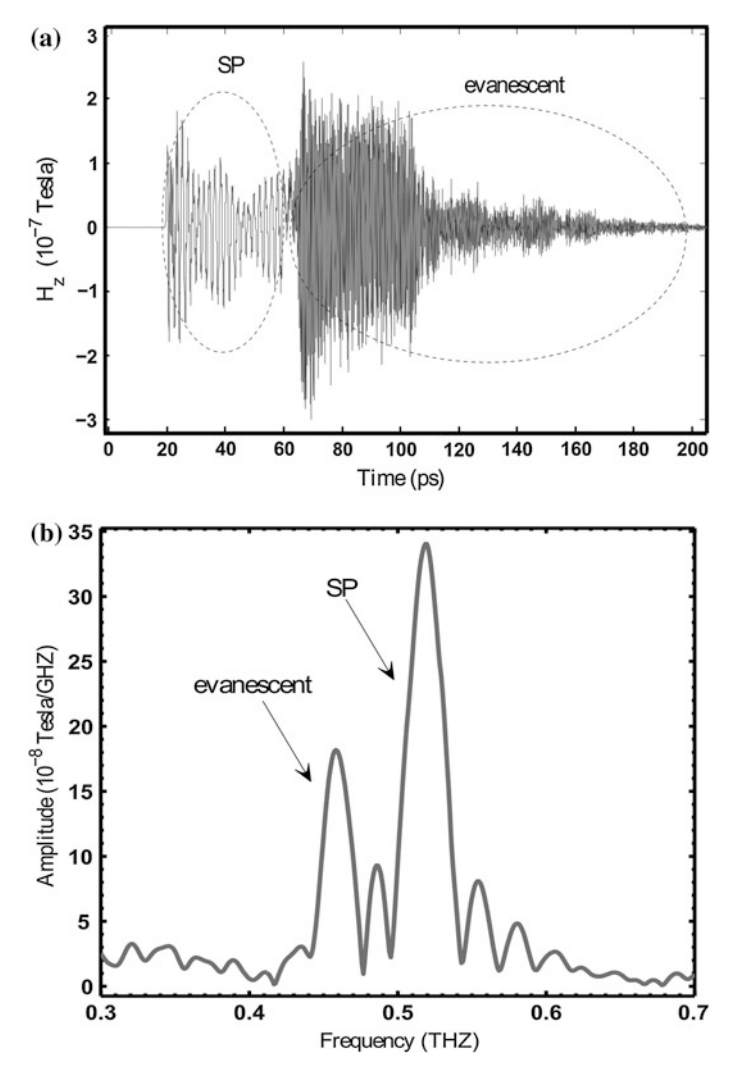
To study the incoherent (spontaneous) SP radiation, first we let the length of the grating to be  $N_g = 20L$  and then we perform the simulation with a single electron bunch which last for 0.1 ps length which carries a charge of q = 0.048 pC. Since this bunch is short enough compared to the longest radiation wavelength, we can assume that the radiation is coherent. Our focus is on the first order SP radiation (|n| = 1). Figure 9.4a illustrates the time evolution of  $H_z$  signal observed by the far detector mounted at angle of  $135^{\circ}$  from the centre of grating (Ng = 20L). Taking fast Fourier transform, we learn that there exists two pure and independent radiation peaks in the spectrum. Figure 9.4b shows that the one which peaked at 525 GHz is the SP radiation, while the other peak at 466 GHz is the evanescent wave.

Figure 9.5 compares the effect of varying the grating width. We can see that by changing the length of grating from  $400{\text -}1600~\mu m$  the amplitude of both SP and evanescent wave increases. Despite of increment of amplitude, the frequency centre of SP and evanescent wave are constant and the same.



**Fig. 9.3** Dispersion diagrams of the first three surface modes of the metallic grating with parameters given in Table 9.1. The 40 and 250 keV beam lines intersect with the fundamental mode in k/K < 0.5 and k/K > 0.5 regions respectively

150 A. Tavousi et al.



**Fig. 9.4** a Evolution of  $H_z$  time signal observed by detector at angle of 135° from the centre of grating (Ng = 20L). b The FFT of the corresponding time signal clearly indicating that SP radiation and evanescent wave are separated

Given the detection angle, period, diffraction order, and the phase velocity of the electron beam to the analytic (9.1), one can predict the wavelength in which the SP radiation occurs. Figure 9.6 compares the analytic expression for wavelength of SP radiation with the centre frequencies recorded by sweeping  $\theta$  with  $6^{\circ}$  step for all detection angles between  $0^{\circ} < \theta < 180^{\circ}$ . From this figure we find out that indeed the longest radiation wavelength (lowest radiation frequency) is equal to the wavelength of the evanescent wave. The results obtained from CST are in good

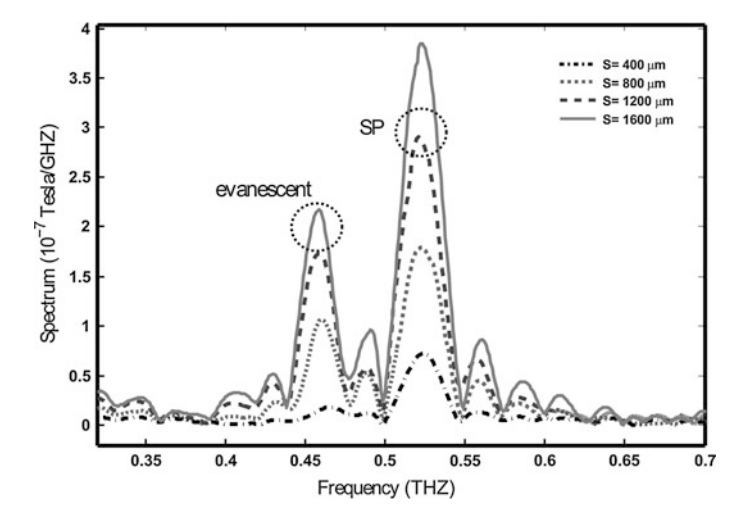
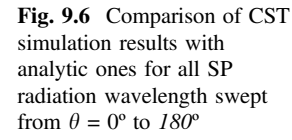
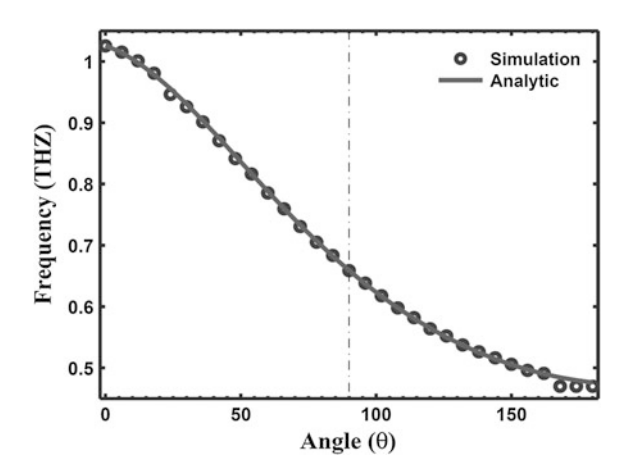


Fig. 9.5 The FFT taken from the temporal behaviour of the radiated signal at the angle  $\theta = 135^{\circ}$  and 5.5 mm distance from the centre of the grating for Ng = 20L for different grating widths





agreement with those obtained via (9.1). As shown in this figure the maximum SP amplitude occurs in angle  $\theta = 90^{\circ}$ . The short come of this equation is that it says nothing about the SP radiation amplitude.

Now, by increasing the grating length we try to neglect the effect of evanescent wave or at least minimize it. In Fig. 9.7a–f, we have recorded the temporal behaviour of the radiated signal (from a longer grating with Ng = 100L) which is detected from different detectors at  $\theta = 70^{\circ}$ ,  $90^{\circ}$ ,  $125^{\circ}$ ,  $135^{\circ}$ ,  $150^{\circ}$ , and  $170^{\circ}$  (and 5.5 mm distance from the centre of the grating). We see that the SP portion of time signal is increased and the evanescent portion is very little with respect to the SP. Taking fast Fourier transform from all signals, and plotting them together for all

152 A. Tavousi et al.

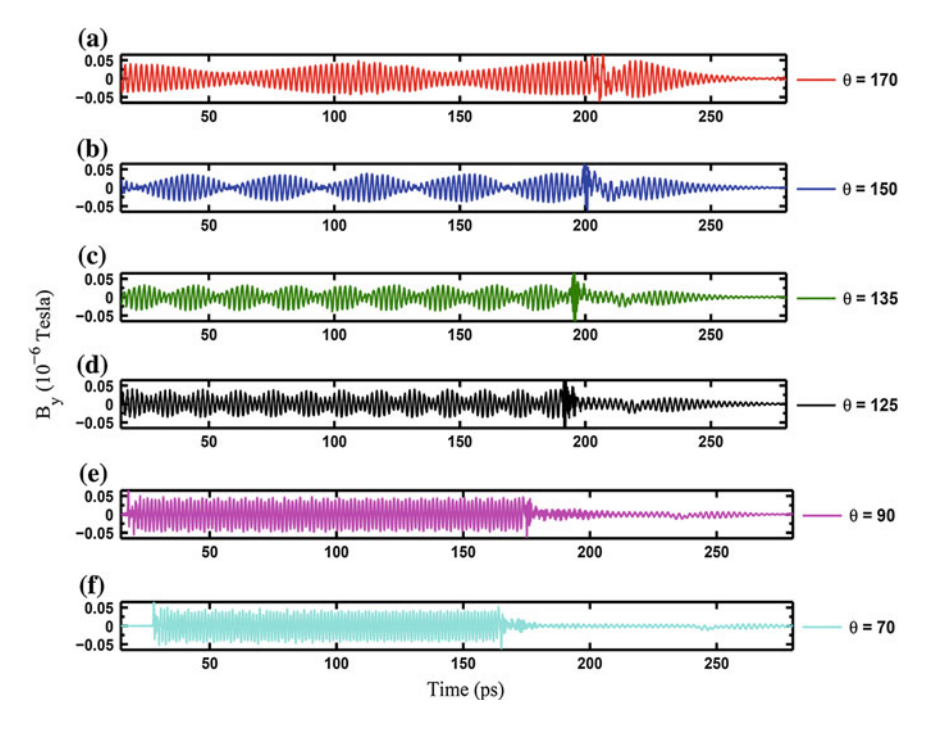


Fig. 9.7 Temporal behaviour of the emitted signal discovered at the angle of  $\theta = 135^{\circ}$  and distance of 5.5 mm from the centre of the grating for Ng = 100L

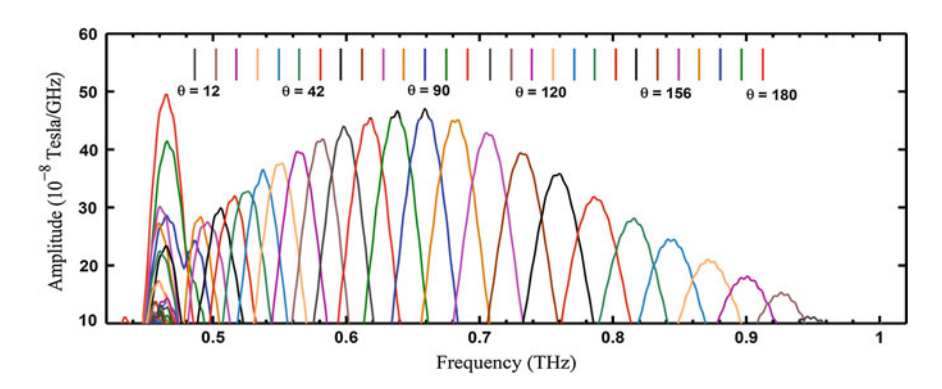


Fig. 9.8 FFT taken from temporal behaviour of the emitted signal which is perceived at the different detection points changing from  $12^{\circ} < \theta < 180^{\circ}$  with step of  $\theta = 6^{\circ}$  for Ng = 100L

swept angles (Fig. 9.8), we learn that unlike the evanescent wave frequency which is angle independent, both SP radiation centre frequency and amplitude are fluctuating by varying the detection angle.

Figure 9.9 shows the normalized far field polar plot for the H-field at different  $\theta$  angels. These plots show that the main radiation lobe of each specific frequency is

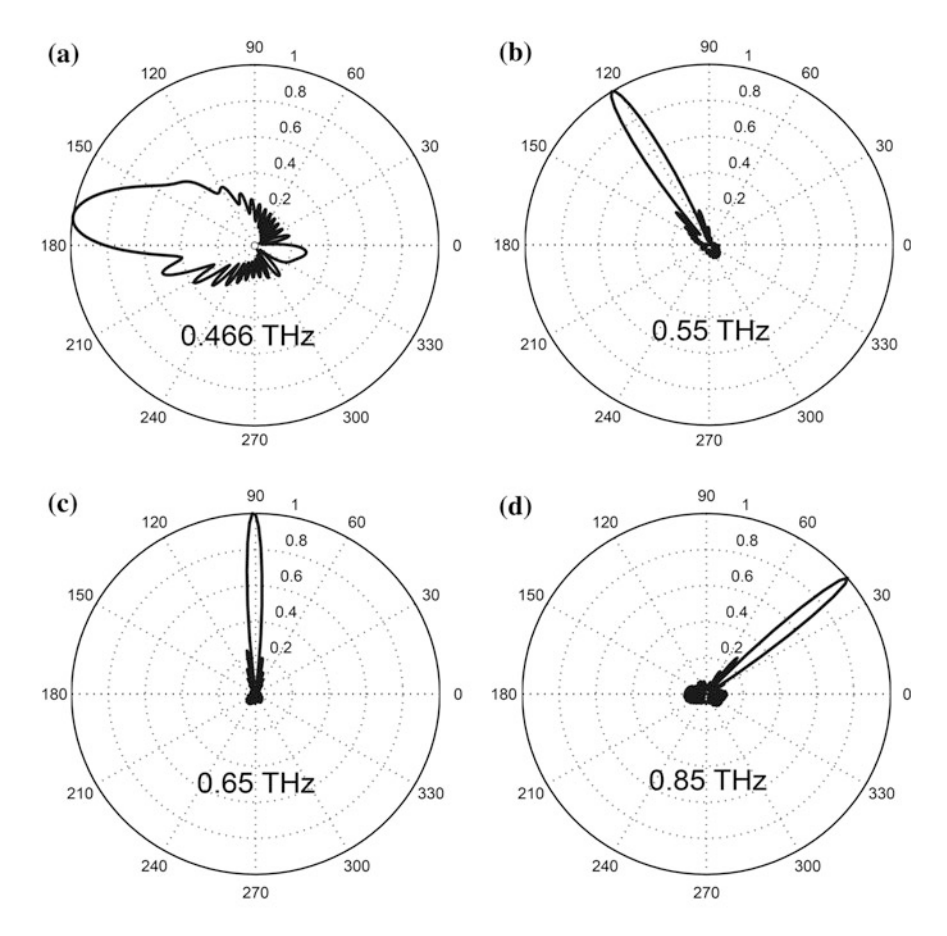
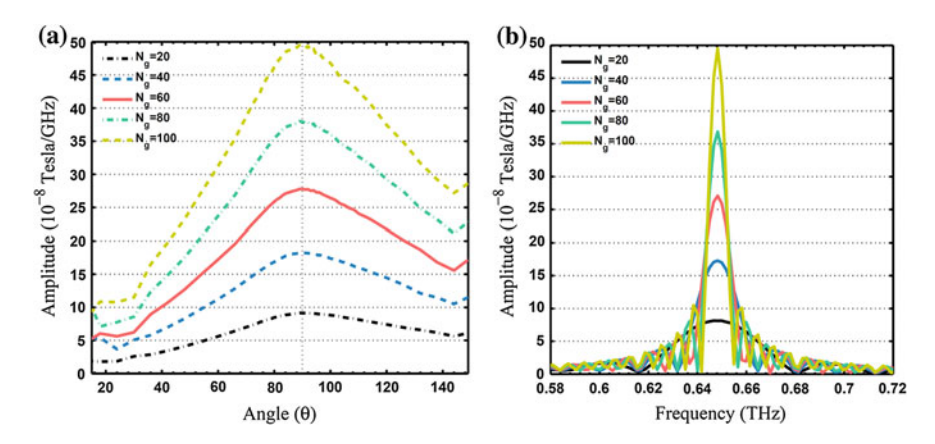


Fig. 9.9 Far field polar plots for H-field at different frequencies of a 0.466 THz, b 0.55 THz, c 0.65 THz, and d 0.85 THz. The plots are normalized

located in the angle which was predicted by (9.1). In the 0.466 THz, our result show that radiation occur near  $180^{\circ}$ , and as we know from previous, this frequency belongs to the evanescent wave so radiates from the upper grating end (near gun). The 0.55, 0.65, and 0.85 THz cases are also radiating at  $120^{\circ}$ ,  $90^{\circ}$ , and  $40^{\circ}$ , respectively.

Figure 9.10a, b both show the FFT amplitudes of time signals for different grating lengths. In Fig. 9.10a, we swept the detection angle from  $0^{\circ}$  to  $180^{\circ}$  and recorded the maximum of FFT amplitude for gratings with Ng = 20, 40, 60, 80, and 100L. We can see that, as the length of grating increase from 20 to 100 periods, the amplitude grows nonlinearly. Given this, we are able to calculate the growth-rate of the produced signal. In Fig. 9.10b, focusing only on one detection angle in which the radiation is maximum (i.e.  $\theta = 90^{\circ}$ ), we find out that by increasing the grating length, not only the FFT amplitude increases but the spectral resolution of the signal increases too.

154 A. Tavousi et al.



**Fig. 9.10** a The max FFT amplitude of time signals versus detection angel for different grating widths of Ng = 20L, 40L, 60L, 80L, and 100L. **b** The max FFT amplitude of time signals versus detection angel of  $\theta = 90^{\circ}$  for different grating widths of Ng = 20L, 40L, 60L, 80L, and 100L

#### 9.4 Conclusions

Surface plasmon polariton (SPP) and its low-frequency counterpart, "spoof" surface plasmon (SSP) confine electromagnetic (EM) waves within sub-wavelength dimensions. Through proximity interaction of a travelling electron beam with high kinetic energy electrons near a micro-meter scale one-dimensional metal grating, we electronically excite the terahertz SSPs. At the frequency harmonics of this surface eigenwave, electrons gather together as bunches and redshifts the SSP momentum beyond the light zone. Due to electron-plasmon momentum coupling spontaneous SP radiation develops which can be used as a frequency multiplication device. Three dimensional simulations on the generation of have been completed with particle-in-cell (PIC) method and these finite integral based PIC results very well satisfied the analytical results.

**Acknowledgements** The authors would like to thank University of Tabriz.

#### References

- Tavousi, A., Rostami, A., Rostami, G., Dolatyari, M.: 3-D numerical analysis of smith-purcell based terahertz wave radiation excited by effective surface plasmon. IEEE/OSA J. Lightwave Technol. pp. 99 (2015). doi:10.1109/JLT.2015.2435255
- 2. Kerecman, A.J.: The Tungsten-P type silicon point contact diode. In: Microwave Symposium, 1973 IEEE G-MTT International, pp. 30–34 (1973)
- Fleming, J.: High-resolution submillimeter-wave fourier-transform spectrometry of gases. IEEE Trans. Microw. Theory Tech. 22, 1023–1025 (1974)
- 4. Siegel, P.H.: Terahertz technology. IEEE Trans. Microw. Theory Tech. 50(3), 910–928 (2002)

- 5. Rostami, A., Rasooli, H., Baghban, H.: Terahertz Technology: Fundamentals and Applications, vol. 77. Springer, Berlin (2010)
- 6. Smith, S.J., Purcell, E.M.: Visible light from localized surface charges moving across a grating. Phys. Rev. **92**(4), 1069 (1953)
- Bratman, V.L., Fedotov, A.E., Makhalov, P.B., Rusin, F.S.: Smith-Purcell frequency multiplier with synchronization of radiation from a wide electron beam. Appl. Phys. Lett. 94(6), 061501 (2009). doi:10.1063/1.3079678
- Cao, M., Liu, W., Wang, Y., Li, K.: Three-dimensional theory of Smith-Purcell free-electron laser with dielectric loaded grating. J. Appl. Phys. 116(10), 103104 (2014). doi:10.1063/1. 4894706
- Price, E., Walsh, J., Kimmitt, M.: Short submillimeter operation of the Planar Orotron. Nucl. Instrum. Methods Phys. Res., Sect. A 304(1), 133–136 (1991)
- Bratman, V.L., Makhalov, P., Fedotov, A., Khaimovich, I.: Excitation of orotron oscillations at the doubled frequency of a surface wave. Radiophys. Quantum Electron. 50(10–11), 780–785 (2007)
- Bratman, V.L., Ginzburg, N., Petelin, M.: Common properties of free electron lasers. Opt. Commun. 30(3), 409–412 (1979)
- 12. Gover, A., Sprangle, P.: A unified theory of magnetic bremsstrahlung, electrostatic brem-sstrahlung, Compton-Raman scattering, and Cerenkov-Smith-Purcell free-electron lasers. IEEE J. Quant. Electron. 17(7), 1196–1215 (1981)
- Mizuno, K., Ono, S., Shibata, Y.: Two different mode interactions in an electron tube with a Fabry-Perot resonator-The Ledatron. IEEE Trans. Electron Devices 20(8), 749–752 (1973)
- 14. Rusin, F., Bogomolov, G.: Generation of electromagnetic oscillations in an open resonator. JETP Lett. 4, 160–162 (1966)
- Schächter, L., Ron, A.: Exponential gain in a Smith-Purcell amplifier. Appl. Phys. Lett. 53 (10), 828–830 (1988)
- Liu, W., Xu, Z.: Simulations of table-top watt-class 1 THz radiation sources with two-section periodic structure. J. Appl. Phys. 115(1), 014503 (2014)
- 17. Tavousi, A., Rostami, A., Rostami, G., Dolatyari, M.: 3-D Analysis of terahertz frequency multiplier excited due to interaction of convection electron beam and surface waves (Smith-Purcell Effect). In: 3rd International Conference on Photonics, Optics and Laser Technology, Berlin, Germany 2015. SCITEPRESS, Science and Technology Publications, Lda (2015)
- Li, D., Imasaki, K., Yang, Z., Park, G.-S.: Three-dimensional simulation of super-radiant Smith-Purcell radiation. Appl. Phys. Lett. 88(20), 201501 (2006)
- 19. Andrews, H.L., Brau, C.A.: Gain of a Smith-Purcell free-electron laser. Phys. Rev. Spec. Topics—Accelerators Beams **7**(7), 070701 (2004)
- Shin, Y.-M., So, J.-K., Jang, K.-H., Won, J.-H., Srivastava, A., Park, G.-S.: Superradiant terahertz Smith-Purcell radiation from surface plasmon excited by counterstreaming electron beams. Appl. Phys. Lett. 90(3), 031502 (2007). doi:10.1063/1.2432270
- Urata, J., Goldstein, M., Kimmitt, M.F., Naumov, A., Platt, C., Walsh, J.E.: Superradiant Smith-Purcell emission. Phys. Rev. Lett. 80(3), 516–519 (1998)
- 22. Li, D., Imasaki, K., Gao, X., Yang, Z., Park, G.-S.: Reduce the start current of Smith-Purcell backward wave oscillator by sidewall grating. Appl. Phys. Lett. **91**(22), 221506 (2007)
- Andrews, H.L., Boulware, C., Brau, C., Donohue, J., Gardelle, J., Jarvis, J.: Effect of reflections and losses in Smith-Purcell free-electron lasers. New J. Phys. 8(11), 289 (2006)

# Chapter 10 Stochastic Resonances and Gated Detection in Photon Number Resolving Detectors

Shree Krishnamoorthy, Harish Ravi, Pradeep K. Kumar and Anil Prabhakar

**Abstract** Gated avalanche photo-detectors (GAPD) use gated detection and thresholding electronics to act as Geiger counters to indicate presence of photons. They show stationary Poissonian average noise statistics, though we see evidence of underlying non-stationary stochastic resonance. Both the Poissonian and stochastic resonance processes contribute to the experimentally observed dark count, and are described theoretically. To resolve photon numbers from coherent faint light pulses, we use GAPD with an optical recirculating loop. With the temporal separation of the input photons from the pulse, we not only achieve photon number resolution up to n = 0.024, but also bypass the stochastic resonance effects

#### 10.1 Introduction

Quantum cryptography holds the promise of unconditional security [1, 2]. However, practical implementations of quantum key distribution, such as DPS-QKD or FC-QKD, use coherent optical states that are susceptible to photon number splitting attacks [3–6]. In the absence of purely single photon sources, development of QKD systems need photon number resolution [7]. While, optical fibers are easily adapted for quantum communication, the detectors needed for photon number resolution are not easily available and the development of photon counting detectors continues to be of current interest [8]. In the telecommunication

S. Krishnamoorthy · A. Prabhakar (🖂)

Department of Electrical Engineering, Indian Institute of Technology Madras,

Chennai, India

e-mail: anilpr@ee.iitm.ac.in

H. Ravi

Indian Institute of Science, Bangalore, India

P.K. Kumar

Indian Institute of Technology, Kanpur, India

<sup>©</sup> Springer International Publishing Switzerland 2016

P. Ribeiro and M. Raposo (eds.), Photoptics 2015,

band, around 1.55 µm, PMTs have very low efficiencies of about 2 % where as InGaAs avalanche photodiodes (APDs) provide an efficiency of 20 % with lower dark counts [7]. APDs operated in Geiger mode indicate only the presence of or absence of photons and cannot resolve the number of incident photons, making their output binary in nature. The Geiger mode enhances the sensitivity, but is accompanied by a degradation in the signal to noise ratio [9]. For photon number resolution, the incoming photons are redistributed to multiple detection slots, using spatial or temporal multiplexing methods [10, 11]. Temporal multiplexing can be achieved by an optical fiber loop connected to the coupler [12, 13], and the timing information can be used to gate the APD.

APDs are based on the avalanche process which dictates the noise characteristics in them [14]. Gated APD (GAPD) systems suffer from dark counts and after-pulsing [15, 16]. Other than the known noises, our implementation of the GAPD shows evidence of stochastic resonance. In this article we analyze the probabilities of occurrence of different bit patterns to extract the photon number statistics in the presence of stochastic resonance. We first characterize the GAPD, and estimate the efficiency of detection. We then measure the photon arrival statistics and compare them to theoretical predictions for a GAPD in the presence of noise and underlying stochastic resonance.

We implement a multi-photon resolving detector (MPRD) with a recirculating optical loop followed by the GAPD. When a coherent state is input to the MPRD, the bit pattern that ensues should follow a statistical distribution. The roundtrip time of the optical loop was less than one-eighth of the time between coherent optical pulses input to the loop. This allowed us to use digital electronics to store and analyze the 8-bit pattern of 1's and 0's following each input pulse, and to repeat the exercise for  $N=2^{24}$  input pulses. Our experiments validate the Poissonian statistics of the coherent state down to an average photon number of 0.024.

#### 10.2 Detector Characterization

When counting photons, we often assume that the sources of noise (typically shot and thermal noise) are independent of the photon counts. In cases where there are other low amplitude stationary processes that look like noise, the assumption of independent noise statistics breaks down. Stochastic resonance is used to boost signal to noise ratio (SNR) in detection schemes. However, stochastic resonances can cause false detections at periodic intervals in a system using gating and threshold [17, 18], as in our system. We find a suitable operating point for the GAPD and extract actual photon detection probabilities with proper data analysis in the presence of stochastic resonances.

#### 10.2.1 Efficiency

In a gated avalanche detector, the detection is performed in a small gate ON time and then the detection is disabled allowing the avalanche process to subside. During the gate ON time an avalanche current could be triggered by either incident photon or a thermal electron. In the absence of both triggers, there is no avalanche current. The dark counts are a result of thermally triggered electron currents.

The decision that an avalanche occurred is done by comparing the current output against a preset threshold value for the current. The triggered avalanche could occur anywhere during ON time, and the probability of '1' is the sum of probabilities of its occurrence anywhere during the detection window. At the end of each detection cycle a digital '1' or '0' is recorded for a positive detection or a null detection, respectively, and the binary information is stored as a bit. This creates a series of bits for subsequent detection cycles. We make a large number of observations over many detection cycles and store them in digital memory. The number of observations is only limited by the size of digital memory available on the digital electronics chosen.

We describe how to find the optimal operating point for the detector. In absence of any incident photons, dark current causing an avalanche is registered as '1'. We assume that dark counts occur with a probability  $p_{\rm d}(1)$ . For a detector with efficiency  $\eta$ , when a pulse with mean photon number n is incident on the detector from a coherent laser source, no detection or '0', occurs when there are no photons and there is also no dark count. The probability of no detection due to photons is  $e^{-\eta n}$  and of no dark count is  $(1-p_{\rm d}(1))$ . The probability p(0) of a '0' is given by

$$p(0) = e^{-\eta n} (1 - p_{d}(1)). \tag{10.1}$$

To arrive at the probability of a positive detection or '1', p(1), we recognize that a detection occurs either due to the presence of a photons, with a probability  $(1-e^{-\eta n})$ , or due to the dark count, with a probability  $p_{\rm d}(1)$ . However, since the two events are independent, we must subtract the probability of both events occurring together, i.e.,  $p_{\rm d}(1)(1-e^{-\eta n})$ . Thus,

$$p(1) = (1 - e^{-\eta n}) + p_{d}(1) - p_{d}(1)(1 - e^{-\eta n})$$
  
= 1 - p(0). (10.2)

It should be noted that both efficiency and dark counts, depend on ambient temperature of the detector. Optimization of the temperature and bias of the detector is necessary for the experiments.

For our experiments, we have used an InGaAs APD (model NR8300FP from NEC) with an internal Peltier cooler. The detector case was further cooled by an external Peltier stage. The breakdown voltage of the APD was about 71 V at a case temperature of 4 °C. To operate the APD in Geiger mode, we bias the APD below 71 V and apply a gating voltage of 3.3 V for 5.2 ns. The GAPD followed by digital

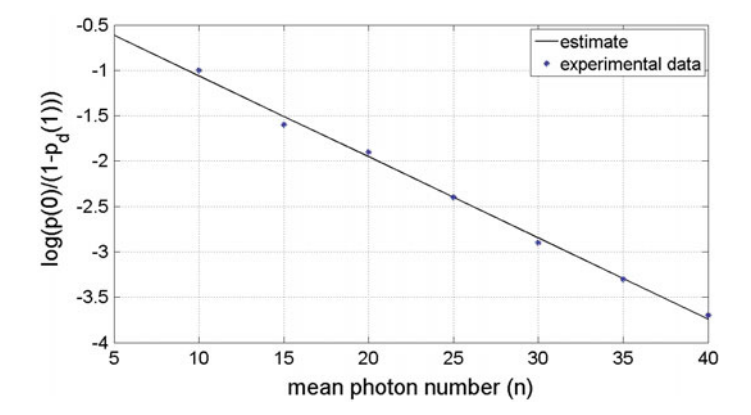
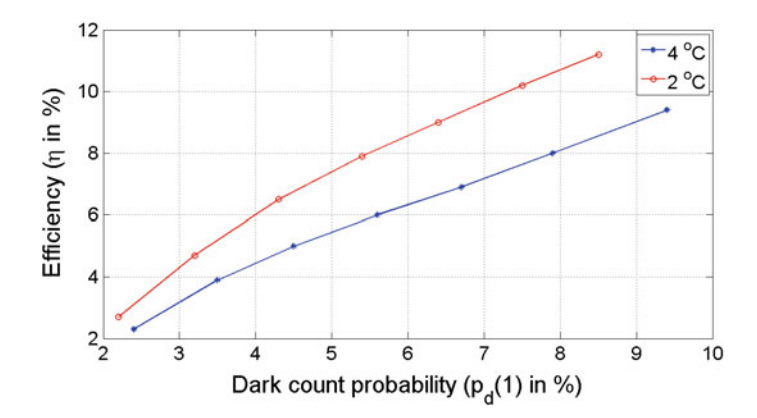


Fig. 10.1 Null detections with increasing mean photon numbers, used to find detector efficiency η

counting electronics (FPGA based), acted as one photon counter. The digital electronics had 2 GB RAM, or 16 Gbits, to easily collect and store obtained statistics.

Figure 10.1 shows the dependence of  $p(0)/(1-p_d(1))$  on n, from which we extract the efficiency  $\eta$  of the detector. At a bias of 69.7 V and a detector case temperature of 4 °C, we found that the efficiency  $\eta$  was  $0.0893 \pm 0.006$ . We also confirm that a change in temperature and bias conditions change the dark count and the efficiency of the detector, as shown in Fig. 10.2. Thus, we find the optimal operating point for the GAPD at a case temperature of 2 °C with a bias voltage of 69.7 V, where  $\eta = 0.11$ , and the dark count  $p_d(1) = 0.085$ . For a 10 % higher detection rate than the dark count the null detection probability is p(0) = 0.9065. Substituting p(0) in (10.1) and using  $\eta = 0.11$ , we estimate the average photons



**Fig. 10.2** Detection efficiency for different case temperatures and dark counts at constant bias. The APD was cooled by an internal Peltier, to about 20 °C below the case temperature

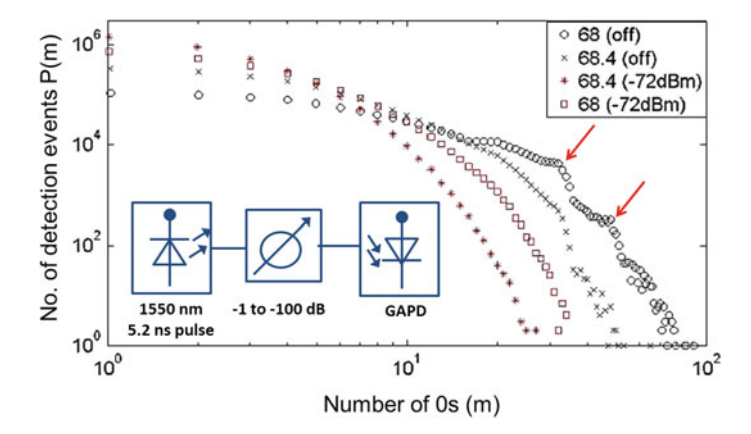


Fig. 10.3 Effect of bias voltage and optical input, on the time between consecutive detections. Each 0 bit corresponds to a delay of 1  $\mu s$ 

per pulse to be n = 0.0848, or one true detection for every 12 detection cycles at the GAPD. The average photon number resolution can be further improved by using this detector after a recirculating loop as described in Sect. 10.3.

#### 10.2.2 Detection Probabilities and Stochastic Resonance

In the previous section, we obtained the optimal operating point for the GAPD by studying the average noise statistics. However, we are in a position to look at the statistics of how the detector responds in Geiger mode, both with and without an incident optical pulse, for consecutive detection cycles.

Consider a coherent optical pulse train, with an average of n photons in each pulse, incident on the detector. For the experimental set-up in the inset of Fig. 10.3, we send N such pulses, and collect statistics on the number of times the detector is triggered. For each received pulse, if a null detection occurs then a "0" is recorded and when a positive detection occurs a "1" is recorded, as described previously. We thus obtain binary statistics of (0, 1) for each received pulse.

For N incident optical pulses, only one of the binary values of (0,1) can occur. This leads to binary probability distribution for each incident pulse, p riangleq p(1) being the probability of a detection registered as "1" and the probability of null detection being 1-p=p(0), as shown in (10.2) and (10.1). For N optical pulses the positive detections will follow a binomial distribution with a mean  $\mu=Np$  and a variance of N(1-p)p. In the binary statistics series,  $\mu$  corresponds to the total number of 1-bits registered, out of a total of N bits corresponding to N incident pulses. Averaging over the number of detection events, we get an estimate  $\bar{p}=\mu/N=p$ , with the standard deviation

$$\sigma_N = \sqrt{\frac{p(1-p)}{N}} \tag{10.3}$$

decreasing with increasing N. This is same as results found in other threshold, gated detectors as in [9].

The time period between successive gates pulses was set to 1  $\mu$ s. Analyzing the digital bit pattern at the output of the GAPD is akin to obtaining a digital frequency spectrum, with a resolution of 1 MHz. In Fig. 10.3, we plot the frequency of occurrence of the m consecutive 0-bits for  $N=2^{24}$  bits collected in each experiment. We observe an increased occurrence of some patterns when compared to others (indicated by arrows). These "resonances" are quenched when optical pulses of power of -72 dBm are provided. The occurrence of patterns at periodic intervals and its reduction due to the incidence of a few photons is suggestive of a stochastic resonance in the system [19].

In Fig. 10.4, we see that these resonances persist, and are even magnified, as we change the bias and increase the temperature. Both bias voltage and the temperature signal change the noise in the system, which affected the intensity of the resonance. To further confirm the stochastic resonance behaviour, we perform a separate experiment with the same detection system. We used a laser modulated by a sinusoidal signal and measured the signal to noise ratio (SNR) at different frequencies of the sinusoidal signal, as shown in Fig. 10.5 with the schematic of the experiment shown in the inset. We found that the GAPD shows a four fold increase in SNR close to 66 kHz. This enhancement in SNR is related to the Kramer's rate of switching between the 0 and 1 bit for the binary output detector system [20].

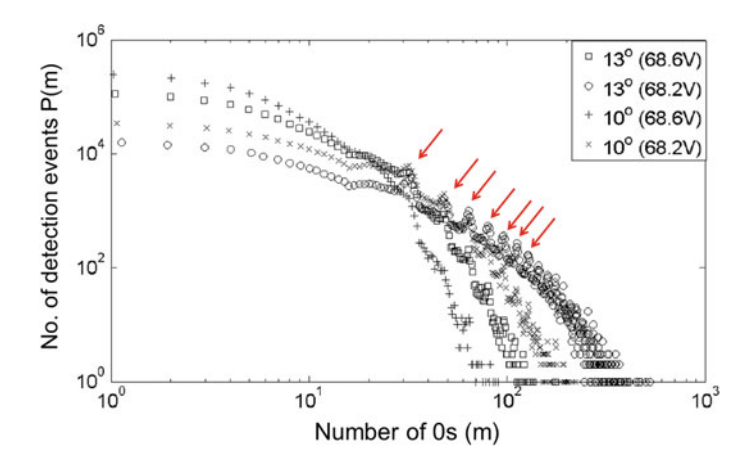


**Fig. 10.4** GAPD behavior in terms of bit pattern occurrences, with change in bias and temperature. The *arrows mark* anomalous increases in event detections, attributed to a stochastic resonance

Previous experiments on the GAPD at a lower bias of 67 V, had established that a 1 µs gap between gate pulses would be sufficient to release any trapped energy [21]. With increasing ON time of the laser pulses (20 ns), longer dead times of up to 10 µs in the GAPD has been reported in other studies [16, 22].

Longer dead times are attributed to after-pulsing effects in the avalanche photodetector. An after-pulse occurs when trapped charges are created and released at random delays after the avalanche current's occurrence. The released charges can trigger another avalanche process. The delay between the first avalanche and the after-pulse would depend on the trap lifetime of the trapped charges. The after-pulses contribute to the false positive detections and is considered as noise.

To understand noise statistics, we take a closer look at one of the data sets in Fig. 10.4, with optics off, and estimate the probability of dark count detection  $(p_d)$  in the presence of stochastic resonances. In absence of any incident photons, n=0, from (10.2) and (10.1) the probability of a "1" is now  $p(1)=p_d$  and the probability of a "0" reduces to  $p(0)=(1-p_d)$ . Since  $p_d<0.1$ , the probability of detecting more than two after-pulses becomes negligible. Hence, we restrict our analysis to understanding the probability of observing two 1s separated by m 0s. This is equivalent to the probability of obtaining m 0s followed by a 1 in the state diagram model for the gated Geiger mode APD, developed by Kolb, for obtaining SNR with after-pulsing [9]. Assuming that our first bit is detected with a probability  $p_d$ , followed by m 0s, the next bit is detected with a probability  $p_d^2(1-p_d)^m$ . Repeating this experiment N times, we obtain

$$P(m) = Np_d^2 (1 - p_d)^m. (10.4)$$

To estimate the probability p from the data we ignore the regions affected by the resonance and fit the remaining data using (10.4). The mathematical treatment of detection probabilities, in the presence of stochastic resonance, is deferred to the Appendix.

In all the collected data-sets, we found that resonance peaks occur every m=16 pulses, consistent with one of the stochastic resonance peaks in Fig. 10.5. The width of each resonance is 4 clock cycles, for all bias and temperature conditions. With this information we exclude the data around the local maxima, fit the rest of the data to a semilog function, find the slope and extract  $p_d=0.024$ . Since the data was obtained in the absence of any optical signal, we found that removing the resonance peak in the collected data, while post-processing, decreased the effective dark counts by a factor of four. In Fig. 10.6, the residuals were scaled with respect to the number of events found experimentally for each point. Figure 10.6 also shows that we can observe stochastic resonances till approximately 0.2 ms, corresponding to m=200, beyond which the residual error in our fit builds up.

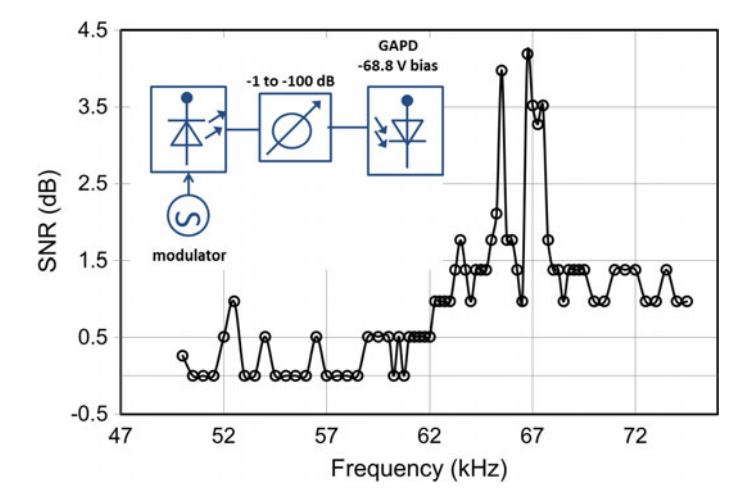
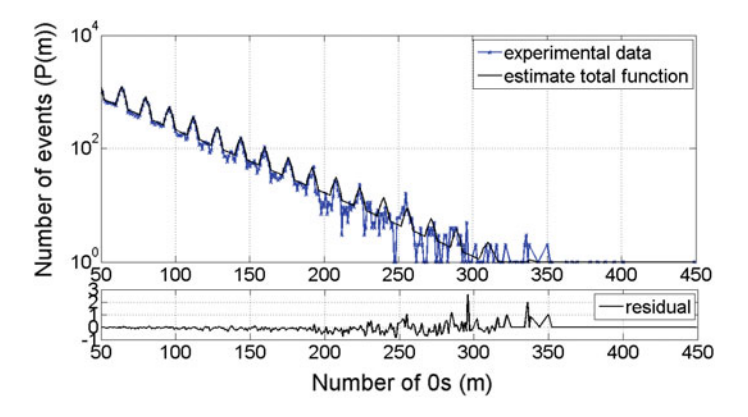


Fig. 10.5 Frequency of stochastic resonance of the GAPD, with inset showing the experimental set-up used



**Fig. 10.6** After-pulsing statistics in presence of stochastic resonances. APD was gated every 1 μs

## **10.3** Resolving Photon Numbers

The MPRD setup consists of a coherent, pulsed laser source, a variable optical attenuator (VOA) followed by an optical recirculating loop and GAPD as shown in Fig. 10.7. The laser pulses, attenuation of the VOA and the gating of GAPD are computer controlled. To analyse the working of the MPRD, we use the GAPD characteristics obtained in Sect. 10.2, and estimate the decrease in detection probability for each recirculation of the optical pulse. Finally, we analyse the bit patterns obtained at the detector for consecutive detections and compare them to theoretical probability estimates. With 2 GB RAM, we were able to collect over a million instances of the experiment.

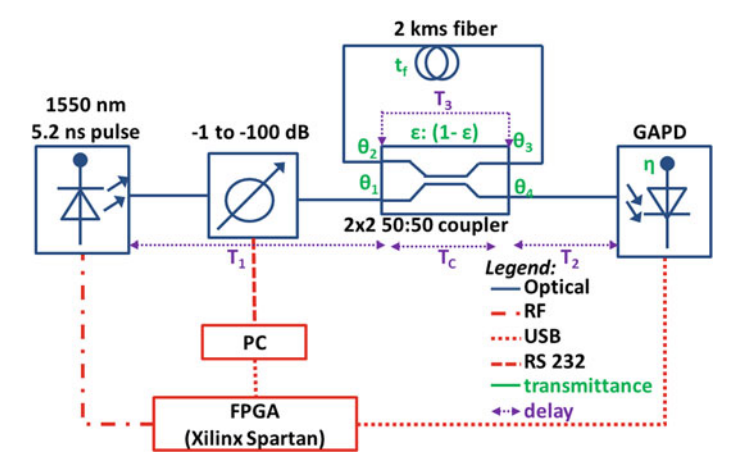


**Fig. 10.7** The MPRD setup showing timing information  $(T_i)$ , coupler splitting ratio  $(\varepsilon)$ , and transmittances  $(\theta_i)$ 

#### 10.3.1 Experimental Setup

The MPRD experiment was first reported in [13]. A laser pulse of 5.2 ns pulse width is sent through the MPRD. We chose a delay fiber length of 2 km, which gave the detector  $10~\mu s$  to recover between successive measurements. The recirculation repeats until the pulses are sufficiently attenuated in the system. We used a 3 dB splitter, connectors with about 0.5 dB loss and a 2 km long spool with 0.4 dB loss. The optical path lengths were adjusted so that the return pulses arrived in synchronization with the system clock. For this purpose, we used an optical fiber array with length increasing in steps of 20 cm (1 ns delay) in series with our fiber spool until our pulses were correctly synchronized and the detection probability was maximized.

All the elements in the MPRD were controlled electronically, by a XILINX (SPARTAN XC3S400) field programmable gate array (FPGA). The FPGA was clocked at 24 MHz and two digital clock managers (DCMs) available on the FPGA were used to multiply the clock frequency to 48 MHz and to provide a 90° phase shifted signal. These were used to generate laser pulses of width 5.2 ns and gating pulses of width 10.4 ns. The FPGA was used for pulsing the laser, gating the APD, setting of bias and threshold. The variable optical attenuator was used to change the incident power or photon number in the optical pulse. At the output of the comparator in the GAPD, eight detections are recorded for each laser pulse transmitted through the MPRD, giving us a byte of data for each laser pulse, with each bit synchronized to the round trip time of the recirculating loop.

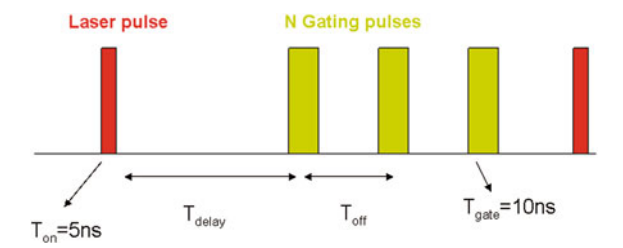


Fig. 10.8 Pulse travel time from the laser to the detector after multiple round trips in the MPRD (Number of gating pulses, N = 8)

#### 10.3.2 Timing Synchronization in MPRD

To synchronize the detector gates to the incoming optical pulses from the recirculating loop, we look at the pulse arrival times in Fig. 10.8. The pulses arrive at the GAPD with a fixed delay  $T_{\rm delay}$  from the laser. The detector has a gating period of 10.4 ns twice that of the optical pulse. The off time  $(T_{\rm off})$  of the detector needs to be precisely matched to the subsequent pulse arrival. If the pulse takes time  $T_1$  to travel up to the coupler, time  $T_2$  to travel from the edge of the coupler to the GAPD, time  $T_3$  to loop once in the fiber and time  $T_c$  to travel through the coupler. Thus, the arrival time for the tth pulse at the detector is t1 to travel through the coupler to the t2. We set t3 to loop once in the fiber and time t4 to travel through the coupler. Thus, the arrival time for the t4 pulse at the detector is t5 to travel through the coupler. Thus, the arrival time for the t6 pulse at the detector is t7 to travel through the coupler. Thus, the arrival time for the t6 pulse at the detector is t7 to travel through the coupler. Thus, the arrival time for the t8 pulse at the detector is t9 pulse.

#### 10.3.3 Photon Redistribution Statistics

The coupler has a division ratio of  $\varepsilon$ :  $1 - \varepsilon$ , the optical delay fiber has a transmittance  $t_f$ , the connectors have a transmittance of  $\theta_i = \theta$  and the detector has an efficiency of detection  $\eta$  as shown in Fig. 10.8. We calculate the transmission of the kth pulse [13].

$$T_{\text{eff}_k} = \theta_2 \varepsilon^{k-1} (1 - \varepsilon)^2 (t_f \theta_3 \theta_1)^k \theta_4 \eta.$$
 (10.5)

For a coherent input with an average photon number n, the kth detection pulse corresponds to an average photon number of  $nT_{\text{eff}_k}$ .

Starting from an average photon number n, the theoretical prediction for the probability of detection  $p_k(1)$  for the kth pulse is,

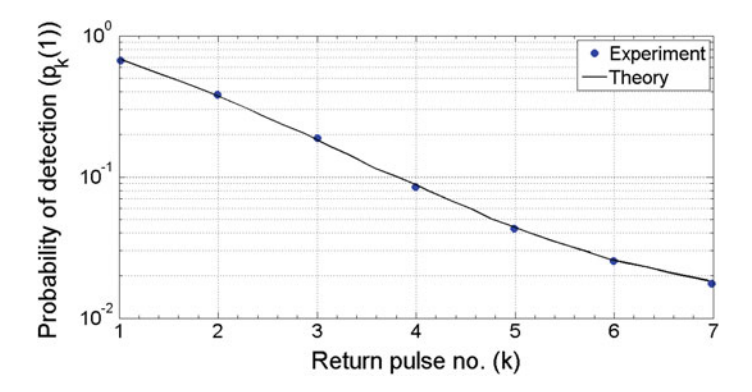


Fig. 10.9 Average detection probability of successive return pulse in MPRD

$$p_k(1) = 1 - \underbrace{e^{-\eta n T_{\text{eff}_k}}}_{\text{no photon}} \underbrace{(1 - p_{\text{d}})}_{\text{no noise}}.$$
 (10.6)

For n = 30,  $\eta = 0.15$ ,  $T_{\text{eff}_k} = 0.398$  (corresponding to 4 dB loss), and  $p_d(1) = 0.014$ , Fig. 10.9 shows the decreasing probability of a detection for each round trip and we observe a good match between our theoretical estimates and our experimental observations.

For each byte recorded, we analysed bit patterns for 3, 4 and 5 bits as shown in Fig. 10.10. An input pulse with average power of -63 dBm at the input of the 3 dB splitter in the MPRD, goes through seven round trips through the optical loop, with a loss of 4 dB per recirculation, to produce the last detection bit. The last bit out of the recirculating loop will, now, have an average power of -94 dBm, assuming a 5.2 ns pulse of optical wavelength 1.55  $\mu$ m, corresponding to an average photon number of 0.024. Even so, the Poissonian statistics of a coherent pulse are well preserved and the occurrence of a bit pattern follows the predicted probabilities.

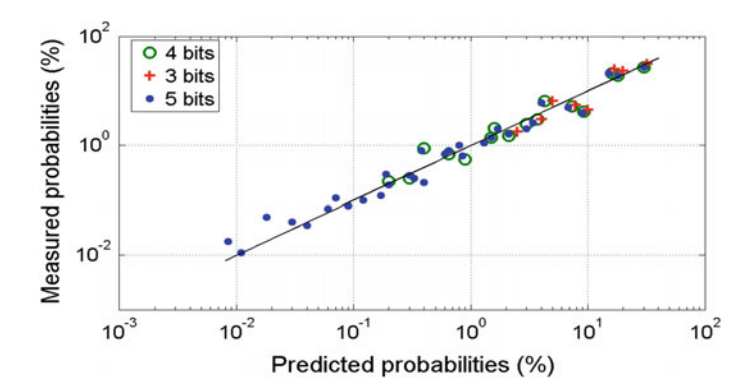


Fig. 10.10 Measured versus predicted bit pattern probabilities of detection patterns obtained in MPRD at -63 dBm. Modified from [13]

#### 10.4 Conclusions

This article describes the characterization of a gated avalanche photo-detector, used subsequently in a multi-photon resolving detector. We first experimentally characterize the GAPD and find its efficiency. We found that the GAPD was susceptible to stochastic resonance, which was affected by temperature and bias. The stochastic resonance was further investigated, and we saw that it had characteristic frequency around 66 kHz. When we used gated detection, with a delay of 1 µs between gate pulses, we were in effect digitally sampling the stochastic resonance. Discounting these resonances in our experimentally measured probabilities, we were able to characterize the GAPD for very low average photon numbers.

A recirculating loop is a simple way of splitting a Poissonian state into a series of temporal pulses. We described the statistical properties of such a multi-photon resolving detector. In our experiments, the recirculating loop was set up to achieve a delay of 10  $\mu$ s between successive optical pulses, while we gated the avalanche photodiode every 1  $\mu$ s. After each input coherent optical pulse we recorded the output for 8 gate pulses as one data byte, and did this for  $N=2^{24}$  optical pulses. We searched for correlations between successive gate pulses in the data bytes by looking at the bit patterns for 3, 4 and 5 bits. The probability of occurrence of a bit pattern followed the predicted probabilities, within the noise bounds of the system. Thus, we conclude that the MPRD could be used for photon number resolution, for average photon numbers as low as n=0.024 per pulse.

We observed that the stochastic resonance depends on both APD bias and temperature. Consequently, we were able to adjust these parameters and avoid the resonance, as we set up our photon number resolving experiments. We believe that we are the first authors to report on stochastic resonances in a GAPD system. Further investigations about the origins of the resonance, along with an appropriate statistical noise model, will help improve the performance of single photon detectors.

**Acknowledgements** This work was partly funded by the Department of Science and Technology, India under Grant No. SR/S3/EECE/21/2005. HR and PK were at IIT-Madras during the course of their studies. HR is also grateful to IIT-Madras for supporting his work as an Innovative Student Project.

## Appendix

Consider many detection cycles as shown in Fig. 10.11 with an underlying stochastic process. Here, from first principles of probability for arrival processes, we include the stochastic process to obtain the probability that an avalanche current is recorded in a detection cycle due noise in the system. This would lead to a dark count probability  $p_d$ . Consider X, a process that an avalanche occurred at

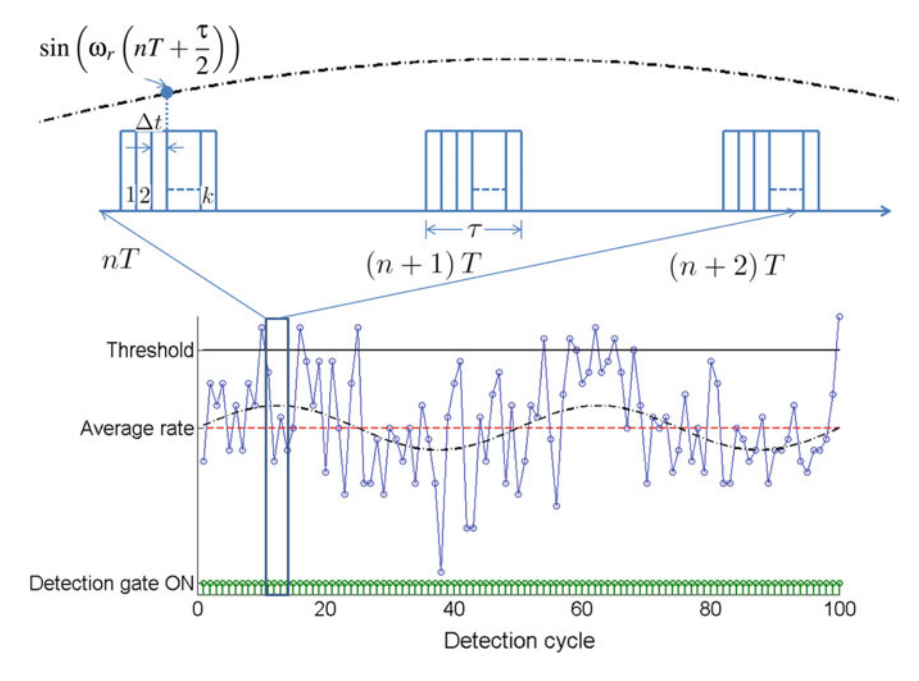


Fig. 10.11 Detection cycles showing gating period  $\tau$ , overlaid with the slowly varying stochastic process. Schematic representation of underlying noise that is referred to a threshold

time t. One would not observe any avalanche if for a given cycle at nT,  $X > (nT + \tau)$ 

$$Pr(X > (nT + \tau)) = \prod_{r=0}^{k-1} Pr(X \notin [nT + (r-1)\Delta t, nT + r\Delta t]).$$
 (10.7)

For any given time step r the probability of no avalanche in the time step  $\Delta t$  is given by

$$Pr(X \notin [nT + (r-1)\Delta t, nT + r\Delta t]) = 1 - Pr(X \in [nT + (r-1)\Delta t, nT + r\Delta t]).$$

$$(10.8)$$

If the rate average of avalanche occurrence is  $\lambda_0$  affected by an underlying slowly varying stochastic resonance that results in periodic change in the number of avalanches that occur  $\left(\lambda_1 \sin\left[\omega_r\left(nT+\frac{\tau}{2}\right)\right]\right)$  [17], giving the total rate of avalanche occurrence to be

$$\lambda(nT) = \lambda_0 + \lambda_1 \sin\left(\omega_r\left(nT + \frac{\tau}{2}\right)\right).$$

By setting  $\Omega_r = \omega_r T$  and  $\phi_\tau = \omega \tau$  the total avalanche rate can be written for each time step n as

$$\lambda(n) = \lambda_0 + \lambda_1 \sin(\Omega_r n + \phi_\tau). \tag{10.9}$$

Using this we can get obtain the probability of no avalanche in (10.8) to be

$$Pr(X \notin (nT + (r-1)\Delta t, nT + r\Delta t]) = 1 - \lambda(n)(nT + r\Delta t) - (nT + (r-1)\Delta t)$$

that reduces to

$$\begin{split} ⪻(X \not\in (nT + (r-1)\Delta t, nT + r\Delta t]) \\ &= 1 - \lambda(n)\Delta t \\ &= 1 - \left\{\lambda_0 + \lambda_1 \sin(\Omega_r n + \varphi_\tau)\right\}\Delta t \\ &= (1 - \lambda_0 \Delta t) \left\{1 - \frac{\lambda_1 \Delta t}{1 - \lambda_0 \Delta t} \sin(\Omega_r n + \varphi_\tau)\right\}. \end{split}$$

For  $\Delta t \rightarrow 0$ ,

$$Pr(X \notin (nT + (r-1)\Delta t, nT + r\Delta t]) = (1 - \lambda_0 \Delta t) \{1 - \lambda_1 \Delta t \sin(\Omega_r n + \phi_\tau)\}.$$
(10.10)

We now have the probability of no avalanche in the gating period  $\tau = k\Delta t$  in the *n*th detection cycle from (10.7) as

$$\begin{aligned} Pr(X > (nT + \tau)) \\ &= (1 - \lambda_0 \Delta t)^k (1 - \lambda_1 \Delta t \sin(\Omega_r n + \phi_\tau))^k \\ &= \left(1 - \lambda_0 \frac{\tau}{k}\right)^k \left(1 - \lambda_1 \frac{\tau}{k} \sin(\Omega_r n + \phi_\tau)\right)^k. \end{aligned}$$

When  $k \to \infty$  the above reduces to

$$Pr(X > (nT + \tau)) = \exp(-\lambda_0 \tau) \exp(-\lambda_1 \tau \sin(\Omega_r n + \phi_\tau)). \tag{10.11}$$

With  $\lambda_1 \ll 1$ 

$$Pr(X > (nT + \tau)) = \exp(-\lambda_0 \tau)[1 - \lambda_1 \tau \sin(\Omega_r n + \phi_\tau)]. \tag{10.12}$$

We now have from first principles, the probability that there is no dark count in the *n*th gate or  $(1 - p_d(n))$ .

We can now, modify the expression for average number of dark counts in (10.4) to include the stochastic resonance. The probability of m consecutive zeros starting from a given detection time n is

$$\begin{split} Pr(m0\text{'s}) &= \prod_{k=n}^{n+m-1} (1 - p_d(k)) \\ &= \prod_{k=n}^{n+m-1} \exp(-\lambda_0 \tau) \exp(-\lambda_1 \tau \sin(\Omega_r k + \varphi_\tau)) \\ &= \left\{ \exp(-\lambda_0 \tau) \right\}^m \left[ \prod_{k=n}^{n+m-1} \exp(-\lambda_1 \tau \sin(\Omega_r k + \varphi_\tau)) \right] \\ &= \left\{ \exp(-\lambda_0 \tau) \right\}^m \left[ \exp\left(-\lambda_1 \tau \sum_{k=n}^{n+m-1} \sin(\Omega_r k + \varphi_\tau)\right) \right]. \end{split}$$

Changing the index of product from k to s = k - n and incorporating the additional phase in the sinusoid by changing the initial phase to  $\phi'_{\tau}$ , we have

$$Pr(m0's) = \left\{ \exp(-\lambda_0 \tau) \right\}^m \left[ \exp\left(-\lambda_1 \tau \sum_{s=0}^{m-1} \sin(\Omega_r s + \varphi_\tau')\right) \right]. \tag{10.13}$$

With  $\lambda_1 \ll 1$  and setting  $\exp(-\lambda_0 \tau) = 1 - p_{d0}$ , we have

$$Pr(m0's) = (1 - p_{d0})^m \left[ 1 - \lambda_1 \tau \sum_{s=0}^{m-1} \sin(\Omega_r s + \phi_\tau') \right].$$
 (10.14)

Now, assuming  $p_d(m+1) \approx p_{d0}$ , we can rewrite (10.4) as

$$P(m) = Np_{d0}^{2} (1 - p_{d0})^{m} \left[ 1 - \lambda_{1} \tau \sum_{s=0}^{m-1} \sin(\Omega_{r} s + \phi_{\tau}') \right].$$
 (10.15)

#### References

- Bennett, C.H., Brassard, G., et al.: Quantum cryptography: public key distribution and coin tossing. In: Proceedings of the IEEE International Conference Computers, Systems and Signal Processing, Bangalore, vol. 175–179, IEEE, Bangalore, New York, (1984)
- Lo, H.-K., Chau, H.F.: Unconditional security of quantum key distribution over arbitrarily long distances. Science 283(5410), 2050–2056 (1999)
- 3. Norbert, L., Mika, J.: Quantum key distribution with realistic states: photon-number statistics in the photon-number splitting attack. New J. Phys. **4**(1), 44 (2002)
- Inoue, K., Waks, E., Yamamoto, Y.: Differential-phase-shift quantum key distribution using coherent light. Phys. Rev. A 68, 022317 (2003)
- Bloch, M., McLaughlin, S.W., Merolla, J.M., Patois, F.: Frequency-coded quantum key distribution. Opt. Lett. 32, 301–303 (2007)
- Valerio, S., Helle, B.P., Nicolas, C., Miloslav, D., Norbert, L., Momtchil, P.: The security of practical quantum key distribution. Rev. Mod. Phys. 81(3), 1301 (2009)

- 7. Hadfield, R.H.: Single-photon detectors for optical quantum information applications. Nat. Photonics **3**(12), 696–705 (2009)
- 8. Blasej, K., Prochazka, I., Kodet, J.: Photon counting detector for high-repetition-rate optical time transfer providing extremely high data yield. Opt. Eng. **53**, 081903 (2014)
- Kolb, K.: Signal-to-noise ratio of geiger-mode avalanche photodiode single-photon counting detectors. Opt. Eng. 53(8), 081904

  –081904 (2014)
- Fitch, M.J., Jacobs, B.C., Pittman, T.B., Franson, J.D.: Photon-number resolution using time-multiplexed single-photon detectors. Phys. Rev. A 68(4), 043814 (2003)
- Mogilevtsev, D.: Calibration of single-photon detectors using quantum statistics. Phys. Rev. A 82(2), 021807 (2010)
- 12. Haderka, O., Hamar, M., Peřina, J, Jr.: Experimental multi-photon-resolving detector using a single avalanche photodiode. Eur. Phys. J. D 28, 149–154 (2004)
- 13. Ravi, H., Prabhakar, A.: Coherent state statistics from time-resolved photon counting. In: SPIE OPTO, pp. 79600S-79600S. SPIE, San Francisco (2011)
- 14. McIntyre, R.J.: Multiplication noise in uniform avalanche diodes. IEEE Trans. Electron Devices **ED-13**(1), 164–168 (1966)
- Cova, S., Ghioni, M., Lotito, A., Rech, I., Zappa, F.: Evolution and prospects for single-photon avalanche diodes and quenching circuits. J. Mod. Opt. 51(9–10), 1267–1288 (2004)
- Tosi, A., Mora, A.D., Zappa, F., Cova, S.: Single-photon avalanche diodes for the near-infrared range: detector and circuit issues. J. Mod. Opt. 56(2–3), 299–308 (2009)
- 17. Wiesenfeld, K., Pierson, D., Pantazelou, E., Dames, C., Moss, F.: Stochastic resonance on a circle. Phys. Rev. Lett. **72**(14), 2125 (1994)
- 18. Zozor, S., Amblard, P.-O.: On the use of stochastic resonance in sine detection. Sig. Process. **82**(3), 353–367 (2002)
- Gammaitoni, L.: Stochastic resonance and the dithering effect in threshold physical systems. Phys. Rev. E 52(5), 4691 (1995)
- McDonnell, M.D., Stocks, N.G., Pearce, C.E.M., Abbott, D.: Stochastic resonance: from suprathreshold stochastic resonance to stochastic signal quantization. Cambridge University Press, Cambridge (2008)
- 21. Kumar, P., Thevan, S., Prabhakar, A.: Optimization of gated photodetection for quantum key distribution. In SPIE Europe Optics and Optoelectronics Conference. SPIE, Prague (2009)
- 22. Ben-Michael, R., Itzler, M.A., Nyman, B., Entwistle, M.: Afterpulsing in InGaAs/InP single photon avalanche photodetectors. In: Digest of the LEOS Summer Topical Meetings, pp. 15–16. IEEE, Quebec City (2006)

# Chapter 11 Design Optimization of Silicon-on-Insulator Slot-Waveguides for Electro-optical Modulators and Biosensors

Patrick Steglich, Claus Villringer, Silvio Pulwer, Mauro Casalboni and Sigurd Schrader

**Abstract** An approach for design optimization of the geometrical parameters of silicon-on-insulator slot-waveguides for electro-optical modulators and biosensors is presented. Theoretical investigations of field confinement factors and effective nonlinear areas for different slot-waveguide structures are critically analyzed and thoroughly calculated. With our simulation results we explain the high efficiency of electro-optical modulators and the enhanced sensitivity of biosensors compared to strip-waveguides. The influence on the effective refractive index, field confinement factor, and effective nonlinear area of the slot width and the silicon rail width were investigated.

## 11.1 Introduction

During the last decade a new waveguide approach based on silicon slot-waveguides have been proposed [1] and experimentally demonstrated to be suitable as optical phase shifter [2, 3]. Slot-waveguides enable a high field confinement in a narrow low-index region. Infiltration of slot-waveguide interior with an electro-optical (EO) polymer allows the use of the Pockels effect. Because of that they have high potential in the field of optical switching and high-speed modulation even at frequencies of 100 GHz [4]. As consequence various devices like Mach-Zehnder

P. Steglich (⋈) · C. Villringer · S. Pulwer · S. Schrader

Faculty of Engineering and Natural Sciences, University of Applied Sciences Wildau,

Wildau 15745, Germany

e-mail: Patrick.steglich@th-wildau.de URL: http://www.th-wildau.de/photonik

P. Steglich · M. Casalboni

Department of Industrial Engineering, University of Rome "Tor Vergata", 00133 Rome, Italy

© Springer International Publishing Switzerland 2016

P. Ribeiro and M. Raposo (eds.), Photoptics 2015,

interferometers [5] and micro-ring resonators [6] have been developed using slot-waveguide structures.

Slot-waveguides are the key element in order to integrate organic materials into silicon photonics. Mach-Zehnder modulators based on slot-waveguides infiltrated with linear EO organic materials are able to generate advanced modulation formats [7] since organic materials have less free-carrier dispersion, which normally leads to an intrinsic coupling of amplitude and phase. For that reason, slot-waveguides are highly promising for developing high-speed modulators for telecommunication interconnects [5].

Integrated optical sensors based on slot-waveguides have also been proposed [8] and developed [9]. In case of label-free bio-sensors it has been shown that the sensitivity of slot-waveguides is more than three times higher compared to conventional silicon strip-waveguides [10]. This fact is due to the high interaction between guided light and the cladding material, in the following named surrounding material.

In this work we present an approach in order to improve silicon-on-insulator (SOI) slot-waveguide structures for electro-optical modulators and integrated biosensors. Typical figures of merit like the field confinement factor and the effective nonlinear area are calculated optimizing the constructive parameters and results are discussed in detail.

# 11.2 Silicon-on-Insulator Slot-Waveguides

# 11.2.1 Theoretical Background

The major advantage of slot-waveguides is the fact that the guided light is confined in-between two silicon rails [11]. Consequently, the light is forced to interact directly with the surrounding material. Figure 11.1 shows a detailed cross-sectional view and compares the guided optical field in a strip-waveguide to that in a slot-waveguide. The reason for such a high confinement is the large-index contrast of the high-index silicon and the low-index surrounding material. At the interface the normal electric field, which is according to Fig. 11.1 the  $E_x$  field component, undergoes a large discontinuity. This results in a field enhancement in the low-index region which is proportional to the ratio of the dielectric constant of the surrounding material (SM) to that of silicon (Si),

$$E_x^{SM} = \frac{\varepsilon_{Si}}{\varepsilon_{SM}} E_x^{Si}. \tag{11.1}$$

Considering silicon with a refractive index of 3.48 and air as surrounding material with a refractive index of 1.0, the resulting field amplitude is 3.48 higher in the slot region. The high confinement inside the slot is of special benefit for EO applications. The so called silicon-organic hybrid (SOH) technology uses organic materials with exceptional high linear EO coefficients as surrounding material [12].

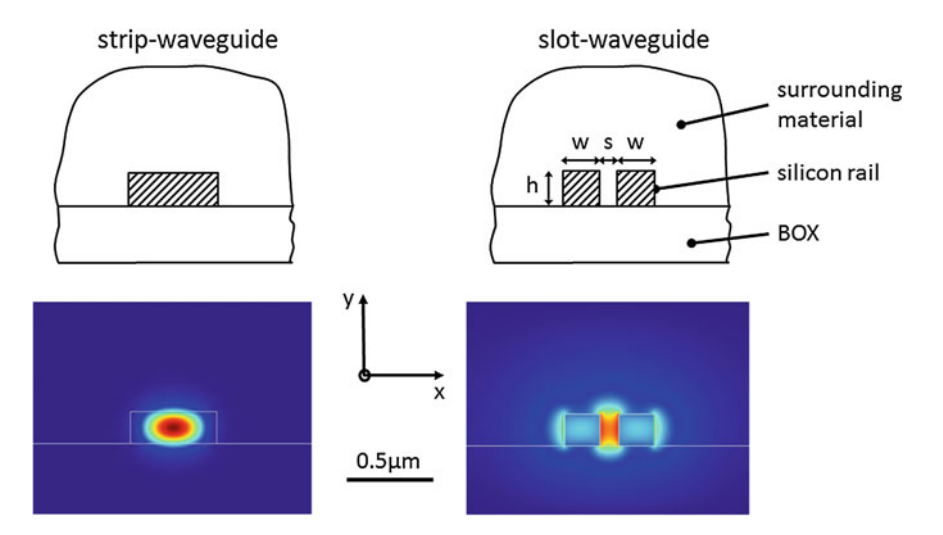


**Fig. 11.1** Cross-sectional view of a SOI strip-waveguide (*left*) and a SOI slot-waveguide (*right*). The *pictures below* show the optical field amplitude distribution. Both waveguide structures are on top of a buried oxide (BOX) substrate

Current integrated modulators are based on semiconductors like GaAs, InP, and silicon. In silicon photonics, fundamental speed limitations are related to carrier injection and removal [12]. Therefore, parametric processes are impaired by non-parametric processes like two-photon absorption and become to the main speed limiting factor. Additionally, silicon has a lack of nonlinear EO coefficients. All this can be overcome by using organic materials with nonlinear optical properties as active material.

The most challenging issue of SOH technology based slot-waveguides is the compatibility with common complementary-metal-oxide-semiconductor (CMOS) fabrication processes since such integrated photonic devices need a high integration rate and a cost efficient mass production environment.

Our SOI slot-waveguide consists of two silicon rails with a fixed height h of 220 nm due to common CMOS-like production restrictions. As illustrated in Fig. 11.1 both silicon rails are located on top of a buried oxide (BOX) substrate and are separated from each other by a slot width s and have a rail width w.

Due to the side-wall roughness slot-waveguides have relatively high optical losses of 10 dB/cm [13], which is five times higher compared to common strip-waveguides [12].

Figure 11.2 shows one scanning electron microscopy picture (top and cross-sectional view) of three slot-waveguides with different slot widths from the top view and one slot-waveguide in the cross-sectional view recorded with a focused ion beam. They are fabricated in a 130 nm SiGe BiCMOS production line at the Institute of High-Performance Microelectronics (IHP) in Frankfurt (Oder) using 200 mm SOI wafers and 248 nm DUV lithography.

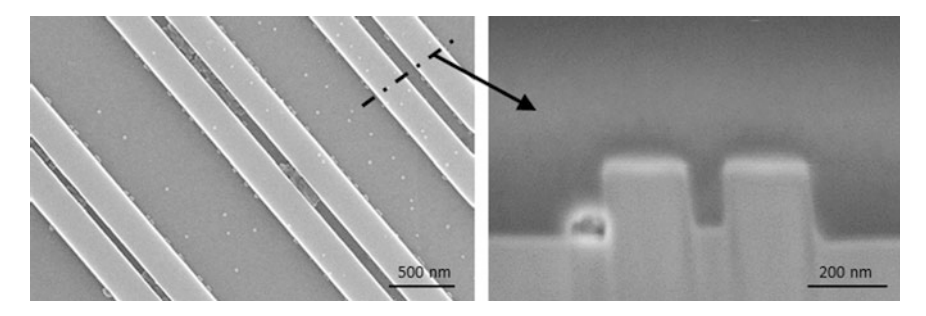


Fig. 11.2 Slot-waveguides with different slot widths fabricated with a 248 nm DUV lithography

# 11.2.2 State-of-the-Art

In 2013 and 2014 several silicon-organic hybrid modulators based on a Mach-Zehnder interferometer operating at 10, 12.5, 40, 84, and 112 Gbit/s have been reported [7, 14–17]. They have demonstrated advanced modulation formats such as 16QAM (Quadrature Amplitude Modulation) as well as OOK (On-Off Keying), BPSK (Binary Phase Shift Keying) and 8-ASK (Amplitude Shift Keying) signals [7, 18]. This is possible due to the fact that organic materials have less free-carrier dispersion which normally leads to an intrinsic coupling of amplitude and phase.

To exploit the advantages of each waveguide type an efficient strip-to-slot waveguide transition is needed. Yang Liu et al. developed in 2011 a so called strip to strip-loaded slot mode converter with losses around 0.81 dB [19]. Palmer et al. published in 2013 a strip-to-slot mode-converter with record-low losses of about 0.02 dB and negligible reflections between 1480 and 1580 nm [20].

A silicon-polymer hybrid slot-waveguide ring-resonator modulator with a 6 dB bandwidth of 1 GHz, a device tunability of 12.7 pm/V, and a Q-factor of 5000 were fabricated with 193 nm optical lithography [6]. However, slot-waveguide structures suffer from relatively high losses, mainly caused by sidewall roughness and Free Carrier Absorption (FCA) [21, 22]. As a consequence, slot-waveguide resonators like micro-ring resonators have typically small optical quality factors (Q-factors) [3, 6, 10]. To overcome this deficiency a novel ring resonator concept where the ring is only partially slotted have been recently proposed [23]. This approach combines an efficient slot-waveguide phase shifter with a low loss and strongly guiding silicon strip-waveguide in the same ring resonator. The device was fabricated on 200 mm SOI wafers using 248 nm DUV lithography and is covered with an EO polymer in a post process. A quality factor of  $\sim 2 \cdot 10^5$  and a DC device tunability of 338 pm/V was experimentally demonstrated.

The deposition of organic materials is typically done by spin-coating. With spin-coating, it is not guaranteed that the slot will be filled due to the centrifugal force and due to the fact that the polymer is liquid phase. With its viscosity and surface tension it precludes the polymer system from filling out the whole interior of the slot homogeneously. Special methods have been developed in order to fill-out

the interior of sub-micrometer slot-waveguide structures with such solid crystals [17]. Furthermore, multi-chromophore dendritic molecules, guest-host and side-chain polymer systems have been used as electro-optical cladding [16].

In the last decade integrated photonic sensors based on slot-waveguide ring-resonators have also been proposed [8] and developed [9]. In case of label-free bio-sensors it has been shown that the sensitivity of slot-waveguides is more than three times higher compared to conventional silicon strip-waveguides [10].

There are several publications about field confinement factors of slot-waveguide structures. These structures consist of vertical silicon rails [24] or multiple nanolayers [25]. However, none of them consider SOI slot-waveguides with typical geometrical dimensions for CMOS-like production processes as presented in the following.

# 11.3 Simulation of Slot-Waveguides

For the calculation of waveguide eigenmodes we employed a commercial full-vectorial 2D finite element method (FEM) based mode solver from COMSOL Multiphysics<sup>®</sup>. Doing this we swept several geometrical parameters like the silicon rail width and slot width whereas the height is fixed to 220 nm and the wavelength is assumed to be 1550 nm. Triangular vector-elements with a maximum and minimum element size of 8 and 6 nm, respectively have been adopted for meshing the profile. We have always used over  $12 \cdot 10^3$  mesh elements. For our simulations we consider a total domain of  $D_{tot} = 3 \, \mu \text{m}^2$  which is illustrated in Fig. 11.1.

In order to yield the mode field distribution and effective refractive index, the refractive index distribution n(x, y) for the structure shown in Fig. 11.1 need to be declared to calculate eigenvalues and eigenfunctions of the wave equation

$$\nabla \times (\nabla \times \mathbf{E}) - k_0^2 n^2 \mathbf{E} = 0, \tag{11.2}$$

where  $k_0$  is the wave number in free space. By doing this we get the optical field distribution for the quasi-TE and quasi-TM mode as shown in Fig. 11.3. In the following we will neglect the quasi-TM mode because it is over two orders of magnitude smaller than the quasi-TE mode. However, it should be mentioned that the cross-section capture area for the surface is typically greater for the quasi-TM mode in biosensing applications due to the difficulty in functionalising the interior of the slot.

Assuming a wavelength of 1550 nm, the refractive index for the silicon is  $n_{si} = 3.48$  and for the BOX substrate  $n_{box} = 1.444$  [26, 27]. The refractive index of the surrounding material  $n_{sm}$  is variable because it can be air, gas, fluid or an optical nonlinear material, depending on the application. In the following we will use  $n_{clad}$  as cladding refractive index instead of  $n_{sm}$  because we will consider in particular an

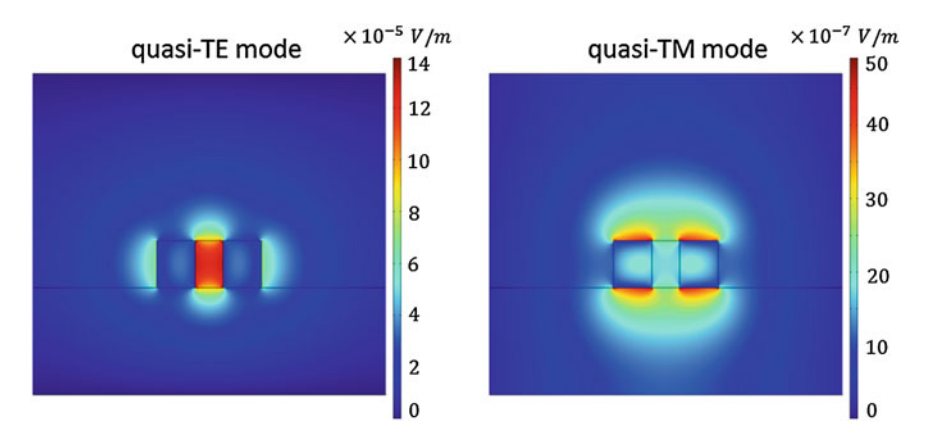


Fig. 11.3 Optical field distribution for the quasi-TE and quasi-TM mode of a SOI slot-waveguide

organic cladding material. We choose  $n_{clad} = 1.8$  which corresponds to a commercially available and reliable organic material named M3 (commercialized by GigOptix Inc.). M3 is successfully used for several slot-waveguide based electro-optical modulators like in [7, 14, 15, 18].

# 11.3.1 Field Confinement Factor of Slot-Waveguides

In order to design, develop and improve slot-waveguides for applications in the field of biophotonic or high-speed modulators it is necessary to calculate characteristic values which describe the confinement and therefore the interaction of light with the surrounding material. One figure of merit of how well the guided modal field is confined in a certain region is the so-called field confinement factor.

The field confinement factor is usually defined as the ratio of the time averaged energy flow through the domain of interest  $(D_{int})$  to the time averaged energy flow through the total domain  $(D_{tot})$ 

$$\Gamma = \frac{\int \int_{D_{int}} Re\{[\mathbf{E} \times \mathbf{H}^*] \cdot \mathbf{e_z}\} dxdy}{\int \int_{D_{int}} Re\{[\mathbf{E} \times \mathbf{H}^*] \cdot \mathbf{e_z}\} dxdy}.$$
(11.3)

E and H are the electric and magnetic field vectors, respectively, and  $e_z$  is the unit vector in z direction [28]. There are three different cases in order to choose the domain of interest. In case of common strip-waveguides the domain of interest is equal to the core region,  $D_{int} = D_{core}$ . In contrast to that, for bio-sensing applications the region of the cover medium is considered to be the domain of interest,  $D_{int} = D_{cover}$ , which is valid for strip- and slot-waveguides as well. Considering slot-waveguides for EO modulators the domain of interest is equal to the slot

region,  $D_{int} = D_{slot}$ . There is also a change of refractive index outside of the slot since the electric field is also located outside. This contribution is, however, very small compared to that one insight the slot if we assume the linear EO effect (Pockels effect)

$$\Delta n = -\frac{1}{2} \cdot n_0^3 \cdot r_{33} \cdot E \cdot \Gamma, \tag{11.4}$$

where  $n_0$  and  $r_{33}$  are the refractive index and the most meaningful coefficient of the linear EO tensor of the organic material, respectively. The Pockels effect require indeed a non centro-symmetrical orientation of the EO polymers or non centro-symmetric organic crystals. Because of that, the main part of the electric field which gives an contribution to the refractive index change is the x-component. The x-component is homogeneous insight the slot. Outside there is just a little projection of the x-component which contributes. All possible domains of interest are illustrated in Fig. 11.4. In case of low-index-contrast waveguides like optical fibers, (11.3) can be simplified using the linear relationship between the electric and magnetic field for a plane-wave

$$\frac{1}{2} \int \int Re\{ [\mathbf{E} \times \mathbf{H}^*] \cdot \mathbf{e}_z \} dxdy = \frac{1}{2} \frac{\beta}{\omega \mu_0} \int \int |\mathbf{E}|^2 dxdy, \tag{11.5}$$

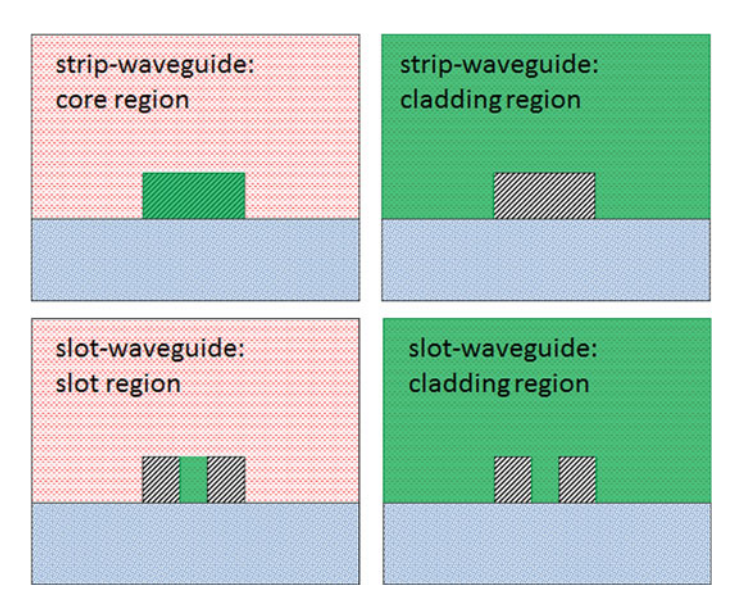


Fig. 11.4 Domains of interest: core  $D_{core}$ , cladding  $D_{clad}$  and slot  $D_{slot}$  regions are highlighted in green. Please note that the substrate is not included in the cladding region

which leads to

$$\Gamma = \frac{\int \int_{D_{tot}} |\mathbf{E}|^2 dx dy}{\int \int_{D_{tot}} |\mathbf{E}|^2 dx dy}.$$
 (11.6)

However, for high-index-contrast waveguides and especially for slot-waveguides different boundary conditions have to be taken in account and therefore this simplified relationship does not apply [24]. Consequently, in this work all confinement factors are calculated according to (11.3). It should be mentioned that in some cases it can be more convenient to apply (11.3) with the approximate numerator which leads to

$$\Gamma = \frac{n_{clad}}{Z_0} \frac{\int \int_{D_{int}} |\mathbf{E}|^2 dx dy}{\int \int_{D_{tot}} Re\{[\mathbf{E} \times \mathbf{H}^*] \cdot e_z\} dx dy},$$
(11.7)

with the free-space wave impedance  $Z_0 = \sqrt{\mu_0/\epsilon_0} \approx 377 \,\Omega$ . Equation (11.7) is useful if one is considering the concentration of the electric field in the region of interest. The reason for this approximation is because the polarizability of matter, and thus its refractive index change, is determined by the material response to the electric field [29].

There are several publications about field confinement factors of slot-waveguide structures. These structures consist of vertical silicon rails [24] or multiple nanolayers [25]. However, none of them consider SOI slot-waveguides with typical geometrical dimensions for CMOS-like production processes using 200 mm SOI wafers with 220 nm high SOH slot-waveguides.

# 11.3.2 Effective Nonlinear Area of Slot-Waveguides

A figure of merit of how well the waveguide geometry supports the nonlinear interaction is the so called effective nonlinear area [30]. The smaller the effective nonlinear area provided by the waveguide structure the higher the nonlinear interaction which is important for electro-optical modulators.

For the analysis of low-index-contrast systems, it is usually assumed that the gradient of the dielectric constant is approximately zero in the entire cross section. But this approximation is not valid for high-index-contrast material systems. Therefore, Koos et al. derived the effective nonlinear area for high-index-contrast waveguides in 2007 by using the slowly varying envelope approximation [30]. The effective nonlinear area results then from the nonlinear Schrödinger equation and is defined as

$$A_{eff} = \frac{Z_0^2}{n_{clad}^2} \cdot \frac{\left| \int \int_{D_{tot}} Re\{ [\mathbf{E} \times \mathbf{H}^*] \cdot \mathbf{e}_z \} dx dy \right|^2}{\int \int_{D_{tot}} |\mathbf{E}|^4 dx dy}.$$
 (11.8)

In our case the domain of interest is equal to the slot domain,  $D_{int} = D_{slot}$ . Equation (11.8) counts for high-index-contrast material systems. In case of low-index-contrast material systems instead it can be assumed that  $n_{core} \approx n_{clad} \approx n_{box} \approx n_{int}$ , and the longitudinal field becomes negligible [30]. Furthermore, the transverse components of the electrical field E and the magnetic field E and be approximated by a scalar function E with the condition  $E \approx F \cdot e_x$  and E0 are the unit vectors in E1 and E2 and E3 are the unit vectors in E3 and E4 direction, respectively [30]. Further it can be stated that E3 are the unit vectors in E4 and E5 are the nonlinearity is homogeneous in E6. Now (11.8) becomes simplified to

$$A_{eff} = \frac{\left(\int \int_{D_{tot}} |F|^2 dx dy\right)^2}{\int \int_{D_{tot}} |F|^4 dx dy},$$
(11.9)

which is similar to the common definition of an effective area [31].

## 11.4 Results and Discussion

Calculated effective refractive indices  $n_{eff}$  as a function of the slot width s of SOI slot-waveguides are shown in Fig. 11.5. For six different values of rail width w it

Fig. 11.5 Calculated effective refractive indices  $n_{eff}$  of SOI slot-waveguides as function of the slot width s and with the rail width w as parameter

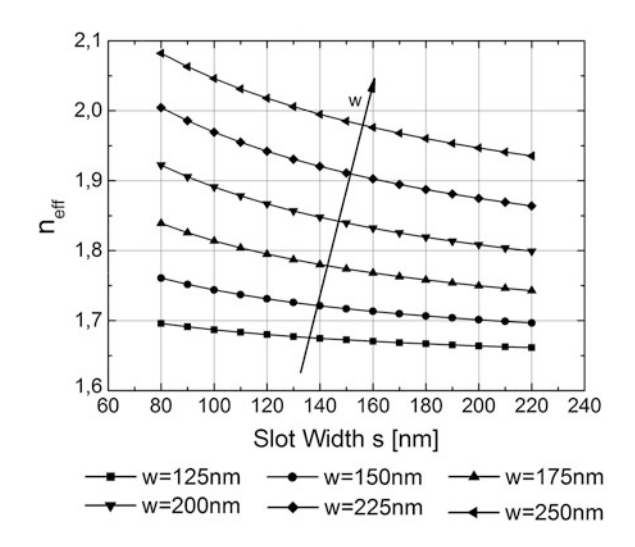
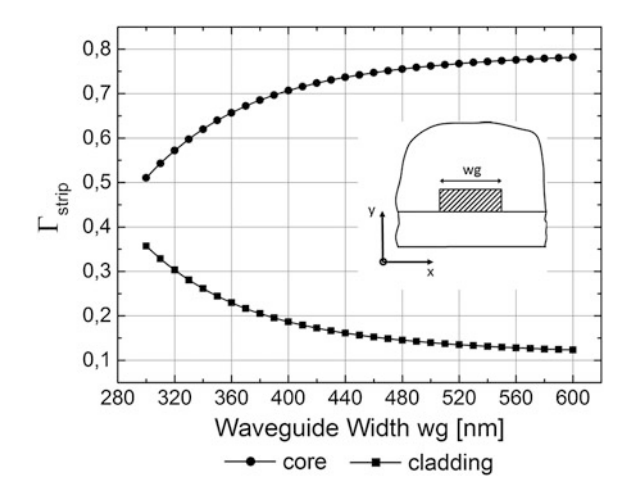


Fig. 11.6 Field confinement factor  $\Gamma_{strip}$  of conventional SOI strip-waveguides for the core and cladding region as a function of the waveguide width wg



can be seen that the effective refractive index becomes higher by increasing the rail width w and by decreasing the slot width s.

Figure 11.6 shows the obtained field confinement factor  $\Gamma_{strip}$  for a silicon strip-waveguide. The domains of interest are the core and the cladding. Note that the substrate is not included in the calculated domain and therefore, the sum of core and cladding field confinement factor is not equal to unity. As it can be seen there is a high light confinement in the core region. These results are in good agreement with the literature [12].

In order to maximize the sensitivity of SOI slot-waveguide based label-free sensors it is necessary to maximize the field confinement factor of the cladding  $\Gamma_{clad}$ . From Fig. 11.7 it can be seen that the confinement in the cladding region is increased by decreasing the rail width w and increasing the slot width s. For w=180 nm the highest confinement in the cladding region is obtained in the parameter range of our simulation. This result is in good agreement with [8]. For the slot-waveguide with w=180 nm and s=180 nm we obtain a field confinement factor of  $\Gamma_{clad}=0.69$ . This is an enhancement of about five times compared to a conventional strip-waveguide with a typical waveguide width of wg=500 nm. With that result, the high sensitivity of slot-waveguide based label-free sensors as stated by Claes et al. can be explained [10]. However, due to the difficulty in functionalising the interior of the slot the sensitivity could be smaller than expected.

In order to improve SOI slot-waveguides for electro-optical applications it is necessary to find the highest confinement in the slot region. Figure 11.8 depicts the obtained field confinement factors for the slot region  $\Gamma_{slot}$  as a function of the slot width s and the rail width s aparameter. It can be seen that there is one maximum of the highest field confinement of  $\Gamma_{slot}=0.216$  at a slot width of s=116 nm and a rail width of s=200 nm. This is about four times smaller compared to a SOI strip-waveguide (see Fig. 11.6). However, in this case it is more convenient to relate the field confinement factor  $\Gamma_{slot}$  to the area where the light is confined as

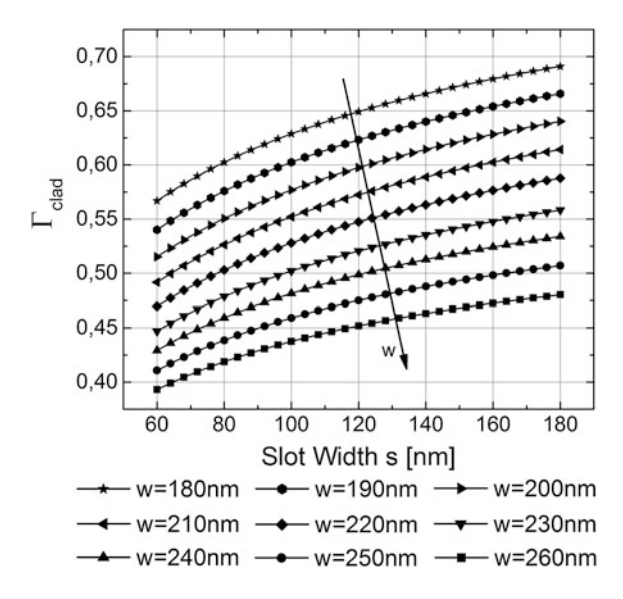


Fig. 11.7 Field confinement factor  $\Gamma_{clad}$  of a SOI slot-waveguide for the cladding region in dependence on the slot width s

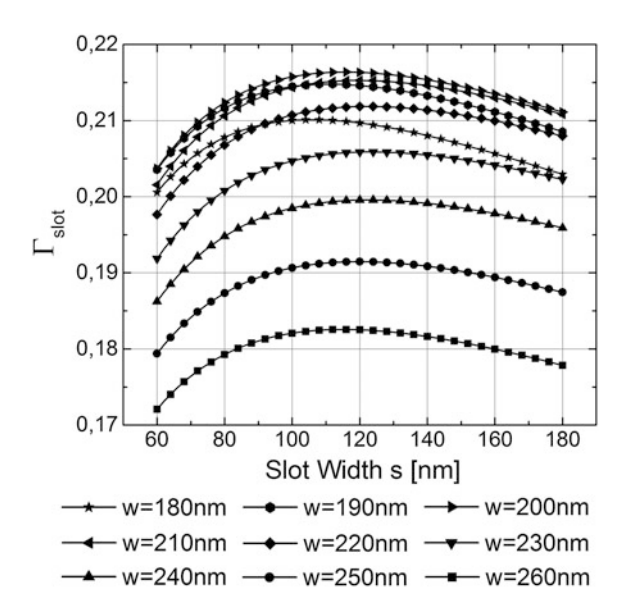


Fig. 11.8 Field confinement factor  $\Gamma_{slot}$  of a SOI slot-waveguide for the slot region as a function of the slot width s and the rail width s and s are rail width s are rail width s and s are rail wi

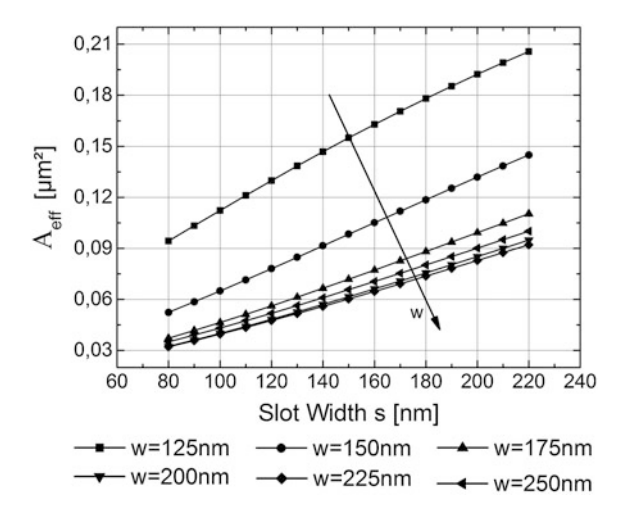


Fig. 11.9 Calculated effective nonlinear area  $A_{eff}$  of SOI slot-waveguides in dependence on the slot width s. The rail width w was varied as parameter

figure of merit,  $FOM = \Gamma_{slot}/A_{slot}$  and  $FOM = \Gamma_{strip}/A_{strip}$ . In our case  $A_{slot}$  is equal to  $D_{slot}$  and  $A_{strip}$  is equal to  $D_{core}$ . With that we can show for our example that the FOM for a SOI slot-waveguide (s = 116 nm, w = 200 nm) is about four times higher compared to that one of a strip-waveguide (wg = 500 nm). However, one should keep in mind that a modulator with extremely high field enhancement usually suffers very high optical loss [32]. This off-loss can make any modulator useless. Please note that the definition of (11.3) is only one possible way to describe the field confinement, as discussed in Sect. 3.1. With this definition an underestimation of the required interaction length for an EO phase modulator is ensured, but such estimation might lead to a field confinement factor that looks prohibitive for using such modulators. The key benefit of slot-waveguides is nevertheless the use of organic materials with EO coefficients which are more than one order of magnitude higher compared to semiconductors like GaAs or strained silicon.

Furthermore, for third order nonlinear applications it is necessary to minimize the effective nonlinear area  $A_{eff}$  in order to improve SOI slot-waveguides efficiency. Figure 11.9 indicates that there is a threshold in the parameter range of our simulation of  $A_{eff} = 0.032 \, \mu \text{m}^2$  for a slot width of  $s = 80 \, \text{nm}$  and a rail width of  $w = 225 \, \text{nm}$ . Also in this case our results are in good agreement with literature data [33].

### 11.5 Conclusion

Simulation and analysis of SOI slot-waveguides have been carried out and both field confinement factors and effective nonlinear areas have been critically analyzed and thoroughly calculated with the Finite Element Method. Field confinement factors have been calculated in the slot and cladding region for electro-optical and biosensing applications, respectively. According to our simulation, SOI slot-waveguides provide about five times higher field confinement in the cladding region compared to conventional SOI strip-waveguides. These results can be used for design optimization in order to achieve optimal SOI slot-waveguide dimensions for sensing applications. For the slot region we have found a maximum confinement of  $\Gamma_{slot} = 0.216$  which is about four times smaller compared to a SOI strip-waveguide. However, normalizing it to the active area, the light confinement is four times higher. For the effective nonlinear area we calculated a minimum of about  $A_{eff} = 0.032 \, \mu m^2$  for our simulated parameter range. In general, we have demonstrated design trade-offs and an approach in order to improve SOI slot-waveguide structures by changing their constructive parameters.

Acknowledgements The authors would like to thank the German Federal Ministry of Education and Research (BMBF) for the financial support under contract no. 03FH086PX2, the University of Applied Sciences Wildau (THWi), Germany, and the Ministry of Science, Technology and Culture of the federal state Brandenburg, Germany, for financial support. The authors would also like to thank P. Prosposito, F. De Matteis, and R. De Angelis from the University of Rome Tor Vergata, Italy, S. Meister, S. Kupijai, and A. Al-Saadi from the Technical University Berlin, Germany, and L. Zimmermann, D. Knoll, D. Stolarek, J. Katzer, S. Lischke, H. Silz, B. Tillack, and W. Mehr from the Institute of High-Performance Microelectronics (IHP), Germany, for their encouragement and support in the framework of the Joint-Lab IHP-THWi.

### References

- Almeida, V.R., Xu, Q., Barrios, C.A., Lipson, M.: Guiding and confining light in void nanostructure. Opt. Lett. 29, 1209–1211 (2004)
- Leuthold, J., Koos, C., Freude, W., Alloatti, L., Palmer, R., Korn, D., Pfeifle, J., Lauermann, M., Dinu, R., Wehrli, S., Jazbinsek, M., Gunter, P., Waldow, M., Wahlbrink, T., Bolten, J., Kurz, H., Fournier, M., Fedeli, J.M., Yu, H., Bogaerts, W.: Silicon-organic hybrid electro-optical devices. Sel. Topics Quant. Electron., IEEE J. 19, 114–126 (2013)
- Baehr-Jones, T., Hochberg, M., Wang, G., Lawson, R., Liao, Y., Sullivan, P., Dalton, L., Jen, A., Scherer, A.: Optical modulation and detection in slotted silicon waveguides. Opt. Expr. 13, 5216–5226 (2005)
- Alloatti, L., Palmer, R., Diebold, S., Pahl, K.P., Chen, B., Dinu, R., Fournier, M., Fedeli, J.M., Zwick, T., Freude, W., et al.: 100 GHz silicon-organic hybrid modulator. Light: Sci. & Appl. 3(2014), e173
- Weimann, C., Schindler, P.C., Palmer, R., Wolf, S., Bekele, D., Korn, D., Pfeifle, J., Koeber, S., Schmogrow, R., Alloatti, L., Elder, D., Yu, H., Bogaerts, W., Dalton, L.R., Freude, W.,

Leuthold, J., Koos, C.: Silicon-organic hybrid (soh) frequency comb sources for terabit/s data transmission. Opt. Expr. 22, 3629–3637 (2014)

- Gould, M., Baehr-Jones, T., Ding, R., Huang, S., Luo, J., Jen, A.K.Y., Fedeli, J.M., Fournier, M., Hochberg, M.: Silicon-polymer hybrid slot waveguide ring-resonator modulator. Opt. Expr. 19, 3952–3961 (2011)
- Korn, D., Palmer, R., Yu, H., Schindler, P.C., Alloatti, L., Baier, M., Schmogrow, R., Bogaerts, W., Selvaraja, S.K., Lepage, G., Pantouvaki, M., Wouters, J.M., Verheyen, P., Campenhout, J.V., Chen, B., Baets, R., Absil, P., Dinu, R., Koos, C., Freude, W., Leuthold, J.: Silicon-organic hybrid (soh) iq modulator using the linear electro-optic effect for transmitting 16qam at 112 Gbit/s. Opt. Express 21, 13219–13227 (2013)
- 8. Dell'Olio, F., Passaro, V.M.: Optical sensing by optimized silicon slot waveguides. Opt. Expr. **15**, 4977–4993 (2007)
- 9. Barrios, C.A., Gylfason, K.B., Sánchez, B., Griol, A., Sohlström, H., Holgado, M., Casquel, R.: Slot-waveguide biochemical sensor. Opt. Lett. 32, 3080–3082 (2007)
- Claes, T., Molera, J., De Vos, K., Schachtb, E., Baets, R., Bienstman, P.: Label-free biosensing with a slot-waveguide-based ring resonator in silicon on insulator. Photon. J., IEEE 1, 197–204 (2009)
- Steglich, P., Villringer, C., Dümecke, S., Michel, Y.P., Casalboni, M., Schrader, S.: Silicon-on-insulator slot-waveguide design trade-offs. In: Ribeiro, P.A., Raposo, M. (eds.) PHOTOPTICS 2015, Vol. 2., SCITEPRESS pp. 47–52 (2015)
- 12. Vivien, L., Pavesi, L. (eds.) Handbook of silicon photonics. 0 edn. CRC Press, USA (2013)
- 13. Baehr-Jones, T., Hochberg, M., Walker, C., Scherer, A.: High-q optical resonators in silicon-on-insulator-based slot waveguides. Appl. Phys. Lett. **86**, 081101 (2005)
- Palmer, R., Alloatti, L., Korn, D., Schindler, P., Baier, M., Bolten, J., Wahlbrink, T., Waldow, M., Dinu, R., Freude, W., Koos, C., Leuthold, J.: Low power mach-zehnder modulator in silicon-organic hybrid technology. Photon. Technol. Lett., IEEE 25, 1226–1229 (2013)
- Leuthold, J., Koos, C., Freude, W., Alloatti, L., Palmer, R., Korn, D., Pfeifle, J., Lauermann, M., Dinu, R., Wehrli, S., et al.: Silicon-organic hybrid electro-optical devices. Select. Topics Quant. Electron., IEEE J. 19, 3401413 (2013)
- Palmer, R., Koeber, S., Woessner, M., Elder, D.L., Heni, W., Korn, D., Yu, H., Lauermann, M., Bogaerts, W., Dalton, L.R., Freude, W., Leuthold, J., Koos, C.: High-speed silicon-organic hybrid (soh) modulators with 230 pm/v electro-optic coefficient using advanced materials. In: Optical Fiber Communication Conference. Optical Society of America, USA (2014) M3G.4
- Korn, D., Jazbinsek, M., Palmer, R., Baier, M., Alloatti, L., Yu, H., Bogaerts, W., Lepage, G., Verheyen, P., Absil, P., Guenter, P., Koos, C., Freude, W., Leuthold, J.: Electro-optic organic crystal silicon high-speed modulator. Photon. J., IEEE 6, 1–9 (2014)
- Palmer, R., Alloatti, L., Korn, D., Schindler, P., Schmogrow, R., Heni, W., Koenig, S., Bolten, J., Wahlbrink, T., Waldow, M., Yu, H., Bogaerts, W., Verheyen, P., Lepage, G., Pantouvaki, M., Van Campenhout, J., Absil, P., Dinu, R., Freude, W., Koos, C., Leuthold, J.: Silicon-organic hybrid mzi modulator generating ook, bpsk and 8-ask signals for up to 84 Gbit/s. Photon. J., IEEE 5, 6600907 (2013)
- Liu, Y., Baehr-Jones, T., Li, J., Pomerene, A., Hochberg, M.: Efficient strip to strip-loaded slot mode converter in silicon-on-insulator. Photon. Technol. Lett., IEEE 23, 1496–1498 (2011)
- Palmer, R., Alloatti, L., Korn, D., Heni, W., Schindler, P., Bolten, J., Karl, M., Waldow, M., Wahlbrink, T., Freude, W., Koos, C., Leuthold, J.: Low-loss silicon strip-to-slot mode converters. Photon. J., IEEE 5, 2200409 (2013)
- Ding, R., Baehr-Jones, T., Kim, W.J., Xiong, X., Bojko, R., Fedeli, J.M., Fournier, M., Hochberg, M.: Low-loss strip-loaded slot waveguides in silicon-on-insulator. Opt. Expr. 18, 25061–25067 (2010)
- Alasaarela, T., Korn, D., Alloatti, L., Säynätjoki, A., Tervonen, A., Palmer, R., Leuthold, J., Freude, W., Honkanen, S.: Reduced propagation loss in silicon strip and slot waveguides coated by atomic layer deposition. Opt. Expr. 19, 11529–11538 (2011)

- Steglich, P., Mai, C., Stolarek, D., Lischke, S., Kupijai, S., Villringer, C., Pulwer, S., Heinrich, F., Bauer, J., Meister, S., Knoll, D., Casalboni, M., Schrader, S.: Novel ring resonator concept combining strong field confinement with high optical quality factor. Photon. Technol. Lett., IEEE 27(16), 1737–1740 (2015)
- Robinson, J.T., Preston, K., Painter, O., Lipson, M.: First-principle derivation of gain in high-index-contrast waveguides. Opt. Expr. 16, 16659–16669 (2008)
- Feng, N.N., Michel, J., Kimerling, L.: Optical field concentration in low-index waveguides. Quant. Electron., IEEE J. 42, 885–890 (2006)
- 26. Palik, E.D.: Handbook of optical constants of solids. 1 edn. Academic Press, USA (1997)
- 27. Tsang, H., Wong, C., Liang, T., Day, I., Roberts, S., Harpin, A., Drake, J., Asghari, M.: Optical dispersion, two-photon absorption and self-phase modulation in silicon waveguides at 1.5 μm wavelength. Appl. Phys. Lett. **80**, 416–418 (2002)
- 28. Chuang, S.L.: Physics of photonic devices. 2 edn. Wiley, New York (2009)
- Robinson, J.T., Chen, L., Lipson, M.: On-chip gas detection in silicon optical microcavities. Opt. Expr. 16, 4296–4301 (2008)
- Koos, C., Jacome, L., Poulton, C., Leuthold, J., Freude, W.: Nonlinear silicon-on-insulator waveguides for all-optical signal processing. Opt. Expr. 15, 5976–5990 (2007)
- 31. Agrawal, G.: Nonlinear fiber optics. 5 edn. Academic Press, USA (2012)
- Steglich, P., Villringer, C., Dümecke, S., Michel, Y.P., Casalboni, M., Schrader, S.: Design optimization of slot-waveguides covered with organic cladding materials for integrated photonic devices. In Middendorf, S., Hüttinger, G. (eds.) NWK 16, BERLINER WISSENSCHAFTS-VERLAG GmbH, 192–198 (2015)
- 33. Muellner, P., Wellenzohn, M., Hainberger, R.: Nonlinearity of optimized silicon photonic slot waveguides. Opt. Expr. 17, 9282–9287 (2009)

# **Author Index**

A André, Ricardo Melo, 3	O Okamura, Yasuyuki, 83
C	P
Casalboni, Mauro, 173	Pain, Frédéric, 19
Cesaro, Stella Nunziante, 53	Palucci, Antonio, 53
Chen, Xiaoyong, 35	Pandey, Praveen Chandra, 119
<b>D</b>	Pereira, G., 63
D	Prabhakar, Anil, 157
Dolatyari, Mahboubeh, 145	Puiu, Adriana, 53
F	Pulwer, Silvio, 173
Frazão, Orlando, 3	R
Tiazao, Offando, 5	Ravi, Harish, 157
G	Rostami, Ali, 145
Giubileo, Gianfranco, 53	Rostami, Ghassem, 145
,	,
H	S
Haidar, Darine Abi, 19	Schrader, Sigurd, 173
Hamzeh, Hussein, 19	Shishegar, Amir Ahmad, 105
Horche, Paloma R., 35	Singh, Bipin Kumar, 119
<b>T</b> 7	Steglich, Patrick, 173
K Vonna Ataushi 92	Т
Kanno, Atsushi, 83 Kawanishi, Tetsuya, 83	Tavousi, Alireza, 145
Krishnamoorthy, Shree, 157	Torabi, Abdorreza, 105
Kumar, Pradeep K., 157	Totabi, Abdoneza, 103
Trainer, Tradeep Tr., 157	$\mathbf{V}$
L	Villringer, Claus, 173
Lefort, Claire, 19	<i>5</i> , ,
	$\mathbf{W}$
M	Wei, Liu, 19
Marques, Manuel J.B., 3	Wijayanto, Yusuf Nur, 83
McGugan, M., 63	
Mikkelsen, L.P., 63	Y
Murata, Hiroshi, 83	Yamamoto, Naokatsu, 83

# Index

A	Crack growing/damage, 63
Absorption peaks, 56	CST simulation, 151
After-pulsing, 163	
Algorithm, 70, 79	D
All-fiber MZI, 36, 38, 49	Data matrix, 59
Antennas, 84	Data transfers, 84
Array, 92	DCF, 31
Avalanche current, 159	DCF core diameter, 29
Average photon numbers, 168	Delamination, 64
Axial resolutions, 21	Delay coefficient, 43, 44
	Deposition, 6
B	Designed device, 94
Band gap, 126	Detect and track cracks, 79
Bandwidth, 126, 131	Detection angles, 150
Beam line, 149	Detection method, 62
Bifurcated fibre, 23	Detect multi-peaks, 71
Binary statistics, 161	DGD, 49
Binomial distribution, 161	Differential phase shift keying, 35
Bit patterns, 167	Digital clock managers, 165
Bragg micro-grating, 11	Digital image correlation, 74
Bragg micro-grating spectra, 13	Dispersion curves, 129
Breakdown voltage, 159	Dispersion diagram, 147, 149
	Dispersion relation, 123
C	Displacement current, 88
Calculation results, 40	Double cantilever beams, 73
Cancer, 20	Double clad fibre (DCF), 21
Cantilever Fabry-Perot, 11	DPSK demodulator, 45, 50
CGF-RFFM, 106	
Characteristic Green's function, 106	E
CO <sub>2</sub> laser, 54	Effective dark counts, 163
Continuous spectrum contribution, 109	Effective dielectric constant, 88
Convergence, 115	Efficiency, 159
Corners, 112	Electric field, 127
Coupling coefficient, 40	Electric field distributions, 90
CPU-time, 116	Electric field intensity, 127
Crack/delamination detection, 67	Electrodes, 91
Crack detection algorithm, 70, 71	Electron-plasmon momentum coupling, 146
Crack/fracture phenomena, 65	Electrons and atoms, 5
Crack growth, 67	Embedded FBG, 69

192 Index

Emission spectrum of the background	Graded layer, 124, 127
fluorescence from the GRIN, 24	Graded photonic crystals (GPCs), 120
End-facet, 105, 114	Gradient index (GRIN), 19
Endomicroscopes, 20	Grading profile parameter, 121, 139
EO crystal, 95	Grating length, 151
EO modulators, 85	Green's function, 107
Evanescent wave, 149, 153	GRIN lens, 21, 25, 31
Excited modes, 37	Guided, 112
Experiment, 43	Guided modes reflectivity, 107
Experimental procedure, 73	•
Experimental results, 74	H
Explosives precursors, 54	Height threshold, 71
Exponential graded layer, 121, 140	High-speed photo detectors, 97
Exponentially varying refractive index, 121	Homemade explosives, 55
Exponential reconvolution, 25	Hydrofluoric acid, 10
	•
F	I
Fabry-Perot cavities, 9	Imaging, 6
Fabry-Perot interferometers, 4	Imbalanced detection, 46
Fabry-Perot micro-cavity, 9	Improvised explosive devices, 53
FBG response, 67	Incoherent (spontaneous) SP radiation, 149
FBG response during a crack growth, 79	InGaAs APD, 159
FBG response stages, 67	Initial values, 111
FBG signal processing, 79	Inorganic substances, 58
Fiber cantilevers, 10	Instrument response function, 25
Fiber microstructure, 3	Integrated photonic, 175, 177
Fiber networks, 99	Interference extinction ratio, 36
Fibre Bragg grating, 63, 66, 68	Ion beam, 3
Fibre Bragg gratings embedded, 79	Ion beam diameter, 5
Fibre bridging, 65	Ion beam technology, 13
Fibre crack bridging, 64	Irradiation angle, 96
Fibre reinforced polymer, 63	Isopropanol, 13
Fibre tip, 28	1 1
Field distribution, 39	K
Field of view (FOV), 21, 31	Kramer's rate, 162
Field programmable gate array, 165	•
Fi-Wi links, 97	L
Fluorescence emission spectrum, 23	Laser photo-acoustic spectroscopy (LPAS), 54,
Focused ion beam (FIB), 4, 6, 12	56, 61
Forbidden, 126	Lateral resolution, 21, 28
Fourier transform, 11	Lifetime, 163
Fracture test, 73, 74	Lifetime decay, 27
Free-space communication, 83	Loading plot, 60
FRP material, 64, 66	Low dielectric constant, 86
FT-IR, 56	,
FT-IR analysis, 55	M
<b>3</b> ,	Mach-Zehnder interferometer (MZI), 36
G	Magnification, 31
GAPD system, 168	Meandering-gap patterns, 97
Gated avalanche detector, 159	Meandering gaps, 87, 93
Geiger, 159	Measurement setup, 95
40 GHz, 95	Metallic grating, 149
, ,,,	Bruning, 1 17

Index 193

Method of moments, 111	Phase difference, 42
Micro-cavity milled, 9	Photoacoustic spectra, 59
Microwave, 83	Photon arrival statistics, 158
Microwave-photonic, 84	Photon counting detectors, 157
Millimeter-wave backhaul, 100	Photonic, 120
Millimeter-wave beam-steering, 98, 100	Photonic band gap, 119, 126, 131, 132, 136
Millimeter-wave frequency, 96	Photonic bands, 124
Millimeter-wave polarization, 90	Photonic band spectra, 132
Millimeter-wave signal, 87	Photonic bandwidth, 139
Milling, 6	Photonic crystal, 119
MIMO, 99	Photon number resolution, 157
Mixed mode crack growth, 77	Piezoelectric scanning system (PZT), 19
MMF model, 45	Pockels EO effect, 87
Modal reflectivity, 106	Poissonian statistics, 167
Mode I crack growth, 77	Polarization mode dispersion (PMD), 49
Mode II crack growth, 78	Power difference, 40
Modes of vibration, 60	Power distribution, 40
Modulation efficiency, 92, 96	Principal component analysis (PCA), 58, 61
Multilayered, 116	Probability, 167
Multi-photon resolving detector (MPRD), 164,	Projected reflection band spectra, 137
168	Projection band structure, 132, 136
100	Proximity interaction, 154
N	Pure solid substances, 55
Narrowband optical filtering, 47	PZT scanning system, 31
Negative group velocity region, 149	121 scanning system, 51
Noise statistics, 163	Q
Nonlinear microscopy, 20	QKD, 157
Non-uniform strain, 76	QPM array, 86
Normalized far field polar plot, 152	QPM EO modulators, 91
Number of peak, 76	QPM structures, 91, 94
rumber of peak, 70	Quarter-wave, 132
0	Quarter wave, 132  Quarter wave arrangements, 126
Object WD, 29, 31	Quarter-wave stacking, 139
Omni-directional band, 132	
	Quazi-leaky wave poles, 112
Omni-directional band gap, 120, 132, 136	R
Omni-directional photonic band gap, 120	
Optical crystal thickness, 89	Rational function fitting method, 106
Optical fiber applications, 8	Receiver, 45
Optical fiber sensors, 3, 4	Recirculating loop, 164
Optical modulator, 84	Reconvolution method, 27
Optical signal to noise ratio (OSNR), 35, 47	Reflection coefficient, 105, 106, 108, 110–112,
Optimization, 111	114–116, 123, 131, 139
Orthogonal optical, 89	Reflection conditions, 127
Overlap integral method, 38	Reflection phase shift, 129
<b>n</b>	Reflection spectra, 124
P	Reflectivity, 114
PA signal, 58	Refractive index, 110
Patch-antennas, 85, 94	Relativistic factor, 147
Peak height, 71	Response to uniform variation of strain, 69
Peak splitting, 76	Response under non-uniform strain, 70
Peak width, 71	Response under transverse force, 69
Peltier, 159	Rhodamine B (RhB), 22

S	TE-polarization, 132, 136
Sample field points, 112	Terahertz, 146
Selective detection, 54	TE-wave, 132
SEM micrograph, 10	THz radiation source, 146
Sensitive elective detection, 54	Time-correlated single photon counting
Sensitivity penalty, 46	(TCSPC), 25
Separable structure, 108	Time delay, 43
Separation, 106	Time Harp 200 acquisition card, 25
Signal processing, 70	TM-polarization, 132, 136
Silicon-organic hybrid (SOH) technology, 174	Traditional explosives, 53
Simulation design, 45	Transfer matrix approach, 122
Single-mode-multimode-single-mode-fiber	Transit-time, 93
(SMS) structure, 36	Transmission, 166
Single photon detectors, 168	Transmission spacing, 42, 44
Single sideband, 97	Transmission spectra, 44
Singularities, 109	Transmission spectrum, 41
$SiO_2$ , 95	Transmittance coefficient, 123
Slot waveguide, 176	Transmitter, 45
Smith-Purcell based THz source, 148	Transverse offset, 37
Smith–Purcell radiation (SPR), 146	Travelling electron beam, 154
SMS structure, 39, 40	Truncated waveguide, 109
Source, 112	Tubular PZT, 28
9.2-10.8 μm spectral range, 56	
Spectral resolution, 153	$\mathbf{U}$
Spectral variance, 59	Uniform representation, 111
Spoof surface plasmon, 154	Uniform strain, 76
Stages of the crack growth, 76	
Stochastic resonance, 162, 168	V
Surface eigenwaves, 146	VECTFIT algorithm, 109
Surface plasmon polariton (SPP), 146	
Synchronous point, 149	$\mathbf{W}$
	Wave width $\Delta \lambda_{IW}$ , 76
T	
Tail fitting, 27	${f Z}$
Tapered fiber tips, 8	Zemax program, 29
Temporal behaviour, 151, 152	